

**FAILURE ASSESSMENT OF BURIED OFFSHORE PIPELINES
SUBJECTED TO UPHEAVAL BUCKLING**

by

© **Rabindra Subedi**

B.E., M.Sc.

A thesis submitted to the
School of Graduate Studies
in partial fulfilment of the requirements for the degree of

Doctor of Philosophy

Faculty of Engineering & Applied Science

Memorial University of Newfoundland

October 2023

St. John's

Newfoundland

Canada

Abstract

Offshore pipelines transport hydrocarbons at high operating pressure and temperature (HPHT) conditions. The thermal expansion and internal pressure can create large axial compressive forces in a pipeline, resulting in global buckling. In offshore, proper trenching and backfilling operations are challenging. Therefore, depending on the soil resistance, the pipeline might experience severe vertical movement during HPHT operating conditions. An insufficient burial depth might result in the pipeline moving upwards (upheaval buckling) from the original configuration, leading to local buckling instability and ultimate plastic collapse. The buckled section of the offshore pipeline may undergo local sectional deformation (ovalization), tensile rupture and fracture due to high levels of stress and strain, depending upon the operating conditions, sectional properties and uplift soil resistance. The initial imperfection is another factor that governs the initiation and buckling types for the buried or surface-laid pipeline.

Recognizing the limitations in the existing theoretical solutions and design guidelines in modelling initial imperfection and soil resistances, the present study focuses on numerical modelling and strain-based structural assessment for global upheaval buckling, local buckling, and fracture in offshore pipelines. Several soil-spring resistance models based on current design guidelines, e.g., bilinear and trilinear, are used to evaluate the upheaval buckling (UHB) behaviour of pipelines. The nonlinear degradation of uplift resistance for dense and loose sand for modelling large vertical displacements (post-upheaval above ground) of the buried pipeline is also investigated. Besides, the present study explores the effects of initially stressed and unstressed imperfections on the upheaval buckling characteristics of the offshore buried pipelines.

The limitation of the one-dimensional finite element model in predicting sectional deformation and local buckling is solved through a hybrid three-dimensional coupled finite element (FE) model. This computationally efficient model integrates a three-dimensional finite element model of the pipe and shell, accounting for operating temperature and pressure effects on a long pipe with nonlinear soil springs. It enables analysis of post-upheaval buckling, local buckling, and

wrinkling failure in the pipelines.

To investigate the tensile fracture associated with local buckling, this study also presents a numerical modelling technique using the eXtended finite element (XFEM) method to analyze the initiation and propagation of tensile fractures in a post-buckled offshore pipeline. Conventional fracture mechanics commonly employ damage initiation criteria based on maximum principal stress (MAXPS) or maximum principal strain (MAXPE) with fixed values. However, these criteria may be overly conservative, neglecting crack-tip constraints during the numerical analysis. To address this challenge, a modified Mohr-Coulomb (MMC) fracture criterion is proposed and implemented into the FE program Abaqus through a user-defined subroutine. The proposed MMC criterion considers shear slip and ductility, providing a more realistic representation of ductile materials than MAXPS and MAXPE models. This study also discusses the calibration of fracture parameters with different damage degradation models.

The proposed modelling techniques for large deformation FE modelling of global upheaval buckling, local buckling (ovalization and wrinkling), and fracture prediction address the design and integrity challenges in the offshore pipeline industry. The outcomes of the present study can play a vital role in assessing the structural integrity of offshore pipelines, leading to improved pipeline design and enhanced operational safety in offshore environments.

This thesis is dedicated to my parents, to whom I owe everything.

Acknowledgements

I am deeply humbled and would like to express my profound gratitude to the remarkable individuals who have played pivotal roles in shaping and completing this thesis:

First and foremost, I express my heartfelt appreciation to my distinguished Supervisor, Dr. Bipul Hawlader, for being an invaluable pillar of support and providing meticulous guidance throughout this research journey. His unwavering faith in my abilities, visionary perspectives, and illuminating feedback has been instrumental in shaping the outcome of this thesis. This work would not have come to fruition without his mentorship and constant motivation.

I am deeply grateful to my co-supervisor, Dr. Ashutosh Dhar, for his valuable guidance, constructive suggestions, and engaging discussions that have refined my ideas and elevated the calibre of this work.

I am deeply grateful for the contributions of my supervisory committee member Dr. Kshama Roy, whose remarkable insights, prompt guidance, and constructive feedback have greatly enhanced the content, coherence, and clarity of this thesis.

I am grateful for the technical help and support from my colleagues, especially Dr. Rajith Dayarathne, Dr. Bipul Mondal, Dr. Jin Chen, and Riadul Arman, during the initial phase of my research.

Additionally, I would like to thank the School of Graduate Studies, MUN, Government of Newfoundland and Labrador, NSERC, Statoil, and Wood Group research chair for their financial support, which has been instrumental in completing this thesis.

I am deeply indebted to my family and in-laws for their support and continuous encouragement throughout this journey.

Last but certainly not least, my beloved wife, Pratibha, and our wonderful daughters, Ritisha and Trisha, deserve special recognition. Their love, patience, understanding, encouragement, and sacrifices fueled my dedication to this thesis. Special thanks go to Er. Dhiraj KC and Nagina Shrestha for their constant help and support during the difficult times in this journey.

Table of Contents

Abstract	ii
Acknowledgements	v
List of Figures	xi
List of Tables	xxi
List of Abbreviations	xxii
List of Symbols	xxiii
Chapter 1 Introduction	1
1.1 Background and motivation	1
1.2 Thesis objectives	7
1.3 Methodology	7
1.4 Thesis organization	8
Chapter 2 Literature Review	10
2.1 Introduction	10
2.2 Literature review on upheaval buckling and soil resistances	10
2.2.1 Upheaval buckling (UHB)	10
2.2.2 Uplift soil resistance	15

3.5.2	Base case FE simulation results	76
3.5.2.1	Pipeline buried in dense sand	76
3.5.2.2	Pipeline buried in loose sand	78
3.5.3	Modelling of differential pressure (p)	79
3.5.4	Effects of axial soil resistance on vertical buckling of pipeline	80
3.5.5	Effects of the shape of post-peak uplift resistance reduction	82
3.6	Parametric Study	84
3.6.1	Effects of initial imperfection and embedment ratio	84
3.6.2	Vertical deformation and plastic shear strain	84
3.6.3	Effects of pipe diameter and wall thickness on upheaval buckling	86
3.6.4	Initial stress	87
3.7	Conclusions	90

Chapter 4 Finite Element Modelling of Buried Offshore Pipeline for Global Upheaval Buckling Leading to Local Buckling 92

4.1	Introduction	93
4.2	Problem statement	96
4.3	Numerical modelling	98
4.4	Soil resistance for buried pipeline	100
4.4.1	Axial, lateral and bearing resistances	100
4.4.2	Uplift soil resistance	103
4.5	Validation of hybrid FE model with analytical solution	104
4.6	Comparison of FE modelling approaches	107
4.7	Results from the hybrid model	113
4.7.1	von Mises stress distribution	114
4.7.2	Plastic strain envelope	116
4.7.3	Plastic strain versus buckle amplitude and temperature	118

5.7	Results of pipeline analysis	193
5.7.1	Results from MAXPS fracture criterion	193
5.7.2	Results from MAXPE fracture criterion	199
5.7.3	Results from MMC fracture criterion	201
5.7.4	Fracture profile comparison with different damage models	204
5.8	Conclusions	211
Chapter 6	Conclusions and Recommendations for Future Research	213
6.1	Conclusions	213
6.2	Recommendations for future research	218
	Bibliography	220
Appendix A	Conference Paper	232
A.1	Some aspects of offshore pipeline design against upheaval buckling	232

List of Figures

Figure 1.1	Typical use of subsea hydrocarbon pipelines, illustrating the potential area of upheaval buckling (after Bai and Bai 2005)	3
Figure 1.2	Stages of deformation in a postbuckled HPHT offshore pipeline, representing the scope and progression of the thesis research (after Shinkai et al. 2012)	4
Figure 2.1	The mechanism of upheaval buckling problem in offshore pipeline (after Thusyanthan et al. 2010)	11
Figure 2.2	Offshore pipeline operating temperature trend (after Carr et al. 2003)	12
Figure 2.3	Large vertically buckled section of pipe in North sea (after Nielsen et al. 1990)	13
Figure 2.4	Field report showing large buckling problem in buried pipeline	14
Figure 2.5	Effect of post-peak degradation on buckling: (a) Effects of soil resistance model on buckling; (b) Uplift soil resistance with nonlinear post-peak degradation (after Klever et al. 1990)	16
Figure 2.6	Uplift force–displacement response: (a) Linear model; (b) With post-peak softening (after Goplen et al. 2005)	17
Figure 2.7	Uplift resistance model for loose and dense sand (after Bransby et al. 2002)	18
Figure 2.8	Uplift soil resistance model: (a) Peak; (b) Infilling with localization; (c) Flow-around mechanism (after Cheuk et al. 2008)	19
Figure 2.9	Uplift soil resistance model (after Wang et al. 2009)	20

Figure 2.10 Bilinear soil spring model for pipe-soil interaction: (a) Axial spring; (b) Bearing and uplift spring; (c) Lateral/horizontal spring (after ALA 2005)	21
Figure 2.11 Trilinear uplift force–displacement response (after DNV 2007)	22
Figure 2.12 Uplift force–displacement behaviour (after Nielsen et al. 1990)	24
Figure 2.13 Soil slip surface models: (a) Vertical slip surface model for loose sand; (b) Inclined slip surface model for dense sand	25
Figure 2.14 Axial force distribution in a pipeline with imperfection (after Hobbs 1984) .	30
Figure 2.15 Analytical solution of temperature rise versus buckle amplitude (after Hobbs 1984)	32
Figure 2.16 Idealization for upheaval buckling of HPHT pipeline (after Taylor and Gan 1986)	33
Figure 2.17 Analytical solution of temperature rise versus buckle amplitude	35
Figure 2.18 Analytical solution of upheaval buckling: (a) Axial force versus buckle amplitude; (b) Compressive stresses versus buckle amplitude	36
Figure 2.19 Typical imperfection configuration: (a) Basic contact undulations (empathetic); (b) Isolated prop imperfection; (c) Infilled prop imperfection (after Taylor and Tran 1996)	38
Figure 2.20 Initial imperfection profiles based on different mathematical models	39
Figure 2.21 Comparisons of initial imperfection profile with the Gaussian shape	41
Figure 2.22 Schematic diagram for modelling stressed initial imperfection: (a) Application of self load on a straight pipeline; (b) Pipe ends are moved down to the bed; (c) Rigid bed is removed and spring can be activated for UHB analysis . .	42
Figure 2.23 Schematic idealization: (a) Pipe/soil interaction with the continuum elements; (b) Idealization of the problem with beam and soil-spring structural elements (after Kenny and Jukes 2015)	44

Figure 2.24 Nonlinear force–displacement response in SPRING1 element (after Simulia 2016)	45
Figure 2.25 Load–displacement response for unstable equilibrium	46
Figure 2.26 Deformation stages in a offshore pipeline during upheaval buckling, local buckling and fracture (after Shinkai et al. 2012)	48
Figure 2.27 Typical sectional moment–curvature response in a pipeline (after Hauch and Bai 2000)	49
Figure 2.28 Typical strain ranges in offshore pipeline based on application (after Bai and Bai 2005)	53
Figure 3.1 Problem layout and spring locations: (a) Problem layout and key features of the postbuckled pipeline; (b) 1D FE model with soil-spring locations	63
Figure 3.2 Mesh sensitivity analysis with varying element size	66
Figure 3.3 Uplift force–displacement response	69
Figure 3.4 Calibration of finite element model by comparing with analytical solutions	75
Figure 3.5 Response of pipeline for the base case simulations: (a) Pipeline buried in dense sand; (b) Pipeline buried in loose sand; (c) Comparison with simulation of unburied conditions	77
Figure 3.6 Comparison of response with direct modelling of differential pressure and equivalent temperature: (a) Dense sand for $\tilde{\nu}_{om} = 0.005$; (b) Dense sand for $\tilde{\nu}_{om} = 0.011$; (c) Loose sand for $\tilde{\nu}_{om} = 0.005$; and (d) Loose sand for $\tilde{\nu}_{om} = 0.011$	81
Figure 3.7 Effects of axial resistance in the buckled section	82
Figure 3.8 Effects of nonlinear and linear post-peak degradation of uplift resistance	83
Figure 3.9 Response of pipeline in medium sand: (a) Effects of burial depth; (b) Pipeline displacement; and (c) Axial strain development	85
Figure 3.10 Effects of pipeline geometry: (a) Effects of diameter; (b) Effects of wall thickness	87

Figure 3.11 Response of initially stressed and stress-free pipelines: (a) Initial stress effects on temperature; (b) Plastic strain development at $\tilde{\nu}_{om} = 0.007$; (c) Plastic strain development at $\tilde{\nu}_{om} = 0.01$	89
Figure 4.1 Problem statement and finite element modelling: (a) Problem layout with initial imperfection; (b) Hybrid finite element model; (c) Soil spring location	97
Figure 4.2 Element shape and sizes used for the mesh sensitivity analysis: (i) Coarse S4R mesh throughout; (ii) Fines S4R quad mesh at the center critical zone; (c) Fine triad (S3) mesh at the central critical zone	101
Figure 4.3 FE simulation results from different mesh sizes: (i) Coarse quad S4R mesh; (ii) Fines quad S4R mesh; (iii) Fine triad S3 mesh; (iv) Experimental result from Murray (1997)	102
Figure 4.4 Modelling of soil resistances: (a) Axial; (b) Lateral; and (c) Vertical (uplift and bearing)	102
Figure 4.5 Validation of FE results with analytical solutions	106
Figure 4.6 Comparison of buckling response from various modelling techniques: (a) Element types	109
Figure 4.6 Comparison of buckling response from various modelling techniques: (b) Effects of spring locations	110
Figure 4.6 Comparison of buckling response for varying modelling techniques: (c) Effects of coupling constraints	111
Figure 4.7 Effects of modelling techniques for varying differential pressure	113
Figure 4.8 Development of von Mises stress in buckled section with vertical displacement of the pipe	114
Figure 4.9 Development of plastic strain envelope at the critical section of buckled pipe	117
Figure 4.10 Plastic strain development at the invert and crown during buckling: (a) Plastic strain development with buckle amplitude	119

Figure 4.10 Plastic strain development at the invert and crown during buckling: (b) Plastic strain development with temperature increase	120
Figure 4.11 Plastic strain development at the invert and crown with the variation in differential pressure: (a) Plastic strain development with buckle amplitude at compression side (invert)	121
Figure 4.11 Plastic strain development at the invert and crown with the variation in differential pressure: (b) Plastic strain development with buckle amplitude at tension side (crown)	122
Figure 4.12 Sectional ovalization during buckling: (a) Ovalization with temperature increase	124
Figure 4.12 Sectional ovalization during buckling: (b) Ovalization with increase in buckle amplitude	125
Figure 4.13 Development of wrinkles sizes with the increases in buckle amplitude . . .	126
Figure 4.14 Moment with plastic strain: (a) Plastic strain variation at invert and crown .	127
Figure 4.14 Axial force with buckle amplitude: (b) Axial force distribution	129
Figure 4.15 Moment–Curvature relation during buckling progression	130
Figure 4.16 Thin and thick pipe buckling behaviour: (a) Effects of temperature	132
Figure 4.16 Thin and thick pipe buckling behaviour: (b) Plastic strain with moment . .	133
Figure 4.17 Ovalization behaviour of thin, thick, and intermediate pipe during buckling .	134
Figure 4.18 Effects of pipeline material models: (a) Buckling response with temperature increase	135
Figure 4.18 Effects of pipeline material models: (b) Moment–curvature behaviour	136
Figure 4.18 Effects of pipeline material models: (c) Plastic strain development at invert .	137
Figure 4.18 Effects of pipeline material models: (d) Plastic strain development at crown	138
Figure 4.18 Effects of pipeline material models: (e) Plastic strain increment with sectional moment	140

Figure 4.18 Effects of pipeline material models: (f) Plastic strain increment with buckle amplitude	140
Figure 4.18 Effects of pipeline material models: (g) Plastic strain profile along the pipe length	141
Figure 4.19 Effects of initial imperfection on local buckling: (a) Buckling response with temperature increase	142
Figure 4.19 Effects of initial imperfection on local buckling: (b) Moment–Curvature response	143
Figure 4.19 Effects of initial imperfection on local buckling: (c) Plastic strain increase with moment	144
Figure 4.19 Effects of initial imperfection on local buckling: (d) Plastic strain development with buckle amplitude	145
Figure 4.19 Effects of initial imperfection on local buckling: (e) Plastic strain development with buckle amplitude	146
Figure 4.19 Effects of initial imperfection on local buckling: (f) Plastic strain development along the pipe length at operating temperature T of 100 °C	147
Figure 4.20 Effects of soil resistance models on local buckling: (a) Temperature–uplift movement	148
Figure 4.20 Effects of soil resistance models on local buckling: (b) von Mises and axial strain distribution along the pipe	149
Figure 4.20 Effects of soil resistance models on local buckling: (c) Plastic strain increment with moments	150
Figure 4.21 Effects of D/t on local buckling: (a) Uplift displacement response with temperature increase	151
Figure 4.21 Effects of D/t on local buckling: (b) Critical temperature trend with variable D/T	152

Figure 4.21 Effects of D/t on local buckling: (c) Plastic strain development with buckle amplitude	153
Figure 4.22 Effects of D/t on local buckling: (a) Plastic strain development for \tilde{v}_{om} of 0.009	154
Figure 4.22 Effects of D/t on local buckling: (b) Plastic strain development for \tilde{v}_{om} of 0.013	155
Figure 4.23 Effects of D/t on local buckling: (a) von Mises stress development for \tilde{v}_{om} of 0.009	156
Figure 4.23 Effects of D/t on local buckling: (b) von Mises stress profile for \tilde{v}_{om} of 0.013	156
Figure 4.24 Effects of D/t on local buckling: (a) Trend of critical buckling strain in primary and secondary local buckling zones with varying D/t.	157
Figure 4.24 Effects of D/t on local buckling: (b) Secondary local buckling span with variable D/t	158
Figure 5.1 Problem statement with an initial imperfection: (a) Problem statement and Inset-I: Coupled 1D pipe and 3D shell (Hybrid FE model); (b) Shape of initial imperfection (\tilde{v}_0)	169
Figure 5.2 Nonlinear soil-spring model used for the 3D FE analysis: (a) Axial; (b) Lateral; and (c) Vertical springs (after ALA 2005; DNV 2007)	170
Figure 5.3 Post-buckled shape of the HPHT pipeline at the onset of local buckle on the compression side	171
Figure 5.4 FE problem description for the post-buckled fracture assessment (not in scale)	172
Figure 5.5 The illustration of displacement jump function across the crack surfaces in XFEM	175
Figure 5.6 The principle of the phantom node approach in XFEM (after Simulia 2016)	177

Figure 5.7	The typical traction-separation laws: (a) For brittle material with linear degradation and (b) For ductile material with inverted cup shape nonlinear degradation (after Schwalbe et al. 2013)	178
Figure 5.8	Representation of lode angle (θ) and MMC yield locus (after Bai and Wierzbicki 2010): (a) Typical coordinate system with lode angle; (b) Yield locus for plane stress condition	183
Figure 5.9	Symmetric finite element model with mesh distribution for post-UHB fracture assessment: (a) Finite element symmetric model with loading and boundary conditions; (b) Location of initial crack and mesh distribution (shape of initial crack at Inset-I)	186
Figure 5.10	True stress–strain curve for X65 steel pipe with power law fitting	188
Figure 5.11	Specimen for SENT and SENB test	190
Figure 5.12	SENT and SENB finite element models with boundary conditions: (a) SENT finite element model; (b) SENB finite element model	192
Figure 5.13	Crack opening and propagation at SENT specimen with linear and exponential softening damage model: (a) Crack propagation in SENT model with linear softening damage model; (b) Crack propagation in SENT model with exponential softening damage model	194
Figure 5.14	SENT and SENB specimen force-deformation responses with XFEM based fracture analysis with MAXPS and MMC: (a) SENT specimen Force-CMOD relation; (b) SENB specimen Force-CMOD relation	195
Figure 5.15	Axial force versus CMOD variation based on MAXPS fracture criterion for pipe	196

Figure 5.16 Fracture profile and status of XFEM enriched elements based on different values of MAXPS damage criterion: (a) MAXPS 960 MPa and fracture energy release rate, G_c of 450 N/mm; (b) MAXPS 1375 MPa and fracture energy release, G_c of 900 N/mm	198
Figure 5.17 Tensile crack propagation stages during uplift movement of the pipeline based on MAXPS damage criterion: (a) Uplift at 0; (b) Uplift at 0.19 m; (c) Uplift at 0.24 m; (d) Uplift at 0.35 m	199
Figure 5.18 Axial compression versus CMOD variation based on fixed MAXPE fracture criterion	200
Figure 5.19 Fracture propagation stages during uplift movement based on MAXPE damage criterion: (i) MAXPS = 0.013, G_c = 450 N/mm; (ii) MAXPE = 0.15, G_c = 200 N/mm	201
Figure 5.20 Axial compression versus CMOD variation based on variable MMC fracture criterion	203
Figure 5.21 Fracture surface profile and XFEM enriched element conditions based on MMC damage criterion: (i) G_c = 450 N/mm; (ii) MMC model with G_c = 200 N/mm	204
Figure 5.22 Fracture propagation stages during uplift movement of pipe based on MMC damage model: (a)–(e) from initial to final stage	205
Figure 5.23 Comparison of fracture opening and deformation with different damage initiation criterion: (a) MAXPE; (b) MAXPS; (c) MMC	206
Figure 5.24 Comparisons of fracture behaviour for three different damage criterion: (a) Axial compression versus CMOD; (b) CMOD versus uplift displacement; (c) CMOD versus crack growth; (d) Tensile strain development during uplift displacement at the crack mouth element	207
Figure 5.25 Tensile strain development during the onset and full separation of crack: (a) Tensile strain at the onset of crack propagation along thickness	208

Figure 5.25 Tensile strain development during the onset and full separation of crack: (b)	
Tensile strain at the instance when the crack fully extends through the thickness . . .	209
Figure 5.26 Crack opening displacement (COD) along the pipe thickness from the crack	
tip	210
Figure 5.27 Crack opening displacement (COD) along the circumferential crack	
propagation	210
Figure 5.28 Variation of stress triaxiality at the crack mouth element during incremental	
uplift movement of pipe	211

List of Tables

Table 2.1	Tensile and compressive strain criterion for onshore pipeline	50
Table 3.1	Geometry and pipeline model parameters used for base case FE simulations .	65
Table 3.2	Soil parameters used to develop nonlinear uplift force–displacement curves .	71
Table 4.1	Soil parameters used to develop force–displacement curves	104
Table 4.2	Geometry and pipeline model parameters used for base case FE simulations .	105
Table 5.1	Soil and geometric parameter used to develop nonlinear force-displacement curves	170
Table 5.2	Geometry and material properties used for the fracture assessment	187
Table 5.3	Plasticity and fracture parameter for strain-based MMC fracture model API X65	189

List of Abbreviations

ALA	American Lifelines Alliance
CSA	Canadian Standard Association
CZM	Cohesive Zone Method
CMOD	Crack Mouth Opening Displacement
COD	Crack Opening Displacement
FE	Finite Elements
HPHT	High Pressure & High Temperature
LB/UB	Lower/ Upper Bound
MAXPS	Maximum Principal Stress
MAXPE	Maximum Principal Strain
MMC	Modified Mohr Coulomb
OOS	Out of Straightness
PEEQ	Equivalent Plastic Strain
PHILSM	Signed Distance Function for crack Surface
PSILSM	Signed Distance Function for crack Front
SMYS	Specified Minimum Yield Stress
SBD	Strain Based Design
SENT	Single Edge Notched Tension
SENB	Single Edge Notched Bend
SIF	Stress Intensity Factor
TSC	Tensile Strain Capacity
UDMGINI	User Defined Damage Initiation
UHB	Upheaval Buckling
XFEM	eXtended Finite Element Method

List of Symbols

A	Cross-sectional area of pipe (m^2);
c_1	friction coefficient;
c_2	Shear resistance
D	Pipe external diameter (m);
D_r	Relative density of soil;
E	Young's modulus (GPa);
f	Uplift resistance factor;
f_o	Ovalization ratio of the pipeline;
F_A	Total axial frictional resisting force (N);
G_c	Critical Strain Energy release rate ($Pa.m^{1/2}$)
H	Cover height to the center of pipe (burial depth);
H_o	Initial depth of soil cover to the pipe crown (m);
$H(x)$	Heaviside function in XFEM
\tilde{H}	Initial embedment ratio (H/D);
I	Moment of inertia of section (m^4) ;
K_0	Coefficient of earth pressure at rest;
K_{IC}	Material fracture toughness (first mode SIF)
L_o	Initial imperfection wavelength (m) ;
L	Buckle wavelength of pipe (m);
N	Represented by Shape function
N_q, N_γ	Bearing capacity factors;
P	Upheaval buckling force (N);
p	Differential pressure ($p_i - p_{ext}$) (MPa);

P_o	The thermally induced axial compressive force;
q	Submerged self weight of pipe (N/m);
R_{max}	Maximum uplift resistance (N);
t	Pipe wall thickness (m);
T_{cr}	Critical buckling temperature;
T_{safe}	Safe buckling temperature;
T_y	Yield temperature;
u_ϕ	Axial displacement;
v_m	Buckle amplitude (m);
v_{om}	Central maximum amplitude of imperfection (m);
v_o	Initial vertical position of the pipeline from the horizontal datum (m);
\tilde{v}	Normalized vertical mobilization displacement (v/D);
\tilde{v}_p	Normalized vertical mobilization displacement at peak (v_p/D);
\tilde{v}_s	Normalized vertical mobilization displacement at post-peak softening state (v_s/D);
α	Coefficient of thermal expansion ($/^\circ C$);
γ	Specific surface Energy
γ_s	Unit weight of soil (kN/m^3);
γ'	Effective submerged unit weight of soil (kN/m^3);
δ_f	Vertical uplift resistance (m);
$\bar{\epsilon}_f$	Equivalent plastic strain at fracture
ϵ_{of}	First onset local buckling strain
ϵ_q^p	Equivalent plastic strain
ϵ_{os}	Secondary onset local buckling strain
$\bar{\theta}$	Lode angle

μ	Poisson's ratio ;
ν	Poisson's ratio of material
η	Stress triaxiality
ρ_s	Density of steel in air (kg/m^3);
ρ_o	Density of oil (kg/m^3);
σ_n	Normal stress
σ_y	Yield stress (MPa);
σ_y	Yield strength of material (Pa)
τ	Shear stress
ψ	Signed distance for the initial crack front in XFEM
ϕ	Friction coefficient between pipe and subgrade;
ϕ_a	Axial friction coefficient;
ϕ'	Effective internal frictional angle of soil;
ϕ'_c	Critical state friction angle;
ϕ'_p	Peak friction angle;
ψ_p	Peak dilation angle;
ϕ	Signed distance for the crack surface in XFEM
Ω	Domain for field of study

"The secret of getting ahead is getting started "

- Mark Twain

Chapter 1

Introduction

1.1 Background and motivation

Oil and natural gas are the non-renewable resources of the continuously increasing energy demand. In the current scenario of the globe, most of the hydrocarbon reserves on land and shallow water depths have been exploited. As the oil and gas recovery technology is developing, continuous exploration in the deep offshore reservoir is economically viable. Offshore oil and gas production has been increasing since the 1960s, where the steel pipeline is crucial for transporting hydrocarbon from the ocean. Although steel pipelines are the safest method for transporting hydrocarbon, their failure is unavoidable. The offshore pipeline might fail due to mechanical damages such as impacts (dents, cracks), surface corrosion, material failure and natural hazards. Typically, offshore buried pipelines operate at a high temperature (70–150°C) and high pressure (5–35 MPa) to prevent the formation of wax on the conveyance system as well as for the smooth flow of hydrocarbon (Carr et al., 2003; Hooper et al., 2004).

The high temperature and pressure in the flow system of a long pipe generate a vast amount of axial compressive stresses (characterized by the expansion due to thermal heating and internal pressure) when its thermal expansion is restrained, resulting in the pipeline buckling. Global buckling can occur in a pipeline either vertically (upheaval) or horizontally (lateral), depending upon its burial condition and soil resistance. The compressive load can cause the pipeline to buckle when the vertical/lateral and axial friction is insufficient to prevent movement. Two major geotechnical components that affect the prediction of upheaval buckling are the axial friction between the seabed soil and the pipeline and the uplift resistance of the backfill above the pipeline. Typically, buried pipelines in offshore environments travel a long distance through different soil

conditions while delivering hydrocarbon from the production to receiving end, as shown in Fig. 1.1.

The immediate purpose of burial is to prevent the pipeline layout from buckling and prevent damage due to trawlers or anchors. The burial provides flow assurance and prevents movement of the pipeline during operation. As the lateral resistance is high, the buried pipeline is typically more susceptible to upheaval buckling (UHB), where the pipeline might move vertically in the upward direction. If an upheaval buckling occurs, the pipeline might come out of the seabed, which creates additional serviceability issues, such as the damage by fishing gears, dropped objects, and submarine debris flow impact on the suspended section of the pipeline. The upheaval buckling of the trenched and buried pipeline is not primarily a failure mode, but the excessive vertical deformation (over-stressing) causes significant bending, leading to fractures in the pipeline. However, the design aim is to prevent upheaval buckling. The full-scale experimental study for the upheaval buckling, local buckling and fracture assessment of the long-buried pipeline is expensive and practically not feasible. Proper numerical modelling of pipe–soil interaction for global and local buckling and fracture assessment is the primary area of research.

The post-buckled section of the offshore pipeline may undergo local sectional deformation (ovalization), tensile rupture and fracture due to high levels of stress and strain, depending upon the operating conditions, sectional properties and soil resistance. The initial imperfection is another factor that governs the initiation and buckling types for the buried or surface-laid pipeline. The existing theoretical solutions and design guidelines have limitations in modelling initial imperfection and soil resistance. The current design guidelines DNV (2007) aim to ensure that the buried pipeline remains in place during operation. Some studies suggest that the buried pipeline can move vertically beyond the original configuration (even above the seabed); however, the failure is not pertinent. The critical strain for upheaval buckling of the pipeline is relatively higher than the strain at the onset of buckling, which varies with the operating conditions, sectional and material properties, initial imperfections (out-of-straightness) and soil resistance.

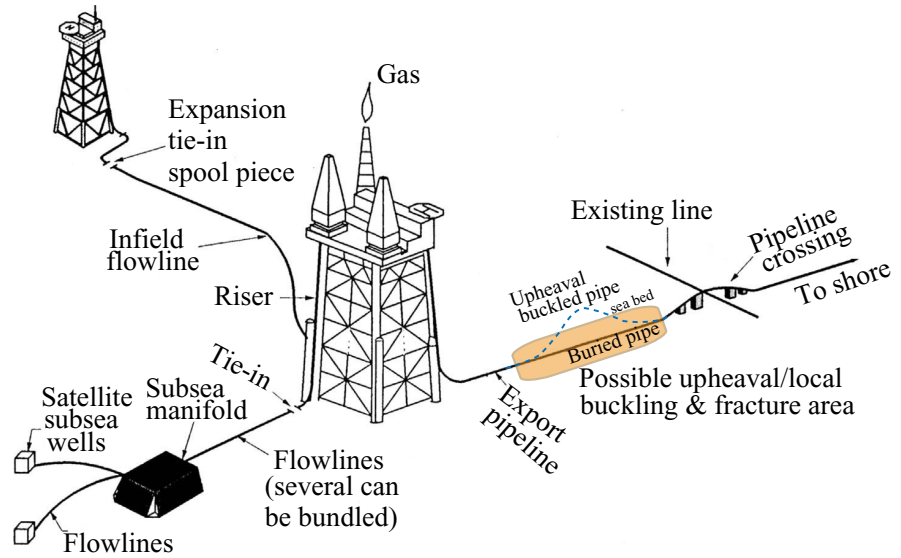


Figure 1.1: Typical use of subsea hydrocarbon pipelines, illustrating the potential area of upheaval buckling (after Bai and Bai 2005)

Over three decades, the upheaval buckling and failure behaviour of pipelines have been studied. However, there is some research gap in the pipe-soil interaction model and the structural response of the pipeline after large vertical deformation. According to Shinkai et al. (2012), the axial strain required to trigger local buckling in an offshore pipeline is generally higher than the onset strain for upheaval buckling. As axial compressive forces increases, the postbuckled pipeline transitions from global to local buckling, eventually leading to fractures. The variation of axial strain with increasing axial compression in the offshore pipeline, highlighting key features such as onset upheaval buckling, local buckling, and fracture, is presented in Fig. 1.2. Conducting an experimental test to conclusively determine the critical features of the postbuckled pipeline's transition from global upheaval buckling to local buckling and fracture is impractical. This research is driven by the objective of numerically simulating and comprehensively studying the failure mechanism of a buried offshore pipeline experiencing substantial movement beyond the seabed. The aim is to capture essential features of the pipeline, as illustrated in Fig. 1.2, including the onset of upheaval buckling (Phase-I), local buckling (Phase-II), and eventual fracture

(Phase-III), which helps the offshore pipeline industry in assessing the serviceability requirements of pipelines, taking into account potential upheaval buckling that may progress to local buckling and fractures.

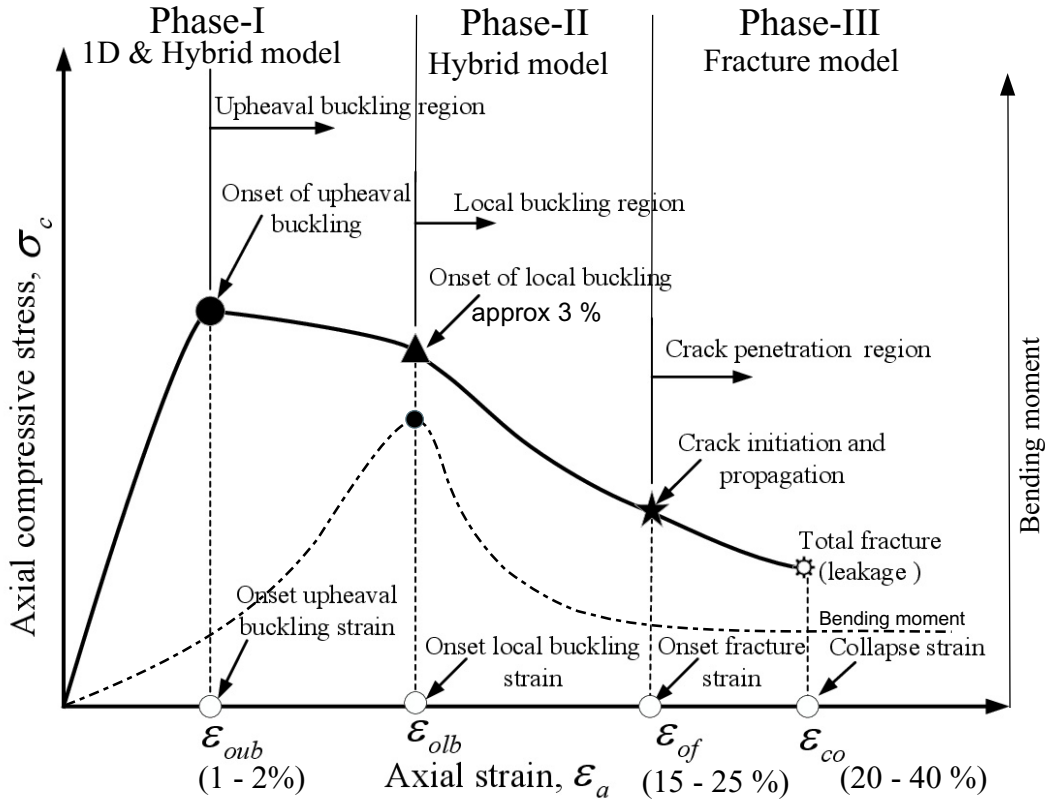


Figure 1.2: Stages of deformation in a postbuckled HPHT offshore pipeline, representing the scope and progression of the thesis research (after Shinkai et al. 2012)

For this purpose, nonlinear finite element modelling techniques in Abaqus Simulia (2016) are used. The computationally efficient numerical technique is developed for the upheaval and post-upheaval buckling of the offshore pipeline in 1D and hybrid coupled 3D framework. The effects of degradation in uplift resistance for dense and loose sand and other parameters are examined for upheaval buckling. The initiation of buckling and post-buckling behaviour are studied from buckled configuration and plastic strain generation in the pipeline. The developed 3D model accurately predicts the strain variation along the pipeline's cross-section, local buckling,

and sectional ovalization due to the combined effects of operating pressure and temperature.

Finally, the tensile fracture/rupture initiation and propagation of the post-buckled pipeline with the initial structural defects such as crack is numerically modelled using the eXtended finite element methods (XFEM) based cohesive segment approach in Abaqus finite element software. The inbuilt damage initiation criterion based on maximum principal stress (MAXPS) and maximum principal strain (MAXPE) assumes the fixed value of critical stress or strain, which might underestimate the fracture behaviour of the pipeline where the crack-tip constraint is ignored. The strain-based modified Mohr–Coulomb (MMC) fracture criterion considers the crack-tip constraint based on the variable strain profile as a function of stress triaxiality and lode angle parameters. The MMC fracture criterion is implemented in Abaqus using the user subroutine UDMGINI for the XFEM-based enriched elements of the pipeline. The FE results from three different damage initiation criteria, i.e., MAXPS, MAXPE and MMC, are compared for the development of crack initiation, propagation, opening and tensile strains in the post-buckled pipeline. The overall research highlights are presented in Chart 1.

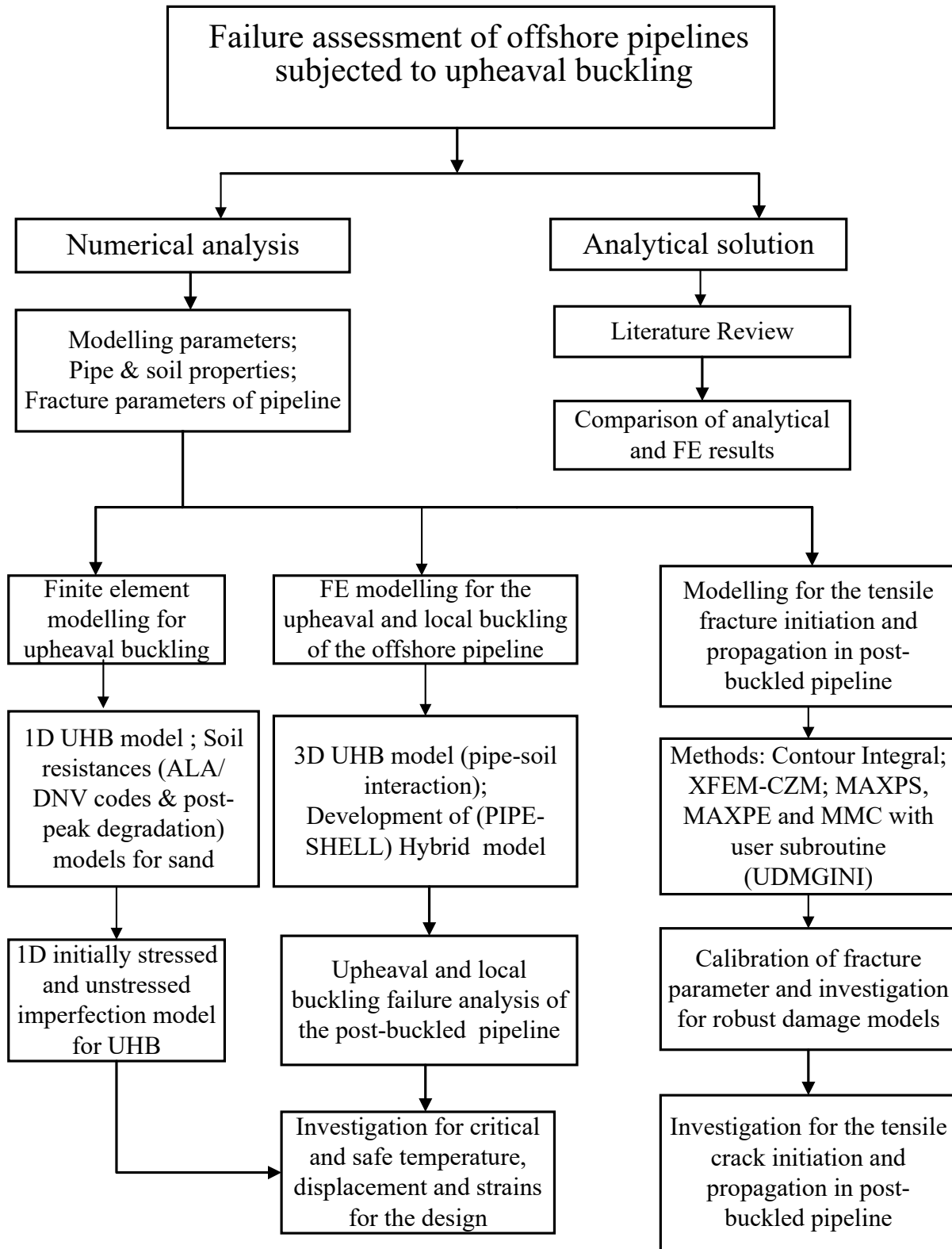


Chart 1: Research overview

1.2 Thesis objectives

The main objective of the thesis is to assess the response of buried offshore energy pipelines at shallow water depths undergoing significant vertical movement beyond the seabed that could cause upheaval and post-upheaval buckling. To achieve this, improved uplift soil resistance models for loose, medium, and dense sand are proposed. Computationally efficient one-dimensional (1D) and three-dimensional (3D) numerical models are developed by implementing the improved soil resistance models into Abaqus/Standard FE software.

Important findings for the design consideration for soil-structure interaction modelling and fracture of the post-buckled pipeline beyond the allowable strain limits are presented. A systematic study of the soil resistance and the structural response of the offshore pipeline during global buckling, local buckling, and fracture is performed.

1.3 Methodology

The following steps are carried out to achieve the objectives of this study:

1. Review of available literature related to this research, including upheaval buckling, local buckling and fracture of the offshore pipeline, soil-resistance model, and FE modelling approaches for the offshore pipelines.
2. Develop analytical solutions and a 1D numerical model based on soil spring for upheaval buckling of offshore pipelines in different soil conditions.
3. Investigate the effects of post-peak soil resistance models, axial resistance and stressed and unstressed initial imperfections on upheaval buckling and the strain-based structural assessment for a post-buckled pipeline.
4. Perform a series of parametric studies to understand the factors affecting the upheaval buckling (e.g., embedment depth, wall thickness, diameter, material and soil properties)

5. Develop a 3D FE model and conduct parametric studies for the global upheaval and local buckling of buried offshore pipelines due to the combined effects of temperature and pressure.
6. Develop a 3D numerical model for the tensile fracture initiation and propagation in a post-buckled offshore pipeline with the initial crack using the eXtended finite element method (XFEM) with user subroutine for damage initiation criterion UDMGINI in ABAQUS.

1.4 Thesis organization

This thesis is in manuscript format and is structured in six chapters with appendix. Chapters 3 to 5 are original manuscripts for publications.

This first chapter describes the background, motivations, scope, objectives and significant contribution of the present study.

Chapter 2 presents a literature review of the available models and research works that have been performed in the past for global buckling, local buckling, and fracture of the offshore pipeline. The analytical and finite element numerical methods for solving buckling and fracture problems of the pipeline are presented.

Chapter 3 presents the numerical modelling techniques of the offshore pipeline upheaval buckling with the unstressed and stressed initial imperfections. The soil resistance models, and design aspects of the offshore pipeline are explained. A part of this study has been published as a technical paper at the 72nd Canadian Geotechnical Conference (Geo St. John's, 2019) (Appendix A.1).

In **Chapter 4**, three-dimensional finite element modelling techniques are presented for the global upheaval buckling leading to local buckling of the buried offshore pipeline. The significant design considerations for the local buckling of the offshore pipeline during upheaval buckling are

discussed. A comparison of the numerical results with the current design codes is presented in this chapter.

In **Chapter 5**, the numerical modelling of the tensile fracture initiation and propagation in the post-buckled pipeline using eXtended finite element methods is presented. The significance of the MMC model with user subroutine UDMGINI for fracture propagation problems in large deformation is discussed. The material parameters for fractures are calibrated with the numerical model.

Finally, the major conclusions drawn from the present research are summarized and outlined in **Chapter 6** of the thesis. The main contribution of this thesis and the limitations are also provided in the conclusion section. The recommendations for further research in this area are included.

Chapter 2

Literature Review

2.1 Introduction

This chapter presents a comprehensive literature review on upheaval buckling, local buckling, and fracture issues in offshore pipeline, encompassing the mechanism involved. This chapter emphasizes the analytical and finite element solution approaches to enhance the better understanding of soil-structure interaction problems concerning upheaval buckling and fracture in offshore pipelines. The analytical solutions presented in the corresponding sections are solved by the author of this thesis using the MATLAB program. The detail literature review is provided unless otherwise specified in the corresponding chapters. Kindly be informed that there might be some overlap between the literature review and the corresponding chapters, considering that this thesis is written in manuscript format.

2.2 Literature review on upheaval buckling and soil resistances

2.2.1 Upheaval buckling (UHB)

Offshore steel pipeline experiences significant axial compression due to the thermal expansion caused by high operating temperature and pressure flow of hydrocarbons. As a consequence of this compression, the pipe is pushed upwards instead of lateral or downward directions, leading to upheaval buckling (Fig. 2.1). This occurs because the buried pipeline attains higher lateral and bearing resistances. The high operating temperature and pressure in the offshore pipeline can reach 150°C, and 35 MPa, respectively (Carr et al. 2003; Hooper et al. 2004; Cheuk et al. 2008). The increasing trend of high operating temperature in offshore pipeline is clearly demonstrated in

Fig. 2.2, as reported by Carr et al. (2003) at different subsea oilfield locations in the North Sea.

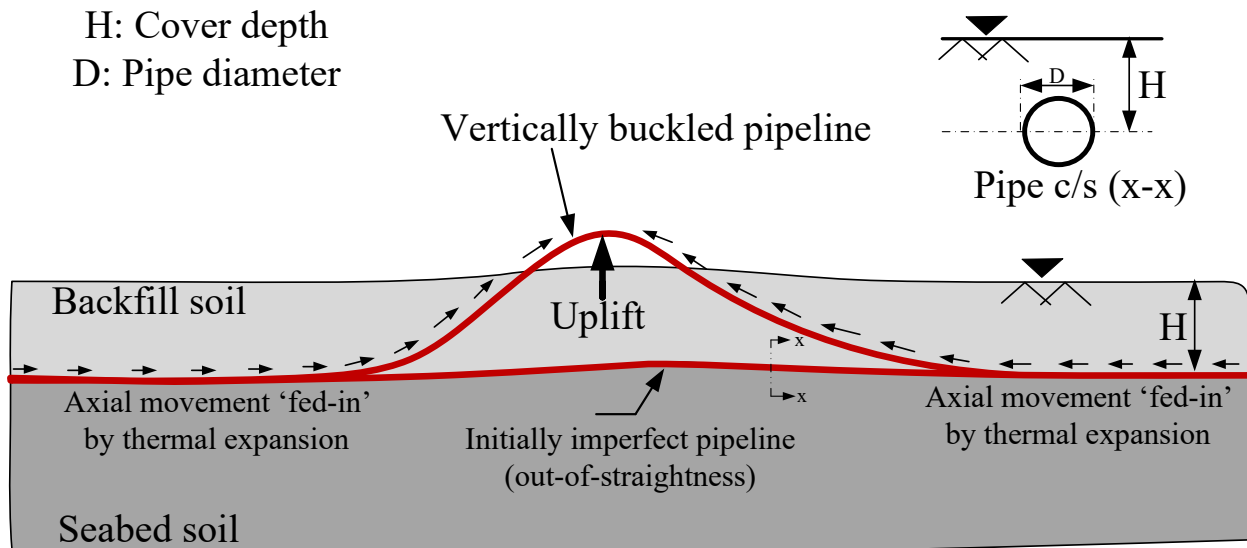


Figure 2.1: The mechanism of upheaval buckling problem in offshore pipeline (after Thusyanthan et al. 2010)

Upheaval buckling is one of the challenging design issues of pipeline in offshore environment. In shallow water, pipelines can be buried using trenching and backfilling techniques. The burial provides flow assurance and prevents movement of the pipeline during operation. Indeed, burying pipelines in offshore environments presents considerable challenges and is complex. The harsh offshore conditions, such as deep-water depths, strong currents, and uneven seabed terrain, make pipeline burial difficult.

Factors such as the availability of suitable equipment, operational logistics, and environmental considerations further contribute to the complexity of offshore pipeline burial. If an upheaval buckling occurs, the pipeline might come out of the seabed, which creates additional integrity issues, such as the damage by fishing gears, dropped object and submarine debris flow impact on the suspended section of the pipeline. The buckle section of the pipeline attains a higher level of stress and strain, leading to local buckling, fracture and fatigue in the long run (DNV, 2007).

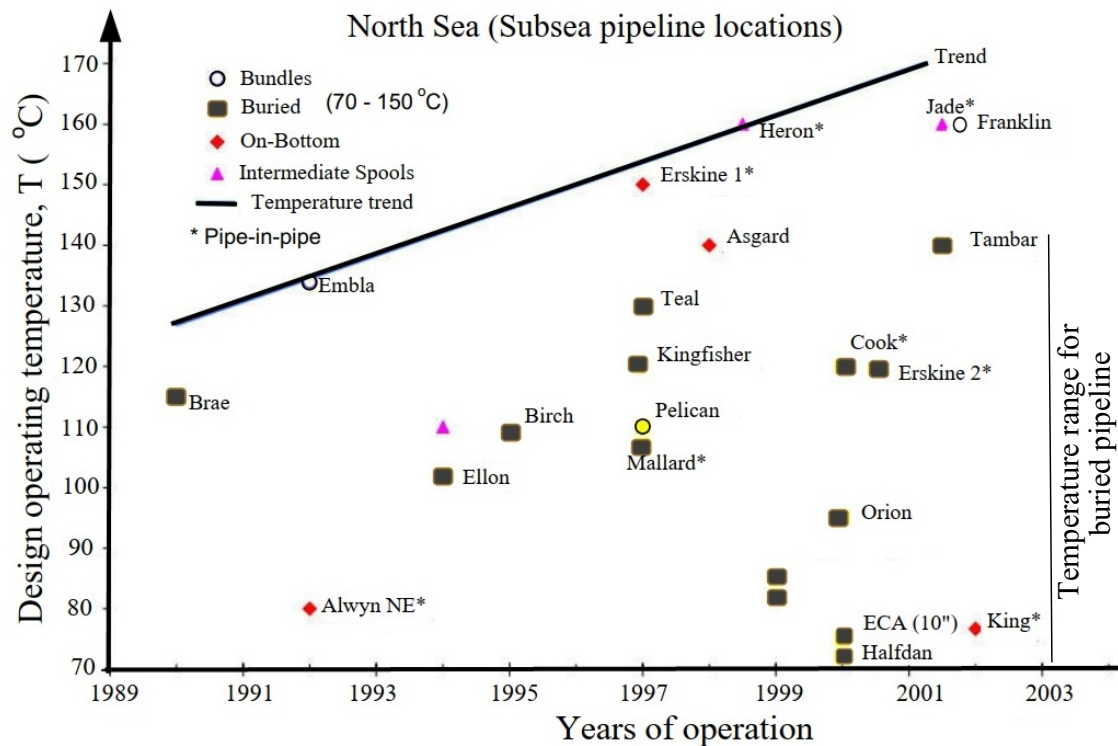


Figure 2.2: Offshore pipeline operating temperature trend (after Carr et al. 2003)

According to a report by Nielsen et al. (1990), an upheaval buckle incident occurred at 26 locations along a buried pipeline in the Danish sector of the North Sea. In one segment, a 10 m section moved 1.1 m above the seabed, although the structural failure of the pipeline did not occur. The buckled pipe section of 0.22 m outer diameter with operating temperature of 82°C after being taken out from the seabed is shown in Fig. 2.3. Figure 2.3 illustrates an offshore pipeline that is vertically buckle, featuring a buckling wavelength of 24 m and a total central rise of 2.6 m. Their field survey of the entire pipeline showed that some sections of the pipeline with severe out-of-straightness (imperfection) had resulted in a pipe moving upwards and above the seabed. Some field failure case studies of the offshore pipeline show that the upheaval buckling occur at a vertical displacement of 0.5–2 m and wavelength ranging from 24–70 m (Liu et al. 2013). Large vertical movement of buried pipelines has been observed in various field conditions within the pipeline industry. For instance, a case near Tashkent in Uzbekistan where a buried pipe section (frost heave zone) with a diameter of 1.02 m experienced vertical buckling of 4 m from the soil

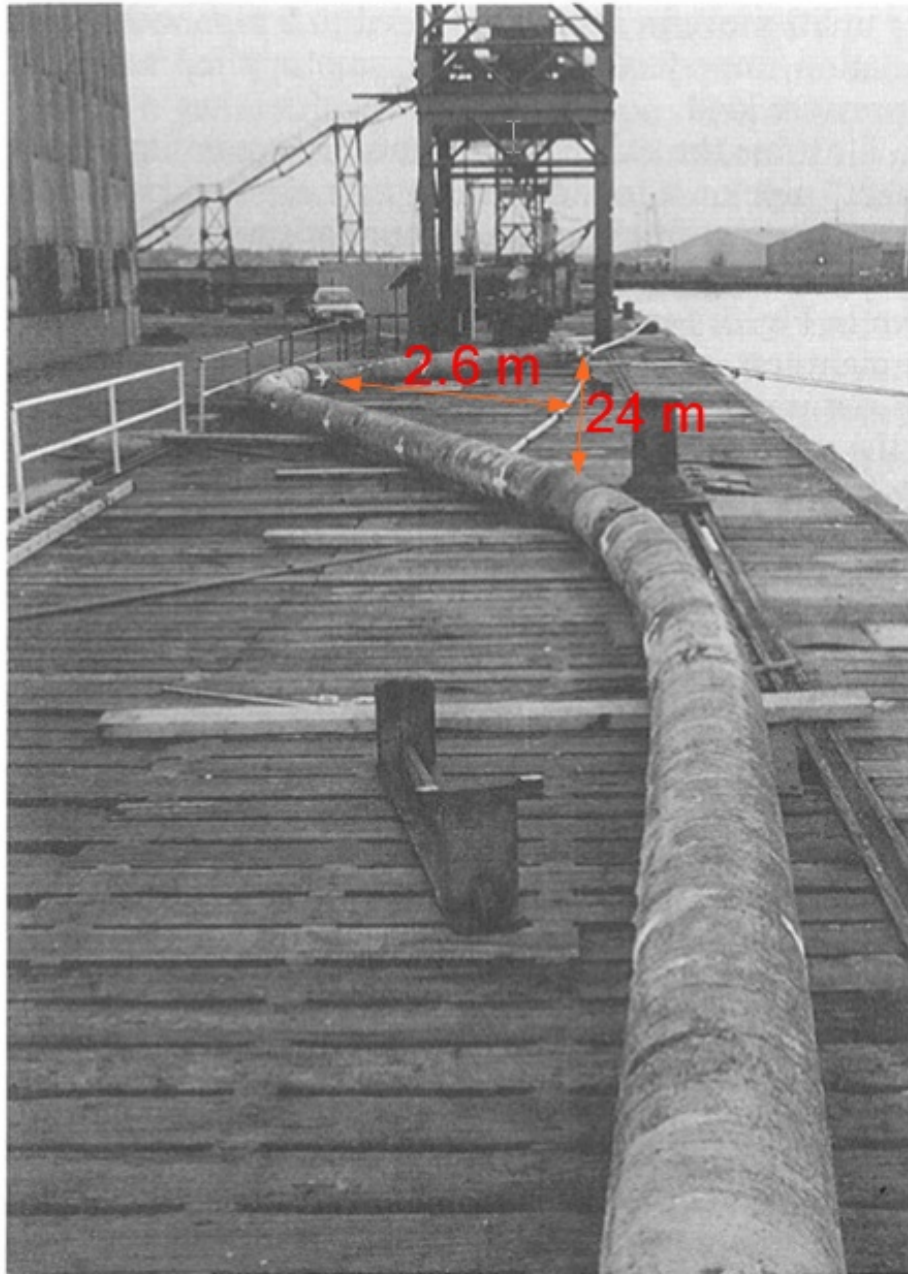


Figure 2.3: Large vertically buckled section of pipe in North sea (after Nielsen et al. 1990)

surface, spanning a wavelength of 70 m (Fig. 2.4) (Palmer and Williams 2003). The field observations indicate that large upheaval buckling is possible in onshore and offshore pipelines. Upheaval buckling and failure behaviour of offshore pipelines have been studied over three decades. The early experimental work conducted by Palmer et al. (1974) demonstrated that an

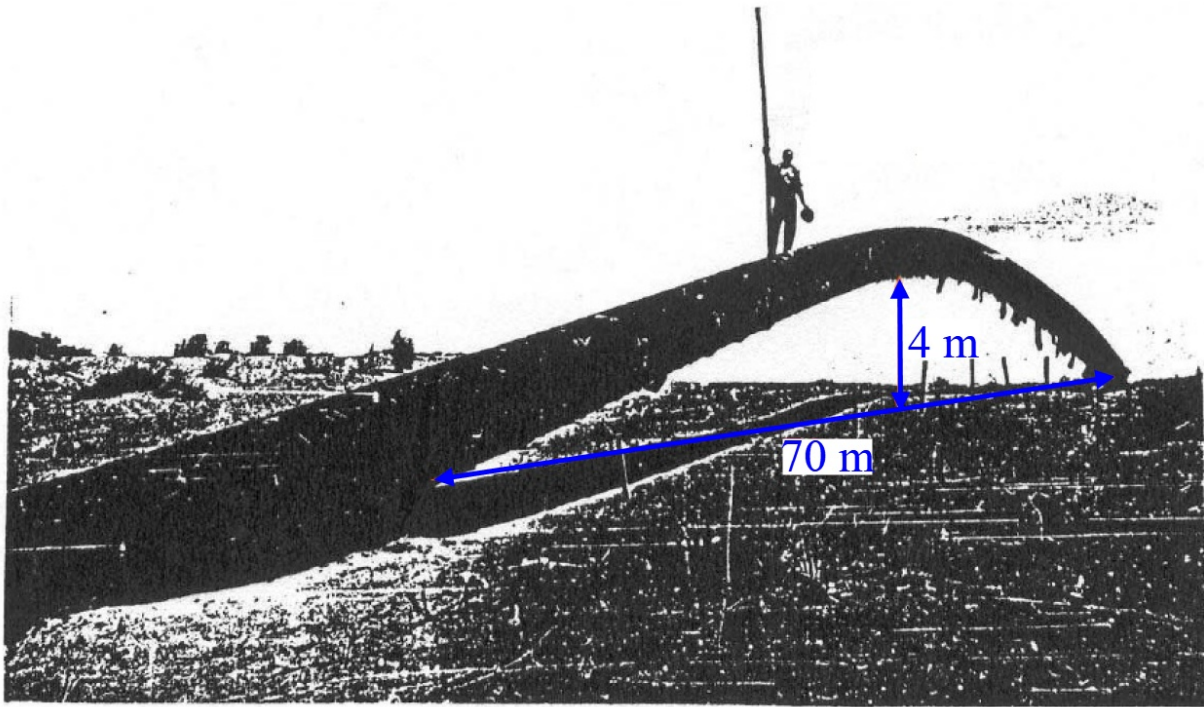


Figure 2.4: Field report showing large buckling problem in buried pipeline
(after Palmer and Williams 2003)

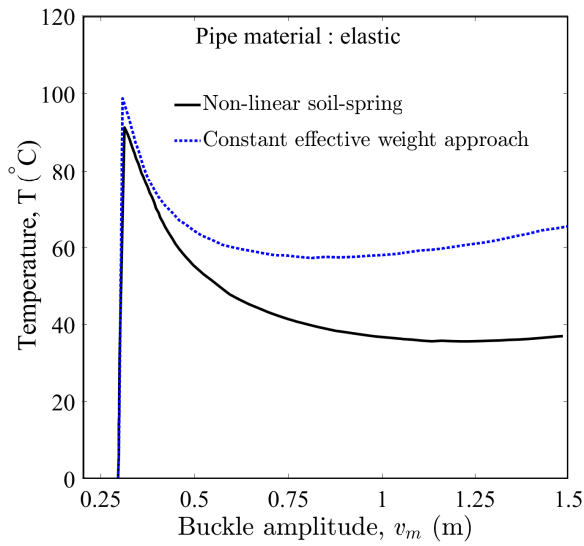
increase in internal pressure could cause the pipe to buckle. Tvergaard and Needleman (1981) developed a numerical solution for the localization of thermal buckling patterns of the railway track (Martinet 1934; Kerr 1972). The concept of buckling in offshore pipeline shares similarities with the phenomenon of buckling observed in railway tracks.

Further, Hobbs (1984) used the concept from Tvergaard and Needleman (1981) to develop analytical solutions for upheaval and lateral buckling of submarine pipelines. Hobbs (1981, 1984) also presented the vertical and lateral buckling modes observed in a offshore pipeline. Pedersen and Jensen (1988) considered the presence of initial imperfections in a pipe for upheaval buckling design and developed a mathematical model to analyze buckling. Palmer et al. (1990) developed a semi-empirical simplified solution for the preliminary design of submarine pipelines against upheaval buckling. Taylor and Gan (1986), and Taylor and Tran (1996) proposed the empathetic, isoprop and blister imperfection models for the submarine pipeline.

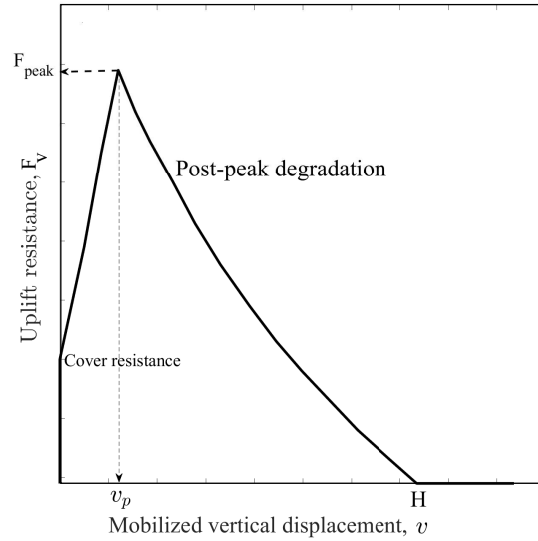
2.2.2 Uplift soil resistance

The uplift soil resistance is an important parameter to be considered for the pipeline design against UHB. Trautmann et al. (1985) performed an experimental study to investigate the uplift force-displacement response of buried pipeline with varying degrees of embedment in loose, medium, and dense sand. They aimed to understand the behaviour of the pipeline under different soil conditions. Nielsen et al. (1990) introduced a new design procedure to ensure sufficient uplift resistance to limit the upward movement of imperfect pipe below critical threshold, thus preventing progressive upheaval buckling. In this context, imperfection refers to the deviation of the pipeline alignment from its original straight configuration. Previous studies conducted physical modeling for assessment of uplift resistance of buried pipelines (Schaminee et al. 1990; Maltby and Calladine 1995a,b; Bransby et al. 2002; Palmer and King 2004; Cheuk 2005). Some studies recognized the effect of post-peak degradation of uplift resistance on UHB. For instance, Klever et al. (1990) showed that classical “effective weight” method is unconservative. They presented that when a complete force-displacement curve is considered, as shown in Fig. 2.5(b), it gives significantly lower permissible temperatures (Fig. 2.5(a)) than the solutions based on the effective weight method.

A similar conclusion has been drawn by Goplen et al. (2005), suggesting that the linear soil stiffness model (Fig. 2.6(a)) for preliminary analysis and a full model (with post-peak degradation) (Fig. 2.6(b)) that determines the failure temperature due to upheaval buckling. Bransby et al. (2002) also performed an experiment on loose and dense sand to study the uplift resistance behaviour. They found that the uplift resistance exhibited a nonlinear post-peak degradation response for loose and dense sand, as illustrated in Fig. 2.7. Cheuk et al. (2008) performed a model test to investigate the uplift mechanism of a pipeline buried in the sand. They showed that shear strain is concentrated within a pair of narrow shear bands after reaching the peak resistance. Subsequently, a flow-around mechanism is formed, accompanied by a reduction in the uplift resistance. This behaviour is illustrated in Fig. 2.8.



(a) Effects of soil resistance model on buckling



(b) Uplift soil resistance with nonlinear post-peak degradation

Figure 2.5: Effect of post-peak degradation on buckling: (a) Effects of soil resistance model on buckling; (b) Uplift soil resistance with nonlinear post-peak degradation (after Klever et al. 1990)

Wang et al. (2009) also recognized the effect of post-peak degradation for failure temperature and conducted buckling analysis using a soil resistance model with post-peak degradation (Fig. 2.9). According to Wang et al. (2009), in the absence of pipe uplift, the uplift resistance is solely determined by the weight of the pipe and the soil. However, when pipe uplift begins, the soil resistance increases linearly with the uplift until it reaches a peak. Subsequently, the soil resistance decreases until it reaches the ground surface, corresponding to pipe breakout.

The current theoretical understanding of uplift resistance of buried pipeline is based on the analysis presented in the works of Randolph and Houlsby (1984), Hobbs (1984), Pedersen and Jensen (1988), and Taylor and Gan (1986). Their studies have contributed to develop the theoretical framework and concepts related to uplift resistance in buried pipelines. In addition to the theoretical analyses, several experimental studies have been conducted to investigate the uplift resistance of soil on buried pipelines. These studies include the works of Vesic (1969), Randolph

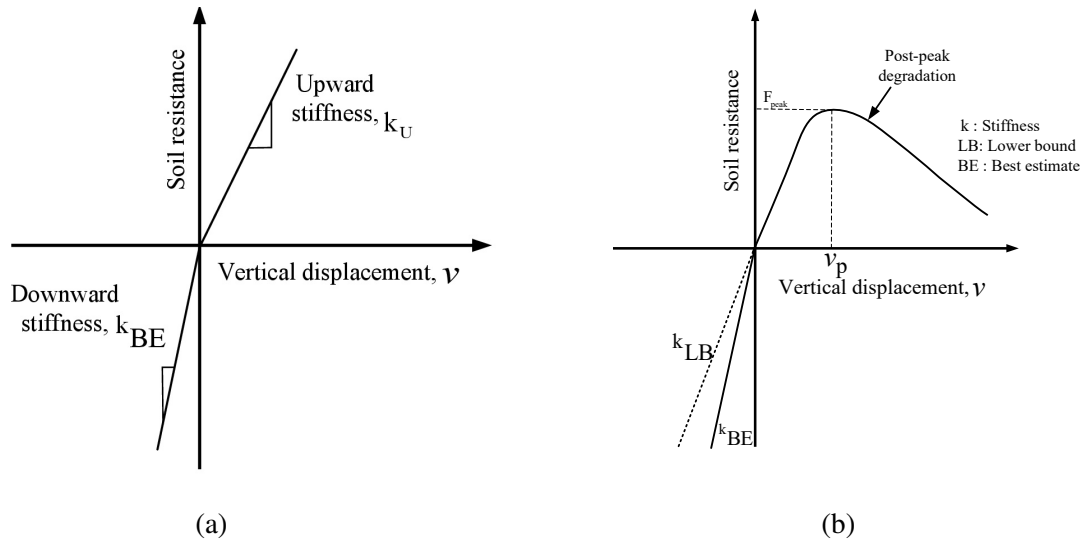


Figure 2.6: Uplift force–displacement response: (a) Linear model; (b) With post-peak softening (after Goplen et al. 2005)

and Houlsby (1984), Trautmann et al. (1985), Palmer et al. (1990), Schaminee et al. (1990), Taylor and Tran (1996), Maltby and Calladine (1995a), Maltby and Calladine (1995b), Croll et al. (1998), White et al. (2000), Cheuk (2005), Wang et al. (2010) and Thusyanthan et al. (2010). These experiments have provided valuable insights into the uplift resistance behaviour of soil related to upheaval buckling. However, it is worth noting that there are still relatively few laboratory experiments conducted specifically on the uplift resistance behaviour of soil, and the mobilization distance continues to be an active research topic in this area.

Roy et al. (2018b) performed a numerical analysis highlighting the significance of post-peak softening in dense sand. This study, along with previous research, emphasizes the practical importance of incorporating post-peak degradation of uplift resistance. While numerous experimental tests are available with empirical equations for calculating uplift and axial forces, notable differences exist in the results obtained from these formulations. Moreover, the offshore pipeline's structural response, considering the post-peak degradation behaviour of soil resistance,

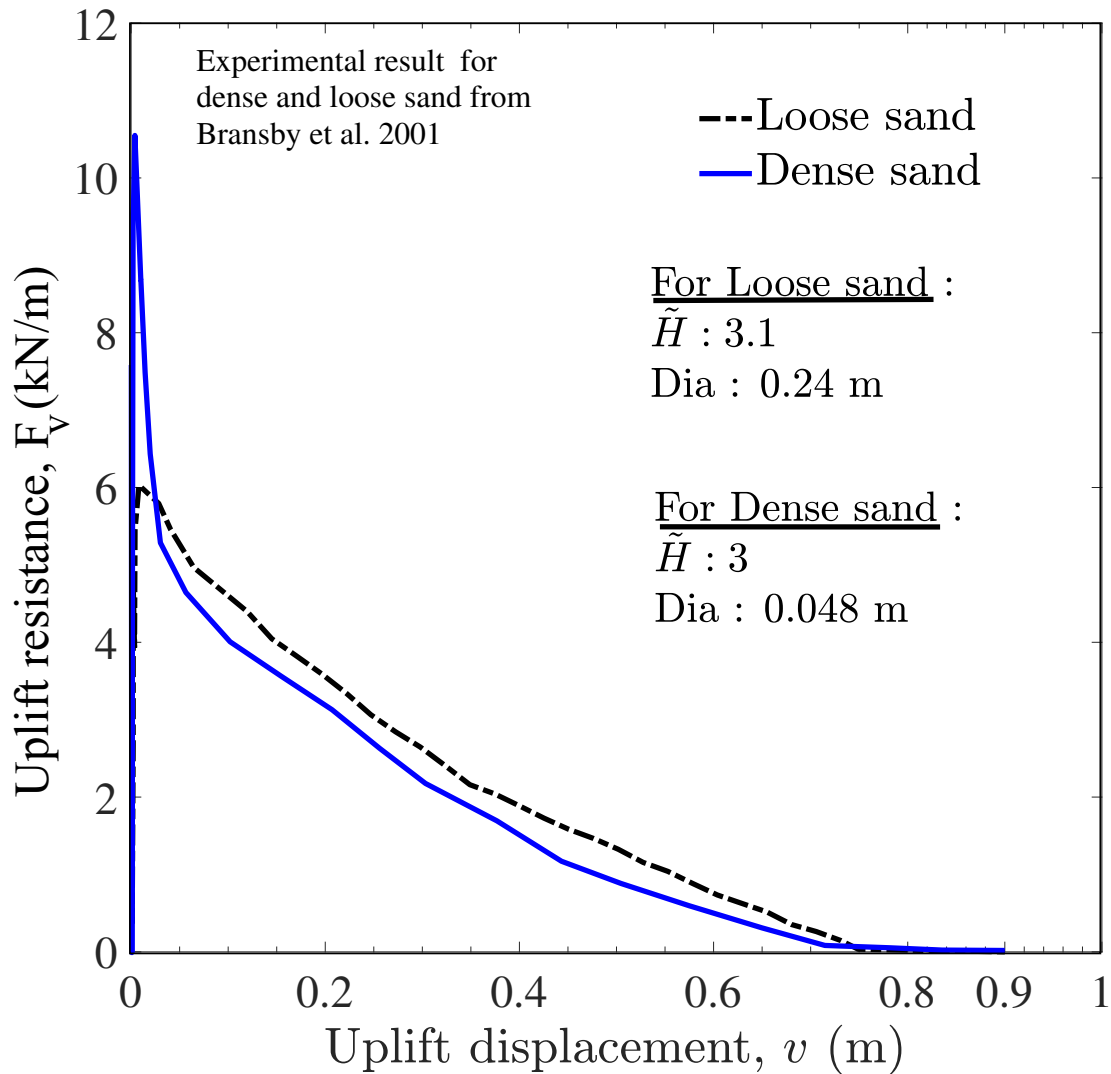


Figure 2.7: Uplift resistance model for loose and dense sand (after Bransby et al. 2002)

has not been adequately studied in the literature.

2.2.3 Soil resistance models based on design guidelines

ALA (2005) and DNV (2007) are the two widely used guidelines for pipeline design. In ALA, bilinear curves (Fig. 2.10) are used to define the force–displacement behaviour using soil springs for axial, lateral, bearing and uplift directions. Based on ALA (2005), the spring force increases

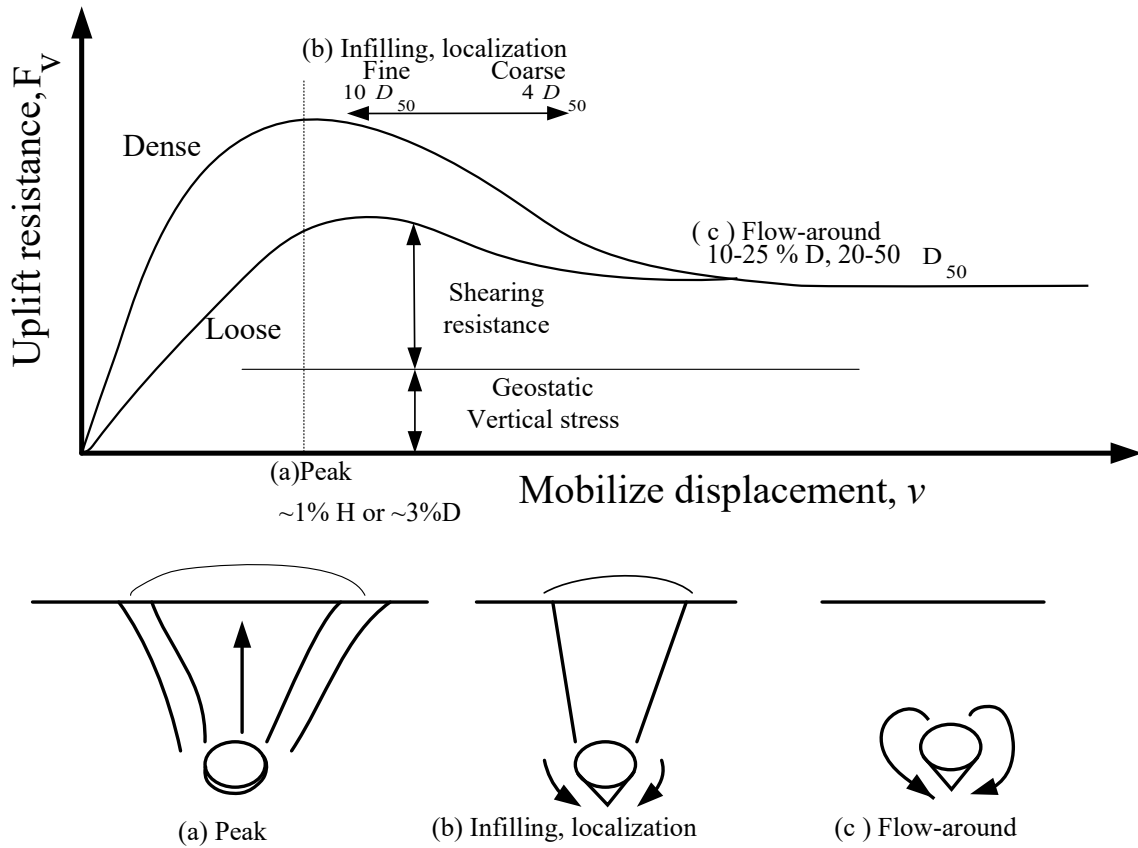


Figure 2.8: Uplift soil resistance model: (a) Peak; (b) Infilling with localization; (c) Flow-around mechanism (after Cheuk et al. 2008)

linearly with relative displacement up to the maximum value and then remains constant. The maximum axial soil resistance per unit length of the pipeline (F_{ap}) buried in sand can be calculated from Eq. (2.1).

$$F_{ap} = 0.5 \pi D H \gamma (1 + K_0) \tan(\phi_\mu) \quad (2.1)$$

where γ is the submerged unit weight of soil; H is the burial depth from the center of the pipe; D is the diameter of the pipe; K_0 is the coefficient of earth pressure at rest; ϕ_μ is the axial interface friction angle between pipe and soil. The burial depth is expressed in a normalized form for using embedment ratio, $\tilde{H}(= H/D)$.

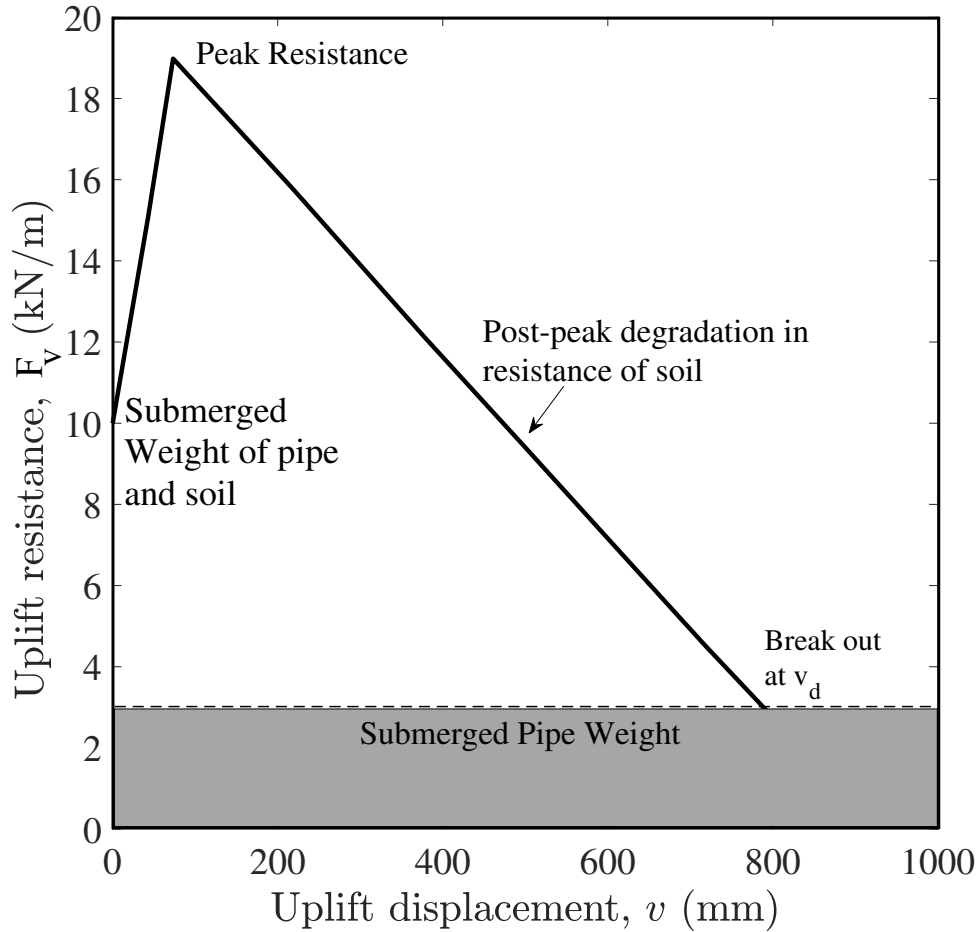


Figure 2.9: Uplift soil resistance model (after Wang et al. 2009)

ALA (2005) also suggested that the relative axial displacement (u) required to mobilize the peak (u_p) is approximately 3 mm and 5 mm for dense and loose sands, respectively.

The maximum bearing resistance (F_{bp}) for sand can be calculated as ALA (2005):

$$F_{bp} = N_q \gamma H D + 0.5 \gamma N_\gamma D^2 \quad (2.2)$$

where $N_q = e^{\pi \tan \phi'} \tan^2 \left(45 + \frac{\phi'}{2} \right)$, $N_\gamma = e^{(0.18 \phi' - 2.5)}$ are the bearing capacity factors. Again, the vertical penetration resistance (F_b) increases linearly with downward movement (v_b), at $v = v_{bp}$, it reaches the F_{bp} and then remains constant. Moreover, v_{bp} is related to the diameter of the pipe

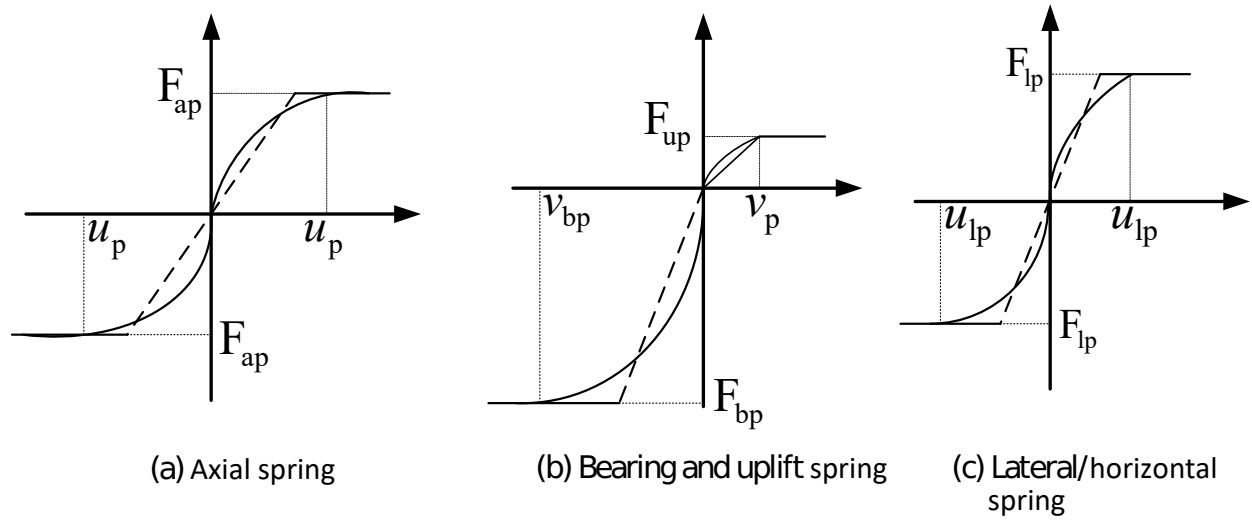


Figure 2.10: Bilinear soil spring model for pipe-soil interaction: (a) Axial spring; (b) Bearing and uplift spring; (c) Lateral/horizontal spring (after ALA 2005)

as $v_{bp} = 0.1D$, for sand. Note that Eq. (2.2) might overestimate F_{bp} , especially for high relative density and low embedment ratio (Kouretzis et al., 2014). Therefore, parametric study for varying F_{bp} is preferred.

The maximum vertical uplift resistance for the pipeline in sand can be calculated based on ALA (2005) Eq. (2.3).

$$F_{up} = N_{qv} \gamma HD \quad (2.3)$$

where $N_{qv} = \frac{\phi' H}{44D} \leq N_q$ and ϕ' is in degree. Again, the upward resistance (F_u) increases linearly with upward displacement (v) and, at $v = v_p$, the maximum resistance F_{up} is mobilized. After v_p , the upward resistance remains constant at F_{up} . ALA (2005) suggested that v_p is related to burial depth (H) as $v_p = 0.01H - 0.02H$ for sand.

The maximum lateral soil resistance for sand is given by Eq. (2.4) .

$$F_{lp} = N_{qh} \gamma HD \quad (2.4)$$

where N_{qh} is the horizontal bearing capacity factor depending upon the angle of internal friction of soil. ALA (2005) suggested that the relative lateral displacement (u_{lp}) required to mobilize the F_{lp} is $0.04(H + \frac{D}{2}) \leq 0.10D - 0.15D$.

DNV (2007) recommends to use a trilinear force–displacement curve (Fig. 2.11) for the uplift resistance of soil. The peak uplift resistance can be calculated as $N_{up} = (1 + f\tilde{H})\gamma\tilde{H}D^2$ where

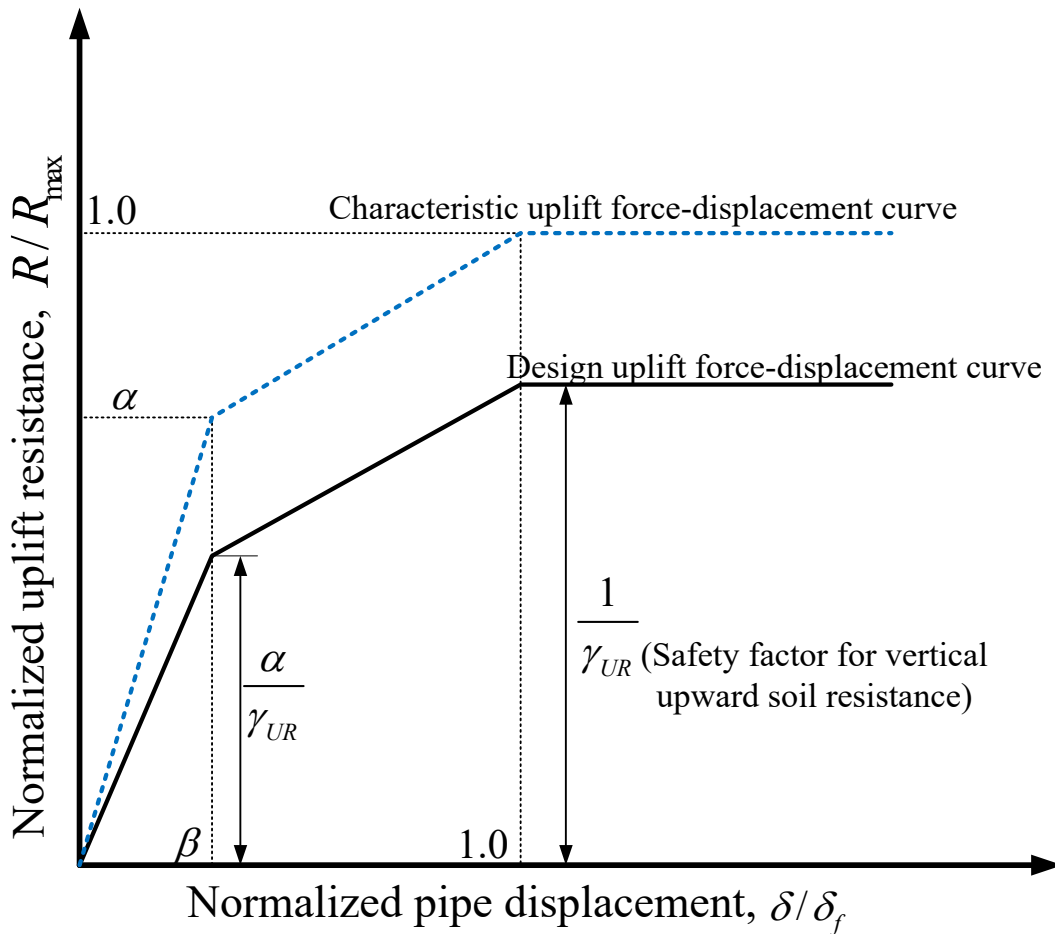


Figure 2.11: Trilinear uplift force–displacement response (after DNV 2007)

f is the uplift resistance factor. DNV (2007) suggest to use $f = 0.10 - 0.3$ and $f = 0.4 - 0.6$ for loose and medium/dense sands, respectively. The maximum uplift resistance mobilizes at $v_p = 0.005H - 0.008H$, which is lower than the v_p recommended by ALA (2005), as mentioned above.

The force–displacement curve prior to the peak is defined by two linear segments that intersect at a point below the peak ($\beta v_p, \alpha F_{up}$, where α and β are two constants). DNV (2007) recommended $\beta = 0.2$, and $\alpha = 0.75 - 0.85$ and $\alpha = 0.65 - 0.75$ for loose and medium/dense sands, respectively. The lower and upper values of f and α represent the lower bound (LB) and upper bound (UB), respectively. The lower value of uplift soil resistance (LB) will allow to form the upheaval buckle more easily and will reduce the axial buckling load. In comparison, the upper bound (UB) with a higher value of uplift soil resistance inhibits the UHB formation and increases the axial buckling load. For the design, local variation in uplift soil resistance is important. Also, it is important to check the bound behaviour of soil resistance. The uncertainty in soil behaviour leads to the large range between the upper- and lower-bound behaviour (Bruton et al., 2006).

2.2.4 Limitations in soil resistance models for uplift behaviour

ALA (2005) and DNV (2007) guidelines suggest that the uplift resistance after the peak remains constant. However, the works by Trautmann et al. 1985, Nielsen et al. 1990, Klever et al. 1990, Bransby et al. 2002, Goplen et al. 2005 and Wang et al. 2010 suggest that the soil resistance gradually decreases after the peak for shallow to intermediate burial depths. At a large displacement, the reduction of uplift resistance is significant. Physical experiments show that it becomes zero (as expected) when the pipeline moves to the ground surface (Bransby et al., 2002; Wang et al., 2012). Observing large upward displacement in the field, Nielsen et al. (1990) schematically show the typical nonlinear uplift resistance curve (solid line in Fig. 2.12). Three discrete points are used to characterize the force–displacement behavior. The submerged self-weight of the pipe and weight of the soil column directly above the pipe corresponds to point 1 where the upward displacement is assumed to be zero. From point 1 to 2, the continuous upward movement of the imperfect pipe section mobilizes at an uplift resistance due to the activation of shear stresses in the soil. The physical experimental results (Trautmann et al., 1985; Nielsen et al., 1990) suggest that the displacement required to reach the peak uplift resistance at point 2 is (0.02

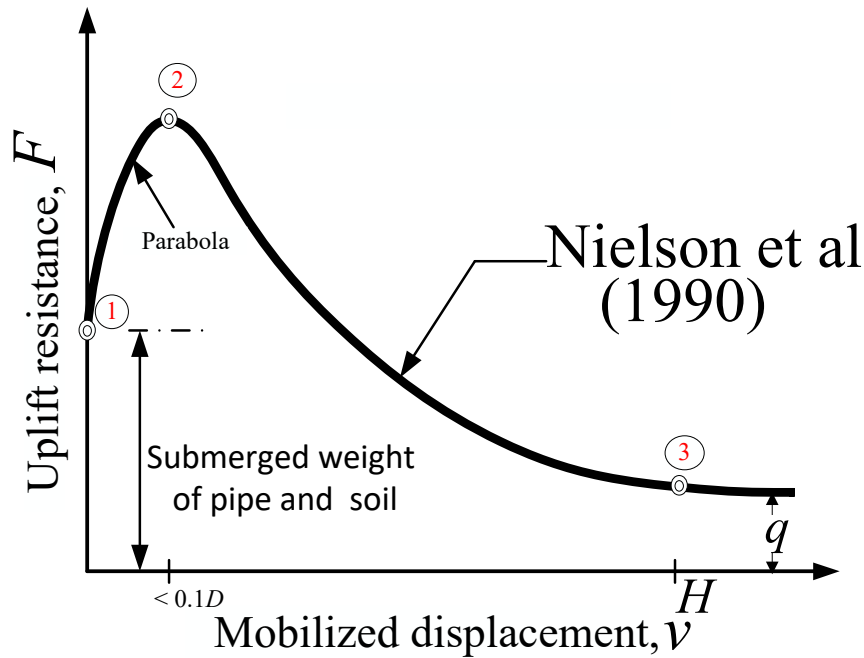


Figure 2.12: Uplift force–displacement behaviour (after Nielsen et al. 1990)

+ $0.008H/D)D \leq 0.1D$. Once the upward movement of the pipe exceeds the displacement required to reach the peak uplift resistance, the general shear failure occurs in the soil, resulting in degradation of uplift resistance until the point 3 when the pipe reaches the ground surface or seabed (Nielsen et al., 1990). For elastic pre-peak behaviour Nielsen et al. (1990) suggested limiting the upheaval deformation of 10–20 mm (up to the peak) to control the upheaval creep failure.

Numerical modeling also shows a nonlinear post-peak reduction of uplift resistance, F_v (Roy et al., 2018b). For dense sand, F_v reduces quickly immediately after the peak, which is due to the reduction of shear strength parameters (friction and dilation angles) with the development of plastic shear strains. At large displacements, the reduction of F_v mainly occurs due to the reduction of cover depth. Although experimental evidence shows that both the loose and dense sands exhibit a post-peak degradation of uplift resistance, the current design guidelines, such as ALA (2005) recommends a bilinear and DNV (2007) recommends a tri-linear force-displacement model. The nonlinear post-peak softening behaviour for loose and dense sand is discussed in the

following subsection.

2.2.5 Uplift resistance of pipeline buried in loose sand

Physical model tests show that the uplift resistance (F_v) gradually increases with upward displacement (v), reaches the maximum value (F_{vp}) at $v = v_p$ and then decreases with v due to the reduction of soil cover as the pipe moves towards the surface (Bransby et al. 2002; Bransby and Ireland 2009; Wang et al. 2012). The maximum uplift resistance for loose sand is generally calculated using the vertical slip-surface model, as shown in Fig. 2.13(a), assuming that, with a displacement of the pipe, a soil wedge form in the backfill material by formation of two vertical slip planes originating from the springline. The pre-peak uplift resistance for the loose sand is

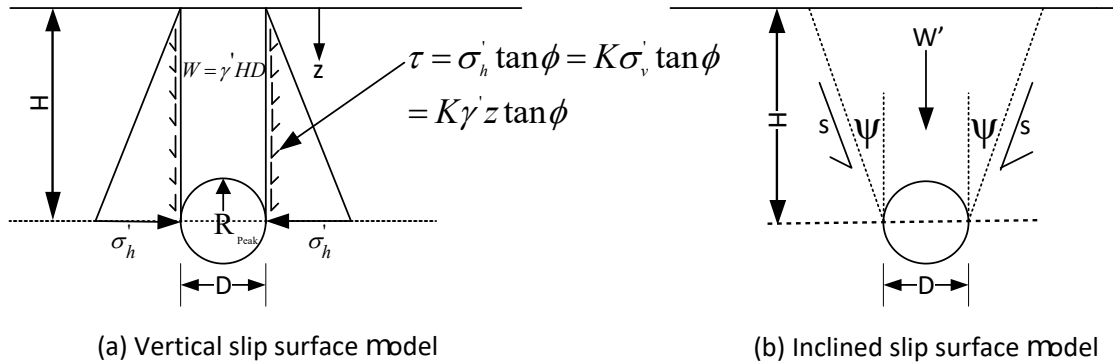


Figure 2.13: Soil slip surface models: (a) Vertical slip surface model for loose sand; (b) Inclined slip surface model for dense sand

given in Eq. (2.5) based on Schaminee et al. (1990), DNV (2007) where the total uplift resistance is equal to the weight of soil above the pipeline and the shear stresses on vertical shear planes at the sides of pipe.

$$F_{\text{peak}} = \gamma \tilde{H} D^2 \left[1 + \left(0.5 - \frac{\pi}{8}\right) \frac{1}{\tilde{H}} + f_p \left(\frac{1}{\tilde{H}} (\tilde{H} + 0.5)^2 \right) \right] \quad (2.5)$$

where \tilde{H} is the initial embedment ratio ($= \frac{H}{D}$) and f_p is the uplift resistance factor based on DNV (2007) design code. The mobilization distance for a different threshold value of peak uplift

resistance is $\delta_f = D(M\tilde{H} + N)$ (Wang et al., 2012). where the coefficients M and N are for different threshold values of uplift resistance. On moving the pipe to a sufficiently large distance, Wang et al. (2012) proposed Eq. (2.6) to calculate the post-peak (residual) uplift resistance for large displacement.

$$\frac{F_{vr}}{\gamma(H_0 - v)D} = 1 + \left(0.5 - \frac{\pi}{8}\right) \frac{D}{(H_0 - v)} + f_r \left[\frac{D}{(H_0 - v)} \times \left(\frac{(H_0 - v)}{D} + 0.5 \right)^2 \right] \quad (2.6)$$

The Eq. (2.7) is the simplified form of Eq. (2.6) for post peak resistance for loose sand.

$$F_{vr} = \gamma D^2 \left[\left\{ (\tilde{H} - \tilde{v}) + 0.5 - \frac{\pi}{8} \right\} + f \left\{ (\tilde{H} - \tilde{v})^2 + (\tilde{H} - \tilde{v}) + 0.25 \right\} \right] \quad (2.7)$$

where \tilde{v} is the normalized vertical mobilization displacement ($= v/D$), and γ' is the submerged unit weight of the soil. The first part of Eq. (2.7) represents the weight of the failure wedge while the second part is for soil shear resistance along the slip planes. Wang et al. (2012) also suggested that, for a reliable and conservative uplift resistance of loose sand, the uplift resistance factor f can be calculated based on the critical state condition as $f = K_0 \tan \phi'_c$, where, ϕ'_c is the critical state friction angle and $K_0 (= 1 - \sin \phi'_c)$ is the coefficient of earth pressure at rest. DNV (2007) suggest that the use of different values of uplift resistance factor for various types of soil. Eq. (2.7) is used to define the force-displacement ($F_v - v_m$) curve from the peak to large displacements.

The pre-peak behaviour is defined by a bilinear curves as DNV (2007), also suggested by Wang et al. (2012), as: F_v increases linearly from $F_v = 0$ at $v = 0$ to $F_v = F_{vp}$ at $v = \beta v_p$, and then F_v increases linearly at a slower rate than before to $F_v = F_{vp}$ at $v = v_p$. The coefficients $\alpha (= 0.75 - 0.85)$ and $\beta (= 0.2)$ are constants based on DNV (2007) guidelines for loose sand. For a given burial depth and pipe diameter, the peak resistance (F_{vp}) is calculated using Eq. (2.6) on replacing $v = v_p$. The uncertainties in estimation of displacement required to mobilize F_{vp} is generally high; and previous studies suggest that it depends on H and D for pipeline buried in sand. For example, it ranges from

$\approx (1\%–3\%)H$ (Cheuk 2005) and from $\approx (1\%–8\%)H$ for $0 < \tilde{H} < 6$, and $\approx (1.5\%–4.5\%)H$ for $2 < \tilde{H} < 5$ (Wang et al. 2012).

2.2.6 Uplift resistance of pipeline buried in dense sand

Similar to tests in loose sand, physical model tests were conducted on dense sands by (Cheuk 2005; Bransby et al. 2002). The main difference in force-displacement behaviour and failure mechanisms between the tests on loose and dense sands are: (i) the peak resistance in dense sand is mobilized at $v = v_p$ by formation of two failure planes inclined to the vertical (θ) approximately equal to the peak dilation angle (ψ_p); (ii) F_{vp} is higher in dense sand; however, F_v decreases quickly with v after the peak, which is primarily due to the reduction of θ and strain-softening behaviour of dense sand, and after a sufficient displacement ($v = v_s$) the rate of decrease in F_v is small then the resistance at $v = v_s$ is called "after-softening resistance (F_{vs})"; (iii) at large displacements ($v > v_s$), the force-displacement curve for dense sand is similar to, but could be slightly above the loose sand case, because the slip surfaces, as shown in Fig. 2.13(b), do not become completely vertical in dense sand even at large displacements ($\theta = 5^\circ - 8^\circ$, Roy et al. 2018b).

Conducting a comprehensive finite element modelling with a soil model that considers the strain-softening behaviour, and calibrating it against physical model test results, Roy et al. (2018b) proposed the following equations Eq. (2.8) to calculate the peak resistance and the mobilization distance. Similar to Eq. (2.7) for loose sand, Eq. (2.8) is also composed of weight and shear components; however, the failure wedge is formed by inclined slip surfaces, as shown in Fig. 2.13(b).

The mobilization displacement at the prepeak $\tilde{v}_p (= v_p/D)$ can be estimated by Eq. (2.9).

$$F_{vp} = R\gamma D^2 \left[\left\{ (\tilde{H} - \tilde{v}_p) - \frac{\pi}{8} + (\tilde{H} - \tilde{v}_p)^2 \tan \theta \right\} + F_A (\tilde{H} - \tilde{v}_p)^2 \right]; \quad (2.8)$$

$$F_A = 0.5 \left(\tan \phi'_p - \tan \theta \right) \left[1 + K_0 - (1 - K_0) \cos 2\theta \right]$$

$$\tilde{v}_p = 0.002\tilde{H} + 0.025 \quad (2.9)$$

where ϕ'_p is the peak friction angle. Roy et al. (2018b) showed that the reduction factor $R = 0.8$ – 0.9 and $\theta \approx \psi_p$ could be used in Eq. (2.8) for the dense sand conditions. Note that, if θ and ϕ'_p in Eq. (2.8) are replaced by 0 and ϕ'_c , respectively; F_A will be same as f in Eq. (2.7) for loose sand. For the residual resistance ($v > v_s$), the Eq. (2.10) proposed by Roy et al. (2018b), in which, in addition to weight and shear components (first and second parts), the surface heave at large displacement is considered (third part).

$$F_{vs} = R\gamma D^2 \left[\left\{ (\tilde{H} - \tilde{v}) - \frac{\pi}{8} + (\tilde{H} - \tilde{v})^2 \tan \theta \right\} + F_A (\tilde{H} - \tilde{v})^2 + 0.9\tilde{v} \{ 1 + (\tilde{H} - \tilde{v}) \tan \psi_p \} \right] \quad (2.10)$$

As the slip plane does not become completely vertical, even at a large displacement, $\theta \approx 8^\circ$ is recommended for Eq. (2.10). Moreover, $\tilde{v}_s (= v_s/D)$ can be estimated based on Eq. (2.11) (Roy et al., 2018b).

$$\tilde{v}_s = 0.035\tilde{H} + 0.1 \quad (2.11)$$

On replacing \tilde{v} by \tilde{v}_s in Eq. (2.10), the post-peak softening uplift resistance (F_{vs}) can be calculated. Between the peak and post-peak softening state, the force-displacement response is assumed to be linear. For the pre-peak behaviour, a bilinear curve as DNV (2007), also described above for the loose sand case, can be used. The post-peak degradation has limited study in terms of pipelines subjected to large movement. The research gap will be filled with the implementation of soil models to study the response of offshore pipelines undergoing above the seabed.

2.3 Studies on the mechanisms and solutions for upheaval buckling

The HPHT pipeline expands longitudinally. The frictional forces develop between the pipe and surrounding soil as well the boundaries controls longitudinal movement of pipe fully or partially. The operating temperature and the internal pressure of fluids acts together for the effective axial

compressive force in a pipeline. The combined effect of temperature difference (ΔT) and the pressure difference between the inner and outer surfaces of the pipe (p) in the pipeline could be converted into a single parameter "effective temperature" by Eq. (2.12):

$$\Delta T_{\text{eff}} = \Delta T + \frac{pD(1-2\nu)}{4Et\alpha} \quad (2.12)$$

$$P_a = EA\alpha\Delta T_{\text{eff}}$$

where D and t are the mean diameter and thickness of the pipe respectively, EA is the axial rigidity of the pipeline, α is the coefficient of linear thermal expansion of pipeline and ν is the Poisson's ratio (Hobbs, 1984). The initial axial compressive force for in-air pipeline (P_a) in the elastic range can be calculated as $EA\alpha\Delta T_{\text{eff}}$. Based on the beam-column theory for the idealized pipeline, the equilibrium equation for the pipeline can be expressed as Eq. (2.13) (Palmer et al. 1990).

$$EI \frac{d^4 y}{dx^4} + P \frac{d^2 y}{dx^2} + q(x) = 0 \quad (2.13)$$

where P is the thermally induced axial compressive force after buckle, $q(x)$ is the total downward force per unit length required to maintain the equilibrium of pipeline; EI is the flexural rigidity of the pipeline. The general solution of the differential is given in Eq. (2.13) is given by Eq. (2.14):

$$y(x) = A_0 + A_1 \cos(kx) - \frac{q}{2P} x^2 \quad (2.14)$$

The Eq. (2.14) represents the shape of initial imperfection consists of sinusoidal functions or polynomial functions or the combination of both. The shape of simple cosine shape with initial imperfection height δ and wavelength L can be expressed as Eq. (2.15).

$$y = \delta \cos^2(\pi x/L) \in -0.5L < x < 0.5L \quad (2.15)$$

The downward force required to maintain the equilibrium of the pipeline profile can be expressed as Eq. (2.16) (Palmer et al., 1990).

$$q(x) = (-8 \delta EI(\pi/L)^4) + 2 \delta p(\pi/L)^2 \cos(2\pi x/L) \quad (2.16)$$

The loading action on an initially imperfect buried pipeline and the vertical deformation is shown in Fig. 2.1. In Fig. 2.1, the pipeline before going to buckle is initially imperfect and buried at a depth of H from the seafloor.

2.3.1 Analytical solution for upheaval buckling

Hobbs (1984) provides the analytical solution for vertical as well as lateral buckling of pipeline without considering initial out of straightness. In this analysis, the pipeline is considered as a Euler–Bernoulli beam, where the axial force (P) and the submerged self-weight (q) per unit length is applied at the deflected shape of the buckled part. It is also assumed that the friction between the pipeline and soil is fully mobilized and the seabed is rigid. The idealized mode for vertical buckling is shown Fig. 2.14. Once the axial strain ϵ_a is fully restrained, the axial compressive force

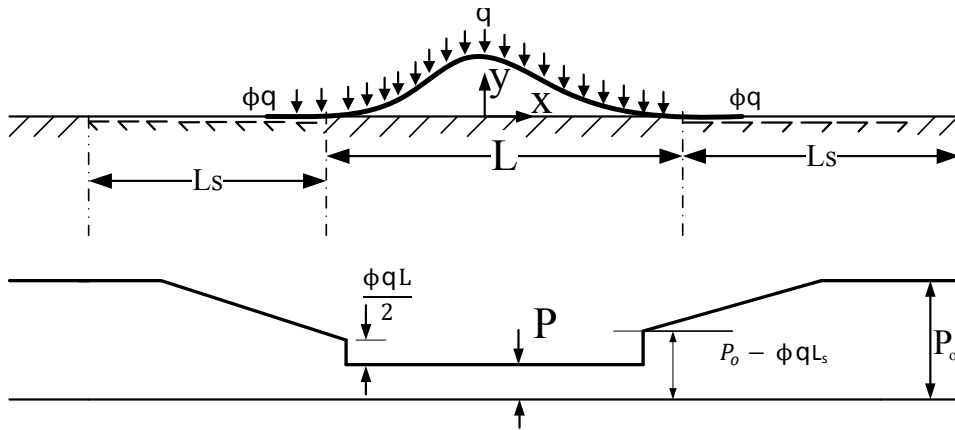


Figure 2.14: Axial force distribution in a pipeline with imperfection (after Hobbs 1984)

available for the buckling is expressed by Eq. (2.17).

$$P_o = \frac{ApD}{2t}(0.5 - \nu) \quad (2.17)$$

where ν is the Poisson's ratio of pipe, p is the internal pressure in the pipeline, A is cross-sectional area of pipe, t is the wall thickness and D is the external diameter of pipe. The deflected shape of the buckled part of the pipeline is mathematically described by the linear differential equation, which is similar to the beam-column under a uniform lateral load. It is assumed that the bending moment at the lift-off point is zero. The equation of the deflected shape of the pipeline can be written as:

$$\frac{d^2y}{dx^2} + n^2y + \frac{m}{8}(4x^2 - L^2) = 0 \quad (2.18)$$

where $m = \frac{q}{EI}$, and $n^2 = \frac{P}{EI}$. On applying the boundary conditions: $y|_{x=0} = v_m, y|_{x=L/2} = 0$, the following equations 2.19 and 2.20 is obtained.

$$P = 80.76 \frac{EI}{L^2} \quad (2.19)$$

$$P_o = P + \frac{qL}{EI} \left[1.597 \times 10^{-5} EA\phi qL^5 - 0.25(\phi EI)^2 \right]^{0.5} \quad (2.20)$$

where P is the axial load in the central buckle zone; P_o is the axial load away for the buckle zone Fig. 2.14; and ϕ is the coefficient of friction between the pipe and soil. The maximum buckle amplitude can be expressed as:

$$v_m = 2.407 \times 10^{-5} \frac{qL^4}{EI} \quad (2.21)$$

and the maximum bending moment, at $x = 0$ is $M_{\max} = 0.06938 qL^2$, and the size of the slipping length adjacent to the buckle is expressed as:

$$L_s = \frac{P_o - P}{\phi q} - 0.5L \quad (2.22)$$

For the various buckle wavelengths (L) ranging from $0.1L-3L$, the correlation between temperature increase (Eq. (2.12)) and buckle amplitude (Eq. (2.21)) is presented in Fig. 2.15. The sectional and materials properties used in this study are consistent with the description from Hobbs (1984). When considering a frictional coefficient (ϕ) of 0.6, the maximum permissible temperature to prevent vertical buckling is observed at 57.5°C at the corresponding buckle amplitude of 2.2 m (Fig. 2.15). Hobbs (1984) gives an idea for the analytical solution of pipeline buckling due to temperature;

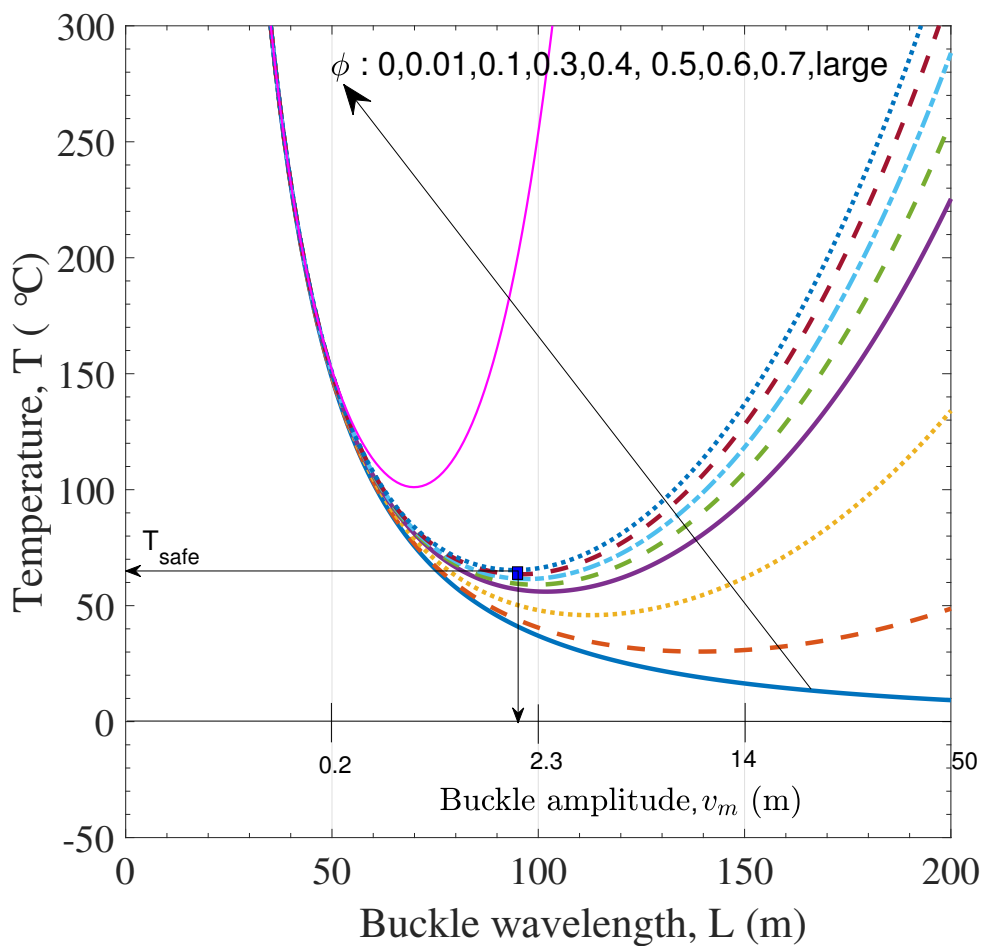


Figure 2.15: Analytical solution of temperature rise versus buckle amplitude (after Hobbs 1984)

however, this method lacks the appropriate consideration for pipe-soil interaction and the initial out of straightness (OOS) or initial imperfection.

To account the initial out of straightness (OOS) of pipeline and the soil interaction behaviour, Taylor

and Gan (1986) provided a modified formulation for pipe-soil interaction with axial resistance, as shown in Fig. 2.16. The initial imperfection wavelength is denoted by L_o , and a ratio of $\frac{v_{om}}{L_o}$ is

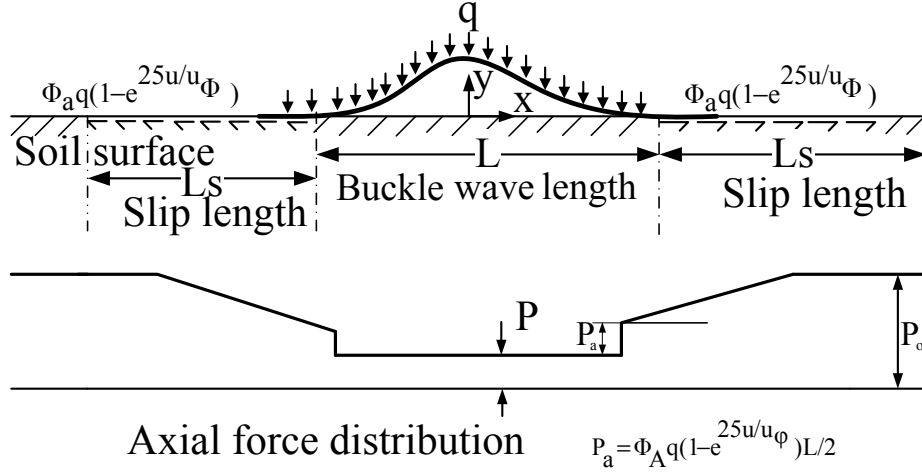


Figure 2.16: Idealization for upheaval buckling of HPHT pipeline (after Taylor and Gan 1986)

indicated by (\tilde{v}_{om}) known as “initial imperfection ratio” which controls the buckling types and plays a unique role in the UHB of pipelines. Moreover, they are related as $v_{om}/L_o^4 = 2.407 \times 10^{-3} q/EI$. where q is the submerged self-weight of the pipe per unit length and EI is the flexural rigidity. It is assumed that the pipeline is stress-free at the initially deformed configuration.

For the different values of imperfection ratio (\tilde{v}_{om}) , the initial imperfection wavelength L_o of the pipeline can be obtained from the modified Eq. (2.23) given by:

$$L_o = \left(\frac{\tilde{v}_{om} EI}{2.407 \times 10^{-3} q} \right)^{\frac{1}{3}} \quad (2.23)$$

The total axial frictional resisting force (F_a) develop along the pipe-soil interface is defined by Eq. (2.24).

$$F_a = q\phi_A \left(1 - e^{-25u/u_\phi} \right) \quad (2.24)$$

where the fully mobilized axial friction coefficient is ϕ_A and the movement corresponding to reach the full mobilization is u_ϕ . Taylor and Gan (1986) suggested $\phi_A = 0.7$ and $u_\phi = 5$ mm for the typical

submarine soil condition. Based on Taylor and Gan (1986), the modified axial buckling force (P) is given by Eq. (2.25):

$$P = 80.76 \frac{EI}{L^2} \left[1 - \frac{R_1}{75.60} \left(\frac{L_o}{L} \right)^2 \right] \quad (2.25)$$

where R_1 is given by Eq. (2.26).

$$R_1 = 4.60314 \left[\sin(4.4934 \frac{L_o}{L}) + 2.30157 \left(\frac{\sin 4.4934(1 + \frac{L_o}{L})}{(\frac{L}{L_o} + 1)} + \frac{\sin 4.4934(1 - \frac{L_o}{L})}{(\frac{L}{L_o} - 1)} \right) \right] \quad (2.26)$$

The non-linear slip length field equation ($P_o - P$) in the final form is given by Eqs. (2.27) and (2.28).

$$(P_o - P) = \left[2\phi_A q A E \left(\frac{e^{25u_s/u_\phi} - 1}{5} - u_s \right) \right]^{1/2} + \phi_A q \frac{L}{2} (1 - e^{25u_s/u_\phi}) \quad (2.27)$$

$$u_s = \frac{(P_o - P)L}{2AE} - 7.9883 \times 10^{-6} \left(\frac{q}{EI} \right)^2 (L^7 - L_o^7) \quad (2.28)$$

After solving the nonlinear slip length field equations given by Eq. (2.27) and Eq. (2.28) using the Newton-Raphson algorithm, the values of ($P_o - P$) and u_s can be obtained for discrete wavelengths (L) corresponding to different imperfection ratios (\tilde{v}_{om}) of 0.003, 0.005, 0.007, and 0.01. The analytical solution provides a temperature rise versus buckle amplitude with a valuable insights into the buckling behaviour of the pipeline, as shown in Fig. 2.17. In Fig. 2.17, the circle represents the critical temperature, whereas the square represents the yield temperature.

The axial buckling force (P) versus the buckle amplitude (v_m) at the central critical section of the pipeline for different values of initial imperfection ratio (\tilde{v}_{om}) is shown in Fig. 2.18(a). Observations indicate that the pipeline with a smaller initial imperfection requires a higher buckling force than the one with a larger initial imperfection. However, once a vertical displacement of approximately 4.0 m is reached, the buckling force becomes nearly the same for all the cases of initial imperfection. This behaviour is observed during the post-buckling stage, where the effect of initial imperfection diminishes, and the pipeline reaches a relatively stable

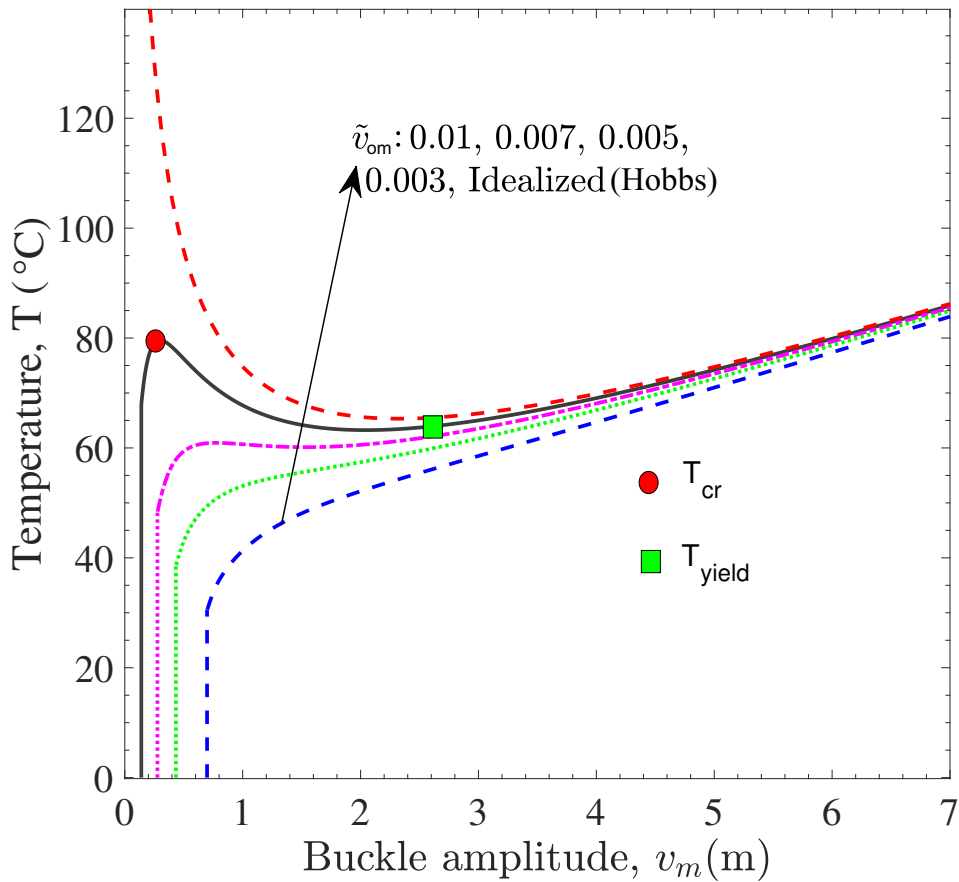


Figure 2.17: Analytical solution of temperature rise versus buckle amplitude

buckling state. In Fig. 2.18(b), the variation of axial compressive stresses during the vertical movement of the pipeline is shown. Notably, the axial compressive stress decreases in a pipeline with the increase in initial imperfection. This behaviour occurs because the smaller initial imperfections necessitate more axial compression than the pipeline with larger initial imperfection.

The analytical solution presented in this study is specifically developed for surface-laid pipelines. However, for buried pipelines, the soil resistance characteristics vary, necessitating the utilization of advanced numerical methods to address the buckling problem. It is important to note that the presented analytical solution has some limitations. It does not account for the nonlinearity of pipe

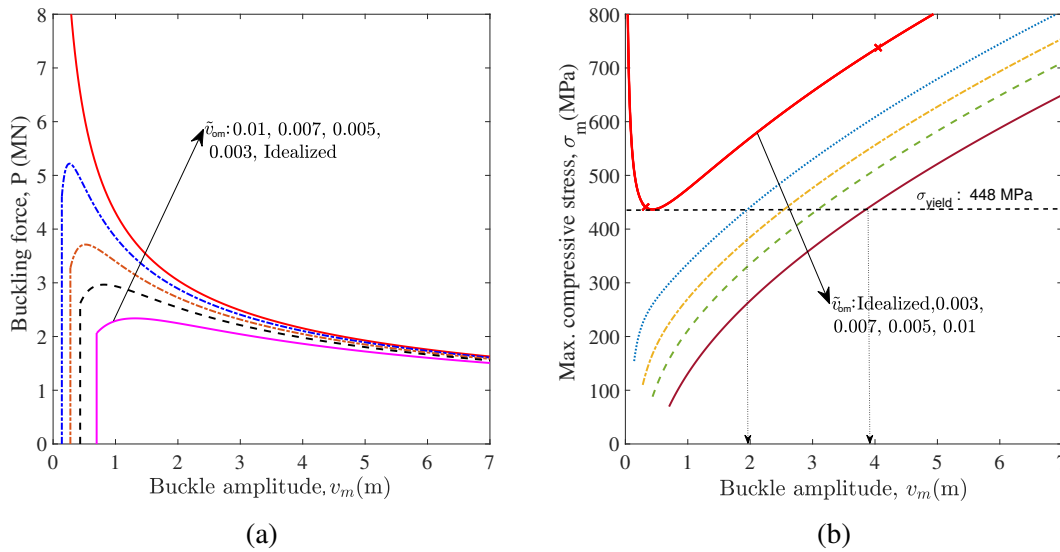


Figure 2.18: Analytical solution of upheaval buckling: (a) Axial force versus buckle amplitude; (b) Compressive stresses versus buckle amplitude

material and geometry, large deformation kinematics in pipeline. To accurately analyze the buckling behaviour of buried pipelines and consider these factors, more sophisticated numerical methods and models need to be employed.

2.4 Studies on the initial imperfection of a pipeline (out of straightness)

It is evident that the shape of a buried pipeline in the field deviates from perfect straightness to some extent. The imperfections may be due to the undulations in the sea bed profile, or a prop (isolated rock located immediately below the line or another pipeline to be crossed). Some possible imperfection might be due to the free span gap in the trench. The initial imperfection (out of straightness) in the pipeline (adds additional residual stresses in the pipeline) results in the second order moments due to the axial compression. The load carrying capacity of the pipeline decreases with the increase in second order moment. The second order moment increase with the increase in initial imperfection in a pipeline. The shape of initial imperfection plays a major role in the prediction of buckling temperature of the pipeline. Those imperfect zones in a pipeline are

vulnerable to buckling and possible failures.

Numerous studies have investigated the shape of initial imperfections in a pipelines. Notable contributions in this area include the works of Taylor and Gan (1986), Ju and Kyriakides (1988), Pedersen and Jensen (1988), Taylor and Tran (1996), Maltby and Calladine (1995a,b), and Croll et al. (1998). It is particularly worth mentioning the studies by Taylor and Gan (1986), Taylor and Tran (1996), and Maltby and Calladine (1995a,b) due to their significant contributions in this area. Taylor and Gan (1986) summarized three basic types of initial imperfection for subsea buried pipeline as shown in Fig. 2.19. The initial imperfection height at the center is denoted by amplitude v_{om} and the initial imperfection wavelength L_o or L_i based on the type of initial imperfection as shown in Fig. 2.19. A proper representation of initial imperfection is necessary for the modelling of UHB problem. A simple mathematical function may not always represent the actual shape of the imperfect pipe. Based on physical imperfection and mathematical reasoning, several methods have been proposed to define the initial imperfection in the buckling analysis, which includes isoprop and blister model, empathetic and sinusoidal model, and pipeline weight dependent shape.

The empathetic initial imperfection equation based on Taylor and Gan (1986) is given in Eq. (2.29).

$$v_o = v_{om} \left[0.707 - 0.262 \frac{\pi^2 x^2}{L_o^2} + 0.293 \cos \left(2.86 \frac{\pi x}{L_o} \right) \right] \quad (2.29)$$

where $-\frac{L_o}{2} \leq x \leq \frac{L_o}{2}$, v_o and v_{om} represents the imperfection (vertical distance from the datum to pipe center) at any point and at the midpoint ($x = 0$), respectively.

Based on Croll et al. (1998) and Palmer and King (2004) the initial imperfection profile for upheaval buckling of the pipeline is in the form of sinusoidal curve expressed by Eq. (2.30).

$$v_o = \frac{v_{om}}{2} \left[1 + \cos \left(\frac{2\pi x}{L_o} \right) \right], \quad -\frac{L_o}{2} \leq x \leq \frac{L_o}{2} \quad (2.30)$$

Karampour et al. (2013) define an equation for the isoprop point imperfection where the initial

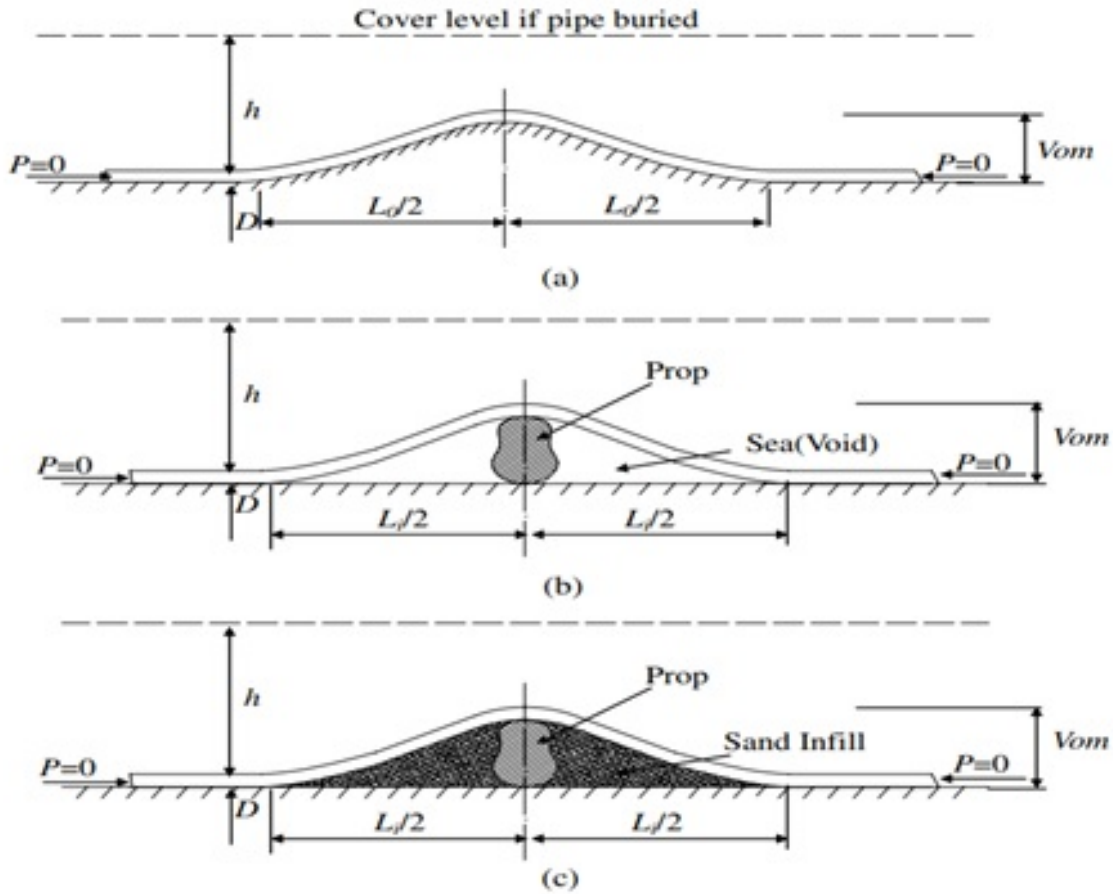


Figure 2.19: Typical imperfection configuration: (a) Basic contact undulations (empathetic); (b) Isolated prop imperfection; (c) Infilled prop imperfection (after Taylor and Tran 1996)

imperfection profile is formulated based on the suspended weight of pipe given by Eq. (2.31).

$$v_{0x} = \begin{cases} \Delta_0 - \frac{qx^4}{24EI} + \frac{qL_0x^3}{18EI} - \frac{qL_0^2x^2}{48EI}, & 0 \leq x \leq \frac{L_0}{2} \\ \Delta_0 - \frac{qx^4}{24EI} - \frac{qL_0x^3}{18EI} - \frac{qL_0^2x^2}{48EI}, & -\frac{L_0}{2} \leq x \leq 0 \\ L_0 = 2 \left(\frac{72EI\Delta_0}{q} \right)^{1/4} \end{cases} \quad (2.31)$$

Zeng et al. (2014) also formulated the initial imperfection based on Buckingham's π dimensional

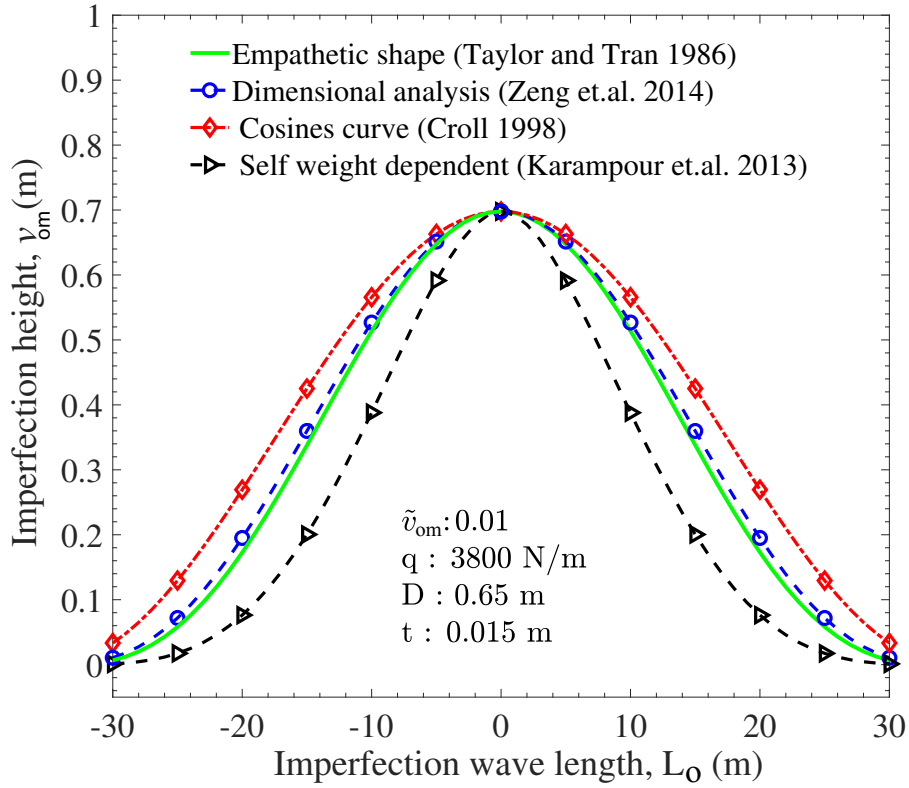


Figure 2.20: Initial imperfection profiles based on different mathematical models

analysis is given by Eq. (2.32) and Eq. (2.33).

$$f_1(x) = \begin{cases} v_{om} \left(\frac{8}{3} \left(\frac{2x}{L_o} \right)^2 + 3 \frac{2x}{L_o} + 1 \right) \left(1 - \frac{2x}{L_o} \right)^3, & 0 \leq x \leq \frac{L_o}{2} \\ v_{om} \left(\frac{8}{3} \left(\frac{2x}{L_o} \right)^2 - 3 \frac{2x}{L_o} + 1 \right) \left(1 + \frac{2x}{L_o} \right)^3, & -\frac{L_o}{2} \leq x \leq 0 \end{cases} \quad (2.32)$$

$$f_2(x) = \begin{cases} v_{om} \left(\frac{8x}{L_o} + 1 \right) \left(\frac{2x}{L_o} - 1 \right)^4, & 0 \leq x \leq \frac{L_o}{2} \\ -v_{om} \left(\frac{8x}{L_o} + 1 \right) \left(\frac{2x}{L_o} + 1 \right)^4, & \frac{L_o}{2} \leq x \leq 0 \end{cases} \quad (2.33)$$

The various imperfection shapes based on the works of Taylor and Gan (1986), Palmer and King (2004), Karampour et al. (2013), and Zeng et al. (2014) are shown in Fig. 2.20. These shapes correspond to a pipe with an external diameter of 0.65 m, a wall thickness of 15 mm, and an initial

imperfection ratio \tilde{v}_{om} of 0.01.

Furthermore, the Gaussian peak (bell shape) imperfection model is used for the UHB analysis by Williams (2014), which is represented by the equation Eq. (2.34).

$$v_o = \frac{a}{\sigma\sqrt{2\pi}} \exp\left(-\frac{x^2}{2\sigma^2}\right) \quad (2.34)$$

where $a = \frac{v_{om}L_o}{2}$ and standard deviation $\sigma = 0.1948L_o$ (Eq.2.23) provides the best fit similar to a cosine function Eq. (2.30). The Fig. 2.21 shows the imperfection shapes for three different initial imperfection ratios (\tilde{v}_{om}) of 0.003, 0.007, and 0.01. These shapes are generated using three approaches described by equations Eq. (2.29), Eq. (2.30), and Eq. (2.34). To calculate the imperfection height, a steel pipe with an outer diameter of 0.65 m, a wall thickness of 15 mm, and a submerged self-weight of 3800 N/m is used. Williams (2014) observed that the Gaussian peak is effective in capturing the smooth and monotonic buckling response during Finite Element (FE) analysis for a specific pipe section. However, it is worth noting that this shape remains dependent on wavelength parameter (L_o) from Taylor and Gan (1986) and requires a larger initial wavelength comparing with the other shapes. Among the different profiles of imperfections, the mode defined by Taylor and Gan (1986) is commonly utilized in the finite element (FE) analysis. This profile is favoured because of its originality with the seabed profile and produces smooth and monotonic buckling responses for various pipe sections. There is some research gap in the type of imperfection model utilization to study the structural aspects of offshore pipelines.

2.5 Study on the initially stressed imperfection in a pipeline

Typically, the initial imperfection discussed in the previous section is utilized to analyze the post-buckling response of a pipeline, assuming that the imperfect pipeline is initially stress-free. However, in reality, some initial stresses will be present in the imperfect pipeline. These imperfections in a pipeline may arise during the manufacturing process, reeling, laying, or due to

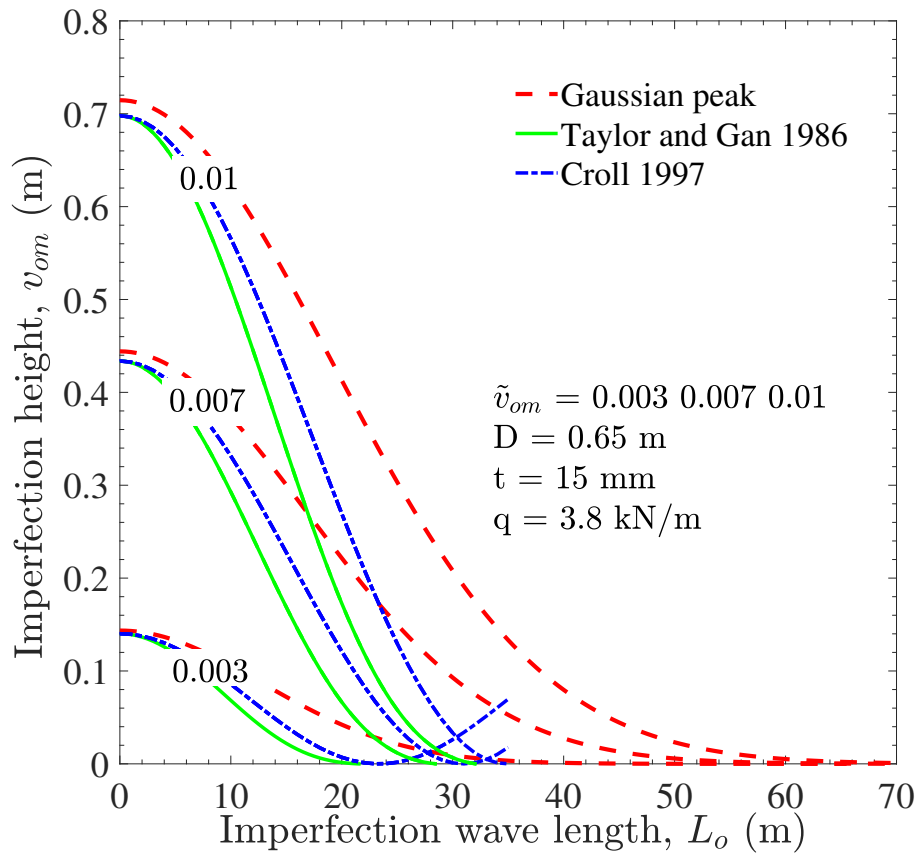


Figure 2.21: Comparisons of initial imperfection profile with the Gaussian shape

impacts during offshore activities. However, accurately accounting for the exact amount of initial stresses in a pipeline can be challenging. DNV (2007) also suggests that the imperfection for triggering buckling modes should be used from the initially straight and stress-free configuration. Some studies, such as Ju and Kyriakides (1988), Thusyanthan et al. (2010), and Mondal and Dhar (2017), have utilized the concept of self-weight dependent stressed imperfection in a surface laid pipeline for the UHB analysis. One of the main assumptions in their study is that the pipeline will exhibit a similar shape of initial imperfection to that of the seabed profile during the laying process.

Here, the finite element (FE) modelling sequence to generate the stressed initial imperfection in an initially straight pipeline is discussed. The FE modelling sequence for generating initially stressed

imperfection is shown in Fig. 2.22 for the buried pipeline. At first, the initial shape (based on Eq. 2.29) of imperfection is introduced on the rigid surface. The straight, stress-free pipeline's middle node is laid on the rigid surface's central node. The interaction between the pipe and the rigid surface (node-to-surface discretization with finite sliding formulation) is activated. In step 1, the submerged self-weight of the oil-filled pipe (q) is gradually applied. During this step, the rigid seabed and the ends of the straight and stress-free pipeline are fixed. The contact constraint is also activated.

The second step is to modify the boundary conditions to lower the pipe ends. After completing the second step, the stressed imperfect model of the pipeline can be obtained. There is some research

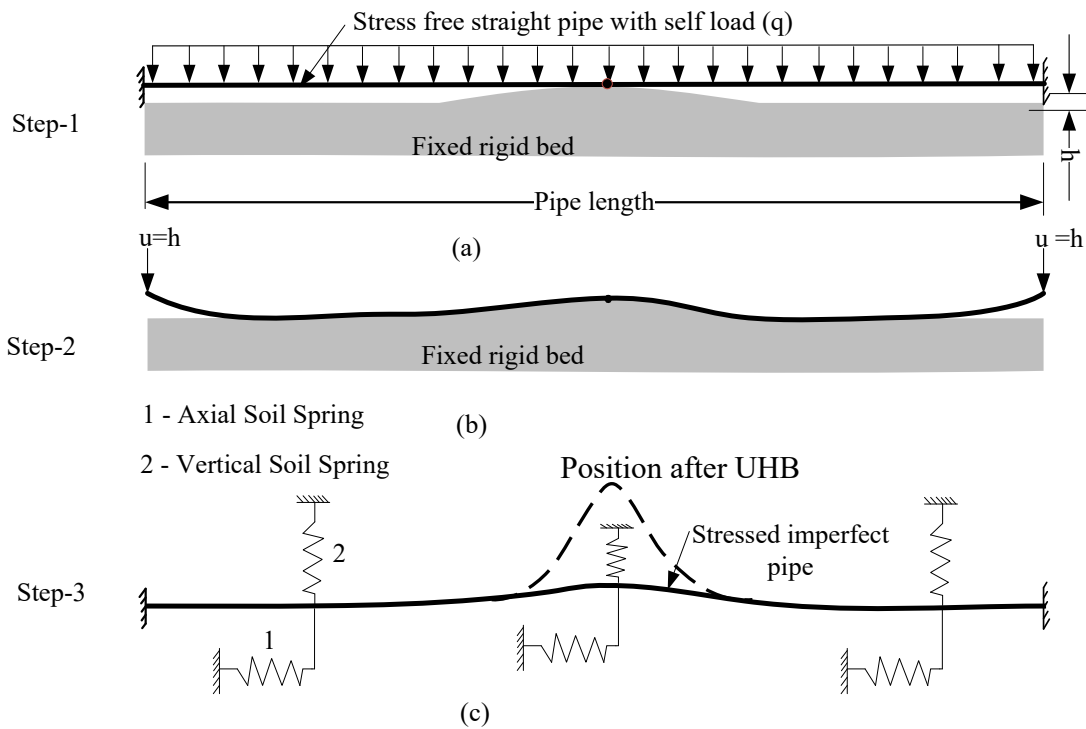


Figure 2.22: Schematic diagram for modelling stressed initial imperfection: (a) Application of self load on a straight pipeline; (b) Pipe ends are moved down to the bed; (c) Rigid bed is removed and spring can be activated for UHB analysis

gap in the modelling and investigation with stressed initial imperfection for the offshore buried pipelines subjected to large upheaval buckling. Further exploration is required in this area. The nature of buckling and strain development might differ with the stressed and unstressed initial imperfection consideration.

2.6 Study on the numerical modelling techniques for UHB

The numerical analysis of the pipe-soil interaction problem can be performed using two different approaches in finite element simulations. One option is to employ the Winkler soil-spring elements, which offer a simplified representation of soil behaviour. Alternatively, a more accurate and detailed analysis can be achieved using soil-continuum 3D elements that consider the full complexities of soil behaviour and interaction with the pipeline. The schematic illustration of the continuum model with pipe/soil interaction and the equivalent structural idealization using beam-spring model is shown in Fig. 2.23. However, when analyzing the UHB behaviour of long offshore pipelines, employing a soil-continuum model can be computationally challenging (Yoosef-Ghodsi, 2015). The major challenges in 3D continuum models are: (a) Generating, discretization, and solving the FE continuum model with a large pipe-soil domain requires significant endeavor; (b) The continuum model cannot capture non-continuum behaviour, such as fracture and flow behaviour, with slip planes developing within the soil mass; (c) Defining extensive soil properties and failure models is required for the continuum model; (d) Limited validation of the continuum model is available in the literature. To address this challenge, numerical solutions for the buckling problem of offshore pipeline can be obtained by employing the pipe-soil-spring approach (Fig.2.23(b)). In this approach, the soil resistance is defined by specifying a spring stiffness (force/relative displacement). The nonlinear behaviour of the soil resistance, as discussed in the previous Section 2.2.3, can be define using a spring by specifying pairs of force–relative displacement values. In the FE program Abaqus (implicit numerical scheme), the spring element is defined as SPRING1, connecting a pipe node to a fixed ground. A

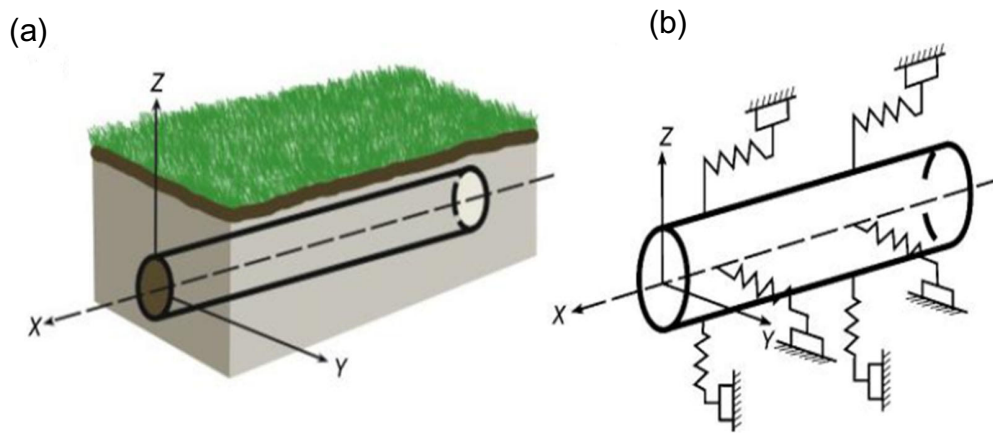


Figure 2.23: Schematic idealization: (a) Pipe/soil interaction with the continuum elements; (b) Idealization of the problem with beam and soil-spring structural elements (after Kenny and Jukes 2015)

frequently used nonlinear soil spring (force-relative displacement relationship) in this research to generate the FE model is shown in Fig. 2.24. When inputting the force-displacement values in Abaqus, it is essential to ensure they are in ascending order, from negative to positive (for example, first, the downward bearing soil resistance to the uplift soil resistances). Furthermore, the spring stiffness can vary depending on temperature and field variables.

For the pipelines with small initial imperfections, unstable snap-through buckling is the dominant behaviour. In an unstable buckling problem, the load-displacement response exhibits negative stiffness, necessitating the structure to release strain energy to attain its equilibrium position.

On the other hand, stable buckling behaviour is observed when the initial imperfection is large (shows the positive stiffness). Implicit dynamic and explicit dynamic algorithms, on the other hand, may not effectively capture the snap-through behaviour but work well for stable problems with higher initial imperfections. The unstable snap-through buckling behaviour can be

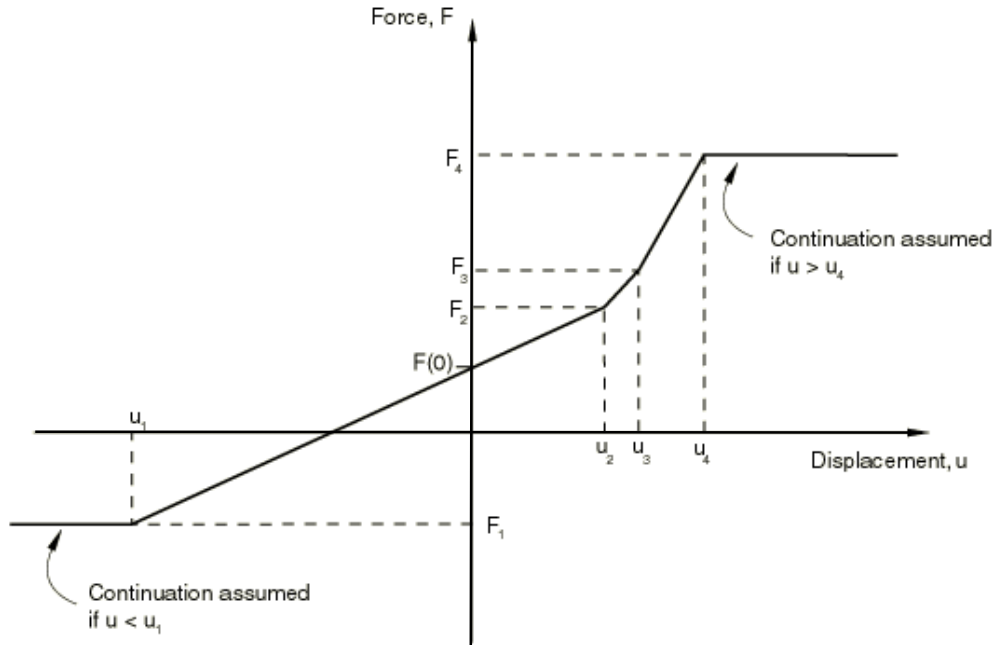


Figure 2.24: Nonlinear force–displacement response in SPRING1 element (after Simulia 2016)

numerically solved using arc-length (modified Riks methods) (Riks 1979; Crisfield 1981; Souza de Neto et al. 2011) method. In arc length method, a set of load factor-displacement pairs $\{\lambda, u\}$ is used to form the equilibrium path (either for stable or unstable). The unstable load-displacement (snap-through behaviour) response during upheaval buckling (Fig. 2.25) necessitates the use of arc-length numerical solution techniques. For the given time interval $[t_n, t_{n+1}]$, the corresponding incremental load factor is given by $\Delta\lambda = \lambda_{n+1} - \lambda_n$, where $\Delta\lambda$ is allowed to be a variable and the residual equation is redefined by Eq. (2.35) (Souza de Neto et al., 2011).

$$r(u_{n+1}, \Delta\lambda) \equiv f^{\text{int}}(u_{n+1}) - (\lambda_n + \Delta\lambda)f^{\text{ext}} = 0 \quad (2.35)$$

According to a previous study, the implicit modified Riks algorithm in the Abaqus FE software Simulia (2016) accurately predicts the unstable upheaval buckling behaviour in long HPHT offshore pipelines. However, this method does have certain limitations. For instance, it cannot be

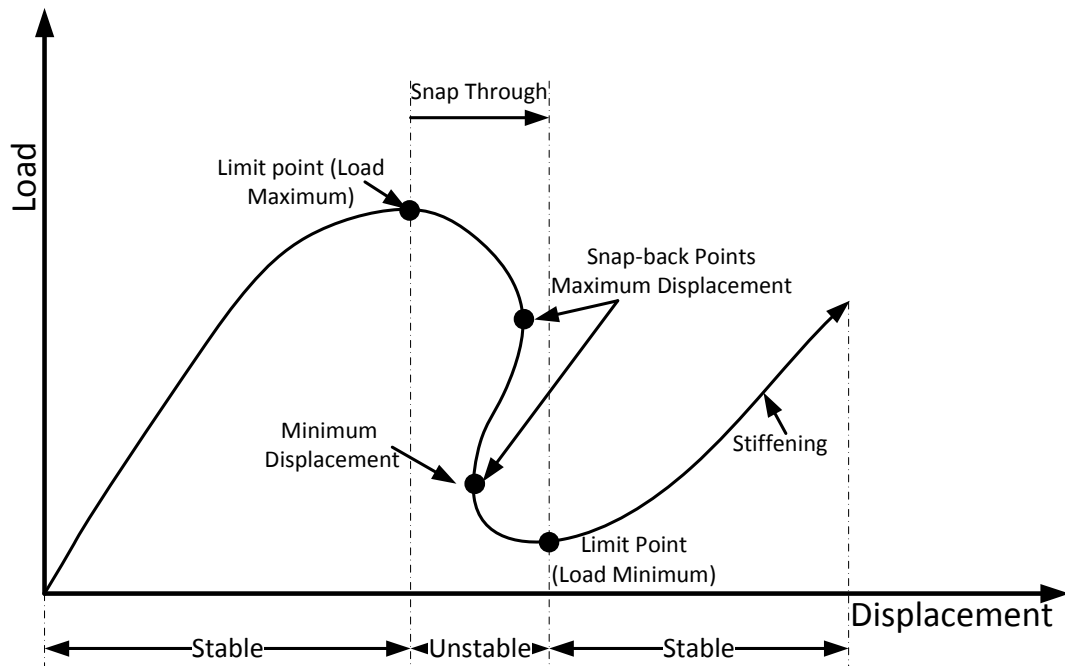


Figure 2.25: Load–displacement response for unstable equilibrium

directly followed by another step in the same analysis, and convergence issues may arise in the problem with contact separation. Additional research is needed to explore the most reliable numerical solution schemes, such as implicit/explicit Finite Element (FE) methods, for solving the post-buckling problem.

2.7 Study on local buckling behaviour in a post-buckled offshore pipeline

The critical strain required to induce local buckling in a pipeline is typically higher than the strain at the onset of upheaval buckling as shown in Fig. 2.26 (Shinkai et al. 2012). With the increase in axial compression in a offshore pipeline, the buckled segment of the pipe tends to deform upwards. At one instance, the local buckling can be observed in a pipeline. Local buckling may occur when the pipeline is exposed to a combination of pressure, temperature (resulting in axial compression), and bending forces. In such cases, failure is typically observed as yielding of the buckled section of the pipe.

Subsequently, during the post-buckling stages, the pipeline may fracture, leading to a loss of hydrocarbons. In Fig. 2.26, the onset strain of UHB (ϵ_{oub}) corresponds to the critical longitudinal strain in the pipe when the axial compressive stress reaches the maximum. The onset local buckling strain (ϵ_{olb}) refers to the moment when the pipeline experiences the highest bending moment, resulting in local buckling. The onset fracture strain (ϵ_{ofb}) is the strain once the crack initiate to propagate and the collapse strain (ϵ_{co}) is the instance, when the material no longer able to sustain the axial compression and total fracture in a pipeline occurs. This critical strain varies depending on factors such as operational conditions, sectional and material properties, and the presence of imperfections in both the seabed and the pipeline.

Figure 2.26 presents the strain generation in the pipeline during the application of bending moment. Initially, the bending moment increases until the point of onset of local buckling strain. At this critical moment, the pipeline experiences significant strain, and local buckling initiates. After reaching this point, the bending moment starts to decrease as the pipeline undergoes sectional wrinkling and fractures. This behaviour is typical in pipelines subjected to bending loads due to axial compression. Initially, the material can withstand increasing bending moments up to a certain limit. Beyond this limit, the material experiences local buckling, leading to a redistribution of stresses and a decrease in the overall bending moment capacity. The formation of wrinkles and fractures further reduces the moment capacity as the pipeline undergoes extensive plastic deformation. This research primarily focuses on addressing numerical challenges related to upheaval, post-upheaval, and fracture in offshore pipelines experiencing large deformation. It aims to characterize the critical strain limit points in a post-buckled offshore pipeline as shown in Fig. 2.26.

The moment–curvature relationship for the pipeline under pressure and axial load (Figure 2.27) reveals significant points, such as the elastic region with no permanent shape changes for small curvatures. Beyond the linear limit, plastic deformation begins, indicating the onset of local buckling, influenced by material nonlinearity, geometric imperfections, and soil resistances. After

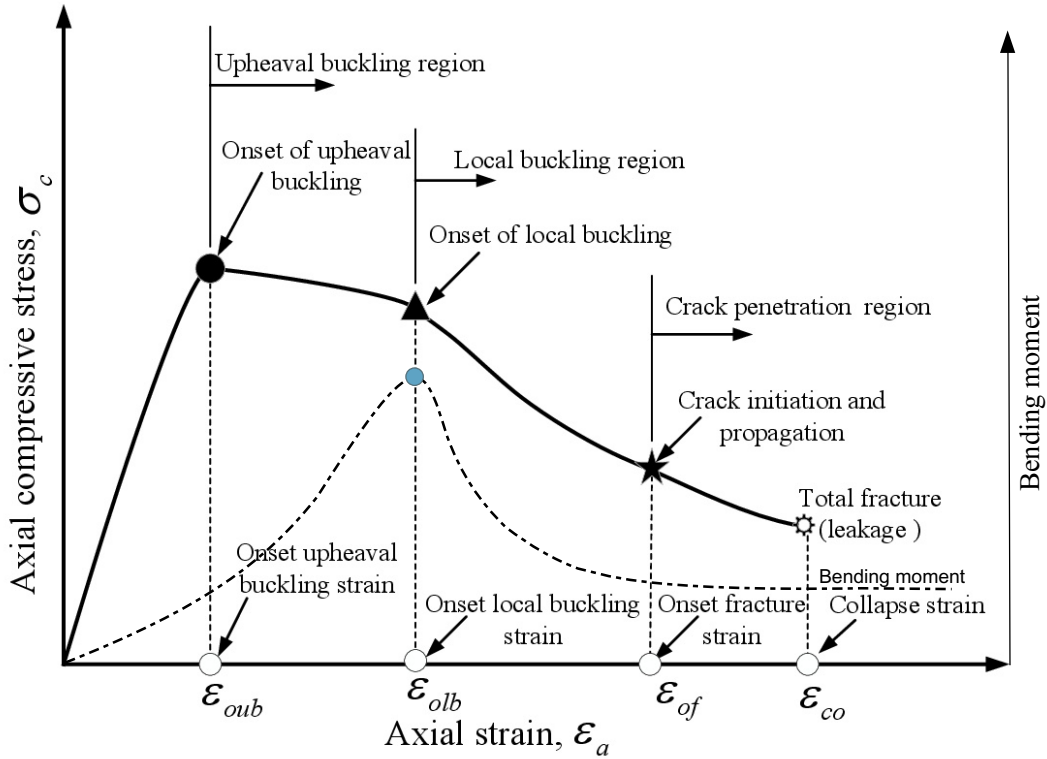


Figure 2.26: Deformation stages in a offshore pipeline during upheaval buckling, local buckling and fracture (after Shinkai et al. 2012)

local buckling initiation, global deformation continues with higher energy until the ultimate capacity of the pipe is reached, followed by a catastrophic capacity reduction with further curvature increase. This moment-curvature behaviour is critical for designing pipelines to withstand bending and buckling failures. The compressive strain concentration at the specific location of the pipe section results in local buckling. Local buckling and wrinkling occurs in the uncontrolled vertically buckled pipeline. The locally buckled pipe wall significantly ovalizes and ruptures for further compressive loading. According to DNV (2010), the ultimate compressive strain in a pressurized pipeline can be estimated using the equation given in Eq. (2.36).

$$\epsilon_{ult,c} = 0.78 \left(\frac{t}{D} - 0.01 \right) \left(1 + 5.75 \frac{\sigma_h}{\sigma_y} \right) \alpha_h^{-1.5} \alpha_{gw} \quad (2.36)$$

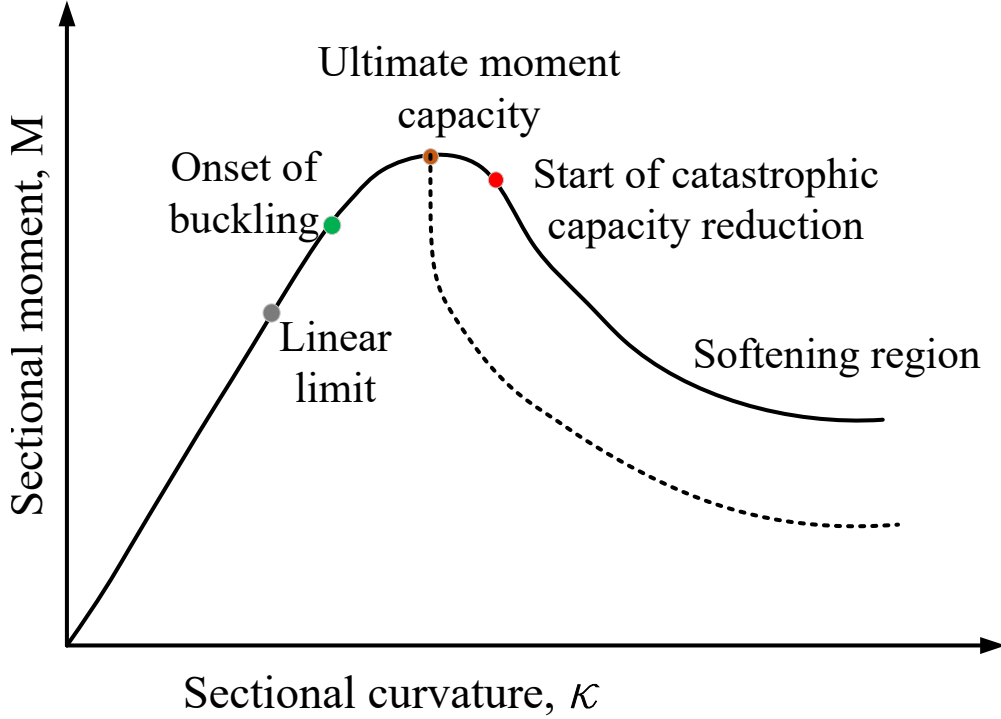


Figure 2.27: Typical sectional moment–curvature response in a pipeline (after Hauch and Bai 2000)

where α_h is the ratio of yield strength to the ultimate strength ($\frac{\sigma_y}{\sigma_{ult}}$) of the steel pipe, α_{gw} is the weld factor and σ_h is the hoop stress caused by the internal and external pressure difference given in Eq. (2.37).

$$\sigma_h = \frac{(P_i - P_e)(D - t)}{2t} \quad (2.37)$$

According to CSA (2007), the ultimate critical compressive strain in a pressurized pipeline is given Eq. (2.38).

$$\epsilon_{ult,c} = \begin{cases} 0.5 \frac{t}{D} - 0.0025 + 3000 \left(\frac{p_d D}{2tE} \right)^2, & \frac{p_d D}{2t} < 0.4\sigma_y \\ 0.5 \frac{t}{D} - 0.0025 + 3000 \left(\frac{0.4\sigma_y}{E} \right)^2, & \frac{p_d D}{2t} \geq 0.4\sigma_y \end{cases} \quad (2.38)$$

The Eq. (2.38) results strain value more than 2.0% for offshore pressurized pipelines. ALA (2005) also suggest to use the critical compressive strain given by the first part of Eq. (2.38) with pressure term. The limiting compressive and tensile strain criterion based on design guidelines are summarized in Table 2.1.

Table 2.1: Tensile and compressive strain criterion for onshore pipeline

Design Guidelines	Compressive limit (ϵ_t^{crit})	Tensile limit (ϵ_t^{crit})
DNV-OS-F101 (DNV, 2010)	$0.78 \left(\frac{t}{D} - 0.01 \right) \left(1 + 5.75 \frac{\sigma_h}{\sigma_y} \right) \alpha_h^{-1.5} \alpha_{gw}$	Plastic strain > 2.0%
CSA-Z662 (CSA, 2007)	$\begin{cases} 0.5 \frac{t}{D} - 0.0025 + 3000 \left(\frac{p_d D}{2tE} \right)^2, & \frac{p_d D}{2t} < 0.4\sigma_y \\ 0.5 \frac{t}{D} - 0.0025 + 3000 \left(\frac{0.4\sigma_y}{E} \right)^2, & \frac{p_d D}{2t} \geq 0.4\sigma_y \end{cases}$	2.5%
EN1998-4 (De Normalisation, 1998)	$\min \{1.0\% \text{ and } 0.4(t/D)\}$	3.0%
ALA (2005)	$0.5 \frac{t}{D} - 0.0025 + 3000 \left(\frac{p_d D}{2tE} \right)^2$	2.0%
ASCE (2009)	$0.4t/D$	3.0%
CSA-Z662 (CSA, 2007)	1.32 (unpressurized), 1.49 % (pressurized)	
ALA (2005)	1.32 % (unpressurized), 1.56 (pressurized)	

Although most of the design guideline provides critical compressive and tensile strain based on operating pressure in a pipeline, the operating temperature dependent strain limit has not been discussed.

Upheaval buckling failure of the pipeline is one of most common issues in offshore. However, most researchers have emphasized the plane-strain analysis for uplift resistance of the soil. Very few research has been done on the structural performance (local buckling and fracture) of the offshore pipeline. Gresnigt (1986) provided the experimental and analytical solution for plastic design criterion of buried steel pipelines. Klever et al. (1990) developed a finite element code-named UPBUCK using the beam elements to analyze upheaval buckling. Shaw and Bomba

(1994) generate a 1-D FE method which includes the nonlinear material and geometric properties for upheaval buckling. The critical buckling strain equations for energy pipelines have been studied and developed by Dorey et al. (2005). Karampour et al. (2013) theoretically analyzed the lateral and upheaval buckling for initially stressed and unstressed 1D pipeline, and they tried to improve some of the shortcomings of Ju and Kyriakides (1988) analysis. Liu et al. (2013) conducted a finite element model for UHB for the elastoplastic pipe where the initially imperfect pipe of 1D beam element and soil as a 2D continuum model is used. Mahdavi et al. (2013) performed the numerical analysis for critical strain capacity of pipeline with the 3D pipe and soil continuum model for the local buckling response of buried pipeline without considering thermal loads. Liu et al. (2014) solved the global buckling issues of the subsea pipeline using the finite element method in Abaqus and compared the buckling result from implicit and explicit integration schemes. Zeng et al. (2014) conducted dimensional and finite element analysis and developed the equations for critical axial force and out-of-straightness. The post-buckling failure modes of pressurized X65 steel pipelines under monotonic loading conditions have been studied by Mohajer et al. (2018). Vazouras et al. (2021) performed experimental analysis and numerical modelling for UHB using beam and shell coupled elements with soil continuum.

The governing failure mode of the pipeline due to excessive material utilization is usually local buckling. Local buckling appears as a wrinkle in the pipeline's cross-section in compression side, leading to sectional ovalization. The large plastic strains (ϵ_p) develops at the compression side of the pipeline. The locally buckled pipeline cannot resist the additional bending moment and could collapse in the long run. The in-air pipeline local buckling and wrinkling failure analysis have been performed by Mohareb (1995), Murray (1997) , Zimmerman et al. (2004), Ozkan and Mohareb (2009a,b), experimentally and numerically for applied moments and internal pressure. They have found that for higher D/t ratio, the moment capacity and buckling strain of the steel pipes decreases significantly. However, they did not consider the soil conditions for local buckling due to thermal and pressure loading. The previous researcher have not well studied the

post-upheaval local buckling and failure of the offshore buried pipeline.

2.8 Review on the modelling of fracture in the HPHT pipeline

Previous research indicates that despite experiencing a significant vertical displacement under high operating conditions, offshore pipelines can still maintain a serviceable condition within a certain range of plastic strain. The main question that arises is the order of occurrence between local buckling and fracture in offshore post-buckled pipelines when subjected to immediate impacts from offshore activities. Given the HPHT conditions, upheaval buckling of the pipe is expected. However, there remains uncertainty whether the pipe will collapse due to local buckling and wrinkling or experience tensile fracture resulting from an initial crack on the pipe surface. The investigation on the two potential failure modes of offshore pipelines, namely local buckling and fracture, is of paramount importance. Structural damages such as dents, cracks, scratches, corrosion and cavities commonly occur in offshore transmission pipelines. The presence of initial structural damage causes the pipeline to fracture during operation. The stress-based and strain-based design methods are commonly used in the pipeline industry. In the stress-based design approach, the applied stress is kept well below the limiting stress (Specified minimum yield stress (SMYS) and the safety factor). Also, the longitudinal strain is kept well below 0.5% in stress-based design (Yoosef-Ghodsi 2015). Strain-based design (SBD) is used for the global large plastic deformation problem in a pipeline. It aims to maintain pipeline service and integrity under large longitudinal plastic deformation (typically greater than 0.5 % strain). The extent of strain in the offshore pipeline varies depending on the specific application, installation and loading conditions. Bai and Bai (2005) reported that the offshore pipelines experiencing large deformation can reach a maximum strain of up to 4% before reaching the point of fracture or rupture. One of the objective of this study is to evaluate the condition of offshore pipelines experiencing upheaval buckling, focusing on local buckling or fractures at high strain levels (3–4%) as reported in Bai and Bai (2005). Figure 2.28 illustrates the typical strain range (0.5–4%) based on pipeline loading

events and applications.

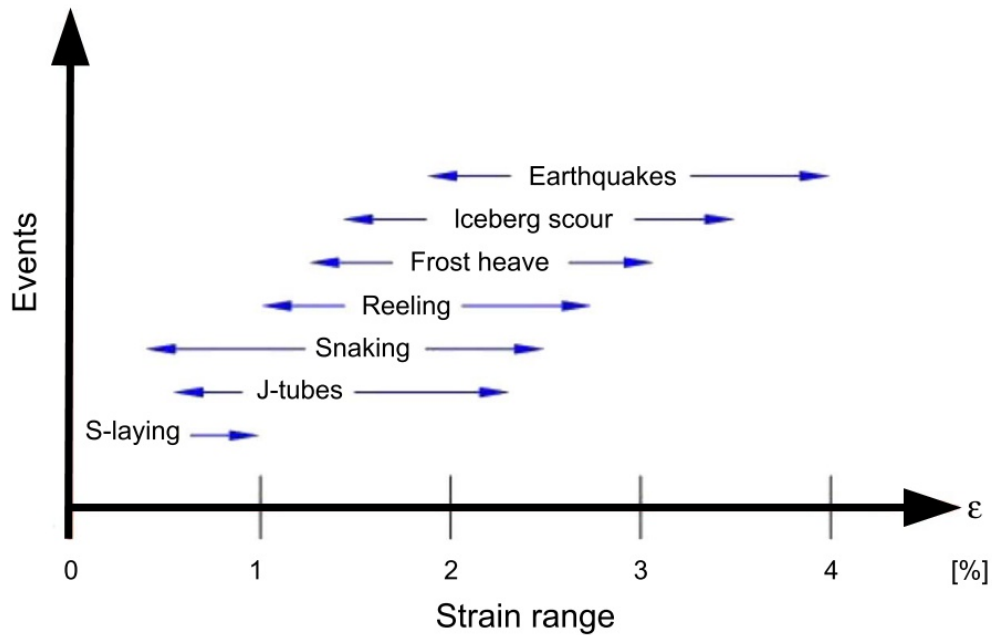


Figure 2.28: Typical strain ranges in offshore pipeline based on application (after Bai and Bai 2005)

The fundamental criteria equation for SBD is the comparison of the applied strain, or strain demand (ϵ_d) to the permissible strain, or strain capacity (ϵ_c) based on the relationship of ($\epsilon_d < \epsilon_c$). Under high-level plastic strains, the buckled pipeline leads to tensile failure. Estimation of tensile strain capacity (TSC) is crucial for the post-buckled pipeline. The study investigates the tensile fracture initiation and propagation in the post-buckled pipeline during large-scale plastic deformation. While some studies examine the fracture behaviour of onshore pipelines (Mohareb 1995; Linkens et al. 2000; Jayadevan et al. 2004, Østby et al. 2005; Zhang et al. 2014a; Agbo et al. 2019; Ameli et al. 2019; Lin et al. 2020) there is limited research on assessing fracture in HPHT post-buckled pipelines. In previous studies, the evaluation of stress intensity factors for pipelines has predominantly relied on J-integral in linear elastic fracture mechanics. However, limited research exists concerning the utilization of advanced FE methods, such as the eXtended Finite Element Method (XFEM), for offshore pipeline fracture assessment.

The post-buckled pipeline with the initial structural defects such as a crack can be numerically

modelled with the use of eXtended finite element methods (XFEM) in Simulia (2016). XFEM overcomes the drawbacks of classical FEM with an enriched shape function basis with discontinuous features for representing the discontinuity in the element, which enables the fracture representation without remeshing the crack-tip field (Dolbow et al. 2000; Moës et al. 1999). Different damage initial criterion, such as the maximum principal stress (MAXPS), maximum principal strain (MAXPE) and the user-defined strain-based modified Mohr-Coulomb (MMC) can be used for the assessment of fracture behaviour in a buckled segment of the pipeline. The XFEM-based cohesive zone model is based on the traction-separation cohesive behaviour used by some researchers for the fracture study of the pipeline. There are several key parameters required in fracture mechanics to understand the behaviour of materials under stress to predict the crack initiation and propagation. These parameters are still require for the prediction of initiation and propagation of cracks in offshore pipeline. The major parameters are:

- Stress intensity factor (SIF) (K) : SIF represents the stress intensity near the crack tip. Three modes of SIF, namely mode-I (opening), mode-II (sliding) and mode-III (antiplane shearing) are commonly used in fracture mechanics. In the pipeline fracture analysis, the mode-I SIF is predominantly used due to its dominance over other fracture modes. To obtain the stress field at the crack tip location (r, θ) for a plane problem in linear elastic fracture mechanics (LEFM), the Westergaard stress function method (Belytschko and Black 1999) is often employed. As $r \mapsto 0$ at the crack tip location with LEFM, it represents an infinite stress (stress singularity). The SIF characterizes the strength of the stress-strain field at the crack tip location. When the SIF is equal or greater than the critical value (K_{cr}), the crack is said to be in an initially unstable state of growth, which results in rupture.
- Energy release rate (G_c) : The rate at which the energy is released (material plastic flow) during the growth of crack is represented by the energy release rate. It is a key parameter used to predict the crack growth and the critical condition for the crack propagation.
- Fracture toughness (K_{IC}) : The critical value of SIF is the fracture toughness. It represents

the materials ability to withstand the crack growth under stress.

- **Crack Propagation Direction:** Different criterion are available in the literature to predict the direction of crack propagation. The maximum tangential stress criterion based on Erdogan and Sih (1963), maximum energy release rate criterion Palaniswamy (1978) and $K_{II} = 0$ criterion are available in Abaqus software. In the maximum tangential stress criterion, the crack propagation occurs in a direction where the maximum principal stress is at its highest. In the maximum energy release criterion, the crack starts to propagate once the maximum energy release rate (G_{θ}) reaches the critical value (G_c). The crack propagates along the direction of the maximum energy release rate. In ABAQUS, the user subroutine UDMGINI serves the purpose of defining the normal direction to the crack plane/line for enriched elements, considering equivalent fracture strain to account the crack tip constraints. It offers the flexibility to specify multiple failure mechanisms within an element, with the most critical mechanism determining the ultimate failure behaviour. Furthermore, this subroutine can be effectively combined with the built-in damage evolution models available in Abaqus (Simulia, 2016). Although there are several studies on the onshore pipeline subjected to fracture, very few studies have taken place on offshore post-buckled pipelines subjected to fracture. This area will be further explored with the implementation of XFEM for fractures behaviour in post-buckled pipeline.

2.9 Summary from the literature review

The literature review highlights the following aspects that should be taken into consideration for the research:

- (a) The upheaval buckling problem is a complex design challenge in offshore environments, where soil resistance significantly affects the buckling behaviour of the pipeline. Field observations indicate that pipelines can move significant distance above the seabed, suggesting that the current design guidelines, which assume the pipeline remains in place,

may be overly conservative.

- (b) Post-peak degradation of soil resistance is a crucial factor to be considered for pipe-soil interaction problem. The nonlinear degradation of uplift resistance in dense and loose sand must be considered to assess the critical and safe temperature in HPHT offshore pipeline. The structural response of offshore buried pipelines subjected to upheaval buckling, and undergoing large deformation has received limited research attention. Developing efficient numerical models incorporating post-peak degradation of soil resistance is essential to address this research gap.
- (c) While analytical solutions exist in the literature, they are typically valid only for surface-laid pipelines and specific soil conditions. Analytical solutions have limitations in addressing nonlinearity and large deformation kinematics, necessitating the development of more comprehensive numerical models.
- (d) The shape and size of the initial imperfection greatly influence the critical and safe temperature in post-buckled offshore pipelines. However, the existing literature lacks a comprehensive numerical model that adequately considers unstressed and stressed initial imperfections in finite element (FE) analysis. The term "unstressed initial imperfections" refers to a condition in the finite element (FE) model for buckling analysis where the initial imperfection is stress-free. In other words, no initial stress is considered when shaping the imperfection in the pipeline model. Conversely, "stressed initial imperfections" describe a condition where the initial imperfection shape is created as the straight, stress-free pipeline descends to the imperfect seabed under the influence of gravity. In this case, the buckling analysis is conducted with the generated imperfect shape that includes initial stresses. It is essential to develop a numerical model that can accurately incorporate and assess the impact of different types of initial imperfections on the critical and safe temperature of post-buckled pipelines.

- (e) The upheaval buckling problem is characterized by a mathematically unstable snap-through buckling behaviour, wherein the pipeline undergoes sudden and rapid deformation. The establishment of an appropriate numerical scheme is necessary to solve snap-through buckling problems in offshore pipelines. This involves considering various options such as implicit methods (static, static Riks, static-stabilization, implicit dynamic (quasi-static)) or explicit dynamic algorithms.
- (f) The buckling strain increases with the vertical movement of offshore pipeline. There is limited research in the literature to predict the local buckling and wrinkling behaviour of post-buckled offshore pipelines, as 1D pipeline models cannot adequately capture sectional deformation, local buckling and failures. Hence, it is imperative to develop a computationally efficient numerical model that can effectively address the local buckling failure of offshore buried pipelines.
- (g) Post-buckled offshore pipelines can be vulnerable to impact from submarine activities, which can lead to the formation of initial cracks or dents on the post-buckled section. It is necessary to develop a suitable numerical model to tackle the challenges associated with large deformation and fracture in a post-buckled pipeline. This model should be capable of accurately capturing the complex behaviour and interactions involved in the post-buckling scenario. This will enable a better understanding of the fracture problem and aid in developing effective strategies to mitigate fracture and ensure the safe operation of offshore pipelines.

Chapter 3

Numerical Modelling of Upheaval Buckling of Offshore Pipelines with Unstressed and Stressed Initial Imperfections

ABSTRACT

Buried offshore pipelines that transport hydrocarbon at high-temperature and high-pressure might experience upheaval buckling (UHB). Although pipelines are designed to remain in place, field evidence show that the buried pipeline might displace a significantly large distance in the upward direction. This implies a reduction of uplift soil resistance with displacement that eventually becomes zero if the buckled section comes out of the seabed. In the present study, the pre- and post-buckling behavior of offshore pipelines buried in sand is investigated considering the degradation of uplift soil resistance with the upward displacement of the pipe. The soil resistance degradation models were implemented in a finite element (FE) program. The FE study reveals that the capacity of the pipeline to carry the load generated from pressure and temperature increase reduces significantly if post-peak degradation of uplift soil resistance is considered. The effects of the uplift soil resistance degradation model, burial depth and pipe dimensions (diameter and thickness) on UHB for varying initial imperfections are investigated. Based on a simplified model for developing initial stresses in pipeline, it has been shown that initial stresses primarily affect the UHB at lower ranges of upward displacement of the pipe.

Keywords: Soil resistance, offshore pipeline; upheaval buckling, finite element analysis; imperfection; plastic strain; large displacement

3.1 Introduction

Pipelines are often used offshore to transport hydrocarbon over a large distance through various landforms, soil types and topographic conditions. In shallow water depths, the pipelines are typically buried through trenching and backfilling. The primary purpose of burial is to assure the flow by maintaining an elevated hydrocarbon temperature and avoiding excessive displacement during operation. The increase in temperature and pressure of hydrocarbon during operation can create large axial compression, resulting in buckling of the buried pipeline in the upward direction as the lateral resistance is higher than the uplift resistance for typical burial depths. The excessive vertical displacement of the buried pipeline resulting from the upheaval buckling can create many issues, including: (i) loss of pipeline integrity due to unacceptable plastic strain and/or fracture failure, and (ii) moving above the seabed, which increases the risk of damage by other seafloor activities, such as fishing gears, dropped objects, and submarine debris flow impact on the suspended sections. The upward displacement of the pipeline depends not only on operating conditions (e.g., temperature and pressure) but also on the uplift soil resistance. The uplift displacement of a pipeline at a large distance resulting from the UHB is the focus of the present study.

The existing design guidelines developed procedures and criteria for pipeline design against UHB based on the assumption that the pipeline remains in place (DNV 2007) during operation, which requires sufficient uplift soil resistance resulting from the weight of the uplifted soil wedge and shear resistance at the side of the wedge. The peak uplift resistance mobilizes at relatively small displacements, which depends on soil density, burial depth (H) and pipe diameter (D) (e.g., $0.03D$ or $0.01H$, Cheuk et al. 2008). Nielsen et al. (1990) suggested a limiting upward displacement of 10–20 mm in natural backfill to minimize the risk of gradual upward movement of pipeline. In the field, however, the pipeline might displace a significantly large distance in the vertical direction during operation. For example, Nielsen et al. (1990) reported upheaval buckling at 26 locations of a buried pipeline in the Danish sector of the North Sea. In one segment, a 10 m section moved 1.1

m above the seabed.

Over the last three decades, a considerable amount of work focused on the issues related to UHB, which include the development of analytical and numerical tools, experimental studies, and assessment of soil resistance. While the analytical solutions are relatively simple, they have been developed based on several simplified assumptions. For example, the pipeline has been idealized as a long heavy beam (Hobbs 1984; Taylor and Gan 1986; Wang et al. 2012; Karampour et al. 2013; Shi et al. 2013). These studies also assume a *wished-in-place* pipeline that rests on a rigid frictional seabed before buckling and does not explicitly model the uplift soil resistance; instead, a uniform "effective weight" (submerged self-weight) per meter length of the pipeline is given. Recognizing the limitations of modelling with submerged self-weight and taking advantage of advanced numerical tools (e.g., finite element (FE) modelling), the soil behaviour has been modelled in a better way using a set of springs (i.e., defining force-displacement curves), where the mobilized soil resistance depends on pipe displacement (Klever et al. 1990; Shaw and Bomba 1994; Maltby and Calladine 1995a,b; Zhang and Tuohy 2002). In most FE models, the pipe is again idealized as a beam where the axial, lateral and vertical springs are attached to the FE nodes to provide soil resistance in the three orthogonal directions (Maltby and Calladine 1995a; Takada et al. 2001; Gao et al. 2011; Liu et al. 2013; Ning et al. 2022). The location of the springs in the 1D FE model is shown in the subsequent section. FE methods has also been used to model UHB of unburied pipelines (e.g., Wang et al. 2015). FE modelling of pipeline with beam elements has some limitations, such as the differential pressure cannot be applied directly.

In most of the above FE analyses, the soil springs have been defined using linear, bi-linear or trilinear force–displacement relationships, based on existing design guidelines (e.g., ALA 2005; DNV 2007). This approach is valid for certain displacement levels, as the design objective for UHB is to keep the pipe in place during operation (practically limited displacement) (DNV 2007). As some sections of the pipeline might displace considerably large distances during operation, the force–displacement behaviour at large displacements needs to be considered in the analysis. For

example, Klever et al. (1990) showed that the classical effective weight method of upward resistance is unconservative, as it gives significantly higher permissible temperatures. Other studies also suggested using the full uplift force versus displacement curve, including the post-peak degradation, for UHB analysis (Goplen et al. 2005; Wang et al. 2010).

Physical model tests were conducted to understand the uplift force–displacement behaviour of pipelines buried in the sand (Trautmann et al. 1985; Cheuk 2005; Chin et al. 2006). While some studies focused primarily on the peak resistance (Trautmann et al. 1985; Cheuk 2005), upward pulling of the pipe was continued in some studies up to the ground surface to examine the behaviour at large displacements (Bransby et al. 2001; Wang et al. 2012). Two-dimensional FE analyses have also been performed to understand the mechanisms involved in uplift tests (e.g., Yimsiri et al. 2004; Jung et al. 2013; Roy et al. 2018b,a). The physical and numerical studies show that the uplift resistance decreases with an upward displacement of the pipe and becomes zero when it reaches the ground surface. The peak uplift resistance and post-peak degradation depend on several factors, including soil density and burial depths (Bransby et al. 2001; Wang et al. 2012; Roy et al. 2018b).

In summary, the existing studies did not consider the post-peak degradation of soil resistance at large displacements, which can have significant impacts on the buried pipelines subjected to UHB. In addition, modelling the pipe with beam elements supported by effective weight or idealized soil spring may not calculate the UHB properly. These issues have been investigated in this study. The paper has been organized in the following way. First, the performance of the present FE model is shown by simulating an unburied pipeline and comparing the results with analytical solutions. Second, two suitable models for uplift force–displacement behaviour are presented and implemented in the FE model to simulate the UHB of pipelines buried in dense and loose sands. Finally, a parametric study is performed to show the effects of various parameters. In addition, FE modelling techniques, including the modelling with beam/pipe elements, differential pressure and the initial stresses in the pipeline are examined.

3.2 Problem statement

As outlined in the research motivation in Chapter 1 (Fig. 1.2), this study predominantly focuses on Phase-I, aiming to identify potential upheaval buckling and strain generation resulting from unstressed and stressed initial imperfections in a buried offshore pipeline. Figure 3.1(a) shows the model layout and key features of the pipeline used in this study, while Fig. 3.1(b) shows the finite element model with the location of springs and loadings. Taylor and Gan (1986) divided the typical initial imperfections into three categories: empathetic, isolated prop and infilled prop. Among them, the empathetic model, where the pipeline remains in contact with the vertical undulation, has been shown to be the worst-case scenario. Using the empathetic model, the initial vertical position of the pipeline from the horizontal datum (v_o) with the horizontal distance (x) is defined using the following equation (Taylor and Gan 1986):

$$v_o = v_{om} \left\{ 0.707 - 0.26176 \frac{\pi^2 x^2}{L_o^2} + 0.293 \cos \left(2.86 \frac{\pi x}{L_o} \right) \right\} ; \frac{-L_o}{2} \leq x \leq \frac{L_o}{2} \quad (3.1)$$

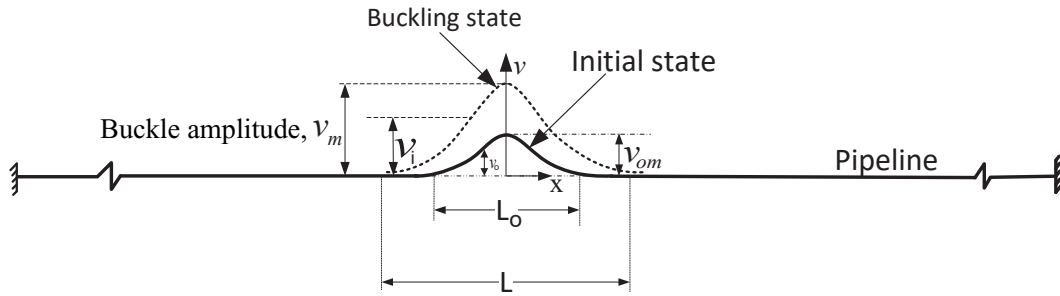
where v_{om} is the maximum amplitude at $x = 0$, and L_o is the initial imperfection length. Moreover, v_{om} and L_o are related as $\frac{v_{om}}{L_o^4} = 2.407 \times 10^{-3} \frac{q}{EI}$, where q is the submerged self-weight of the pipe per unit length, and EI is the flexural rigidity.

FE simulations are performed for the following conditions:

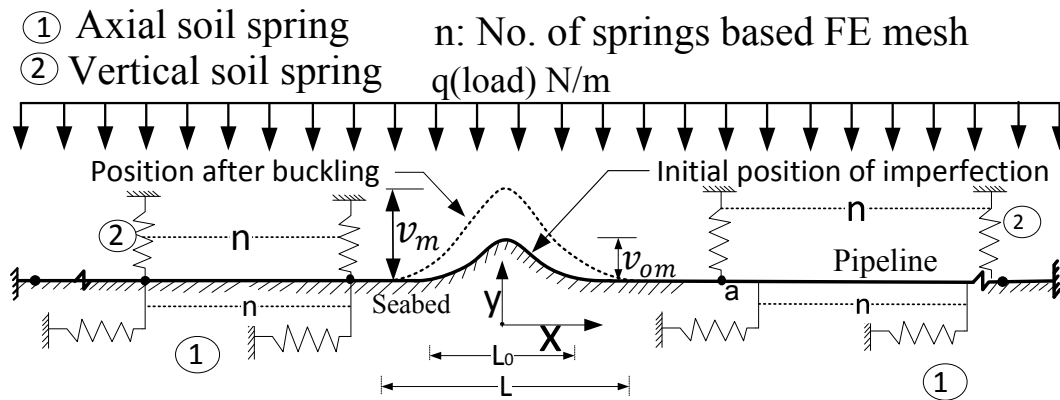
Set I:

This set of analyses is performed to validate the developed FE analysis through comparison with analytical solution of Taylor and Gan (1986). In this case, the pipeline is placed on top of an imperfect rigid seabed defined by Eq. (3.1) ("unburied" condition). The soil resistance per unit length of the pipeline in the axial direction (F_a) with axial displacement (u_a) is given by (Taylor and Gan 1986):

$$F_a = q \phi_a (1 - e^{-25 u_a / u_\phi}) \quad (3.2)$$



(a) Problem layout and key features of the postbuckled pipeline



v_m : Current position after buckling
 v_{om} : Initial position of imperfection

(b) 1D FE model with soil-spring locations

Figure 3.1: Problem layout and spring locations: (a) Problem layout and key features of the postbuckled pipeline; (b) 1D FE model with soil-spring locations

where ϕ_a is the axial friction coefficient and u_ϕ is the axial displacement when full axial resistance mobilizes. In FE analysis, the rigid seabed is defined using a large bearing resistance. The analytical solution for this case is obtained by implementing the method developed by Taylor and Gan (1986) in Matlab.

Set II:

This set of analyses is performed for buried pipelines in loose and dense sands with and without post-peak softening. Nonlinear and linear post-peak degradation of uplift resistances is used. FE analyses are performed using one-dimensional beam elements, except for some analyses to show the effects of modelling differential pressure where one-dimensional pipe elements are used (Section 3.5.3).

Initially, the pipeline lies on an imperfect seabed Eq. (3.1) without any initial stresses (i.e., stress-free initial conditions), which represents a 'wished-in-place' configuration. The authors understand that, prior to the application of operating loads (temperature and pressure), the pipeline might have some stresses that generate from uneven seabed profile and installation, requiring implementation of complex modelling techniques. Simulations are mainly performed for stress-free initial conditions except for some cases discussed in the later sections where the pipeline is placed on the uneven seabed profile Eq. (3.1) under the submerged weight of the pipeline, which is called "initially stressed" pipeline.

In the validation model (Set I), the geometry and other model parameters are the same as Taylor and Gan (1986), as the results are compared ($D = 650$ mm, $t = 15$ mm, $q = 3.8$ kN/m, $\phi_a = 0.7$, $u_\phi = 5$ mm). In the 'base case' simulations for Set II, a steel pipe of 300 mm outer diameter (D) and 12.7 mm wall thickness (t), having a 50 mm concrete coating is considered. Using the density of steel, concrete, seawater and oil of 7850 kg/m³, 2800 kg/m³, 1025 kg/m³ and 800 kg/m³, respectively, $q = 1.59$ kN/m is calculated. For the base case, the burial depth (H) (i.e., depth of the center of the pipe) is $3D$. The pipe is modelled as an elastic-plastic material with Young's modulus ($E = 206$ GPa), yield strength ($\sigma_y = 448$ MPa) and coefficient of thermal expansion

($\alpha = 11 \times 10^{-6}$ per $^{\circ}\text{C}$). All the model parameters are listed in Table 3.1.

Table 3.1: Geometry and pipeline model parameters used for base case FE simulations

Parameters	Value
Length of Pipe, L (m)	3,000
External diameter of pipe, D (mm)	300
Wall thickness of pipe, t (mm)	12.7
Young's modulus of pipe, E (GPa)	206
Poisson's ratio of pipe (μ)	0.3
Pipe-soil interface friction coefficient (f)	0.8
Yield stress of pipe, σ_y (MPa)	448
Coefficient of thermal expansion, α (per $^{\circ}\text{C}$)	11×10^{-6}
Thickness of concrete cover (m)*	0.05
Density of steel, ρ_s (kg/m^3)*	7850
Density of concrete, ρ_c (kg/m^3)*	2800
Density of oil, ρ_o (kg/m^3)*	800

* Parameters used to calculate submerged weight of pipe per meter length

3.3 Numerical modelling

Numerical analyses are performed using Abaqus/Standard FE software. A 3,000 m long pipeline is discretized using one-dimensional 1.0 m long 2-node linear beam (B21H) or linear pipe (PIPE21H) elements with hybrid formulations. One advantage of using PIPE21H elements is that the differential pressure can be applied separately. A mesh sensitivity analysis is performed by varying element lengths from 0.1 to 1.0 m for the exact analytical problem available in Taylor and

Gan (1986), utilizing the proposed 1D finite elements with soil springs. However, no significant difference in buckling behaviour is observed for element size less than 1.0 m, as shown in Fig. 3.2. Therefore, all the analyses are performed using 1.0 m long beam or pipe elements.

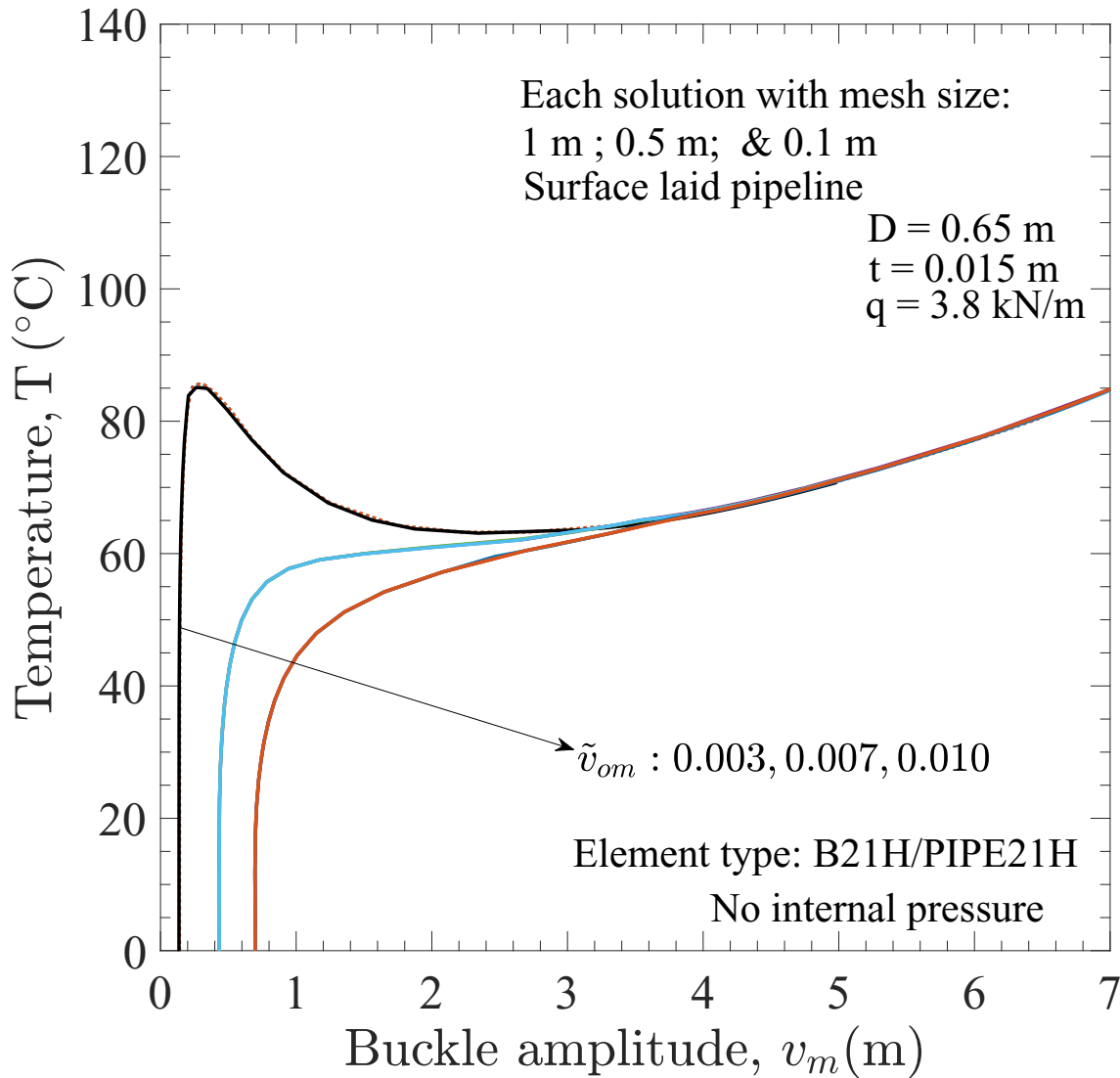


Figure 3.2: Mesh sensitivity analysis with varying element size

The soil resistance to pipeline displacement is modelled using nonlinear springs (SPRING1 in the software) based on the force–displacement curves described in the following sections. The FE analysis consists of two steps: (i) the general static step where the submerged weight (q) is applied

as a line load for both unburied (Set I) and buried (Set II) conditions; and (ii) the static Riks step where the vertical displacement of the pipeline is calculated with an increase in temperature. When the pipeline is modelled using pipe elements, the internal operating pressure p is applied in another step before step (ii). In the second step, the modified Riks (Riks 1979) algorithm available in the Abaqus FE software is used to avoid numerical issues related to unstable buckling in snap-through cases, as described later. The initial and final temperatures are defined using the predefined fields. The geometric nonlinearity is considered in both steps.

Fixed boundary conditions are applied to both ends of the pipe. Note, however, that the end conditions do not have a significant effect on buckling in the mid-section as the pipeline is long. The simulation is continued for a sufficiently large temperature increase (T) above the ambient temperature. As a result, the pipeline displaces vertically to a considerably large distance ($v_m > 3.0\text{m}$). At this stage, a section of the pipeline moves above the seabed, which was also reported from some field investigations (Nielsen et al. 1990; Liu et al. 2013), and there is no soil resistance on this section.

3.4 Modelling of soil resistance for buried pipeline

The vertical upward (uplift), vertical downward (bearing) and axial force–displacement relations are required for the analysis of the buried pipeline (Set II in Section 3.2). The axial (F_a) and bearing (F_d) resistances are defined using ALA (2005).

3.4.1 Uplift resistance

The uplift resistance is one of the main factors that control upheaval buckling. The uplift resistance consists of: (a) the submerged weight of the oil-filled pipeline with the coating (e.g., concrete) (q), and (b) the uplift resistance resulting from the weight of the lifted soil wedge and soil shearing resistance.

3.4.1.1 Uplift resistance of pipeline buried in loose sand with post-peak reduction

Physical model tests show that the uplift resistance (F_v) gradually increases with upward displacement (v), reaches the maximum value (F_{vp}) at $v = v_p$ and then decreases to zero when the pipe moves to the ground surface (Bransby et al. 2001; Bransby and Ireland 2009; Wang et al. 2012; Williams 2014). Based on the experimental results where the pipe was displaced to a large distance (up to the ground surface), Wang et al. (2012) proposed an empirical equation to calculate the uplift resistance for the peak and post-peak regions, which can be written in a simplified form as:

$$F_v = \gamma' D^2 \left[\left\{ (\tilde{H} - \tilde{v}) - \frac{\pi}{8} \right\} + f(\tilde{H} - \tilde{v})^2 \right] \quad (3.3)$$

where \tilde{H} is the initial embedment ratio ($= H/D$), \tilde{v} is the normalized vertical displacement ($= v/D$). The first part of Eq. (3.3) represents the weight of the failure wedge, while the second part is for soil shearing resistance along the vertical slip planes from the springlines. Inserting $v = v_p$ in Eq. (3.3), the peak uplift resistance can be calculated. Wang et al. (2012) also suggested that, for a reliable and conservative uplift resistance of loose sand, the uplift resistance factor f to be calculated based on critical state condition as $f = K \tan \phi'_c$, where ϕ'_c is the critical state friction angle and K is the coefficient of lateral earth pressure ($= 1 - \sin \phi'_c$, DNV (2007)). Equation (3.3) is used to define the nonlinear force–displacement (F_{v-v}) curve from the peak to large displacements (line L in Fig. 3.3). A linear force–displacement line is used for the pre-peak behaviour.

The uncertainties in estimating the displacement (v_p) required to mobilize F_{vp} is generally high; and previous studies suggested that it depends on H and D ; for example, at $\approx 1\%H$ or $\approx 3\%D$ (Cheuk et al. 2008), and $(1-8\%)H$ (Wang et al. 2012). In the present study, $v_p = 0.012$ m is used.

3.4.1.2 Uplift resistance of pipeline buried in dense sand

Similar to tests in loose sand, physical model tests were conducted on dense sands (Bransby et al. 2001; Cheuk et al. 2008). The main difference in force–displacement behaviour and failure

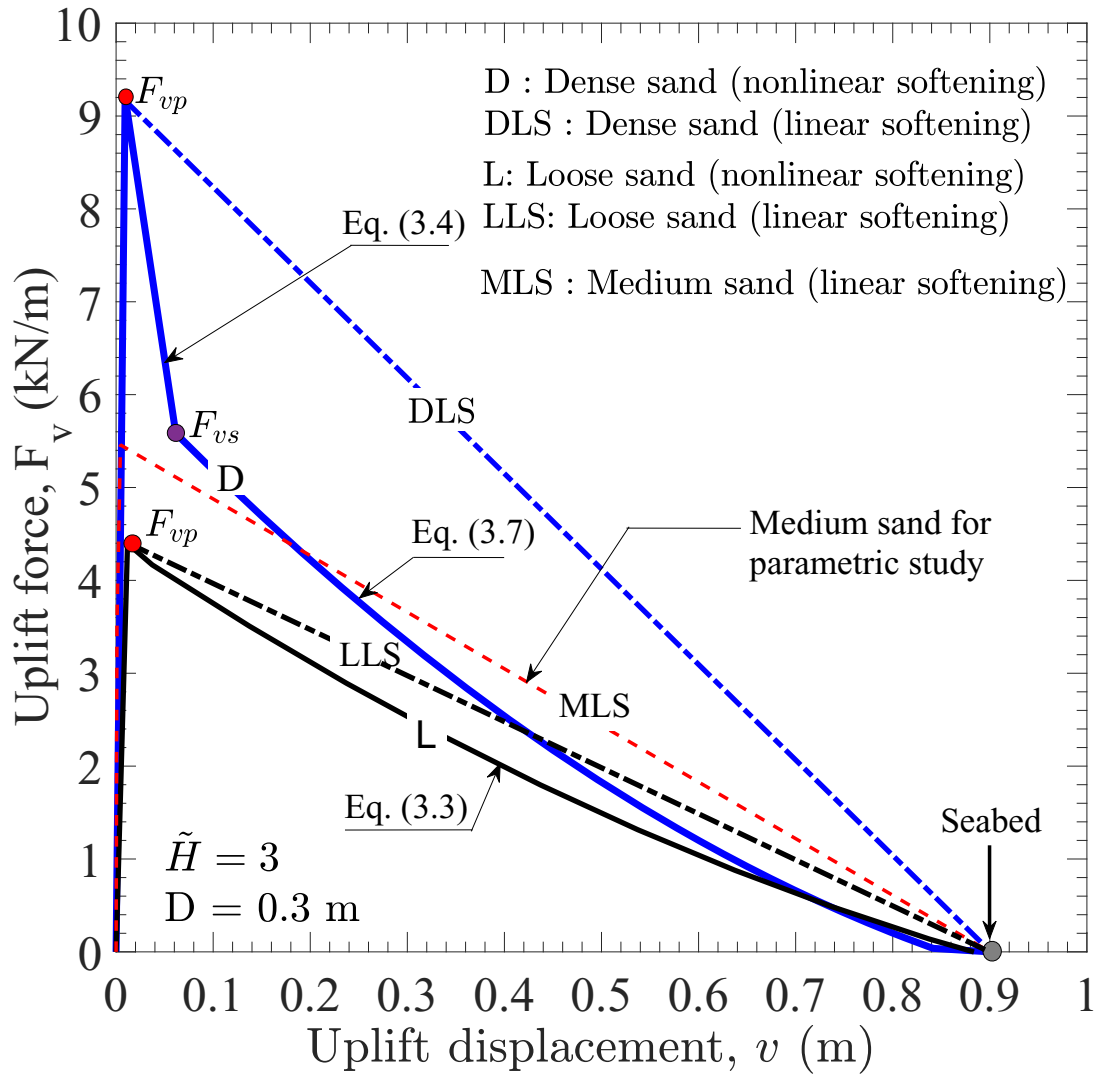


Figure 3.3: Uplift force–displacement response

mechanisms between tests on loose and dense sands are: (i) the peak resistance in dense sand is mobilized at $v = v_p$ by formation of two failure planes inclined to the vertical (θ) approximately equal to the peak dilation angle (ψ_p); (ii) F_{vp} is higher in dense sand; however, F_v decreases quickly with v after the peak, which is primarily due to reduction of θ and strain-softening behaviour of dense sand, and after a sufficient displacement ($v = v_s$) the rate of decrease in F_v is small, and the resistance at $v = v_s$ is called as "after-softening resistance (F_{vs})" in this paper; (iii) at large displacements ($v > v_s$), the force–displacement curve for dense sand is similar to, but can

be slightly above, the loose sand case, because the slip surfaces do not become completely vertical in dense sand even at large displacements ($\theta = 5-8^\circ$, Roy et al. 2018b).

Conducting a comprehensive finite element modelling with a soil model that considers the strain-softening behaviour, and calibrating it against physical model test results, Roy et al. (2018b) proposed the following equations to calculate the peak resistance and pipe displacement required to mobilize it. Similar to Eq. (3.3) for loose sand, Eq. (3.4) is also composed of weight (first part) and shear (last part) components; however, the failure wedge is formed by inclined slip surfaces.

$$F_{vp} = R \gamma D^2 \left[\left\{ (\tilde{H} - \tilde{v}_p) - \frac{\pi}{8} + (\tilde{H} - \tilde{v}_p)^2 \tan \theta \right\} + F_A (\tilde{H} - \tilde{v}_p)^2 \right] \quad (3.4)$$

where

$$F_A = 0.5 \left(\tan \phi'_p - \tan \theta \right) \left[(1 + K_0) - (1 - K_0) \cos 2\theta \right] \quad (3.5)$$

$$\tilde{v}_p = 0.002 \tilde{H} + 0.025 \quad (3.6)$$

where ϕ'_p is the peak friction angle and $\tilde{v}_p = v_p/D$; Roy et al. (2018b) also showed that $R \approx 0.9$ and $\theta \approx \psi_p$ can be used in Eq. (3.4) – Eq. (3.5). For the residual resistance ($v > v_s$), the following equation has been proposed, in which, in addition to weight and shear components (first and second parts), the surface heave at large displacement is also considered (third part in Eq. 3.7).

$$F_{vs} = R \gamma D^2 \left[\left\{ (\tilde{H} - \tilde{v}) - \frac{\pi}{8} + (\tilde{H} - \tilde{v})^2 \tan \theta \right\} + F_A (\tilde{H} - \tilde{v})^2 + 0.9 \tilde{v} \left\{ 1 + (\tilde{H} - \tilde{v}) \tan \psi_p \right\} \right] \quad (3.7)$$

As the slip plane does not become completely vertical, even at a large displacement, $\theta \approx 8^\circ$ is recommended for Eq. (3.7). Moreover, $v_s (= v_s/D)$ can be estimated as (Roy et al. 2018b).

$$\tilde{v}_s = 0.0035 \tilde{H} + 0.1 \quad (3.8)$$

Now replacing \tilde{v} by \tilde{v}_s in Eq. (3.7), the after-softening resistance (F_{vs}) can be calculated. Between the peak and after-softening state, the force–displacement curve is assumed to be linear (Fig. 3.3).

Finally, using Eqs. (3.4–3.8) , the nonlinear post-peak degradation of uplift resistance (line D in Fig. 3.3) can be obtained. Similar to loose sand, a linear line is used for the pre-peak behaviour. Table 3.2 shows the soil parameters used to define the nonlinear force–displacement curves using Eqs. (3.3–3.8) for loose and dense sands. The solid lines in Fig. 3.3 show the calculated results for 0.3 m diameter pipe having an initial embedment ratio (\tilde{H}) of 3. A similar pattern of F_v-v curves have been reported from physical model tests on dense and loose sands (Bransby et al. 2001).

Table 3.2: Soil parameters used to develop nonlinear uplift force–displacement curves

Parameters	Loose sand	Dense sand
Submerged unit weight of soil, γ (kN/m ³)	9.19	10
Critical state friction angle, ϕ'_c (°)	32	-
Peak friction angle, ϕ'_p (°)	-	55
Peak dilation angle, ψ'_p (°)	-	25
Slip plane angle at large displacement, θ (°)	-	8
Model parameter, R	-	0.87
Lateral earth pressure coefficient	0.47	0.5
Nomralized displacement required to mobilize peak uplift resistance, v_p (m)	0.0118	$(0.002\tilde{H} + 0.025)D$
Normalized displacement required to mobilize after softening resistance, v_s (m)	-	$(0.0035\tilde{H} + 0.1)D$

3.4.1.3 Simplified model for uplift resistance

In addition to the above, analyses are also performed with the following simplified force–displacement curves for uplift resistance. Two commonly used guidelines are used for this purpose.

1. Bilinear force–displacement curve recommended by ALA (2005) is used. The peak uplift resistance F_{vp} is calculated as:

$$F_{vp} = N_{qv}\gamma HD \quad (3.9)$$

where $N_{qv} = \frac{\phi'H}{44D}$ in which ϕ' is in degree. The uplift resistance increases linearly with upward displacement and, at $v = v_p$, the peak resistance is mobilized and then remains constant. ALA (2005) suggested $v_p = 0.01H - 0.02H$ for sand. No post-peak soil strength degradation is considered in the analysis with ALA recommendations.

2. A trilinear force–displacement curve is considered for parametric study (Section 3.6). In this case, the pre-peak uplift resistance is defined by following DNV (2007), where the peak uplift resistance is calculated as:

$$F_{vp} = (1 + f\tilde{H})\gamma\tilde{H}D^2 \quad (3.10)$$

where f is the uplift resistance factor. DNV (2007) suggested $f = 0.10 - 0.3$ and $f = 0.4 - 0.6$ for loose and medium/dense sands, respectively. The maximum uplift resistance mobilizes at $v_p = 0.005H - 0.008H$. The force–displacement curve prior to the peak is defined by two linear segments that intersect at a point below the peak ($\beta v_p, \alpha F_{vp}$, where α and β are two constants). DNV (2007) recommended $\beta = 0.2$, and $\alpha = 0.75 - 0.85$ and $\alpha = 0.65 - 0.75$ for loose and medium/dense sands, respectively. The lower and upper values of f and α represent the lower bound (LB) and upper bound (UB), respectively.

The backfill soil in many offshore pipelines is in loose to medium dense state because the compaction is a challenging task. Therefore, the uplift resistance curve for a medium dense soil is developed using $f = 0.4$ in Eq. (3.10), $\alpha = 0.65$ and $\beta = 0.2$. These analyses are performed using a linear post-peak degradation curve as shown line MLS in Fig. 3.3 for $\tilde{H} = 3$ and $D = 0.3$ m.

3.4.2 Axial and bearing resistances

Based on ALA (2005), the resistances in the axial (F_a) and vertical downward (F_b) directions are defined using bi-linear curves. F_a and F_b increases linearly with axial displacement (u_a) and vertical downward displacement (v_b) to the peak values of F_{ap} and F_{bp} at the peak mobilized displacements of u_{ap} and v_{bp} , respectively. After that, F_a and F_b remain constant. The peak axial resistance is calculated as (ALA 2005):

$$F_{ap} = 0.5 \pi DH \gamma (1 + K_0) \tan(\phi_\mu) \quad (3.11)$$

where γ is the effective unit weight of soil; K_0 is the coefficient of earth pressure at rest; ϕ_μ is the axial interface friction angle between pipe and soil. In this study, $\phi_\mu = 24^\circ$ and 28° are used for loose and dense sands, respectively. Based on ALA (2005) recommendations, $u_{ap} = 3$ mm and $u_{ap} = 5$ mm are used for dense and loose sands, respectively.

The maximum bearing resistance is calculated as (ALA 2005):

$$F_{bp} = N_q \gamma HD + 0.5 \gamma N_\gamma D^2 \quad (3.12)$$

where $N_q = e^{\pi \tan \phi'} \tan^2 \left(45 + \frac{\phi'}{2} \right)$, $N_\gamma = e^{(0.18 \phi' - 2.5)}$ are the bearing capacity factors. $v_{bp} = 0.1D$ is used (ALA 2005).

ALA (2005) does not consider the post-peak reduction of uplift resistance, rather a constant value of ϕ' is required. In this study, $\phi' = 30^\circ$, 35° and 45° are used for loose, medium, and dense sands, respectively, for Eqs. (3.9, 3.11 and 3.12).

3.5 Results

3.5.1 Validation of FE modelling technique

Figure 3.4 shows the buckling behaviour of the idealized unburied pipeline (Set I). The FE simulations are performed for three initial imperfection ratios \tilde{v}_{om} ($= \frac{v_{om}}{L_o}$) of 0.003, 0.007 and 0.010 (Inset-I Fig. 3.4), and the results are shown by solid lines. In Inset-I, the empathetic shape of initial imperfection based on Eq. (3.1) is shown, where v_o is the initial vertical position of the imperfection in a pipeline from the horizontal datum, and x is the horizontal distance along the pipeline from the center.

For the low initial imperfection ($\tilde{v}_{om} = 0.003$), snap buckling occurs where the temperature increases rapidly with buckle amplitude (v_m) and reaches the critical temperature (T_{cr}), then drops to the safe (lowest) temperature (T_{safe}) and finally increases with the further displacement of the pipe. The lowest temperature in snap-through cases is considered safe (T_{safe}), considering both stability and safety perspectives in offshore pipeline. Additionally, ensuring a safety margin from a design standpoint, the lowest temperature serves as a precaution against potential buckling.

The modified Riks algorithm used in this study allows the simulation of snap buckling. For larger initial imperfections ($\tilde{v}_{om} = 0.007$ and 0.01), a stable buckling occurs without reduction of temperature with v_m . The critical buckling temperature for the stable buckling cases is defined by the intersection of the two tangent lines drawn from the initial and final part of the $T-v_m$ (Fig. 3.4).

The buckling behaviour of the same pipeline with the same submerged weight is calculated using the analytical solution developed by Taylor and Gan (1986). As shown, the FE-calculated curves match well with the analytical solution. This implies that the developed FE model can adequately capture both snap-through and stable buckling processes. The slight difference in FE and analytical results is potentially due to the consideration of geometric and material nonlinearity in FE analysis with Riks algorithm which are not used in the analytical solution. It is essential to highlight that the snap-through buckling problem in finite element analysis is inherently nonlinear.

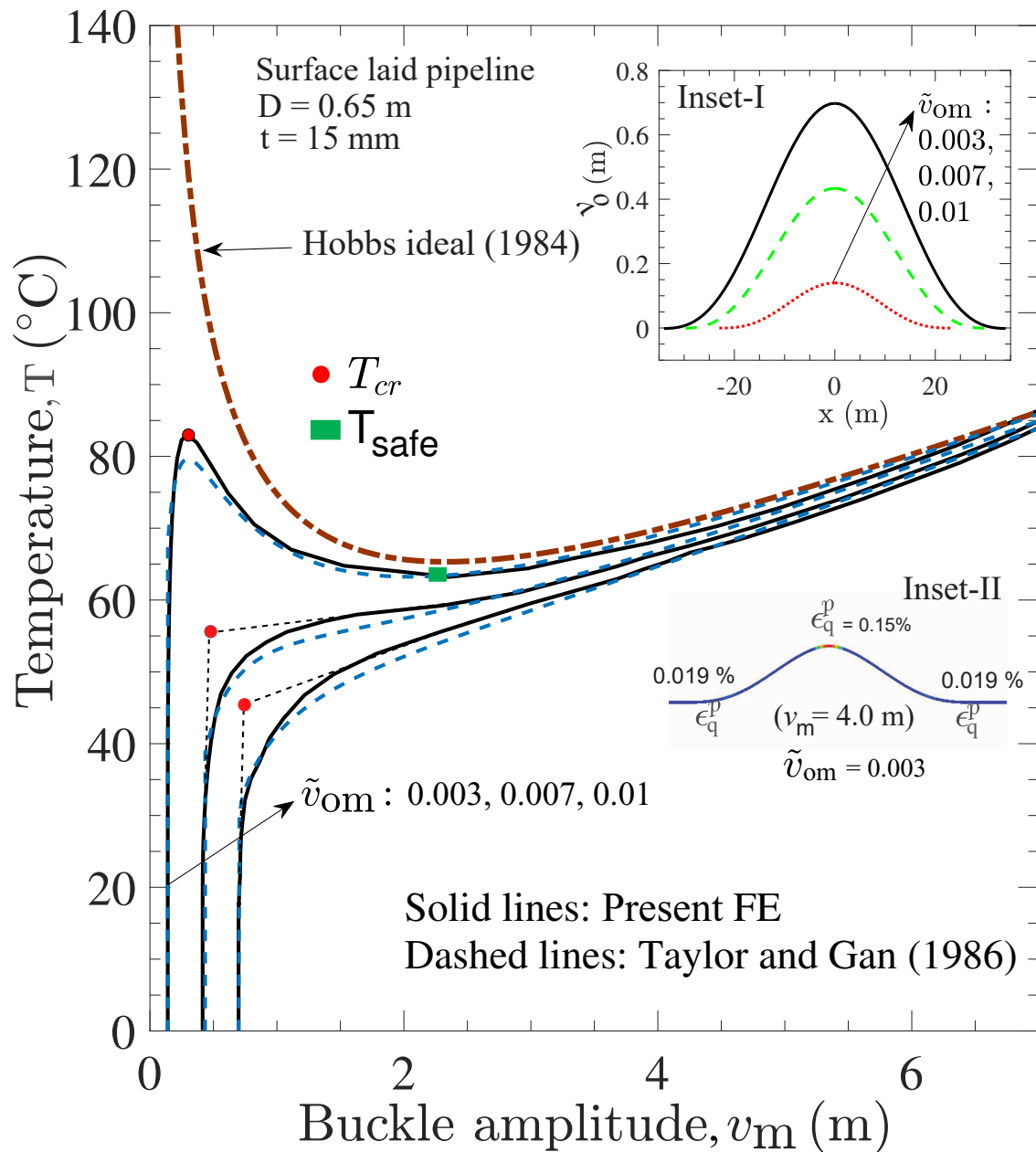


Figure 3.4: Calibration of finite element model by comparing with analytical solutions

To address this nonlinear snap-through problem, the Riks algorithm is employed in the FE model. Without accounting for geometric and material nonlinearity in finite element model, the Riks algorithm fails to capture snap-through buckling behaviour. Consequently, this study excludes a

comparison of results without considering geometric and material nonlinearity against the analytical solution.

Figure 3.4 also shows the results obtained from the analytical developed by Hobbs (1984) for a perfect pipeline (i.e., no initial imperfection) for comparison. The Inset-II in Fig. 3.4 shows FE calculated plastic shear strain (ϵ_q^p) in the pipe for buckle amplitude of 4 m. The plastic shear strain is a scalar measure encompassing all components of the equivalent plastic shear strain at each position within the model. In FE software Abaqus, it is obtained through PEEQ keyword and symbolized as $\epsilon_q^p = \int \sqrt{\frac{2}{3} \dot{\epsilon}^{pl} : \dot{\epsilon}^{pl}} dt$. where, $\dot{\epsilon}^{pl}$ is the second order plastic strain rate tensor. As shown in Inset-II of Fig. 3.4, the plastic shear strains generate near the point of buckle amplitude ($x = 0$) and two locations of 37 m from the center. The maximum equivalent plastic shear strain ϵ_q^p at $x = 0$ is 0.15%, which is considerably higher than that in other two locations.

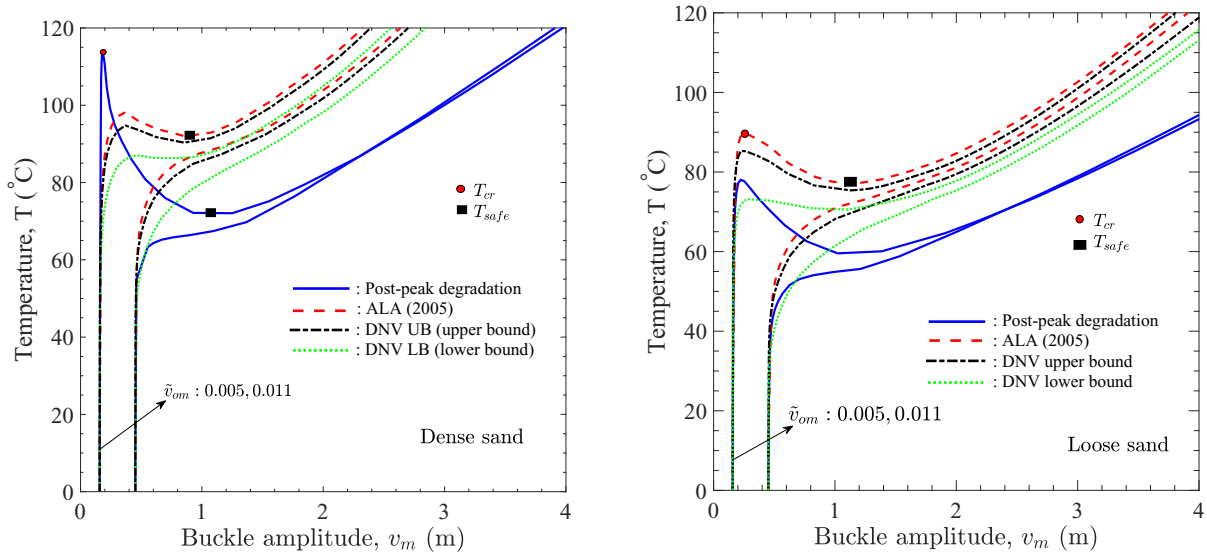
3.5.2 Base case FE simulation results

For the base cases, FE simulations are performed for two initial imperfections ($\tilde{v}_{om} = 0.005$ and 0.011), and the analyses are performed for the pipes buried in loose and dense sands. Recall that the burial depth and relative density are not given as the input parameters in FE analysis rather, they are used to develop the force–displacement curves (Eqs. (3.3)–(3.11)) for FE inputs.

3.5.2.1 Pipeline buried in dense sand

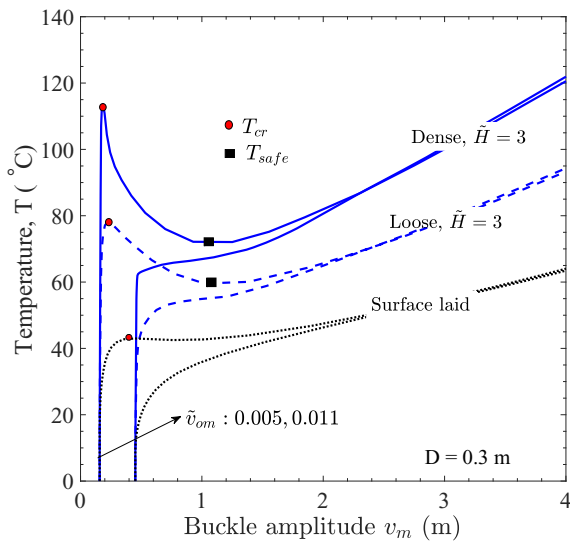
Figure 3.5(a) shows that snap-through and stable buckling occur for $\tilde{v}_{om} = 0.005$ and $\tilde{v}_{om} = 0.011$, respectively, for the pipe in dense sand. In this set of analysis, there is no post-peak reduction of uplift resistance in ALA, DNV UB and DNV LB. For $\tilde{v}_{om} = 0.005$, an apex appears at the critical temperature in all temperature–displacement relationships. The critical temperature is higher for the nonlinear dense sand model (line D in Fig. 3.3) than that of other uplift resistance models (ALA and DNV), which is primarily due to the difference in calculated peak uplift resistances (see

Eqs. (3.4), (3.9), and (3.10)). When post-peak degradation of the uplift soil resistance is considered, the safe temperature (the lowest point of $T-v_m$ curve) is significantly smaller than that obtained with other uplift resistance model.



(a) Pipeline buried in dense sand

(b) Pipeline buried in loose sand



(c) Comparison with simulation of unburied conditions

Figure 3.5: Response of pipeline for the base case simulations: (a) Pipeline buried in dense sand; (b) Pipeline buried in loose sand; (c) Comparison with simulation of unburied conditions

For the larger initial imperfection ($\tilde{v}_{om} = 0.011$), a stable buckling occurs—that means, temperature increases with an increase in buckle amplitude. However, when the post-peak reduction of uplift resistance is considered, very small displacements of the pipe occur until the temperature increases to $\approx 60^\circ\text{C}$. After that, a rapid increase of pipe displacement occurs for a small increase in temperature. The $T-v_m$ curves for $\tilde{v}_{om} = 0.005$ and 0.011 are almost the same at large buckle amplitudes when post-peak degradation is considered.

This set of analyses clearly shows that $T-v_m$ changes significantly if the post-peak reduction of uplift resistance is considered. Therefore, the post-peak reduction of uplift resistance should be considered, particularly when the pipe displacement is large due to upheaval buckling.

3.5.2.2 Pipeline buried in loose sand

The UHB response of a pipeline buried in loose sand (Fig. 3.5(b)) is significantly different from that in dense sand (Fig. 3.5(a)). Overall, $T-v_m$ curves for loose sand (Fig. 3.5(b)) are significantly at a lower level than that of dense sand (Fig. 3.5(a)). For example, T_{cr} is $72\text{--}92^\circ\text{C}$ for $\tilde{v}_{om} = 0.005$ in case of loose sand while it was $85\text{--}115^\circ\text{C}$ for the dense sand. Similarly, T_{safe} is 60°C and 72°C for loose and dense sand cases, respectively, for $\tilde{v}_{om} = 0.005$, when post-peak degradation of uplift resistance is considered. For the larger initial imperfection ($\tilde{v}_{om} = 0.011$), the shape of the $T-v_m$ curves for loose sand (Fig. 3.5(b)) are similar to but at the lower level than that in dense sand (Fig. 3.5(a)).

For a better comparison, the UHB response of the pipelines buried in loose and dense sands is compared with the results of simplified modelling where the pipeline is assumed to be laid on an imperfect rigid seabed (unburied assumption, see Section 3.5.1). For the buried cases, post-peak degradation of uplift resistance is considered for both dense and loose sands. For the unburied conditions, only submerged self-weight is considered. The following are the key findings from the simulation results presented in Figs. 3.5 (a–c). Firstly, the post-peak degradation of uplift resistance increases the tendency of snap buckling, and such as in Fig. 3.5(a) is higher for denser sands

because the strength reduction occurs rapidly. Secondly, loose sand can allow significantly lower operating temperatures than that of dense sand. These simulation results have some major practical implications. In offshore environment, it is difficult to control the density of backfill materials. In many cases, the soil might be loose to medium dense, although the density might increase due to the effects of natural events (e.g., wave loading at shallow water depths) (Clukey et al. 1989). Therefore, the post-peak degradation of uplift resistance should be considered if the pipeline is expected to experience a temperature above the critical temperature, which should be calculated considering other factors, including soil density, pipeline geometry and burial depth. Otherwise, pipeline can suffer from a large displacement that might bring a buckled section above the seabed and become vulnerable to third party activities (e.g., trawling gear) and even local buckling as examined in the following chapters.

3.5.3 Modelling of differential pressure (p)

The increase in temperature (ΔT) and differential pressure (p), which represents the difference between internal fluid and external hydrostatic pressures, acts together to develop the effective axial compressive force in a pipeline, which can cause upheaval buckling. In typical approaches of upheaval buckling analysis using analytical methods or beam elements in FE analyses, the differential pressure cannot be directly applied. Therefore, the combined effects of these two factors (ΔT and p) are calculated in terms of temperature as the following equation, which is known as "effective temperature (T)" (Hobbs 1981).

$$\Delta T_{\text{eff}} = \Delta T + \frac{pD(1-2\nu)}{4Et\alpha} \quad (3.13)$$

where E is the Young's modulus of the pipeline, α is the coefficient of thermal expansion, ν is the Poisson's ratio of the pipeline.

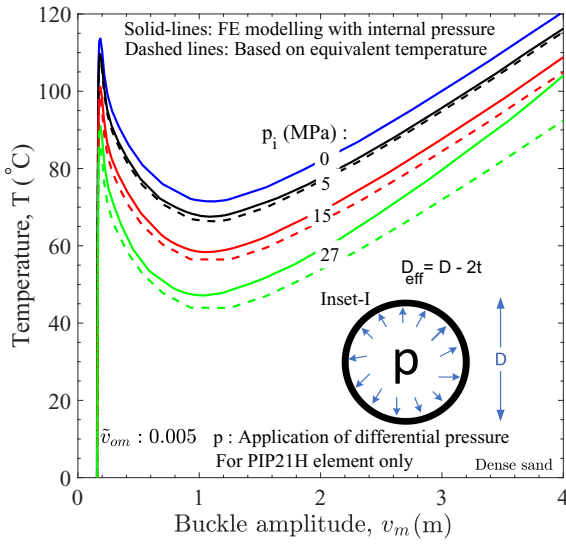
In the present study, the differential pressure (p) can be directly applied when pipe elements are used

in FE simulation. The differential pressure can be applied through the effective internal diameter of pipe with the uniform pressure in FE model as show in Inset of Fig. 3.6(a). The solid lines in Figs. 3.6(a–d) show the response of pipeline for varying applied pressure ($p = 0\text{--}27$ MPa) for two initial imperfections ($\tilde{v}_{om} = 0.005$ and 0.011). The shape of the $T\text{--}v_m$ curves is similar to that discussed before (snap through or stable buckling) for all the simulations. The topmost line in these figures is for $p = 0$ (i.e., $T = \Delta T$), which represents the response only due to temperature increase without any differential pressure. Note that, for a given pressure, the second part of Eq. (3.13) is constant. Now, subtracting the second part of Eq. (3.13) (i.e., pressure effect), $T\text{--}v_m$ curves for only due to temperature increase based on equivalent temperature (Eq. (3.13)) can be calculated, which are shown by dashed lines in Fig. 3.6. All the simulation results show that the simplified effective temperature approach gives conservative operating temperatures (lower than that calculated with direct application of differential pressure). The difference in temperature using these two modelling approaches is higher for larger differential pressures, especially at large buckle amplitude.

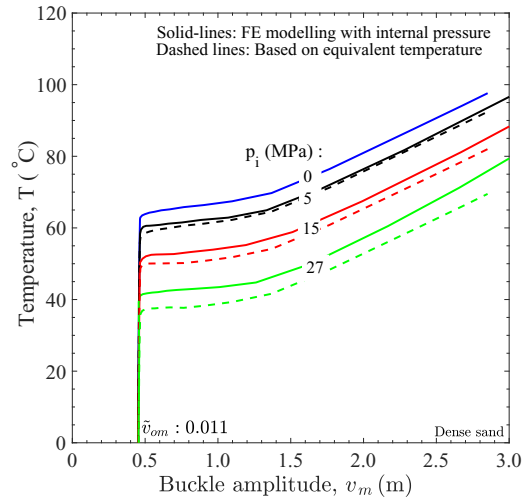
3.5.4 Effects of axial soil resistance on vertical buckling of pipeline

The axial soil resistance has a significant impact on the UHB behavior of pipelines. Theoretically, the axial resistance should be reduced once the pipe moves upward from the initial position because of the reduction of cover depth. The axial resistance will be zero when it moves above the seabed. However, the variation in axial spring resistance with upward displacement is not usually considered due to the additional complexities in numerical simulation using the built-in modelling approaches available in the software. To examine the effect of this, analyses are performed with varying axial resistances in the central portion ($2L_0$) of the pipeline (Fig. 3.1) where upward displacements take place.

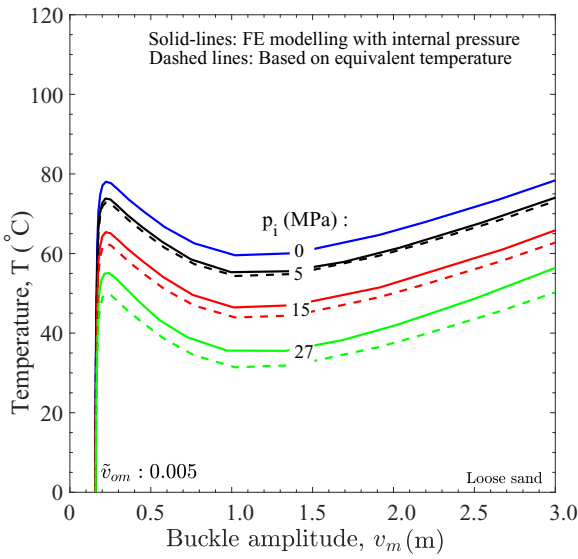
The following cases of the axial resistance over the distance of $2L_0$ were considered: (i) full axial resistance using Eq. (3.11), (ii) no axial resistance, which is a conservative assumption, and (iii) average of the above two. Outside the buckled zone (i.e., outside $2L_0$ in Eq. (3.11)) full axial



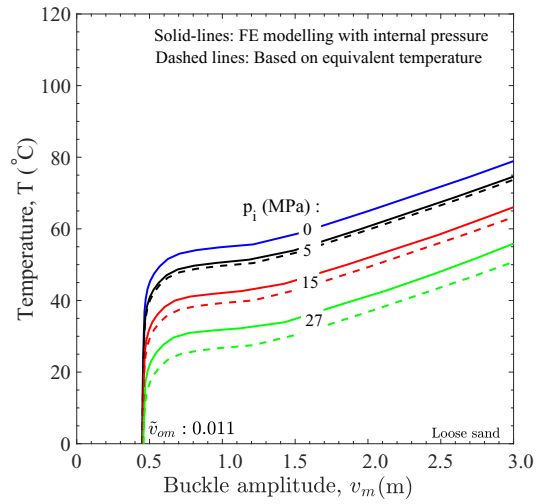
(a) Dense sand for $\tilde{v}_{om} = 0.005$



(b) Dense sand for $\tilde{v}_{om} = 0.011$



(c) Loose sand for $\tilde{v}_{om} = 0.005$



(d) Loose sand for $\tilde{v}_{om} = 0.011$

Figure 3.6: Comparison of response with direct modelling of differential pressure and equivalent temperature: (a) Dense sand for $\tilde{v}_{om} = 0.005$; (b) Dense sand for $\tilde{v}_{om} = 0.011$; (c) Loose sand for $\tilde{v}_{om} = 0.005$; and (d) Loose sand for $\tilde{v}_{om} = 0.011$

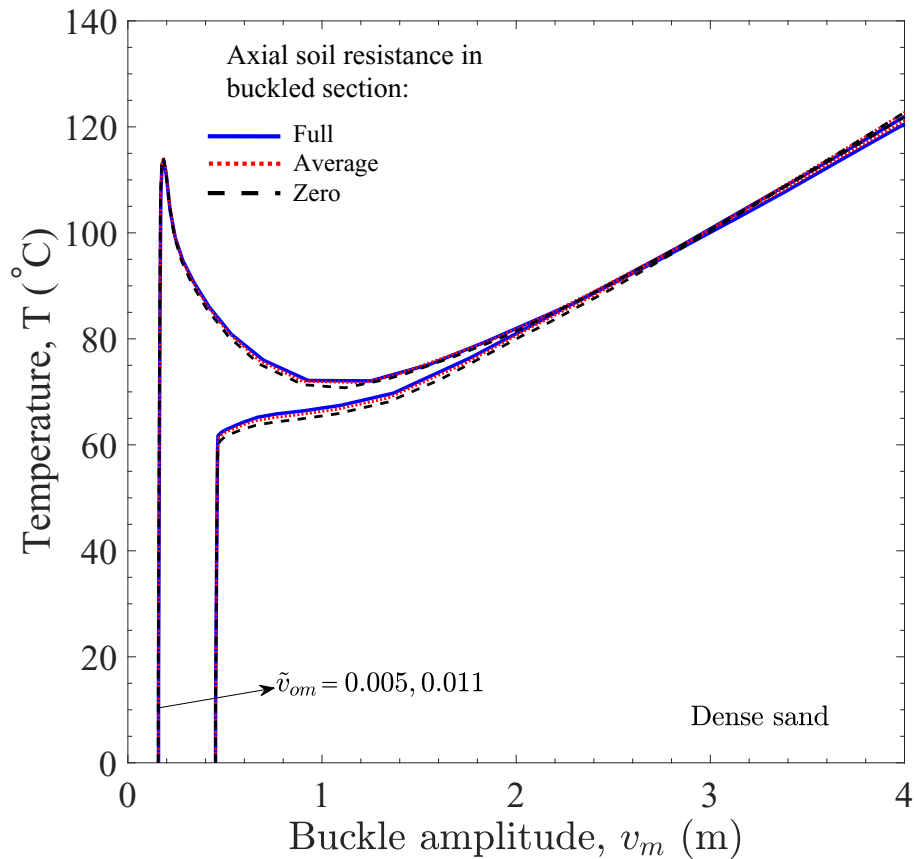


Figure 3.7: Effects of axial resistance in the buckled section

resistance is used for all three cases. Fig. 3.7 shows that the variation in axial resistance in the buckled segment (full to zero) does not have a significant effect on the $T-v_m$ curves for both $\tilde{v}_{om}(= 0.005 \text{ and } 0.011)$. Note that, in the analytical solutions (e.g., Taylor and Gan 1986), the change in axial resistance with an upward displacement of the pipe was not considered. Therefore, except for this set of analyses, all the analyses are performed with the full axial resistance (i.e., without decreasing axial resistance with upward displacement of the pipe in the buckled section).

3.5.5 Effects of the shape of post-peak uplift resistance reduction

As described before in Sections 3.4.1 and 3.4.2, both non-linear and linear model can be used to define the reduction of post-peak uplift resistance. This section examines how accurately a linear

uplift resistance reduction model can simulate the UHB of the pipeline. To examine that, linear (lines LLS and DLS in Fig. 3.3) and nonlinear (lines L and D in Fig. 3.3) post-peak uplift resistance reduction models are used.

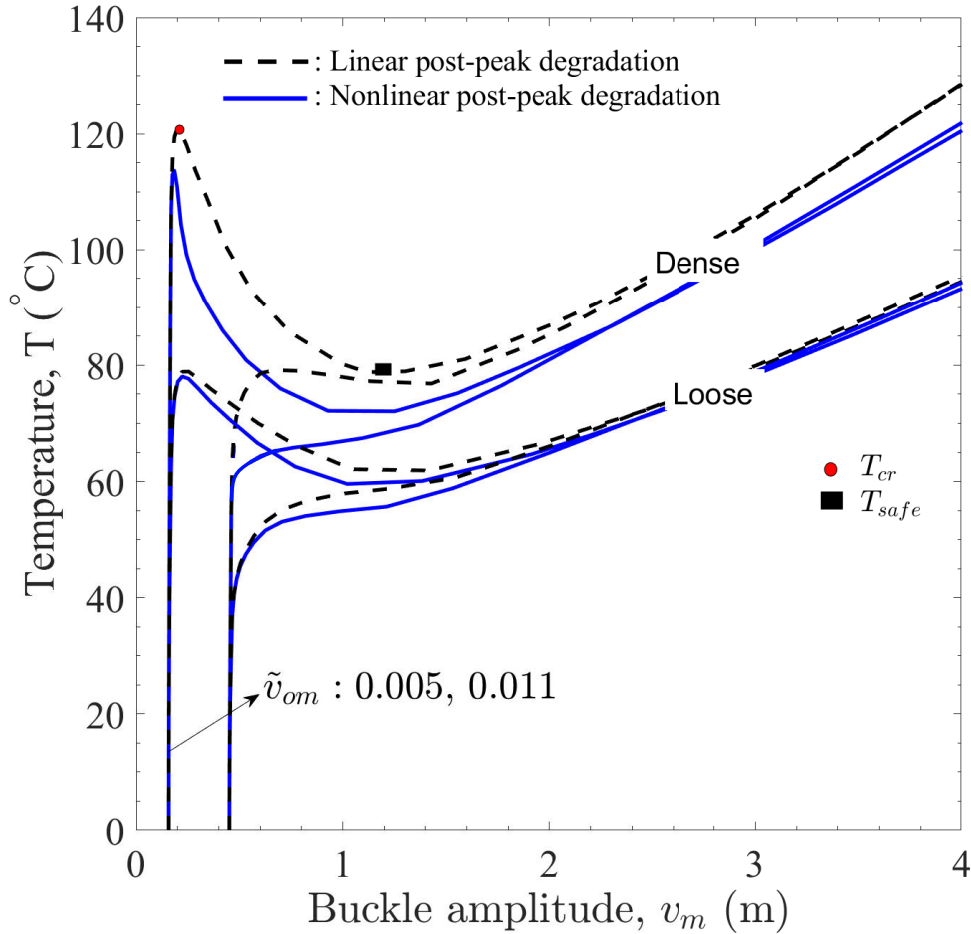


Figure 3.8: Effects of nonlinear and linear post-peak degradation of uplift resistance

Fig. 3.8 shows the simulated results for two initial imperfections ($\tilde{v}_{om} = 0.005$ and 0.011). For a given buckle amplitude, the calculated T is higher for the linear degradation model than that for the nonlinear model. The difference between the temperatures is higher for the pipe buried in dense sand and with higher initial imperfection. This behaviour is expected as for the dense sand, the simplified linear post-peak softening line is considerably above the nonlinear uplift resistance degradation model (see lines DLS and D in Fig. 3.3). However, the difference between $T-v_m$ curves

for loose sand is relatively small with the linear and nonlinear uplift resistance models as they are not significantly different (see LLS and L in Fig. 3.3). A linear degradation is therefore used in the analyses presented in the following sections.

3.6 Parametric Study

As mentioned in Section 3.4.1.3, a bi-linear pre-peak (similar to DNV 2007) together with linear post-peak degradation of uplift resistance of medium dense sand is used for the parametric study (see line ML in Fig. 3.3 and inset in Fig. 3.9(a)). The calculated response is compared with the simulations using ALA (2005) where the uplift resistance increases linearly up to the peak value (Eq. (3.9)) and then remains constant (no degradation), to show the effects of uplift resistance degradation.

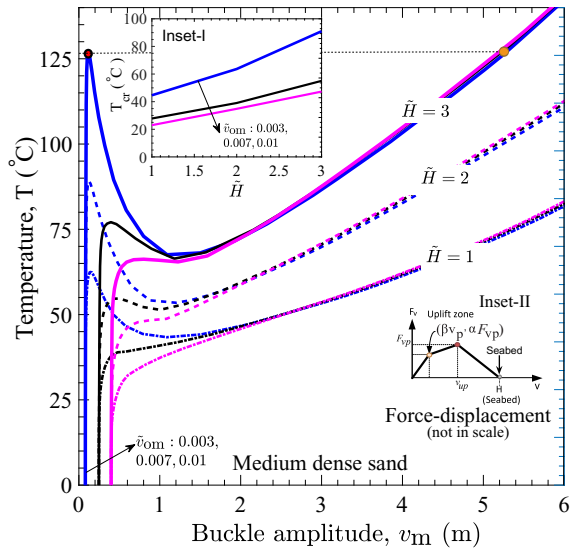
3.6.1 Effects of initial imperfection and embedment ratio

The temperature versus buckle amplitude for different initial imperfections ($\check{v}_{om} = 0.003, 0.007$ and 0.01) and embedment ratios ($\check{H} = 1-3$) are shown in Fig. 3.9(a). Both critical and safe temperatures increase with the embedment ratio, and these temperatures are higher if the post-peak degradation of uplift resistance is not considered (i.e., soil resistance remains constant after the peak). The post-peak degradation reduces the safe temperature more than the critical temperature, and the reduction is more significant for larger burial depths.

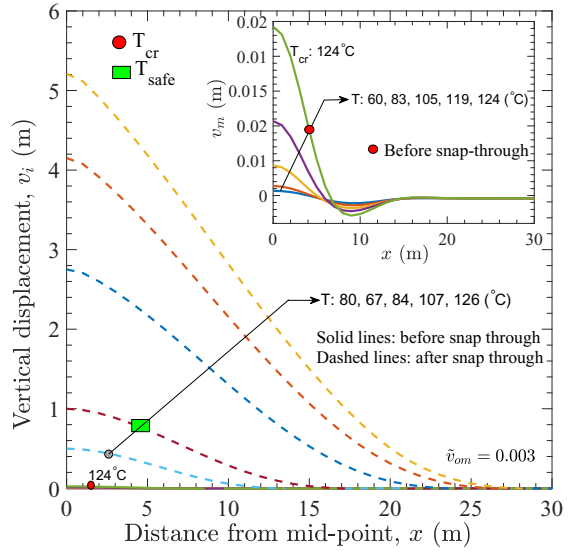
The variation of critical temperature obtained from these analysis are shown in the inset in Fig. 3.9(a). For all the conditions, T_{cr} increases almost linearly with the embedment ratio.

3.6.2 Vertical deformation and plastic shear strain

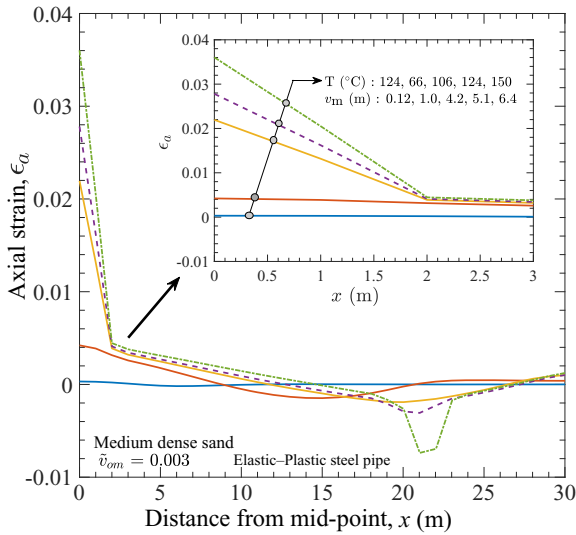
The selection of maximum operating temperature and pressure is the key design requirement. While the guidelines (e.g., DNV 2007) suggests to keep the pipeline in place (minimal



(a) Effects of burial depth



(b) Pipeline displacement



(c) Axial strain development

Figure 3.9: Response of pipeline in medium sand: (a) Effects of burial depth; (b) Pipeline displacement; and (c) Axial strain development

displacement), the upward displacement of the pipe occurs in the field as discussed in the introduction. Currently, the strain-based design criterion is used for pipeline design. Therefore, the strain development in the buckled section is evaluated in this section.

Figure 3.9(b) shows the vertical displacement of the pipe (including the initial imperfection v_0)

along the length for $\tilde{v}_{om} = 0.003$ and $\tilde{H} = 3$ in Fig. 3.9(a). Very small upward displacement ($v_m = 0.096$ m) occurs at T_{cr} ($= 124^\circ\text{C}$). After that, the pipe temperature decreases, but the vertical displacement continues because of snap buckling. The displacement primarily occurs within 25 m from the center.

Figure 3.9(a) also shows that if the operating temperature somehow exceeds the critical temperature, a sudden upward displacement of 5.25 m could occur in case of $\tilde{H} = 3$ and $v_{om} = 0.003$, as shown by drawing a horizontal line from T_{cr} to the $T-v_m$ curve. This could result in the movement of a segment of the pipe above the seabed. Now the question is whether such deformation could cause the failure of the pipe. Figure 3.9(c) shows the logarithmic axial strain (ϵ_a) at the crown of the pipe. Considerable tensile strain develops at $x = 0$ where the curvature is high and some compressive strains generate around 20 m distance from the center. The inset of Fig. 3.9(c) shows the closer view of axial strain near the mid-point. The corresponding buckle amplitude is also shown in this inset. The axial strain exceeds 2% (typically allowable strain is 1%—2%, Palmer et al. (1990) when the v_m is 4.2 m.

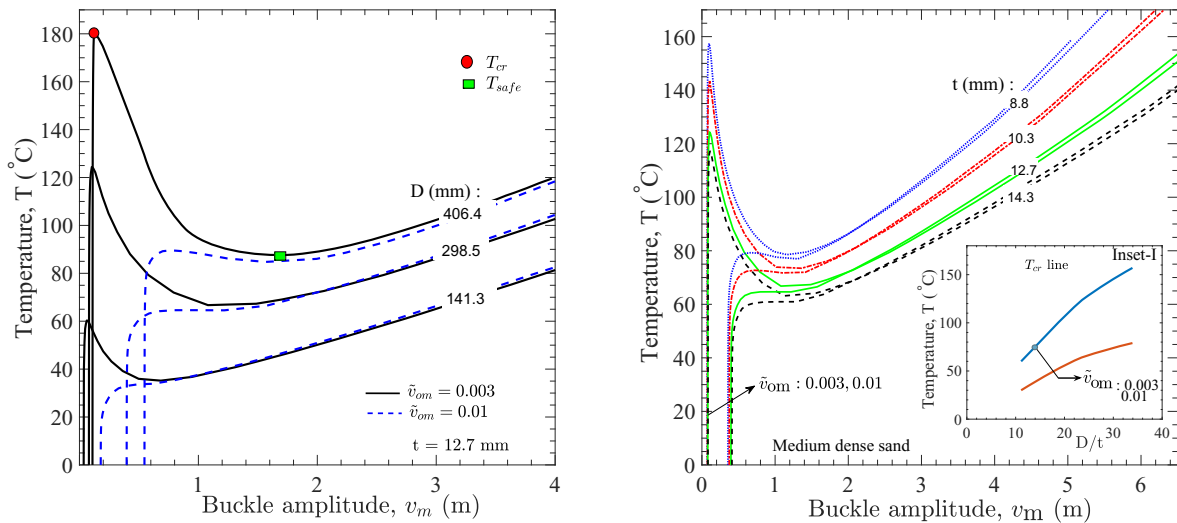
3.6.3 Effects of pipe diameter and wall thickness on upheaval buckling

The cross-sectional properties of pipe play an important role in buckling, which is investigated by varying pipe diameter and wall thickness. Only one parameter is varied in the analysis, while the other parameters are the same as Table 3.1. Again the analyses are performed for medium sand with linear post-peak degradation, similar to line MLS in Fig. 3.3, but the values are diameter dependent (3.10). Analyses are performed for $\tilde{H} = 3$, and two imperfection ratios, $v_{om} = 0.003$ and 0.01.

For diameter effects, three pipelines of 0.1413 m, 0.2985 m, and 0.4064 m diameter, with the same wall thickness of 0.0127 m, are considered. The submerged self-weight of the pipeline (q) for the oil-filled condition is calculated as 0.85 kN/m, 1.59 kN/m, 2.05 kN/m, respectively. Figure 3.10(a) shows the buckling response for six analyses. As the pipe diameter is different, the initial imperfection, including the initial buckle amplitude v_{om} is different for a given v_{om} . Figure 3.10(a)

shows that the critical and safe buckling temperature increase with pipe diameter. For example, $T_{cr} = 60^\circ\text{C}$ and 125°C for 141.3 mm and 298.5 mm diameter pipes, respectively, for the initial imperfection ratio of 0.003.

To investigate the effects of wall thickness, four analyses are performed for varying wall thickness, t ($= 8.8$ mm, 10.3 mm, 12.7 mm, and 14.3 mm) for the same pipe diameter of 0.3 m. The other parameters are kept the same as listed in Table 3.1. The numerical analyses show that the thinner pipe wall has higher upheaval buckling resistance for the same outer diameter (Fig. 3.10(b)). The critical and safe buckling temperatures decrease with an increase in pipe thickness. Palmer et al. (1990) suggested to reduce wall thickness to minimize potential upheaval buckling.



(a) Effects of diameter

(b) Effects of wall thickness

Figure 3.10: Effects of pipeline geometry: (a) Effects of diameter; (b) Effects of wall thickness

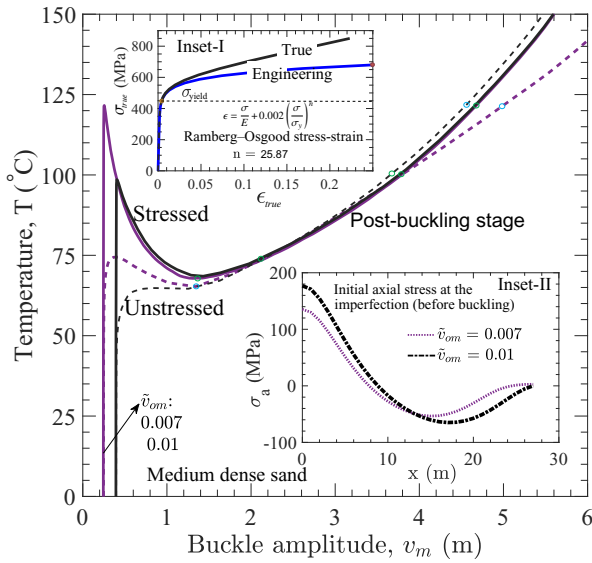
3.6.4 Initial stress

All the analyses in the previous sections have been performed for "wished in place" pipelines (i.e., the pipeline is initially stress free on the uneven seabed). However, the pipeline is expected to be

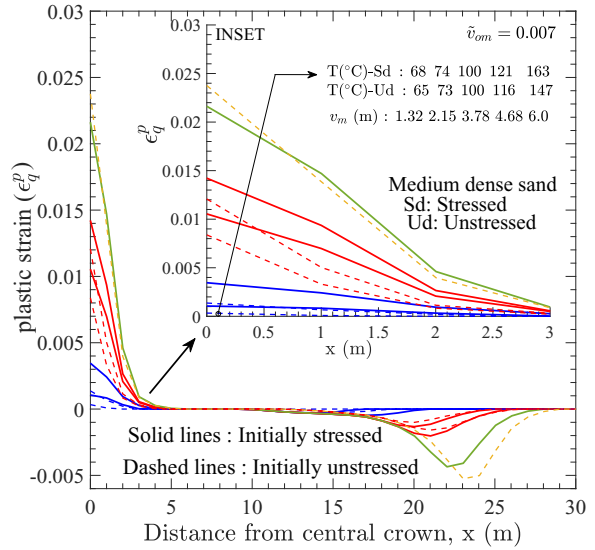
“initially stressed” prior to an increase in temperature and differential pressure at any stage of operation due to several reasons, including installation effects, uneven seabed, and displacement of pipeline in previous temperature and pressure loading cycles. Establishing the initial stresses considering all these factors is a complex process. Therefore, in this section, an initial stress condition is established simply due to placing of pipeline under gravity load on an uneven seabed with a focus to show the trend of initial stress effects on UHB.

Similar to the base case, a 1,200 m long pipe of 0.3 m diameter and thickness of 12.7 mm is considered. To capture the significant plastic deformation behavior of a steel pipe, this analysis also utilizes the Ramberg–Osgood formulation (Ramberg and Osgood 1943) to model its nonlinear elasto-plastic behavior (Inset-I of Fig. 3.11(a)). The following steps are followed to create the initial stress. First, the midpoint of the invert of the pipe is placed on the crest of an imperfect ‘virtual’ seabed defined by Eq. (3.1). Second, the submerged weight of the oil-filled pipe ($q = 1.59$ kN/m) is applied that brings the pipeline on the uneven seabed that creates initial imperfection and generates initial stress. In this step, the Coulomb friction model (friction coefficient of 0.4) is used for modelling interface behavior between the pipeline and rigid seabed. Finally, the virtual seabed is removed and soil springs are attached to the initially imperfect pipe, and then the analysis is continued following the steps used in previous analyses (Section 3.3).

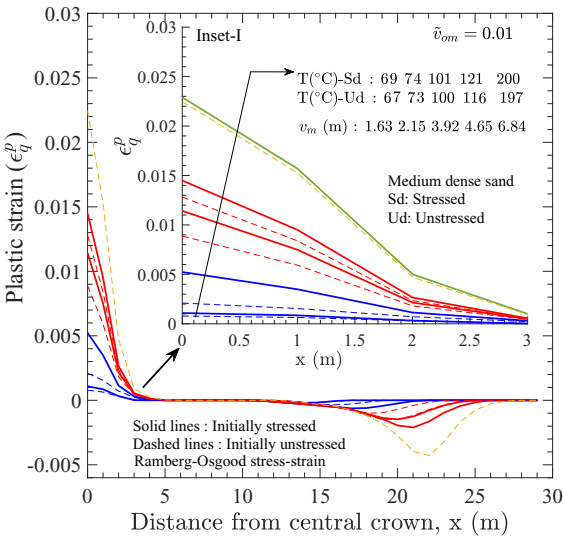
Figure 3.11(a) shows the comparison of the response of initially stressed and stress-free pipelines. The inset-II in Fig. 3.11(a) shows the initial axial stresses in the stressed pipeline for $\tilde{v}_{om} = 0.007$ and 0.01. The critical temperature is significantly higher for the initially stressed pipe—for example, $T_{cr} = 123^\circ\text{C}$ and 74°C for the stressed and stress-free pipelines, respectively, for $\tilde{v}_{om} = 0.007$. The presence of initial stress (similar to pre-stress) demands more axial compression (i.e., higher temperature) to start buckling than the stress-free pipe. The effects of initial stress reduce with post-buckling. Therefore, no significant difference in safe temperature is found. At large buckle amplitudes, $T-v_m$ curves are the same for both initially stressed and stress free pipes. In other words, while the initial stress can significantly influence the initiation of buckling, it does



(a) Initial stress effects on temperature



(b) Plastic strain development at $\tilde{v}_{om} = 0.007$



(c) Plastic strain development at $\tilde{v}_{om} = 0.01$

Figure 3.11: Response of initially stressed and stress-free pipelines: (a) Initial stress effects on temperature; (b) Plastic strain development at $\tilde{v}_{om} = 0.007$; (c) Plastic strain development at $\tilde{v}_{om} = 0.01$

not influence the post-buckling response.

Figure 3.11(b) and Fig. 3.11(c) shows the plastic strain development in the post-buckling stage for $\tilde{v}_{om} = 0.007$ and 0.01 for five different temperatures starting from a temperature close to the safe temperature (open circles on $T-v_m$ curves in Fig. 3.11(a)). The plastic shear strains mainly develop around the central crown and a smaller amount around ≈ 20 m distance. For clarity, ϵ_q^p around the central crown is shown in the inset of Fig. 3.11(b) and Fig. 3.11(c). The corresponding buckle amplitudes for these five temperatures are also listed in the inset. Note that such large displacements at higher temperature (e.g., $v_m = 4.65$ m at $T = 121^\circ\text{C}$) is not expected in the field because, in that case, the pipeline might fail due to other reasons (e.g., local buckling and fracture). However, the results are shown here for completeness.

Figure 3.11(b) and Fig. 3.11(c) shows that the plastic strain and corresponding buckled amplitude is higher for initially stressed pipeline (solid lines) at lower temperatures (e.g., $T = 74^\circ\text{C}$). However, there is no significant difference between calculated plastic strain for larger temperatures.

3.7 Conclusions

The current design guidelines for upheaval buckling aim to ensure that the pipeline remains in place during operation. However, many field observations show significant upward displacements due to upheaval buckling. The present study examines pre- and post-buckling response of buried offshore pipelines. The reduction of uplift resistance with an upward displacement of the pipe is incorporated in the analysis using nonlinear and linear post-peak uplift degradation models. It is shown that the uplift resistance degradation significantly reduces the capacity of the pipeline to carry the load generated by pressure and temperature. The following conclusions can be drawn from this study:

- a) Post-peak degradation of uplift resistance significantly reduces the safe operating temperature in snap buckling cases, and the effect of degradation on UHB is more evident

for the pipeline buried in dense sand. Such degradation also increases upheaval buckling potential and pipeline displacement in stable buckling cases.

- b) The upheaval buckling potential and post-buckling deformation are more for pipelines buried in loose sand than in dense sand. Also, the classical approach of analysis assuming the pipeline on a rigid imperfect seabed with an effective weight for the upward resistance is overly conservative.
- c) FE modelling with direct application of differential pressure using pipe elements gives higher capacity (i.e., higher temperature for a given buckle amplitude) than that of the conventional effective temperature approach using beam elements. The difference between the calculated temperatures using these two approaches is higher for a larger differential pressure.
- d) The reduction of axial resistance with an upward displacement of the pipe in the buckled section does not significantly affect upheaval buckling.
- e) The linear post-peak degradation model gives a similar upheaval buckling response as obtained with the nonlinear degradation model for loose sand.
- f) Initial stresses in an imperfect pipeline primarily affect the response at lower upheaval displacements of the pipeline approximately up to the displacement at the safe temperature. However, at larger displacements, the response of initially stressed and unstressed pipeline is almost the same.

Although the present simulations using one-dimensional beam elements give strains within acceptable limits, even at considerably large upward displacements, other factors, such as local failure and potential damage of the protruded section due to third-party activities should be considered in the design.

Chapter 4

Finite Element Modelling of Buried Offshore Pipeline for Global Upheaval Buckling Leading to Local Buckling

ABSTRACT

Subsea buried pipelines operating under high pressure and high temperature are susceptible to upheaval buckling (UHB). While the pipeline is designed to be at a certain burial depth during operation, some sections of the pipeline might move vertically upward to large distances due to global upheaval buckling. This global buckling can be followed by local buckling on the compression side of the pipe wall at larger displacements, causing pipeline failure. However, the traditional beam element based finite element modelling cannot capture the local buckling of the pipeline. Therefore, in the present study, finite element modelling of upheaval buckling is performed using shell elements to further investigate the local buckling. The post-peak degradation of uplift soil resistance with pipe upward displacement, which is zero at and above the seabed, is implemented in the FE analysis. The role of differential pressure on UHB is evaluated by direct application of pressure and then comparing the results with equivalent temperature approach based on the traditional beam element type modelling. Near the point of buckle amplitude, the plastic strains develop in the pipe section both in tension (top crown) and compression (bottom invert) sides; however, at larger displacements, the plastic shear strains in the compression side increase rapidly, which causes local buckling and wrinkling. The response of pipeline is investigated in terms of local strains and ovalization by comparing the FE results with acceptable strain-based design criteria. A parametric study is performed to show the effects of key factors that affect global and local buckling.

Keywords: Upheaval buckling; Local buckling; Post-peak uplift resistance; Local strains; Sectional ovalization

4.1 Introduction

Offshore pipelines buried in shallow seabed depths generally operate under high pressure and temperature (HPHT) conditions. To ensure the smooth flow of hydrocarbon without solidifying the wax formation, the high temperature and pressure within the pipeline can reach up to 150°C and 35 MPa, respectively (Hooper et al., 2004; Palmer and King, 2004). The pipe–soil surface friction acts against the expansion caused by high temperature and differential pressure increase during operation and generates compressive stresses in the pipeline wall. When the axial compressive forces exceed a critical limit of soil resistance, buckling can occur either vertically (upheaval) or horizontally (lateral), depending on the pipeline’s burial conditions. Upheaval buckling is a major design and integrity issue for a pipeline buried at shallow depths while its thermal expansion is restricted in other directions. The severity of buckling can be exacerbated by various factors, including material and sectional properties, bed soil conditions, structural defects, initial imperfections, seabed profile, and the method of handling and installation (DNV 2007). When the pipeline is subjected to a large vertical displacement (beyond the seabed), there comes a point where local buckling and wrinkling may begin to occur at the critical section. Typically, local buckling is the primary failure mode that governs the pipeline due to excessive material utilization. This phenomenon manifests as a wrinkle in the pipeline’s cross-section, causing sectional ovalization. As the pipeline becomes locally buckled, its ability to withstand additional bending moments decreases, which could ultimately lead to its collapse over time.

Large vertical deformations of buried pipelines have been observed in many field conditions in the pipeline industry. Field observations (Nielsen et al. 1990; Palmer et al. 1990; Palmer and Williams 2003) indicate that the buried offshore pipelines can move significantly beyond the seabed. In a field study of a pipeline operating in a permafrost zone, a buried pipe section with a diameter of 1.02 meter underwent significant upheaval buckling, causing a displacement of over 4 meter from the soil surface (Palmer and Williams 2003). This observation suggests that HPHT pipelines are

susceptible to significant upheaval buckling above the ground. According to the case study by Nielsen et al. (1990), the buried pipeline in the North Sea experienced a significant vertical movement of 2.6 meter from the original position, although no rupture was reported due to local buckling.

In offshore pipelines, a key design concern revolves around accurately predicting potential failure modes of the pipe, such as global buckling, local buckling, or fractures, if present. Despite this, most researchers have primarily focused on plane-strain analysis to assess the uplift resistance of the soil. Unfortunately, limited research has been conducted on the structural behaviour of HPHT pipelines, particularly when the pipeline undergoes large deformations leading to local buckling and wrinkling.

Gresnigt (1986) presented both experimental and analytical solutions for the plastic design criterion of buried steel pipelines. Klever et al. (1990) developed a finite element code called UPBUCK, which utilized beam elements to analyze upheaval buckling. Shaw and Bomba (1994) demonstrated the effectiveness of a 1-D finite element method in solving the upheaval buckling problem. Dorey et al. (2005) studied and developed critical buckling strain equations applicable to onshore energy pipelines. Mahdavi et al. (2013) conducted a numerical analysis to determine the critical strain capacity of a pipeline. Their analysis involved a segment of 3D pipe and soil continuum model to assess the local buckling response of a buried pipeline subjected to lateral buckling. However, the temperature-dependent loading conditions were not considered.

Several authors, including (Mohareb 1995; Murray 1997; Zimmerman et al. 2004; Ozkan and Mohareb 2009a,b) have conducted both experimental and numerical analyses on local buckling and wrinkling failures behaviour of in-air pipelines. These analyses considered applied moments and differential pressure as critical factors influencing the pipeline's behaviour. They reported that for a higher D/t ratio, the moment capacity and buckling strain decreases significantly. However, they did not consider the surrounding soil conditions for local buckling due to thermal and pressure loadings. Shi et al. (2013) presented a study demonstrating the axial strain distribution in

a pipe during the transition from upheaval buckling to local buckling and eventual failure. Their research provided valuable insights into pipeline deformation behaviour and failure mechanisms when subjected to upheaval buckling conditions. Mohajer et al. (2018) investigated the post-buckling failure modes of pressurized unburied steel pipelines under monotonic loading conditions. They explored how the pipeline responded and failed after experiencing buckling. Vazouras et al. (2021) carried out a study that involved experimental and numerical analyses to examine the behaviour of the pipeline subjected to UHB conditions for small vertical movement, leading to local buckling, but the post-peak degradation in soil resistance was not considered. Furthermore, it is essential to note that the existing literature for UHB largely relies on 1D beam models with finite elements that are limited in their ability to capture the local buckling and wrinkling behaviour accurately. These 1D models may not fully capture the three-dimensional complexities of such phenomena. More sophisticated modelling techniques, such as three-dimensional finite element analysis with shell or solid elements, are necessary for a more comprehensive understanding of local buckling and wrinkling behaviours.

The primary emphasis of this study is on 3D finite element (FE) modelling to investigate upheaval, post-upheaval, and local buckling behaviours of buried offshore pipelines, considering the combined effect of temperature and pressure. By adopting this approach, the study aimed to address some of the limitations of the 1D upheaval buckling finite element model and provide a more comprehensive analysis of the pipeline's local buckling response. Modelling the entire 3D shell or solid FE model for a long-buried pipe with the soil as a continuum is computationally expensive and numerically challenging. The present work adopts a more efficient approach using the FE software Abaqus to address this modelling issue. It involves a 3D coupled pipe and shell model for the buried pipeline, incorporating nonlinear soil springs to represent the behaviour of sand. This coupled model allows for the investigation of UHB and the post-buckling behaviour of the pipeline.

To validate the accuracy of the finite element model, comparisons are made with analytical

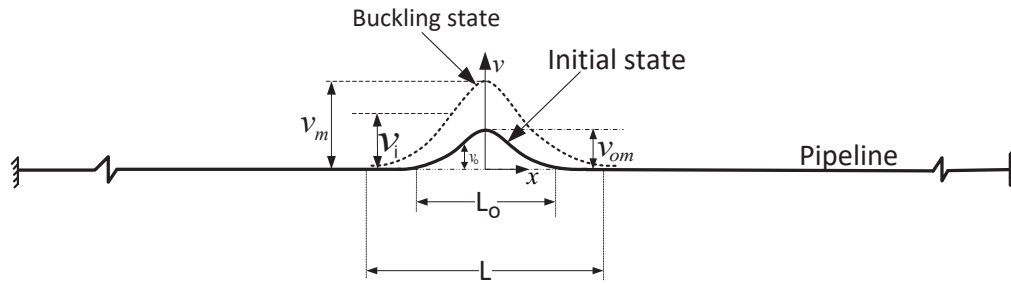
solutions available in the literature. The study further explores the influence of various factors, such as operating temperature, pressure, initial imperfection, material properties, and sectional properties, on the onset of buckling, local buckling, and wrinkling in the pipeline. The large plastic shear strain distribution on compression and the tension sides of the post-buckled pipeline are also investigated.

4.2 Problem statement

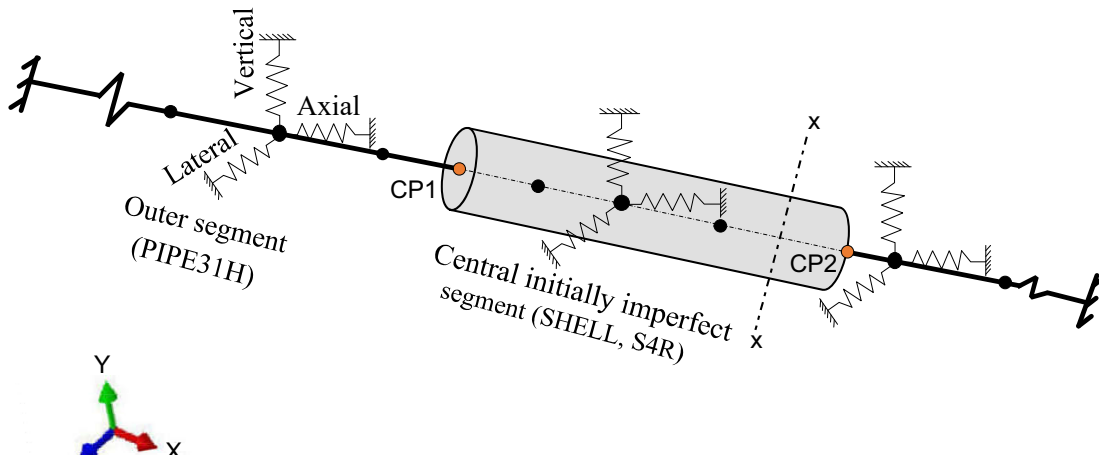
This research primarily focuses on phase II as detailed in the research motivation in Chapter 1 Fig. 1.2. The objective is to pinpoint potential upheaval buckling that progresses to local buckling, resulting in significant sectional deformation and ovalization characterized by the development of high plastic strain in the invert and gradual transfer of strain to the crown. The upheaval buckling of an offshore pipeline depends on its initial longitudinal profile resulting from seabed imperfections. Taylor and Tran (1996) proposed different idealized profiles of pipelines for various seabed imperfections. Figure 4.1(a) shows the problem model layout and key features of the pipeline used in this study, after Taylor and Tran (1996). The initial state of the imperfect pipeline is defined using the empathetic model of Taylor and Tran (1996) in Eq. (4.1).

$$v_o = v_{om} \left\{ 0.707 - 0.262 \frac{\pi^2 x^2}{L_o^2} + 0.293 \cos \left(2.86 \frac{\pi x}{L_o} \right) \right\} ; \frac{-L_o}{2} \leq x \leq \frac{L_o}{2} \quad (4.1)$$

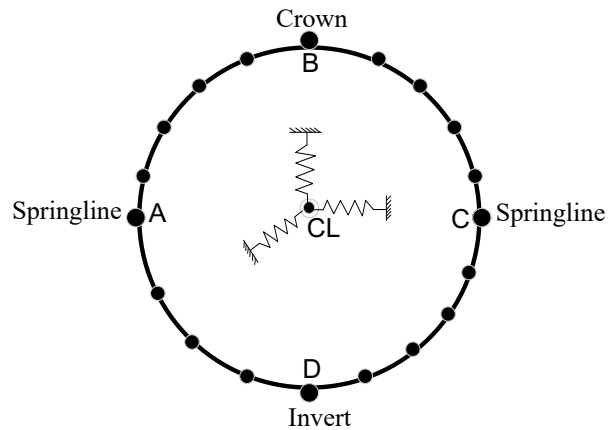
where \tilde{v}_o is the initial vertical distance of the center of the pipeline from the horizontal datum at the horizontal distance (x), v_{om} is the initial buckle amplitude (i.e., at v_o at $x = 0$), and L_o is the initial imperfection length. v_{om} and L_o are related as $v_{om}/L_o^4 = 2.407 \times 10^{-3} q/EI$, where q is the submerged self-weight of the pipe per unit length, and EI is the flexural rigidity (Taylor and Tran, 1996).



(a) Problem layout with initial imperfection



(b) Hybrid finite element modelling



(c) Spring location around the pipe circumference and center

Figure 4.1: Problem statement and finite element modelling: (a) Problem layout with initial imperfection; (b) Hybrid finite element model; (c) Soil spring location

4.3 Numerical modelling

Numerical analyses are performed using Abaqus/Standard FE software. A 3,000 m long pipeline is considered in the present study. Three-dimensional shell elements (S4R in Abaqus software Simulia 2016) are used for the central segment (Fig. 4.1(b)) of at least 2 times the initial imperfection wavelength (L_0) to avoid any coupling effects. Outside the central segment, the pipeline is discretized using 1.0 m long linear pipe elements with hybrid formulations (PIPE31H). Material response is numerically integrated at 32 integration points around the circumference in the PIPE31H element. The Timoshenko beam formulation used by PIPE31H elements allows for the transverse shear deformation, and hybrid element formulation is used for better numerical convergence when the axial stiffness is much larger than the bending stiffness. This is particularly useful for pipelines that undergo large amounts of rotation during buckling. The central segment is connected to the outer segments using kinematic/distributed structural coupling constraints (CP1 and CP2 in Fig. 4.1(b)). Kinematic/distributed structural coupling constraints is used to transfer the rigid body motion of the outer pipe node to the edge nodes of the shell. These coupling constraint ensures an even distribution of axial loads and moments from the outer pipe to the shell element, thereby minimizing stress concentration. The hybrid FE model with shell and pipe elements (Fig. 4.1(b)) is computationally efficient than the full shell element-based FE model.

To check the performance of the hybrid FE model, some analyses are conducted by modelling the full pipeline using shell elements. The shell element allows the simulation of local buckling, which might be occurred in the central part of the pipeline at large displacements. The local buckling analysis cannot be conducted using linear beam and linear pipe elements, as used in Chapter 3. Modelling the outer segment using PIPE31H elements allows direct application of the differential pressure, as applied during operation.

The soil resistance to pipeline displacement is modelled using three sets of nonlinear springs in the orthogonal directions (SPRING1 in the software). The spring behaviour is defined based on

the force–displacement curves described in the following sections. A tiny wire (negligible weight and stiffness) is placed along the centerline of the imperfect pipe, which is then discretized into small segments of the same length as the shell elements. The nodes of this wire are tied to the nodes of the shell elements to evenly distribute the soil–spring resistance on the entire surface of the 3D pipe. The springs in the three orthogonal directions are connected to the nodes of the central elements. Similar approach of the coupled beam and shell elements with soil springs has been successfully used for the 3D modelling of buried steel pipes crossing active faults by Takada et al. (2001). Analyses are also performed by placing the springs at nodes on the pipe surface (e.g., at points A, B, C, D of the pipe section shown in Fig. 4.1(c)).

The FE analysis consists of three steps: (i) apply the submerged weight of the pipeline (q) as a line load; (ii) apply the differential pressure (p), and (iii) increase the temperature to calculate the vertical displacement of the pipeline using static Riks method (Simulia 2016). The Riks approach can model snap-through buckling cases without numerical issues related to unstable buckling. The initial and final temperatures are defined using the predefined fields. The geometric nonlinearity is considered. Boundary conditions are set as fixed at both ends of the pipe. It is worth noting that these end conditions do not significantly impact buckling behaviour in the mid-section due to the long length of the pipeline. The simulation continues by applying a substantially large temperature increase (T) above the ambient temperature. Consequently, the pipeline undergoes significant vertical displacement exceeding 3 meters ($v_m > 3.0$ m). At this stage, a section of the pipeline rises above the seabed, where the soil resistance is zero, which has also been reported in previous field investigations (Nielsen et al. 1990; Liu et al. 2013).

Analyses are performed with a sufficiently large number of 4-node quadrilateral shape doubly curved reduced integration shell elements (S4R) placed around the circumference of the pipe. Study shows that S4R shell elements are suitable for local buckling analysis of the pipeline undergoing large deformation (Simulia 2016). The outer pipe is discretized with the PIPE31H element of 1 m length. At the straight portion of shell (away from L_0), the element size of 0.025 m

in circumference and 0.07 m in the longitudinal direction is used. Within the central imperfection zone (2 meter length Fig. 4.2(ii)), which is critical for undergoing local buckling (Fig. 4.2), the element size is further reduced to 0.01 meters in circumference and 0.0125 meters in the longitudinal direction (Fig. 4.2). This finer mesh is employed to accurately capture the local buckling behaviour of the hybrid model undergoing global buckling.

Mesh sensitivity analysis is also performed with different element types (S3(3-node triangular shell) and S4R (4-node quadrilateral shell)) and sizes (Fig. 4.2). Results show that the most computationally efficient element of S4R with the mesh size, as discussed earlier, is best for modelling the upheaval buckling, leading to local buckling, and wrinkling. The subsequent section contains the details of the soil springs utilized for this analysis. Figure 4.2 illustrates the mesh shape and sizes used to investigate the post-buckling behaviour. Figure 4.3 shows the FE results obtained using three different mesh sizes and types. Notably, the fine mesh employed at the center yields the most reliable results with the outward wrinkle formation, comparable to those obtained for a pressurized pipeline Fig. 4.3(Inset-iv) analyzed by Murray (1997).

4.4 Soil resistance for buried pipeline

4.4.1 Axial, lateral and bearing resistances

Based on ALA (2005) guidelines, the soil resistance in the axial (F_a), lateral (F_l) and vertical downward (F_b) directions are defined by bi-linear curves where F_a , F_l and F_b , respectively, increase linearly with displacement in the axial (u_a), lateral (u_l) and vertical downward (v_b) directions to the peak values (F_{ap} , F_{lp} and F_{bp}) at the peak mobilized displacements (u_{ap} , u_{lp} and v_{bp}), and then remain constant (Fig. 4.4). Equations (4.2)–(4.4) are used to calculate the peak values.

$$F_{ap} = 0.5 \pi DH \gamma' (1 + K_0) \tan(\phi_\mu) \quad (4.2)$$

$$F_{lp} = N_{qh} \gamma' HD \quad (4.3)$$

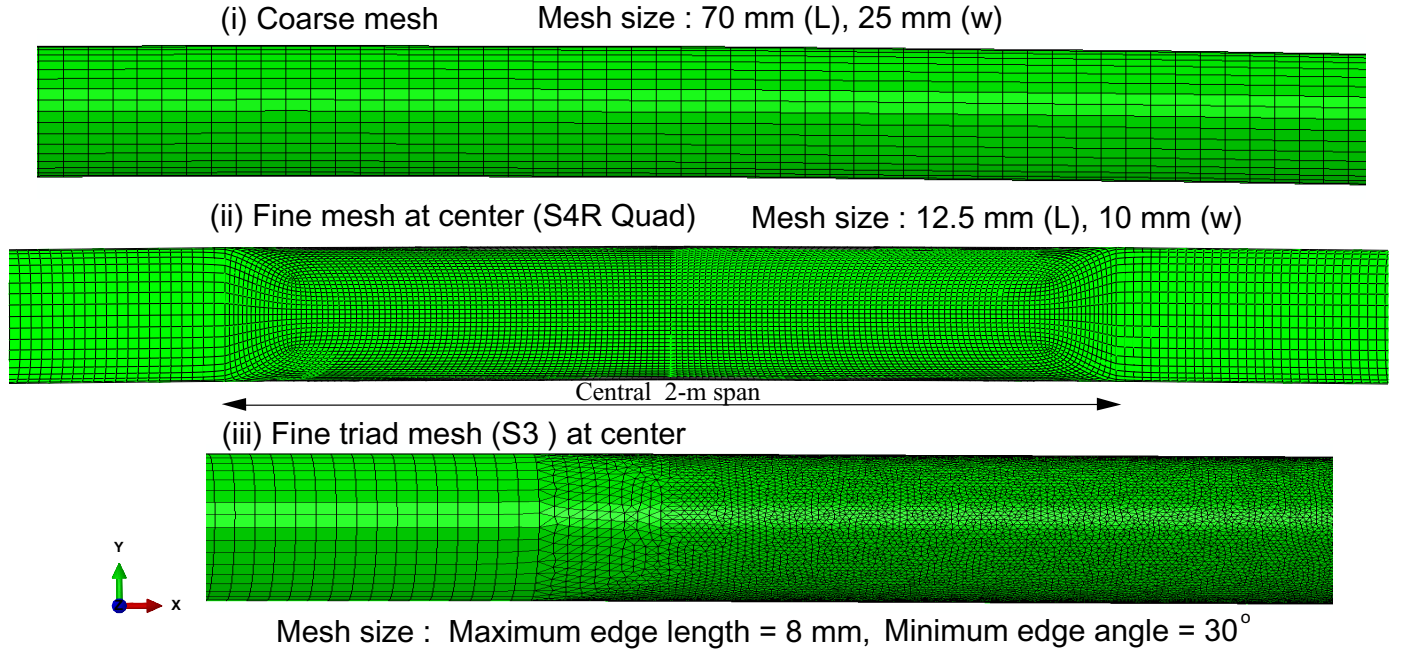


Figure 4.2: Element shape and sizes used for the mesh sensitivity analysis: (i) Coarse S4R mesh throughout; (ii) Fines S4R quad mesh at the center critical zone; (c) Fine triad (S3) mesh at the central critical zone

$$F_{bp} = N_q \gamma' HD + 0.5 \gamma' N_\gamma D^2 \quad (4.4)$$

where γ' is the effective unit weight of soil; K_0 is the coefficient of earth pressure at rest ($=1-\sin\phi'_c$); ϕ_μ is the axial interface friction angle between pipe and the soil; N_{qh} is the horizontal bearing capacity factor ($=f(\phi')$) given by $N_{qh} = a + b(\tilde{H}) + c(\tilde{H})^2 + d(\tilde{H})^3 + e(\tilde{H})^4$; where a, b, c, d, and e are constants given in Table 4.1, $\tilde{H}(=H/D)$ is the normalized burial depth. $N_q \left(= e^{\pi \tan \phi'} \tan^2 \left(45^\circ + \frac{\phi'}{2} \right) \right)$ and $N_\gamma \left(= e^{(0.18 \phi' - 2.5)} \right)$ are the vertical bearing capacity factors; ϕ' is the angle of internal friction; D is the diameter of the pipeline; H is the depth of the center of the pipeline from the seabed (burial depth).

For the base case simulation ($D = 300$ mm, $H = 900$ mm, $\gamma' = 10$ kN/m³, $\phi' = 45^\circ$, $\phi_\mu = 0.8\phi'$), $F_{ap} = 4.53$ kN/m, $F_{lp} = 75.1$ kN/m and $F_{bp} = 486.02$ kN/m (Eqs. (4.2)–(4.4)) are used. Based on

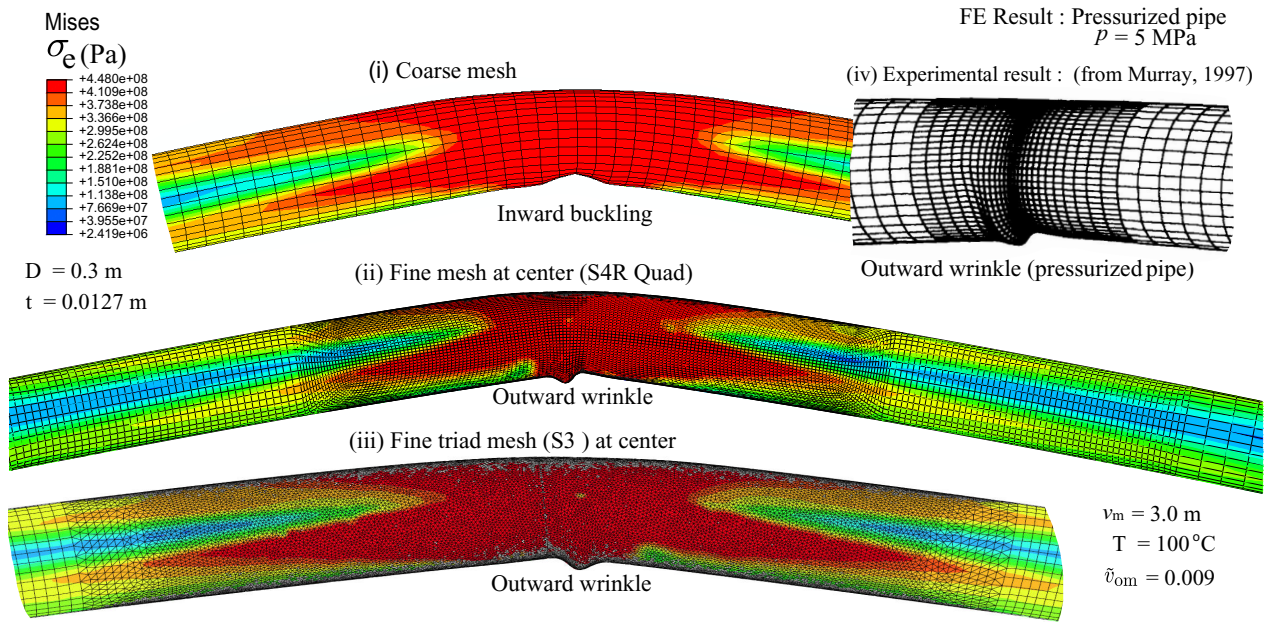


Figure 4.3: FE simulation results from different mesh sizes: (i) Coarse quad S4R mesh; (ii) Fines quad S4R mesh; (iii) Fine triad S3 mesh; (iv) Experimental result from Murray (1997)

ALA (2005), $u_{ap} = 3 \text{ mm}$, $u_{lp} = 0.04(H + D/2)$ (but $\leq 0.10D - 0.15D$), and $v_{bp} = 0.1D$ are used.

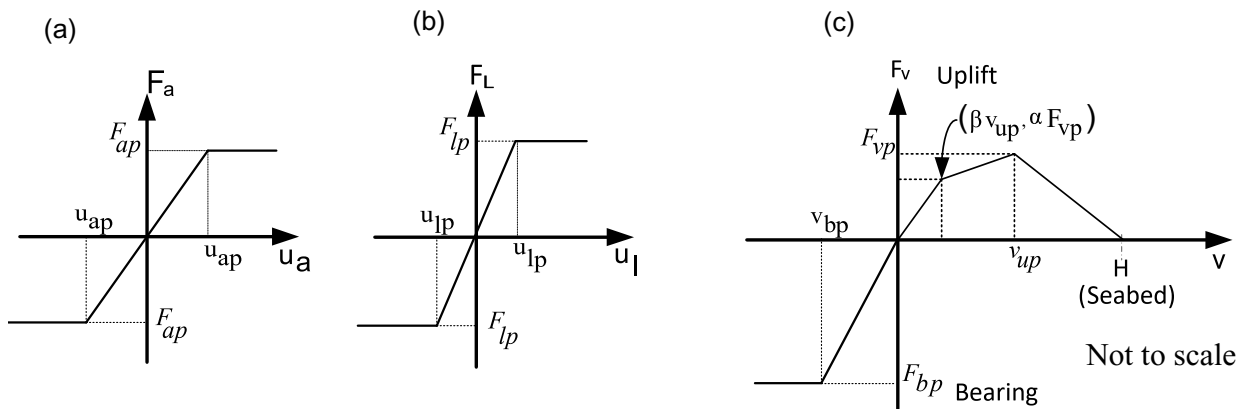


Figure 4.4: Modelling of soil resistances: (a) Axial; (b) Lateral; and (c) Vertical (uplift and bearing)

4.4.2 Uplift soil resistance

A detailed discussion on uplift resistance and its effects on upheaval buckling has been presented in Chapter 3. The following are the key findings: (i) experimental results show that uplift resistance (F_v) increases with upward displacement (v_u) and reaches at the peak (F_{vp}) at a displacement of v_{up} ; (ii) F_v decreases non-linearly after the peak, initially due to the reduction of shear resistance for denser soil and then reduction of cover depth; (iii) $F_v = 0$ at the ground surface/seabed; (iv) most of the existing studies and design guidelines did not consider such a large decrease in F_v , although some studies showed that neglecting post-peak F_v degradation could give unsafe results (Klever et al. 1990; Bransby et al. 2001; Wang et al. 2010). While post-peak uplift resistance is nonlinear, a linear F_v degradation from the peak to zero at the seabed can reasonably capture the UHB response, especially for loose to medium dense sand (Chapter 3). Therefore, in the present study, a linear post-peak F_v degradation model is used (Fig. 4.4(c)). The peak uplift resistance per unit length of the pipeline is calculated as (DNV 2007):

$$F_{vp} = (1 + f\tilde{H})\gamma\tilde{H}D^2 \quad (4.5)$$

where f is the uplift resistance factor, which is $f = 0.10$ – 0.3 and $f = 0.4$ – 0.6 for loose and medium/dense sands, respectively. F_{vp} mobilizes at $v_{up} = 0.005H$ – $0.008H$ (DNV 2007).

The force-displacement curve prior to the peak is defined by two linear segments that intersect at a point below the peak ($\beta v_p, \alpha F_{up}$, where α and β are two constants). DNV (2007) recommended $\beta = 0.2$, and $\alpha = 0.75$ – 0.85 and $\alpha = 0.65$ – 0.75 for loose and dense sands, respectively. The lower and upper values of f and α represent the lower bound (LB) and upper bound (UB), respectively.

In the base case analysis, $f = 0.6$, $\beta = 0.2$, $\alpha = 0.75$ are used, which gives $F_{vp} = 7.56$ kN/m for a 300 mm diameter pipe buried at $H = 900$ mm. It is also assumed that F_{vp} mobilizes at ($\beta v_{up} = 7.2$ mm). Based on the above calculated values, the tri-linear uplift resistance in Fig. 4.4(c) is defined. The soil parameters used to develop axial, lateral, bearing, and uplift resistance are listed in

Table 4.1.

Table 4.1: Soil parameters used to develop force–displacement curves

Parameters	Dense sand	Medium sand
Submerged unit weight of soil, γ (kN/m ³)	10	9.19
Angle of internal friction, ϕ' (°)	45	35
Axial interface friction angle between pipe and soil, ϕ_μ (°)	36	28
Coefficient of earth pressure at rest, K_0	0.47	0.5
β^*	0.2	0.2
α^*	0.75	0.75
f^*	0.6	0.6
a^{**}	17.658	6.816
b^{**}	3.309	2.019
c^{**}	0.048	-0.146
d^{**}	$-6.443(10)^{-3}$	$7.651(10)^{-3}$
e^{**}	$-1.299(10)^{-4}$	$-1.683(10)^{-4}$

* Parameters used to calculate uplift soil resistance (DNV (2007))

** Parameters used to calculate lateral soil resistance (ALA 2005)

4.5 Validation of hybrid FE model with analytical solution

The FE model is validated against the analytical solution proposed by Taylor and Gan (1986) for the unburied pipelines. Three imperfection ratios, i.e. $\tilde{v}_{om} = v_{om}/L_o$, of 0.003, 0.007 and 0.01 are considered to cover a wide range of buckling phenomenon (snap through and stable). To be consistent with the analytical solution, a 0.65 m external diameter pipe with a wall thickness of 15 mm is used for these analyses. The total submerged self-weight of the pipe is considered as 3800

Table 4.2: Geometry and pipeline model parameters used for base case FE simulations

Parameters	Value
Length of pipe, L (m)	3,000
External diameter of pipe, D (mm)	300
Wall thickness of pipe, t (mm)	12.7
Young's modulus of pipe, E (GPa)	206
Poisson's ratio of pipe (μ)	0.3
Pipe-soil interface friction coefficient (f)	0.8
Yield stress of pipe, σ_y (MPa)	448
Thickness of concrete cover (m)*	0.05
Coefficient of thermal expansion, (α (per °C))	11×10^{-6}
Density of steel, ρ_s (kg/m ³)*	7,850
Density of concrete, ρ_c (kg/m ³)*	2,800
Density of oil, ρ_o (kg/m ³)*	800
Submerged weight of oil-filled pipe, q (N/m)	1,594
Specified minimum tensile strength, SMYS (MPa)	531

* Parameters used to calculate submerged weight of pipe per meter length

N/m which is also consistent with the analytical solutions of Taylor and Gan (1986).

The initial imperfection (Eq. (4.1)) considered in the FE model is unstressed . The nonlinear response of the axial soil spring is implemented using the analytical solution proposed by Taylor and Gan (1986), while the bearing soil resistance, which assumes a rigid seabed, is modeled with a value calculated from Eq. (4.4). To ensure numerical convergence, the lateral soil spring resistance described in Eq. (4.3) is used.

The static Riks algorithm available in Abaqus FE software is used for the numerical solution. The hybrid pipe-shell model with soil-spring at the centerline as described in Fig. 4.1(b) is used for the verification of finite element model. After conducting a mesh sensitivity analysis by varying the element size in the shell part as discussed in Section 4.3, it was concluded that using an element size of 0.0125 m in the longitudinal direction and 0.010 m in the circumferential direction (central 2 m Fig. 4.2(ii)) and 0.07 m in longitudinal and 0.025 m in circumferential direction beyond the central 2 m length provides reliable results with no significant variation. The FE calculated buckle

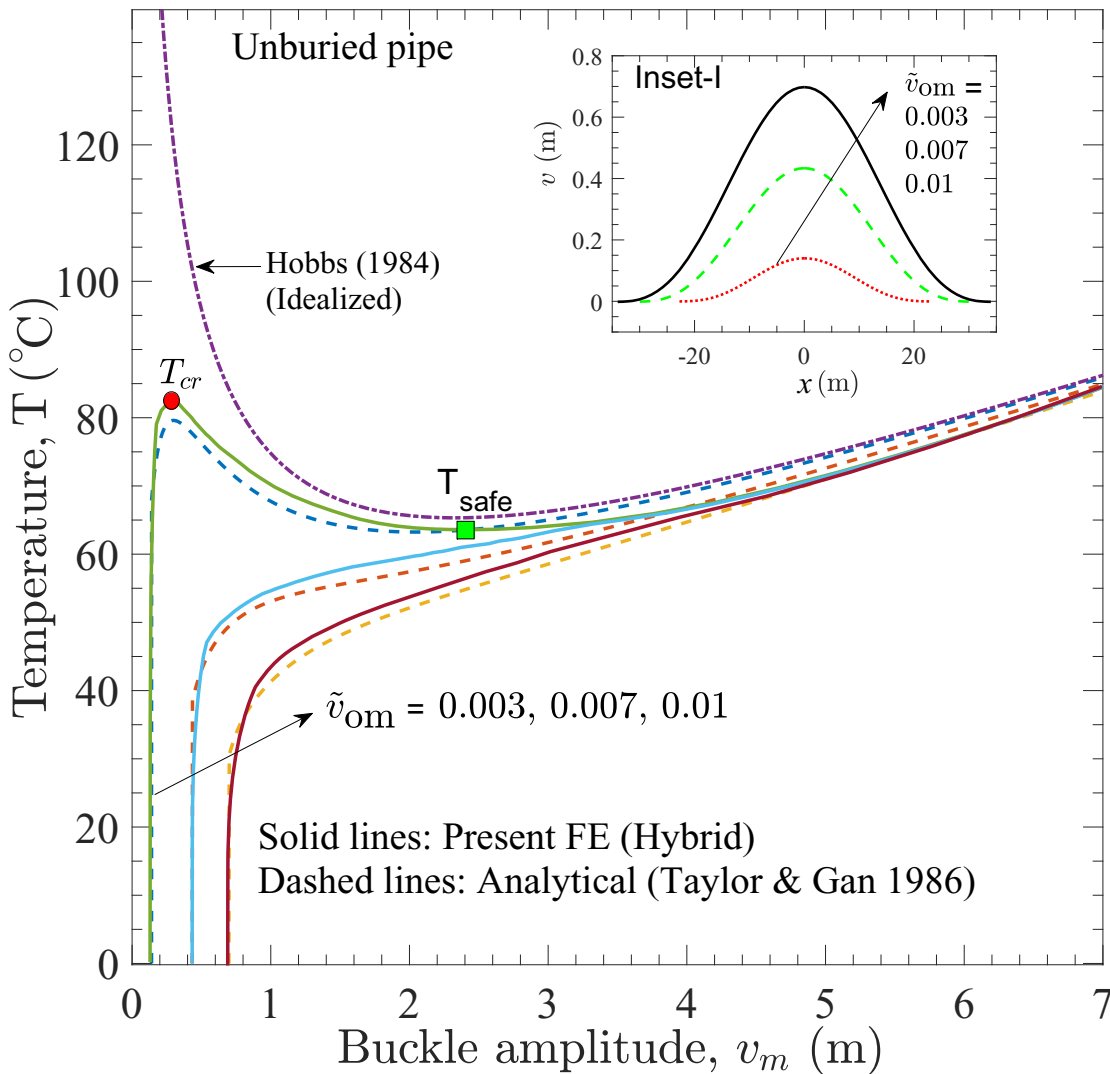


Figure 4.5: Validation of FE results with analytical solutions

amplitude (v_m) with pipe temperature (T) is shown in Fig. 4.5. The dashed lines in Fig. 4.5 shows the $T-v_m$ curves obtained from analytical solutions proposed by Taylor and Gan (1986). As the same pipe–soil interaction properties (spring constants in FE) are used, the FE calculated curves match well with the theoretical solution. Note that the slight differences in the curves near the peak temperature rise might be due to the geometrical nonlinearity and bearing resistances used in the FE simulations for the numerical convergence) with the Riks algorithm.

The FE results show that the coupled pipe-shell soil-spring model can properly capture snap-through and stable buckling. The $T-v_m$ curve for a perfect pipeline i.e., no initial imperfection as defined by Hobbs (1984) is also included in Fig. 4.5. The FE results show an unstable buckling for a small initial imperfection of 0.003, whereas buckling is stable for higher values of initial imperfection (\tilde{v}_{om}) of 0.007 and 0.01. This behaviour is also consistent with Taylor and Gan (1986) analytical solution.

4.6 Comparison of FE modelling approaches

In the above section, the numerical model is validated using the analytical solution from Taylor and Gan (1986). However, it is important to note that this analytical solution only applies to the unburied pipeline conditions. Besides, the differential pressure was not considered; instead, an equivalent temperature approach was used to calculate the buckling response of the pipeline.

Finite element analysis with beam, pipe and shell elements might be used for post-buckling analysis. However, the weak formulations in FE for beam (B31/B31H), pipe (PIPE31/PIPE31H), and Shell (S3/S4/S4R/S8R5) are distinct, leading to slightly different results for the same numerical problem. Moreover, when coupling between PIPE and SHELL elements is needed, the results may differ due to the need for stress transfer between the single node pipe element and the Shell (edge elements) and vice versa. Stress concentration at the coupling zone and the spring location is an important factor to be considered during the FE analysis to ensure accurate and reliable results. Another challenge is that the initially imperfect pipe considered in this study is

already bent, which might create additional numerical issues with the stress transfer from the PIPE element to the SHELL. Also, soil resistance is another factor to be considered to finalize the most effective and computationally reliable approach to solve the post-buckling problem leading to local buckle and wrinkle. Therefore, to validate the numerical approach used in this study, various approaches for the element type, spring location, and coupling are performed to assess their effectiveness and accuracy in predicting the post-buckling behaviour of the pipeline.

The initial FE analysis includes four different numerical models: beam in 3D space (B31H element), pipe in 3D space (PIPE31H element), full-length shell (S4R), and hybrid (PIPE+SHELL) models with soil-springs. The pipeline considered for analysis has a diameter of 0.3 meters and a thickness of 12.7 millimeters, length of 3000 m with an initial imperfection of 0.009. The pipeline is buried in dense sand at a depth of $H (= 3D)$ from the seabed to the center of pipe. All other geometry and pipeline model parameters used for this analysis are listed in Table 4.2. Figure 4.6(a) presents the FE results for the beam, pipe, shell, and hybrid models.

In this initial analysis, the internal pipe pressure is not considered, because unlike other element types, beam elements do not support the direct application of differential pressure in Abaqus. The beam, pipe, and hybrid models with soil springs show very similar temperature-displacement responses, for temperatures (T) from 77–79°C (no significant variation in safe temperature). However, the full shell model provides a slightly lower critical and safe temperature of 75°C (Fig. 4.6(a)). This difference may be attributed to the mesh size and spring location for a long shell and SHELL formulation (S4R) in Abaqus, which considers the behaviour of thin and thick pipes based on the provided section size (D and t). It is also observed that after reaching a certain displacement of 1.7 meter, the full shell model undergoes a rapid increase in temperature with uplift compared to the other models. This behaviour suggests that the full shell model might overestimate the buckling behaviour once it experiences higher uplift movements. Overall, the beam, pipe, and hybrid models with soil springs provide consistent and reliable results with minor variations in critical and safe temperatures, making them suitable for further numerical analysis.

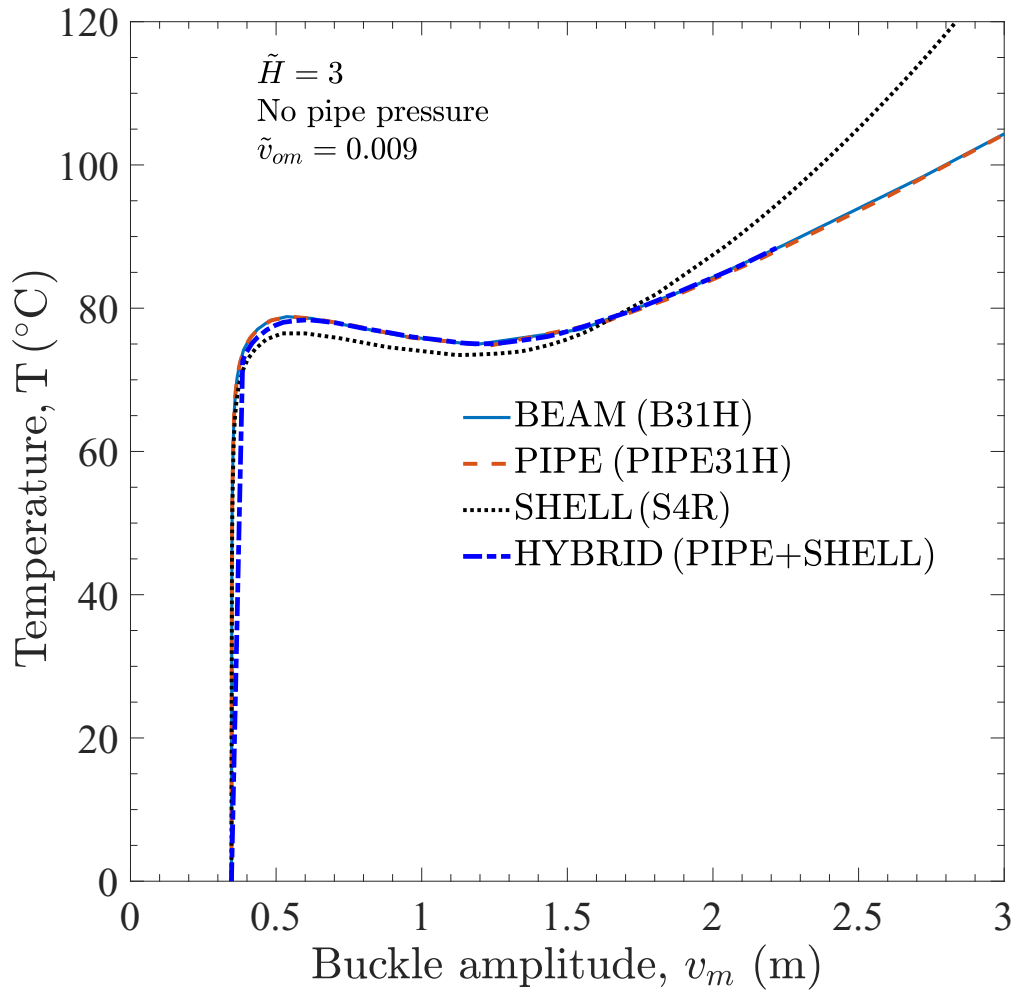


Figure 4.6: Comparison of buckling response from various modelling techniques: (a) Element types

To assess the reliability and accuracy of the spring locations in the FE model, additional analyses are conducted for the hybrid model with centerline springs node (CL) in Fig. 4.1(c), springs at the springlines along the pipe length (nodes A and C), four side springs nodes along the pipe length (A, B, C, D) and springs at all node at the circumference of pipe along the length. The summation of the soil reaction per unit length along the Shell should be equal to the corresponding value for the beam model. The soil spring force contributed by each node will be (force per meter)/(no of

nodes per meter). Figure 4.6(b) shows the temperature-displacement results with all four-spring approach used in the numerical analyses. In this numerical model, the pipe is applied with the differential pressure of 5 MPa before the application of temperature increase. No significant differences in result is obtained from the hybrid model comparing with the PIPE31H only model.

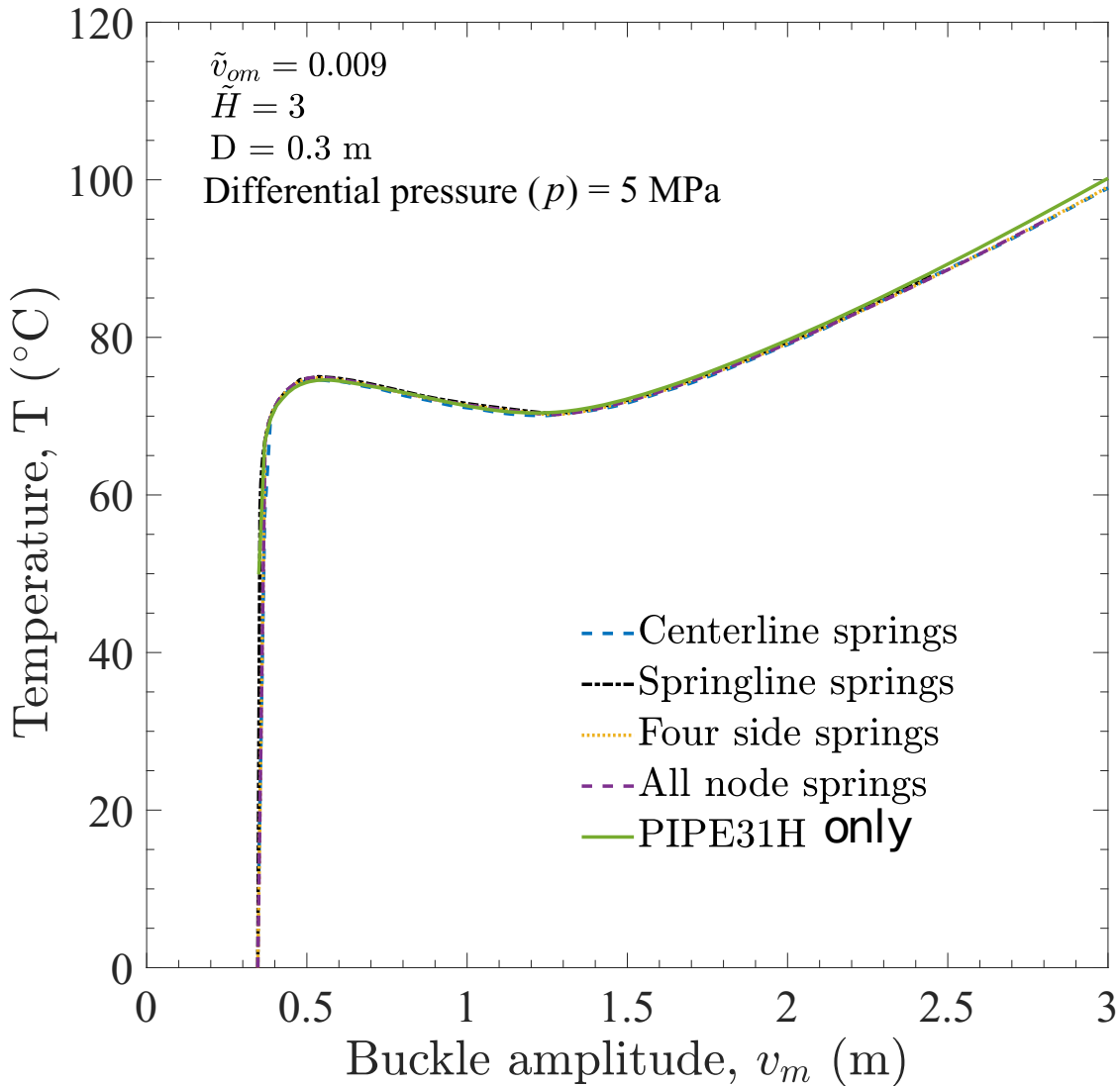


Figure 4.6: Comparison of buckling response from various modelling techniques: (b) Effects of spring locations

Furthermore, an additional numerical analysis is carried out to examine the impact of applying a

coupling technique in the FE model. Kinematic and distributed structural coupling approaches, available in Abaqus, were used to check the variation in numerical results. FE results show no significant difference in temperature-displacement response between these two different coupling approaches (Fig. 4.6(c)).

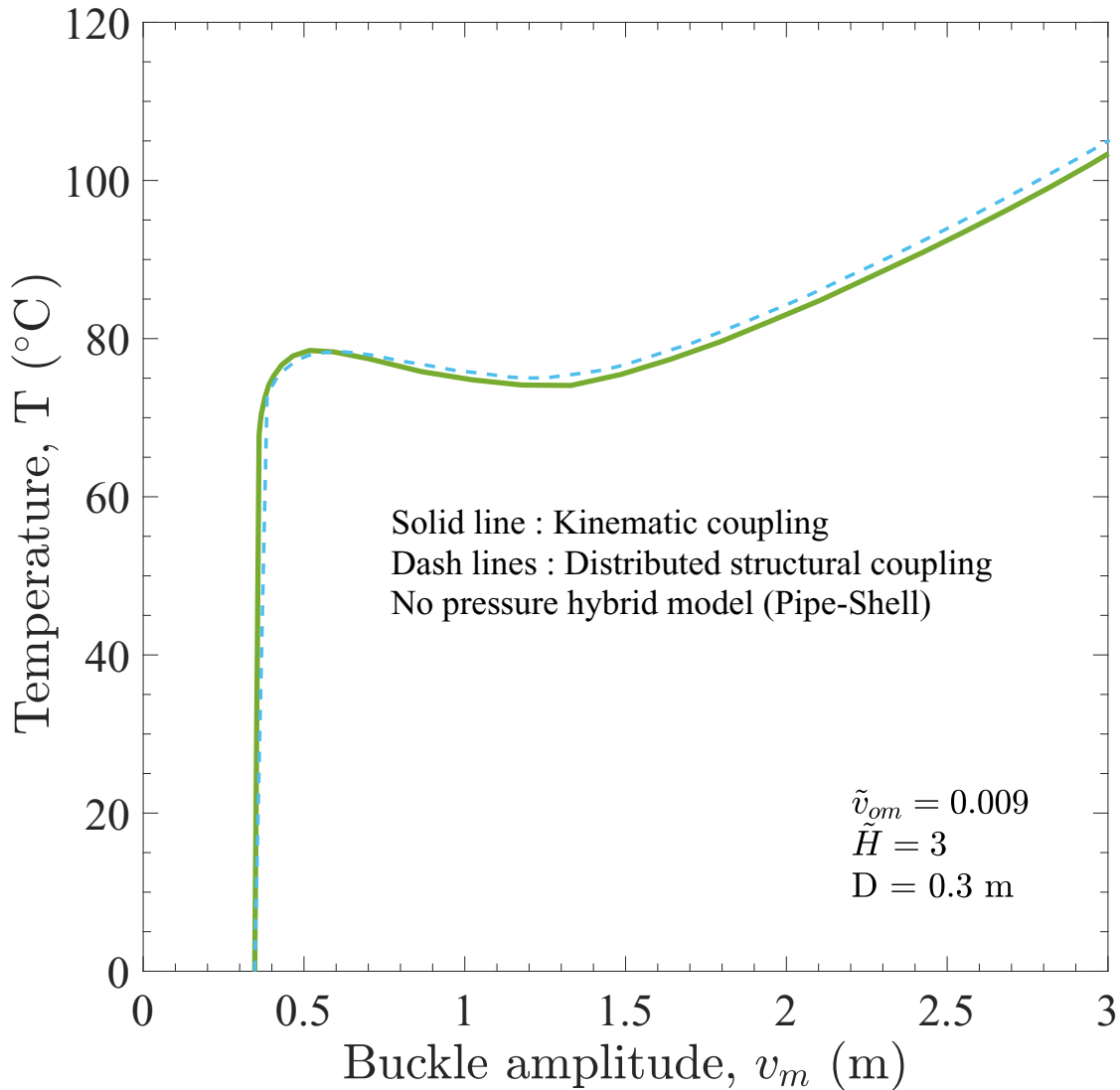


Figure 4.6: Comparison of buckling response for varying modelling techniques: (c) Effects of coupling constraints

Furthermore, another set of numerical analyses are conducted using the hybrid model and

PIPE31H only model to investigate the effects of an increase in operating pressure (p) from 0–15 MPa (Fig. 4.7). At the zero-pressure condition, PIPE31H and hybrid models show no significant difference in temperature-displacement responses. However, interesting results emerge as the differential pipe pressure (p) is raised from 5–15 MPa. Surprisingly, no significant differences in the critical temperature are observed for the differential pressure (p) of 5, 7.5, 10, and 15 MPa. This is because the pipe is still in the global buckling stage, and no local buckling has started. However, considerable differences in safe temperature for higher differential pressure is obtained. This is because the pipe model cannot capture the local buckling behaviour at a large uplift displacement of 1.5 m. However, the hybrid pipe-shell model can capture global and localized buckling behaviour.

As the local buckling process occurs, the hybrid model effectively utilizes strain energy, causing a weakening of the pipe's capacity and resulting in a lower temperature during the buckling process than the pipe only model. An increase in pipe pressure further accentuates this behaviour. A comparison is made between the CPU computational times for the full shell model and the proposed hybrid centerline spring model. The results indicate that the total computational time for the full shell model, incorporating a non-linear soil spring is 32,731 seconds (9.09 hours). The same problem with mesh size solved with the proposed hybrid model utilizing the centerline spring model is achieved in 9,190.3 seconds (2.55 hours).

In conclusion, after conducting various numerical analyses, the hybrid model utilizing the centerline spring approach is identified as the most reliable and computationally efficient method for accurately capturing both global and local buckling behaviour in offshore pipelines operating under combined pressure and temperature conditions. A 3D hybrid model (Fig. 4.1(b)) is employed for the subsequent analysis, incorporating soil springs at the centerline with a kinematic coupling approach.

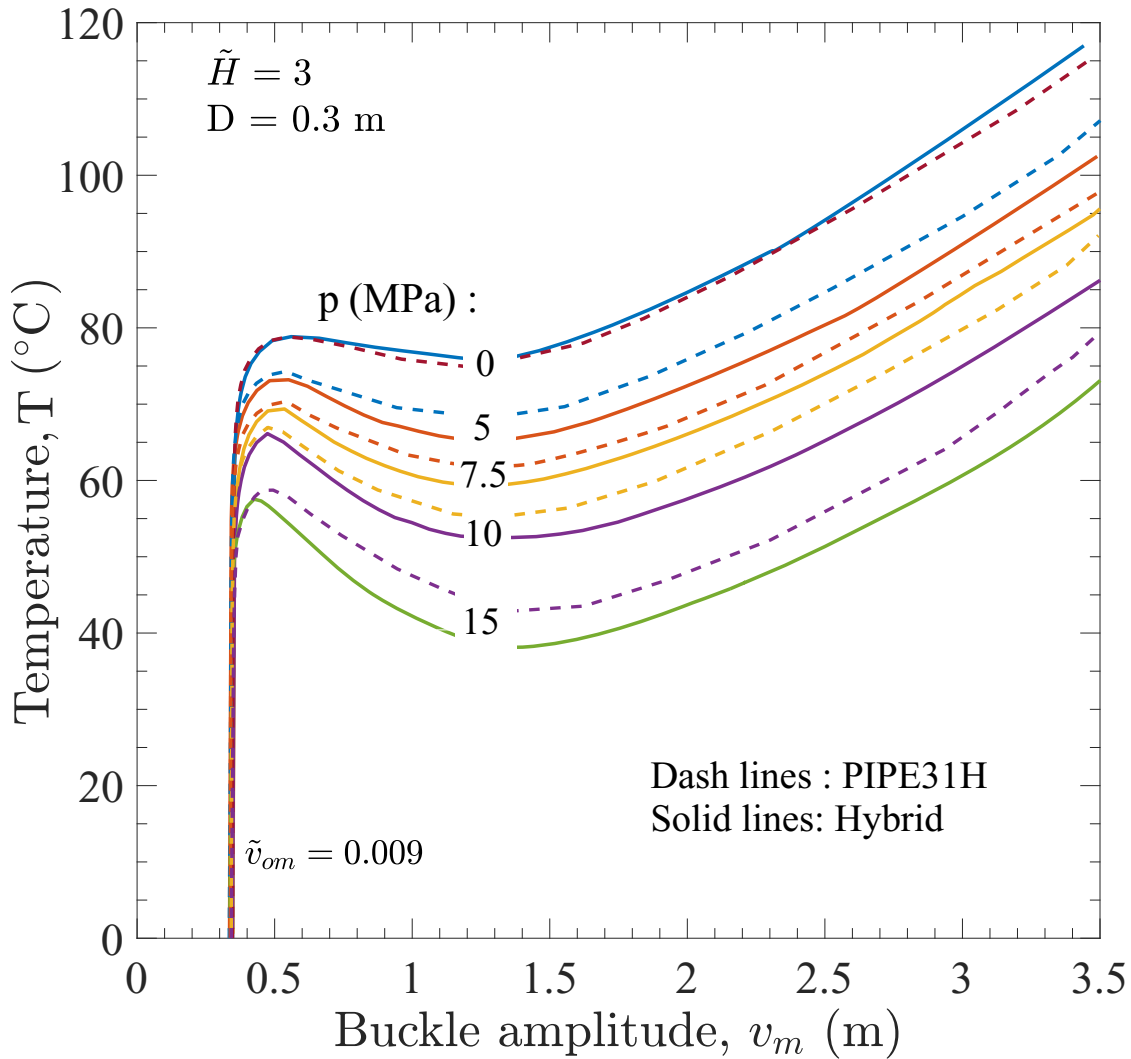


Figure 4.7: Effects of modelling techniques for varying differential pressure

4.7 Results from the hybrid model

This section presents the detailed analysis and numerical results obtained from the hybrid FE model, as discussed in the previous section. The analysis focuses on a specific pipe section of 0.3 m outer diameter, wall-thickness of 12.7 mm, differential pressure of 5 MPa and buried at a depth of 3D in dense sand condition (linear degradation (LD) model) unless otherwise specified. The

amplitude of initial imperfection ratio (\tilde{v}_{om}) used for all the analyses is 0.009. The pipe material is considered as elastic-perfectly plastic with a yield stress of 448 MPa. All other modelling parameter are provided in Table 4.2. In this study, the global buckling behaviour leading to large plastic strain, resulting in sectional ovalization, local buckling, and wrinkle formation on the pipeline is investigated.

4.7.1 von Mises stress distribution

Figure 4.8 illustrates the sequence of uplift displacement in the longitudinal profile of the hybrid FE model. The analysis begins with the pipeline in its initially imperfect state, experiencing self-loading conditions, and then progresses to the effects of pressure and temperature. The step-by-step evolution of the von Mises stress (σ_e) in a pipeline as it undergoes uplift movement, and the corresponding increase in operating temperature is shown in Fig. 4.8.

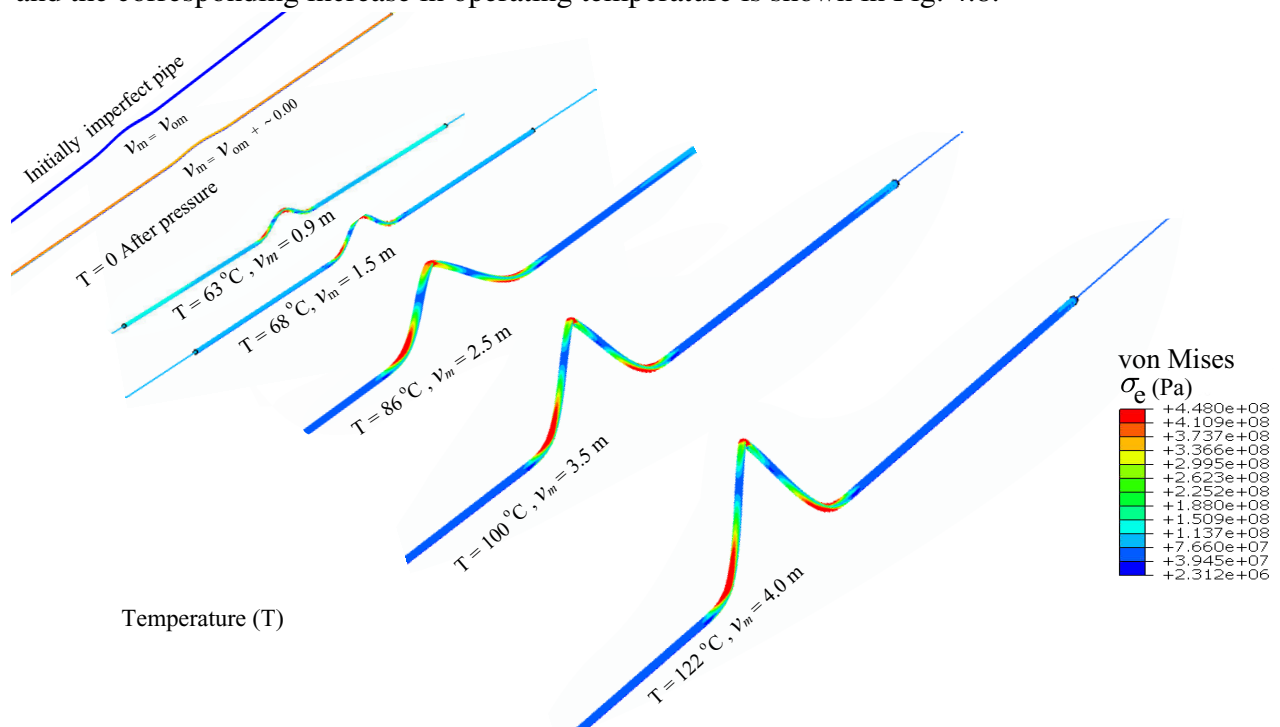


Figure 4.8: Development of von Mises stress in buckled section with vertical displacement of the pipe

In the FE analysis, the simulation begins with the self-loading step, which considers the submerged weight of the pipeline, cover, and contents. At this stage, the stress distribution is uniform throughout the length of the pipe. Next, the pipeline is subjected to an differential pressure of 5 MPa, which induces hoop and longitudinal stresses. At this point, the pipeline remains in the elastic limit state, and the hoop stress ($pD/(2t)$) is calculated as 59.06 MPa for the elastic condition.

Following the pressure stage, the pipeline experiences an increase in operating temperature (T varies from 0–125°C in this analysis). The combined effect of pressure and temperature acts as a progressive compressive force in the pipeline. This force exceeds the limiting resisting force in the pipe, causing it to move in the weaker zone, which is in the upward direction. It is essential to note that the burial condition provides significantly high bearing and lateral resistance, resulting in the pipeline moving in the upward direction. At a temperature of 63°C, the pipeline undergoes an uplift movement of 0.9 m, reaching just at the seabed level. At this point, the central imperfect segment of the pipeline reaches a yield stress condition, but local buckling has not yet started; subsequently, with a slight increase in temperature to 68°C, the pipeline experiences buckling to a height of 1.5 m, which is 0.7 m above the seabed.

The rapid increase in uplift movement is because the soil resistance becomes zero once the pipe reaches the seabed. Despite this, local buckling is still not appeared in the pipeline. Further increasing the temperature to 86°C, the pipeline moves 2.5 m from its initial position, and at this stage, local buckling starts to appear (detailed in the subsequent section). Once the operating temperature increases to 100°C and 122°C, the pipeline experiences uplift movements of 3.5 m and 4 m from its initial position, respectively. This observation indicates the offshore pipeline's large upheaval buckling behaviour, where it undergoes yielding and severe plastic deformation, including local buckling (Fig. 4.8), before going to failure/collapse.

4.7.2 Plastic strain envelope

As upheaval buckling progresses, the pipeline experiences fluctuations in stresses and strains within the compressed and tensile zones of the buckled section. The pipeline section ovalizes at a specific buckling limit and collapses with the combined effect of pressure and temperature. The large vertical deformation during UHB process of the offshore pipeline is associated with the stress and strain beyond yield limit of the pipe which necessitates strain-based limit state i.e., tensile failure, local buckling and sectional ovalization. The recommended tensile strain limit ϵ_{tu} for buckled pipeline ranges between 2–5% based on design guidelines such as ALA (2005) and CSA (2007). PRCI (2009) recommends a tensile strain limit of 2–4% for pressure integrity and a limit within 1–3% for normal pipeline operation. In this study, a baseline plastic strain of 3% is used to examine the local buckling behaviour of the pipeline at that strain level.

Figure 4.9 shows the distribution of equivalent plastic strain along the circumference at the critical section of the pipeline ($x = 0$ in Fig. 4.1(a)) during its vertical movement for the selected operating temperature. The circular contour envelope in the figure represents the varying plastic strain values, ranging from 0–0.8. The radial lines extending from the center of the figure indicate the positions of the pipe's cross-section. Specifically, the 0° position corresponds to the compression side (invert) of the post-buckled pipe, while the 180° position represents the tension side (crown) of the pipe located at the top. Additionally, the angles 90° and 270° correspond to the lateral sides (springlines) of the cross-section. Critical insights into the deformation behaviour during vertical movement at increased operating temperature are revealed by visually examining the distribution of plastic strain across the circumference of the post-buckled pipe.

At a temperature of 65°C , no significant plastic deformation occurred at the pipe's cross-section. However, upon increasing the temperature to 80°C , plastic deformation initiates on the compression side, forming local deformation. As the temperature further increase to 90°C , the plastic deformation increases. Subsequently, with temperature increases from 100 – 120°C , the compression side experiences significant plastic strain with outward wrinkling, while the tension

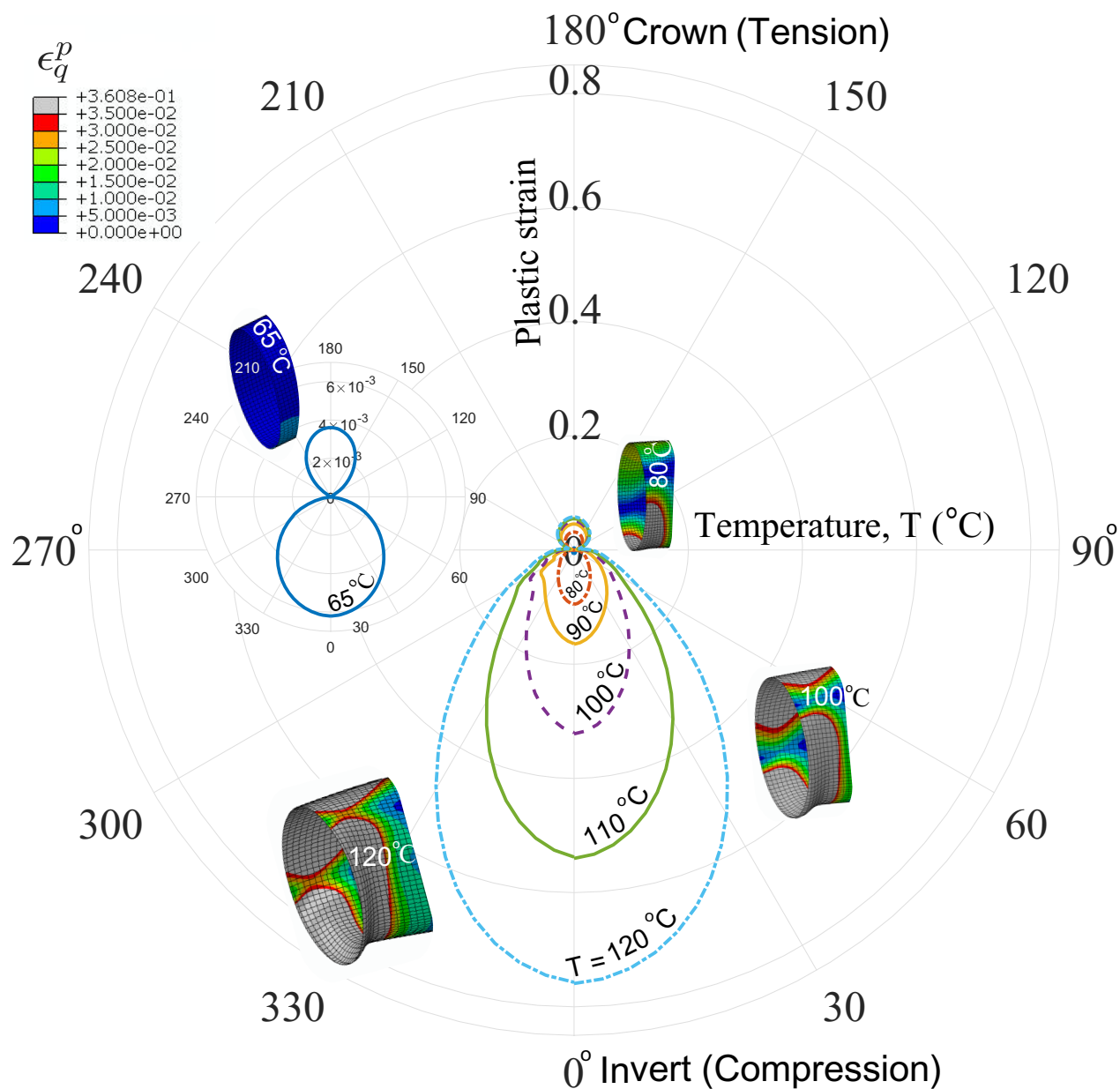


Figure 4.9: Development of plastic strain envelope at the critical section of buckled pipe

side still exhibits a smaller level of plastic strain (less than 3%).

The strain envelope shows that the maximum critical plastic strain occurs at the compression side and gradually transfers towards the tension side. This characteristic plastic deformation profile provides valuable insights into predicting the critical temperature of the pipeline such that the amount of local buckling and wrinkle formation can be accurately predicted.

4.7.3 Plastic strain versus buckle amplitude and temperature

Figure 4.10(a) illustrates the evolution of plastic strain in the compression (bottom or invert) and tension (top or crown) sides of the pipeline at the critical section at center during the process of vertical movement. The results indicate that the compression side experiences significantly higher level of plastic strain during the uplift movement of the pipeline starting from no movement. In contrast, the tension side demonstrates a considerably lower level of plastic strain until a notable outward wrinkle develops on the compression side. After the formation of significant wrinkle, the plastic strain on the tension side rapidly increases.

At the selected operating temperature of 80 °C (Inset Fig. Fig. 4.10(a)), the pipeline achieves an uplift displacement of 2.17 m, signaling the onset of local buckling with the formation of wrinkles (outward) in the compression side (ϵ_q^P of 0.025). In contrast, the tension side still maintains a lower level of plastic strain (ϵ_q^P of 0.008), indicating that it has not yet undergone significant deformation. To achieve a plastic strain (ϵ_q^P) of 0.03 at the tension side of the pipeline, the pipeline must vertically move approximately 2.65 m. However, it is important to note that this strain level has already reached in the compression side at an uplift displacement of 2.21 meters. This asymmetry in plastic strain distribution between the compression and tension sides emphasizes the localized nature of buckling behaviour and the significance of considering both sides for the overall structural integrity assessment of the pipeline.

Figure 4.10(b) presents the plastic strain evolution during the increased in operating temperature. As observed in the previous case, the compression side continues to experience a higher level of plastic strain than the tension side. The snap-through nature of the post-buckling process is evident between temperatures of 63–72 °C in Fig. 4.10(b). After the snap-through, to reach the plastic strain level of 0.03, an operating temperature of 82 °C is required at the tension side, whereas the compression side has already reached that level of strain at 74 °C.

At the operating temperature of 109 °C, the pipeline experiences a significant upward displacement of 3.5 m, resulting in critical local buckling with noticeable outward wrinkle formation. At this

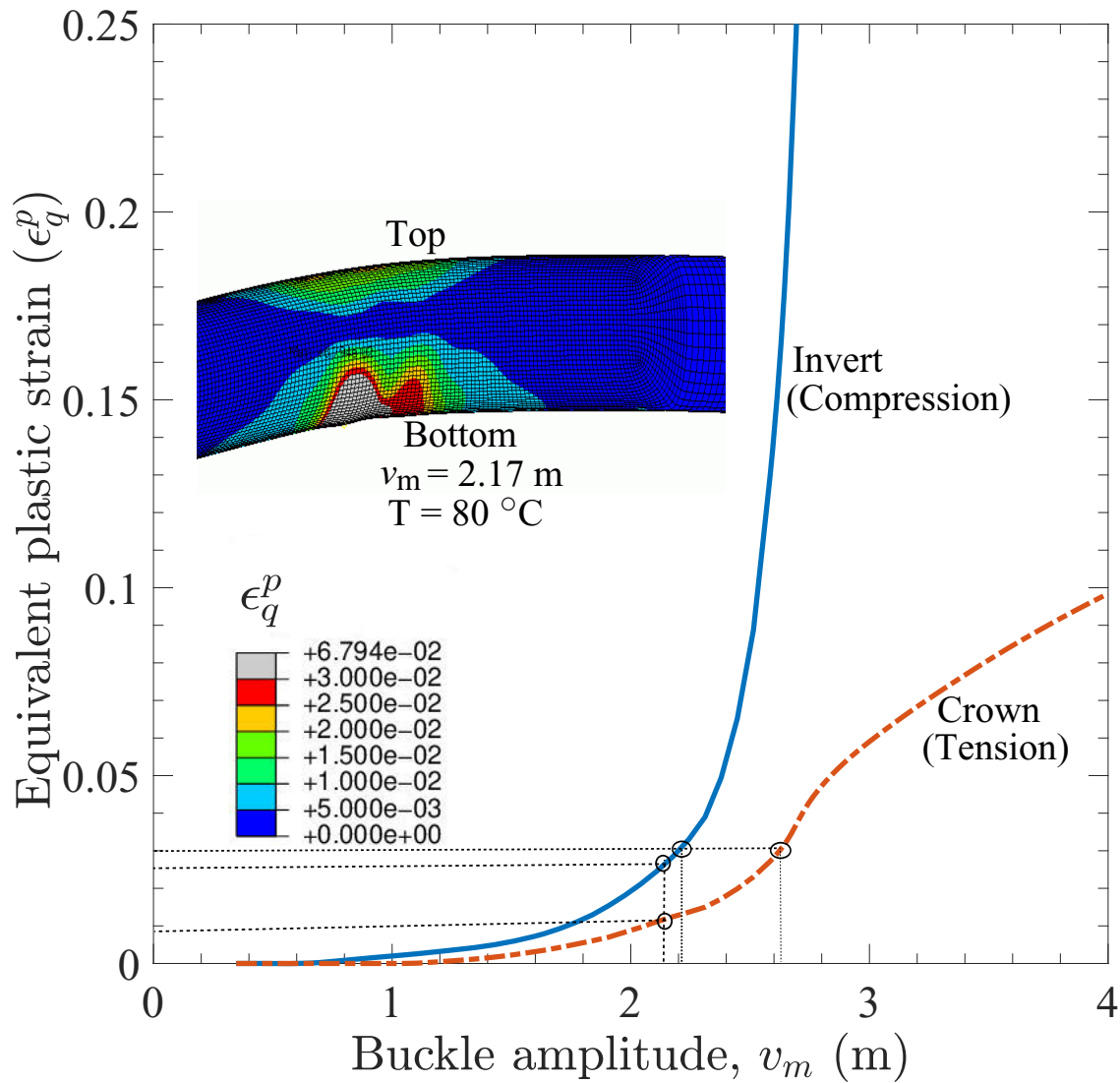


Figure 4.10: Plastic strain development at the invert and crown during buckling: (a) Plastic strain development with buckle amplitude

uplift level, the plastic strain (ϵ_q^p) reaches 0.586, which is deemed undesirable for the safety and integrity of the pipeline. This high level of plastic strain indicates potential failure due to the onset of local buckling in a post-buckled pipeline with the formation of a noticeable outward wrinkle lobe.

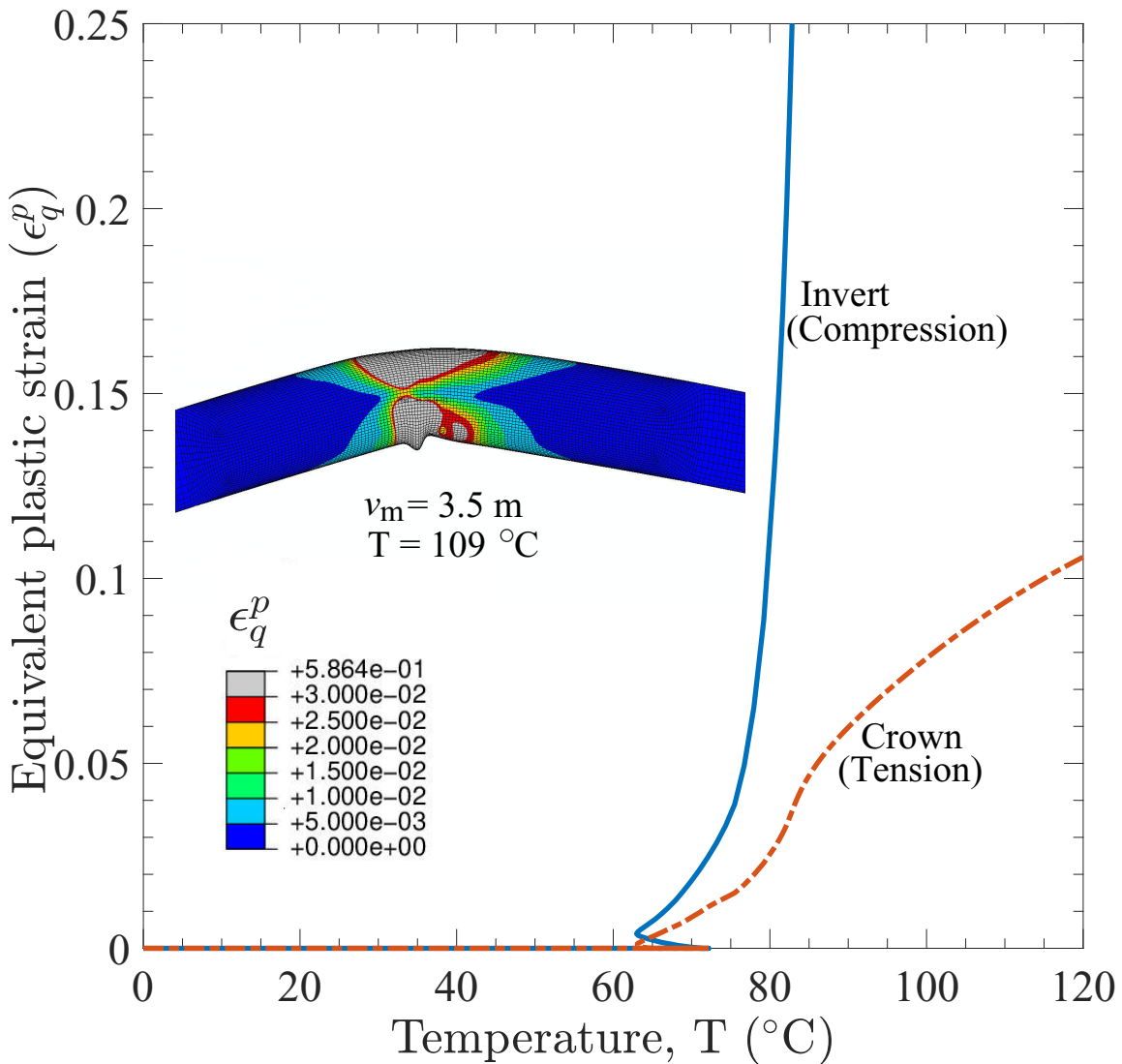


Figure 4.10: Plastic strain development at the invert and crown during buckling: (b) Plastic strain development with temperature increase

4.7.4 Plastic strain development with the pressure variation

Figure 4.11(a) and Fig. 4.11(b) shows the plastic strain generation in the post-buckled pipeline for varying differential pressure (0–15 MPa) in the compression and tension sides, respectively. As previously observed, increasing operating pressure decreases the critical buckling temperature (i.e.,

pipe capacity reduces after undergoing local buckling). The Fig. 4.11(a) shows inward wrinkling at the compression side (diamond-like shape) for unpressurized pipe ($p = 0$) (left bottom inset Fig. 4.11(a)), while wrinkles form outward lobes in pressurized pipes ($p = 5$ MPa). Similar strain localization and wrinkling behaviour were reported in experimental studies for pressurized and non-pressurized pipelines (Murray 1997).

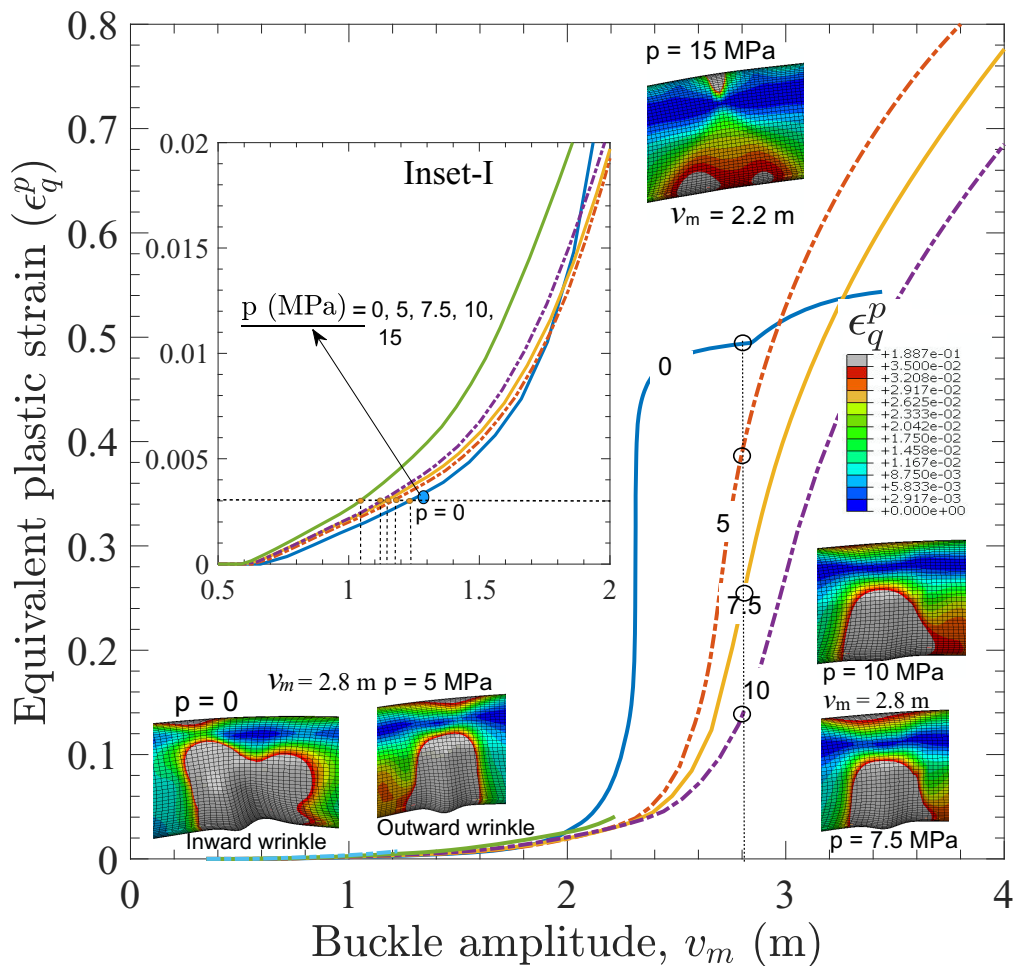


Figure 4.11: Plastic strain development at the invert and crown with the variation in differential pressure: (a) Plastic strain development with buckle amplitude at compression side (invert)

With increasing operating pressure, the localized strain zone in the compression side grows with the outward lobe. Notably, at lower uplift displacements (less than 1.5 m), pipes with higher pressure

(15 MPa) attain a plastic strain of 0.003 at approximately 1.05 m uplift, while pipes with lower pressures need to move farther to reach the same strain level. However, as vertical movement increases, the strain behaviour reverses. At a large displacement of $v_m = 2.8$ m, the unpressurized pipe exhibits a significantly higher plastic strain of approximately 0.48, while pressurized pipes at 5 MPa, 7.5 MPa, and 10 MPa exhibit plastic strains of 0.36, 0.21, and 0.12, respectively. At 15 MPa pressure, the pipe experiences significant plastic strain in both compression and tension sides (strain reversal).

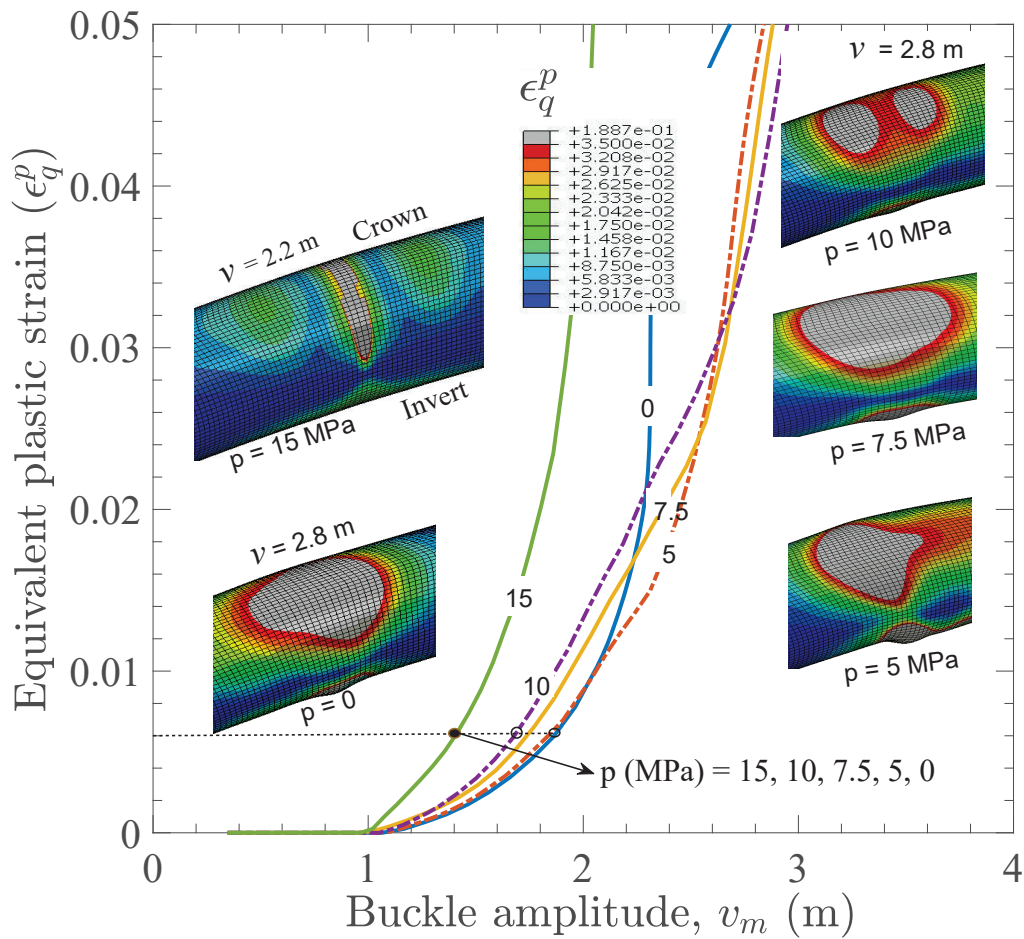


Figure 4.11: Plastic strain development at the invert and crown with the variation in differential pressure: (b) Plastic strain development with buckle amplitude at tension side (crown)

As shown in Fig. 4.11(b) , noticeable changes in plastic deformation are observed at the tension side. Increasing pressure (from 0–15 MPa) leads to higher plastic strain levels on the tension side. This study provides valuable insights into the effects of internal operating pressure on the pipeline’s plastic strain behaviour and formation of local buckle and wrinkle.

4.7.5 Sectional ovalization behaviour

In this section, a detailed study of sectional ovalization in the pipeline is performed, considering the effects of local buckling and wrinkling discussed in the previous section. Sectional ovalization refers to the distortion of the pipeline’s perimeter from its original circular configuration and is a critical serviceability limit state. Sectional ovalization is defined as the ratio of the change in pipe diameter over the undeformed pipe diameter, as expressed in Eq. (4.6) (DNV 2007):

$$O_v = \frac{D_{\max} - D_{\min}}{D} \quad (4.6)$$

The limiting sectional ovalization, also known as the flattening factor, throughout the pipeline’s operational life is typically set at 3%, according to guidelines from DNV (2010) and CSA (2007). However, API (1999) suggests a higher limiting value ranging from 5.5–6.2%. Excessive sectional deformation, such as ovalization, can compromise the pipeline’s serviceability limit state, and therefore, it is crucial to analyze and control this aspect during design and operation.

Figure 4.12(a) illustrates the pipeline’s sectional ovalization as the operating temperature increases. At an operating temperature of 80°C, the section remains within the ovalization limit of 2.5% specified by DNV (2010). Considering the higher ovalization limit recommended by API (1999) guidelines (maximum 6%), the pipeline can still sustain temperatures of approximately 90°C without exceeding the ovalization threshold. Beyond this temperature level, the pipeline section undergoes significant distortion, including inward and outward wrinkling.

Figure 4.12(b) presents the sectional ovalization corresponding to the buckle amplitude. At an

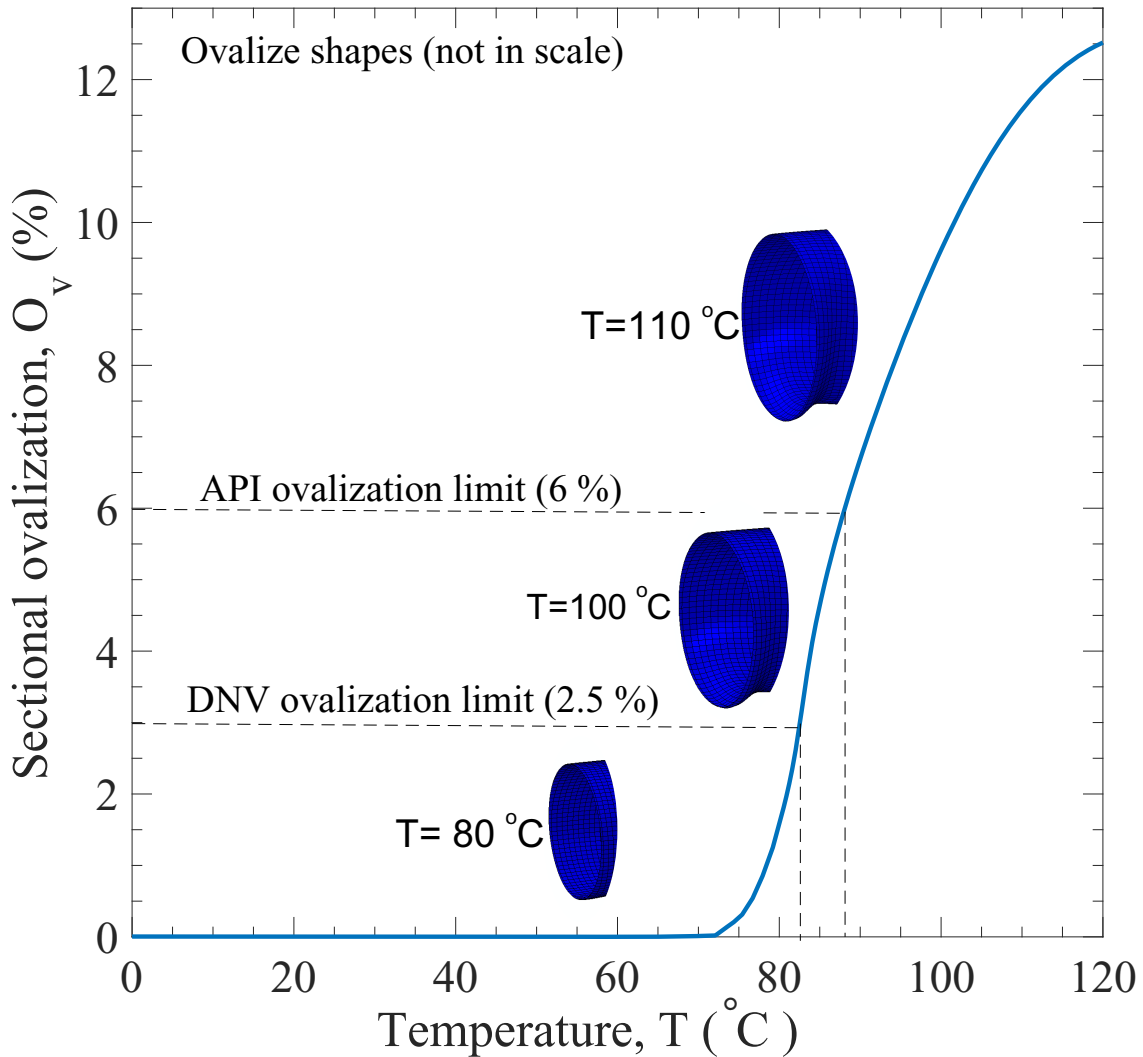


Figure 4.12: Sectional ovalization during buckling: (a) Ovalization with temperature increase

uplift displacement of 2.4 meters, the section is still within the ovalization limit of 2.5%, according to DNV (2010) . However, considering the maximum ovalization limit of 6% from API (1999) guidelines, the pipeline can tolerate an uplift displacement of approximately 2.9 meters. This study provides valuable insights into predicting the possible ovalization ranges under different operating temperatures and uplift displacements for a post-buckled pipeline. It aids in understanding the serviceability and safety limits of the pipeline to prevent excessive deformation

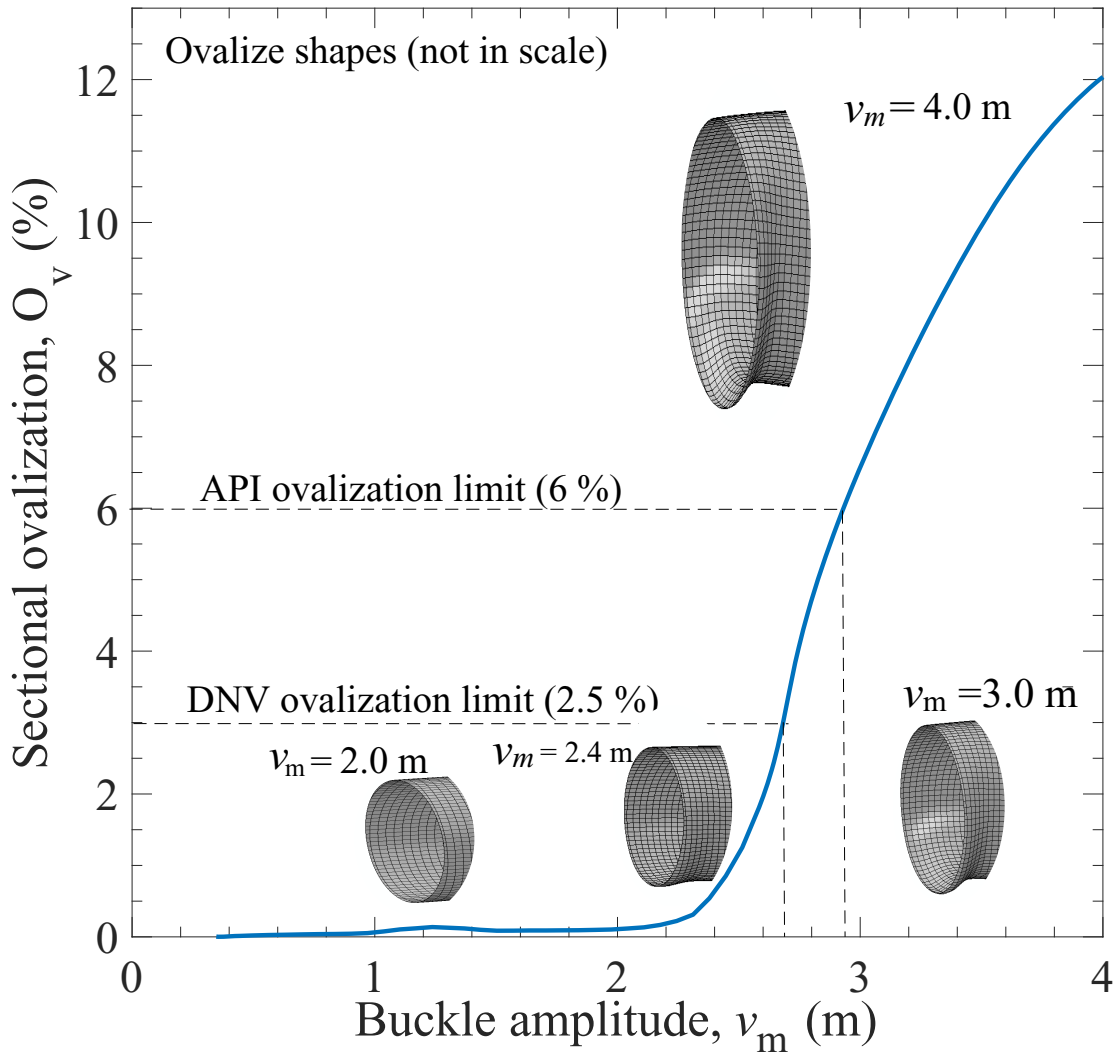


Figure 4.12: Sectional ovalization during buckling: (b) Ovalization with increase in buckle amplitude

and potential failure.

In Fig. 4.13, plastic strain development in the post-buckled pipeline is presented at the compression and tension sides during vertical movement. The main focus of this figure is to showcase the shape of the wrinkle's formation on the compression side of the post-buckled pipeline. At an uplift displacement of 2.0 meters (Fig. 4.13(a)), the maximum plastic strain of 0.04

is reached at the compression side. As the vertical displacement increases, the plastic strain in the compression side continues to rise, accompanied by the formation of wrinkles Fig. 4.13(b). As depicted in the Fig. 4.13(c), the noticeable wrinkles on the compression side bulge outward with the increase in uplift displacement (2.8 m). As the uplift displacement reaches a significant level of 3.5 meters, the wrinkle size increases and bends to the right side (Fig. 4.13(d)). At this stage, the plastic strain (ϵ_q^p) in the pipeline reaches a maximum value of 0.58. This behaviour is a result of the pipeline's effort to maintain its equilibrium state by undergoing wrinkling at the compression side. As the strain energy is released, excessive strain localization occurs, leading to

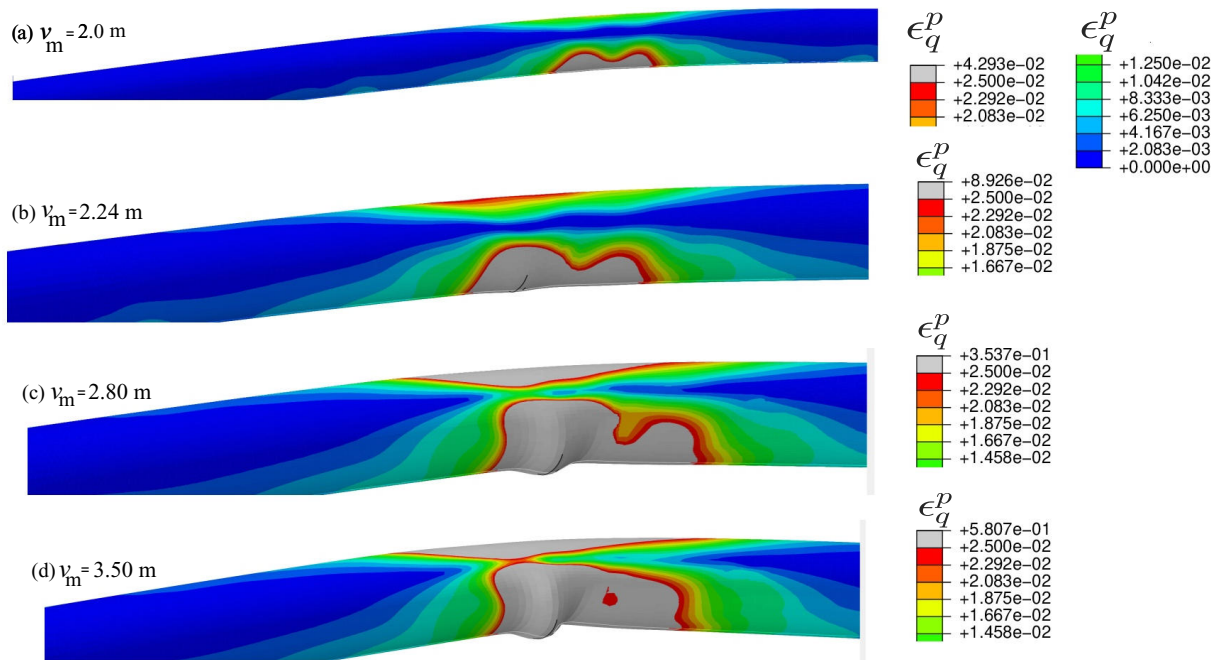


Figure 4.13: Development of wrinkles sizes with the increases in buckle amplitude

4.7.6 Moment-strain and curvature behaviour

Figure 4.14(a) shows the developed moment with equivalent plastic strain for the post-buckled conditions both in compression (invert) and tension (crown) sides. The pipeline can sustain an ultimate sectional moment of 510 kN-m before the onset of local buckling shown by circles. For

the pipeline the subjected to pure bending, the moment capacity can be calculated from (Bai and Bai 2005):

$$M_{cr} = \left(1.05 - \frac{0.0015D}{t} \right) .SMYS.D^2 t \quad (4.7)$$

In this case, no soil information is available. With the pipe of 0.3 m diameter, thickness of 12.7 mm and specified minimum yield stress (SMYS) of 448 MPa, M_{cr} is calculated as 519.5 kN-m. At a plastic strain of 0.03 (the pipe is in local buckling stage), the sectional moment reduces to

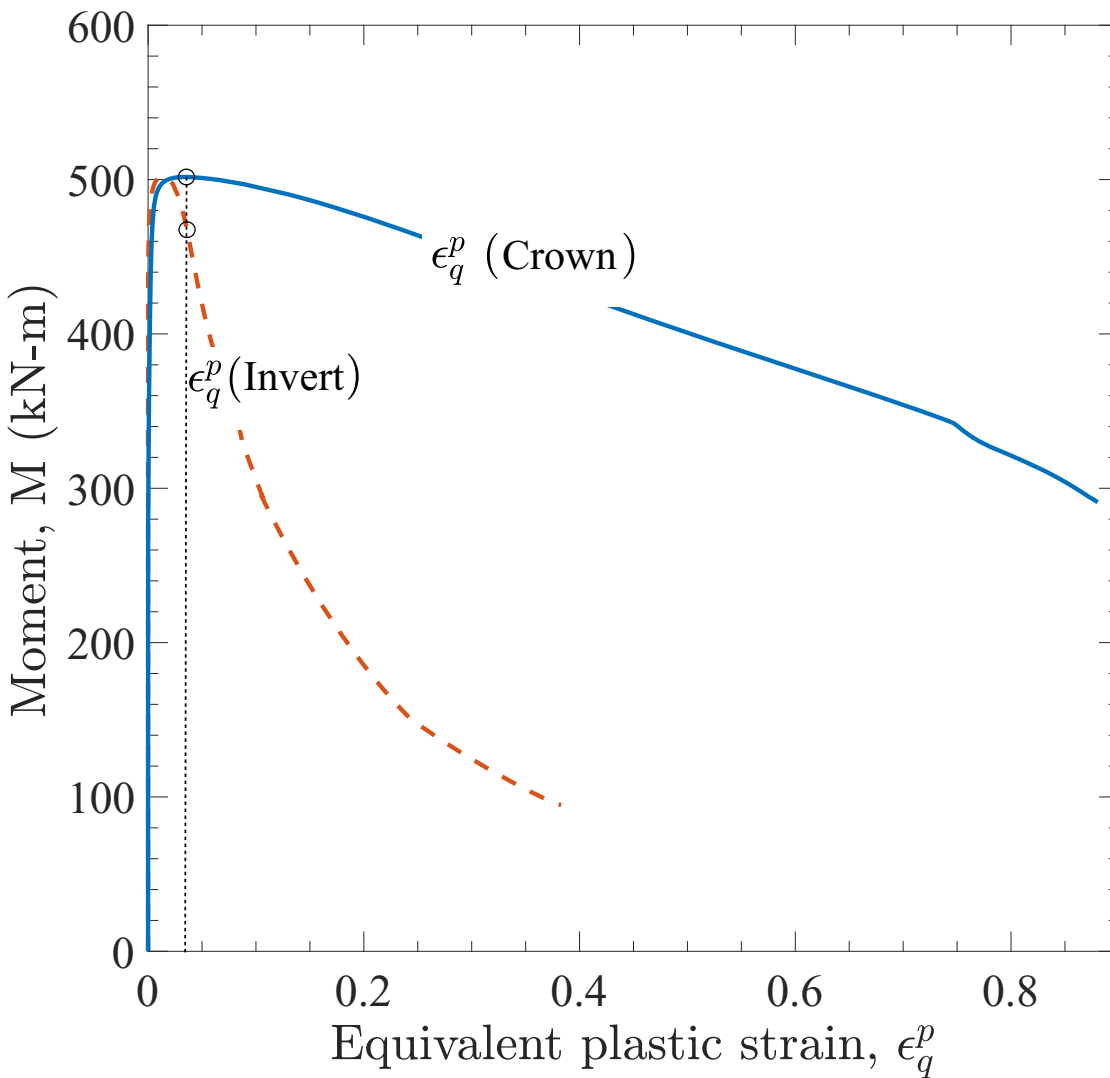


Figure 4.14: Moment with plastic strain: (a) Plastic strain variation at invert and crown

500 kN-m on the compression side and 470 kN-m on the tension side (open circles). Beyond the ultimate limit, the reduction in moment capacity occurs in the pipeline, leading to local buckling and wrinkling. This behaviour highlights the critical importance of the moment-plastic strain relationship in understanding the pipeline's post-buckling response and failure mechanisms.

In Fig. 4.14(b), the axial force distribution in the pipeline during the uplift movement is presented. At the critical section, the maximum resultant axial force reaches 1,560 kN and then starts to degrade. This degradation in axial force occurs after local buckling and the formation of wrinkles. At an uplift displacement of 2.21 m, the axial force is reduced to 170 kN, and the pipeline undergoes wrinkling and local deformation under the curvature. As the uplift displacement continues, the pipe section attempts to transfer stresses from the compression to the tension side to maintain equilibrium, leading to a slight increase in axial force.

Figure 4.15 presents the sectional bending moment-curvature relationship of the post-buckled pipeline. The bending moment increases beyond the linear limit and reaches the ultimate moment capacity of the pipe. After the ultimate moment, local buckling starts to occur. It is normalized to highlight the critical points such as peak moments, yield points or failure points, irrespective of the specific material and dimensionality. The pipeline will be in a plastic state at the ultimate moment level (M_{ult}). Therefore, the plastic bending moment capacity of the circular pipe is used for normalization, allowing for a better understanding of the pipeline's behaviour under bending conditions. The plastic bending moment of the pipe section used for normalization is defined by Eq. (4.8). (Limam et al. 2010):

$$M_o = \sigma_o D_o^2 t \quad (4.8)$$

where $D_o = D - t$, is the mean diameter of the pipe. For the elasto-plastic material behaviour $\sigma_o = \sigma_y$ is used. Also, the curvature is normalized with the curvature-like expression given by Eq. (4.9):

$$k_o = \frac{t}{D_o^2} \quad (4.9)$$

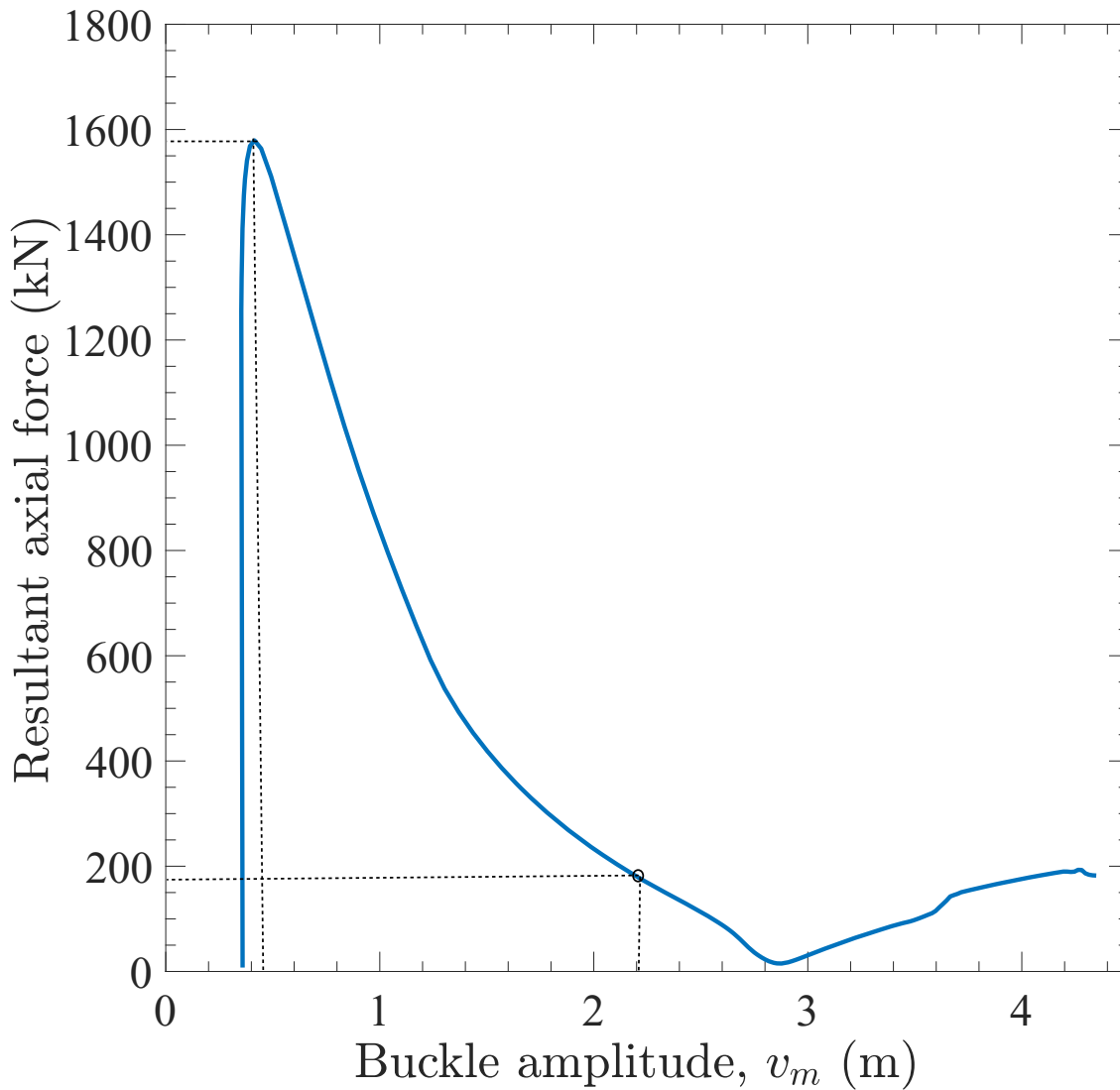


Figure 4.14: Axial force with buckle amplitude: (b) Axial force distribution

In the 3D pipe model, the significant changes in curvature in both the lateral (k_1) and vertical (k_2) directions are caused by local buckling with wrinkling. The sharp changes in curvature denoted by k_1 result in the formation of an excessive outer lobe in the lateral direction, indicating a significant outward bulging of the pipe's cross-section. On the other hand, the smooth curvature change denoted by k_2 shows a small segment of the section going inward due to local buckling, resulting in inward deformation of the pipe's cross-section.

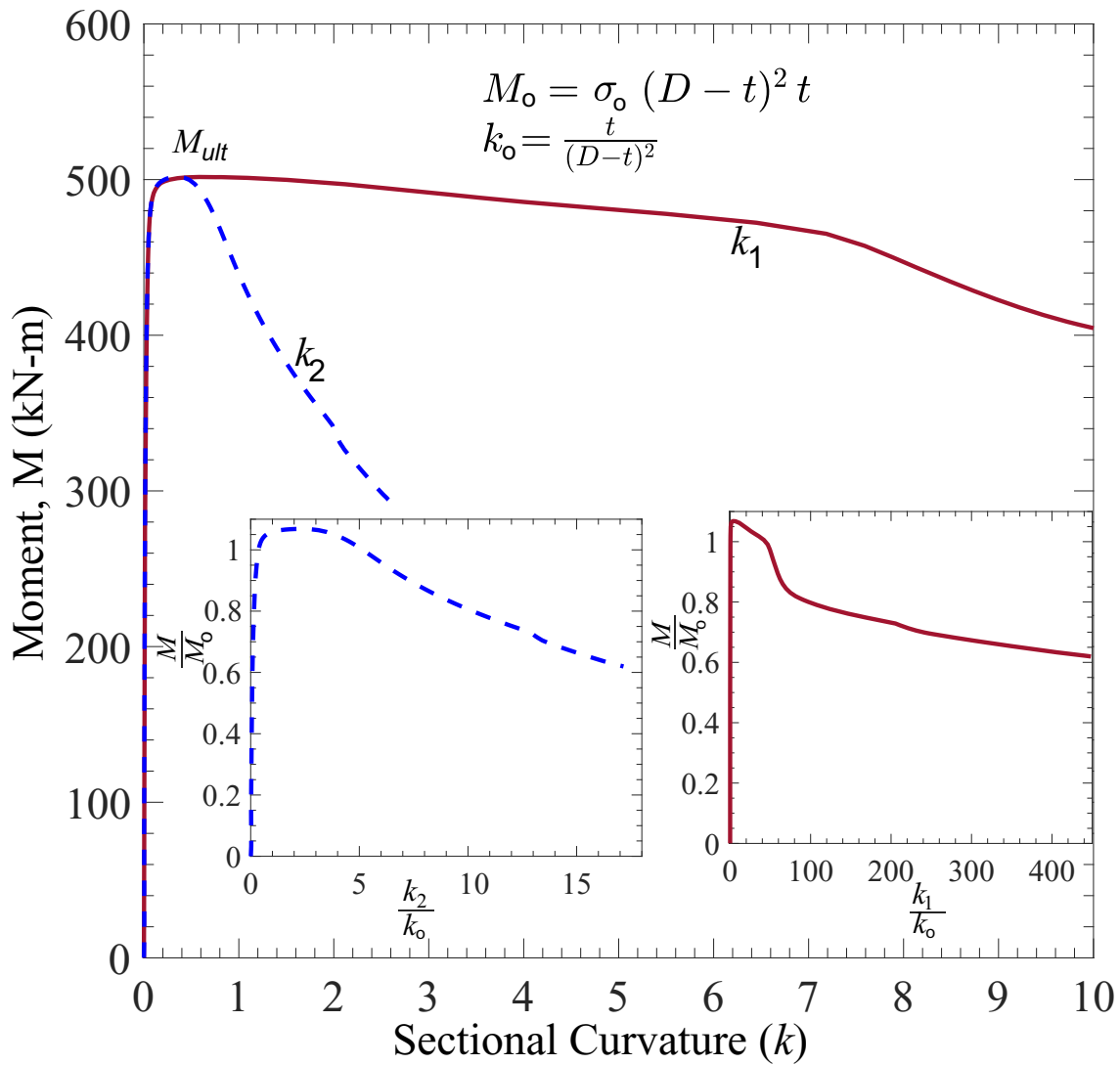


Figure 4.15: Moment–Curvature relation during buckling progression

4.7.7 Thin and thick pipe local buckling behaviour

In the previous section, we considered a pipeline with a 0.3 m outer diameter and a wall thickness of 12.7 mm, resulting in a D/t ratio 23.6. According to DNV (2010), a pipeline with a D/t ratio greater than 21 is considered a thin-wall pipeline, while a D/t ratio less than 21 is considered a thick-wall pipeline. This section examines the local buckling behaviour of the post-buckled

pipeline under thick, intermediate, and thin wall conditions.

Figure 4.16(a) shows the relationship between temperature and displacement for the three different pipe thickness. For the pipe with a wall thickness of 25.4 mm ($D/t = 11.81$), which is considered thick, buckling starts at a critical temperature of 50°C in a stable manner. On the other hand, for the pipe with a wall thickness of 6.35 mm ($D/t = 47$), which is considered overly thin, buckling starts at a critical temperature of 115°C in a snap-through manner. For the intermediate pipe with a thickness of 12.7 mm ($D/t = 23.62$), the critical buckling temperature is 74°C , and the buckling behaviour is also snap-through. The results indicate that the thickness of the pipe significantly affects the critical buckling temperature and the way buckling occurs. Thin-wall pipes are more susceptible to snap-through buckling at higher temperatures, while thick-wall pipes exhibit more stable buckling behaviour at lower temperatures. The intermediate wall thickness shows an intermediate behaviour between the thin and thick pipes.

Figure 4.16(b) shows the moment versus plastic strain development in the three different thicknesses of pipes. The results indicate that the moment capacity varies significantly among the three pipe thicknesses. At a plastic strain (ϵ_q^p) level of 0.03, the moment capacity of the thin-wall, intermediate and thick pipes are 175 kN-m, 500 kN-m, and 1025 kN-m, respectively. These results demonstrate that the thick pipe is much stronger in resisting the bending moment than the intermediate and thin-wall pipes. The higher moment capacity of the thick pipe makes it more capable of withstanding larger external forces and bending loads. On the other hand, the thin-wall pipe has the lowest moment capacity, making it more susceptible to buckling and failure under similar loading conditions.

Figure 4.17 shows the sectional ovalization behaviour of the pipe for thin, intermediate, and thick wall condition. The thin wall pipes start ovalization and wrinkling at an early stage of vertical displacement than the other pipes. The intermediate starts ovalization at 2 m and the thick pipe did not ovalizes even at the large displacement of 3.5 m. The thick pipe has higher bending stiffness resulting in stable buckle without local buckling and deformation.

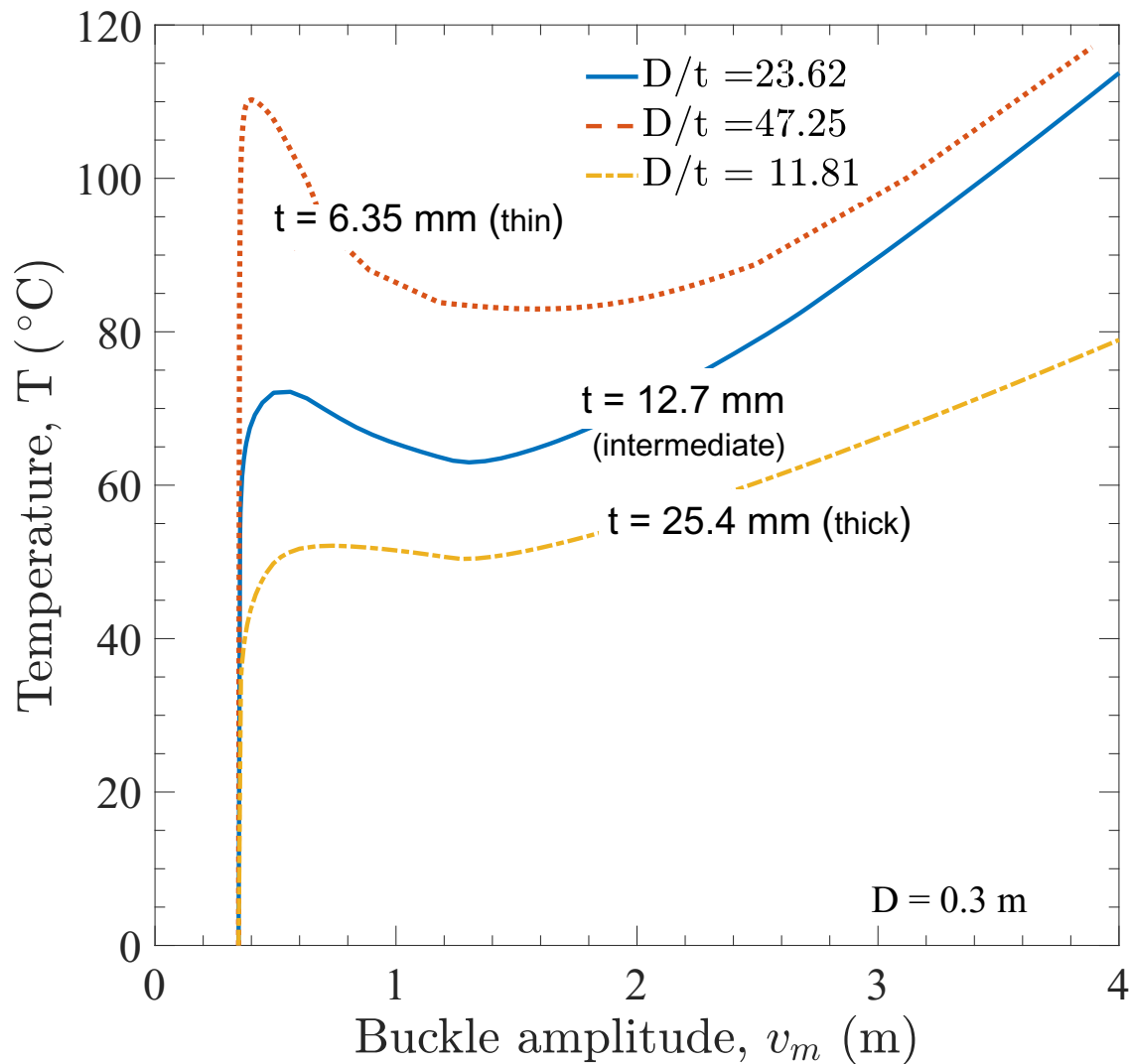


Figure 4.16: Thin and thick pipe buckling behaviour: (a) Effects of temperature

4.8 Parametric study

In the following sections, some key factors that can affect the upheaval buckling, leading to local buckling, and wrinkling are presented. The hybrid model (Fig. 4.1(b)), as described in Section 4.3 is used for all the analyses in this section. All the analyses are performed for a pipe of $D = 450$ mm, $t = 12.5$ mm buried at $3D$ in a medium sand having $\gamma' = 9.19$ kN/m³, $\phi' = 35^\circ$, $\phi_\mu = 0.8\phi'$ and

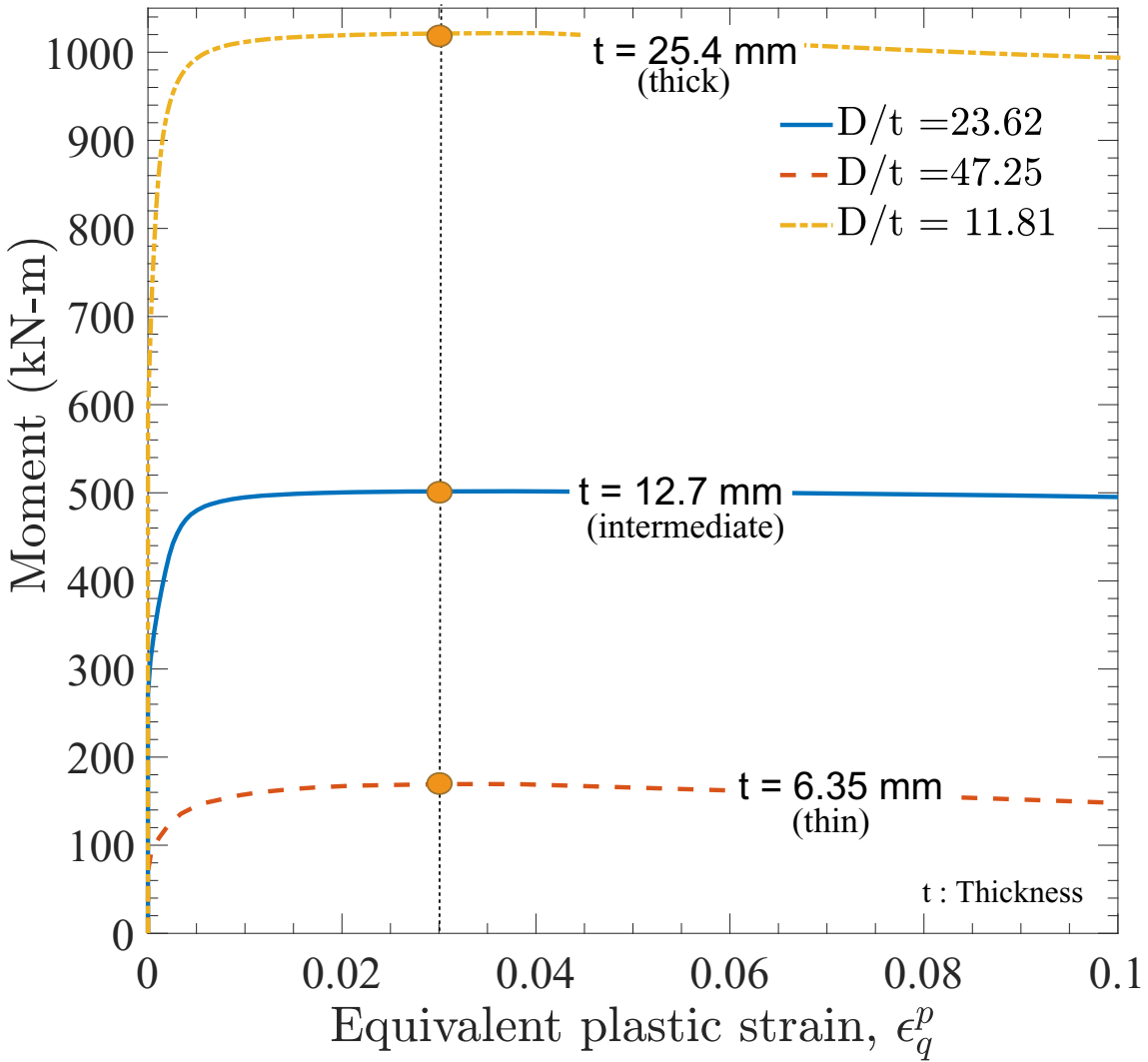


Figure 4.16: Thin and thick pipe buckling behaviour: (b) Plastic strain with moment

$K_0 = 0.5$. For these soil conditions and pipe dimensions, $F_{ap} = 6.9$ kN/m, $F_{lp} = 65.61$ kN/m and $F_{bp} = 227.48$ kN/m, and $F_{vp} = 15.63$ kN/m can be calculated using Eqs. (4.2)–(4.4) with $f = 0.6$, $\beta = 0.2$ and $\alpha = 0.75$. In this set of analyses, $u_{ap} = 3$ mm, $u_{lp} = 10.8$ mm, and $v_{bp} = 0.1D$ are used (ALA 2005). Other parameters are the same as before (Table 4.2).

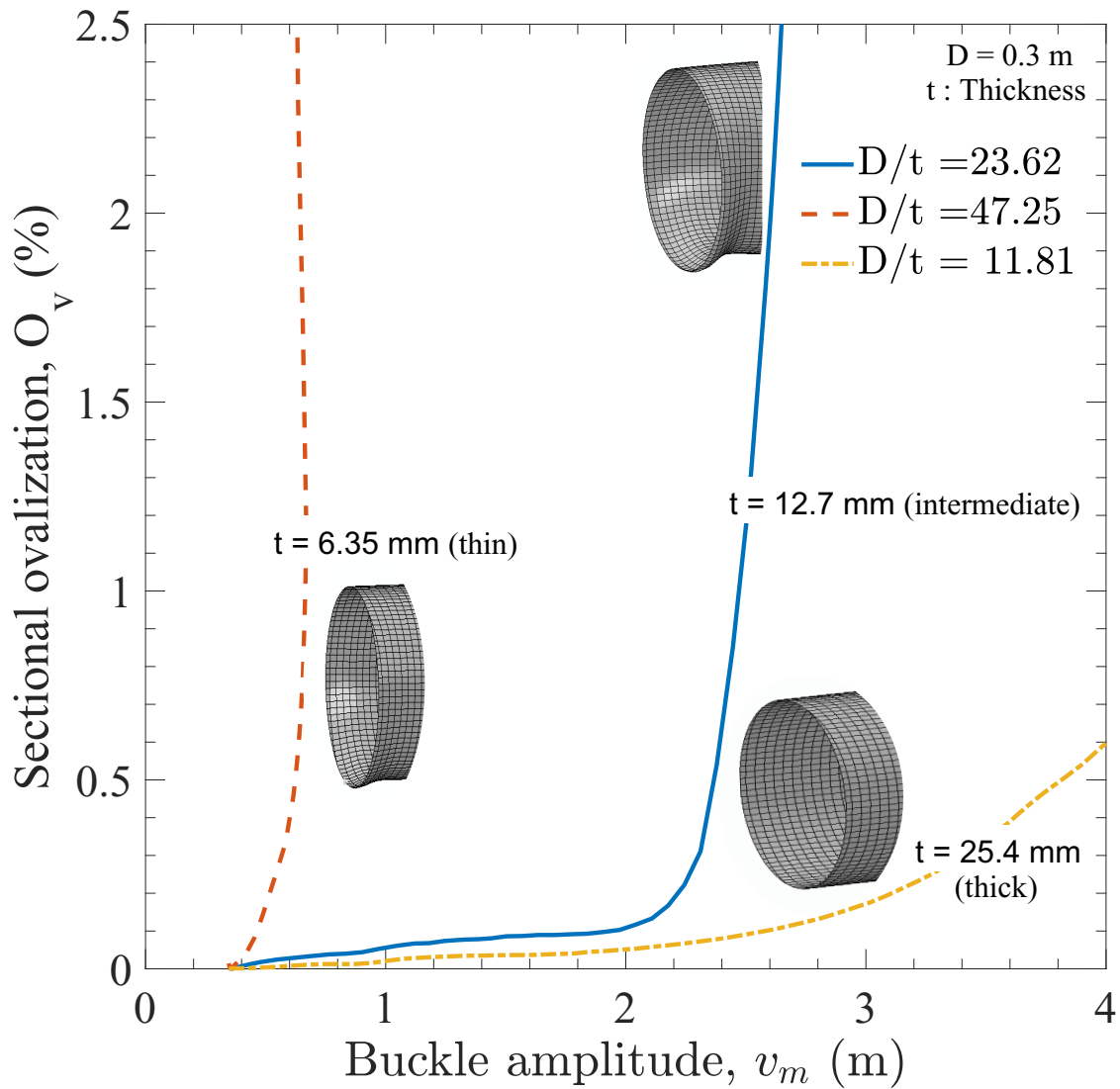


Figure 4.17: Ovalization behaviour of thin, thick, and intermediate pipe during buckling

4.8.1 Pipeline material model

In previous sections, an elastic-perfectly plastic material model is used for the pipe. As significant plastic strains generate in the critical sections, the strain-hardening behaviour of the pipeline might play a significant role. To investigate the effects of strain-hardening, analyses are also performed using the Ramberg–Osgood (R–O) model (see inset of Fig. Fig. 4.18(a)), and compared the

response with the results with the elastic-plastic (E–P) model. The ultimate tensile strength of 535 MPa and rupture strain (ϵ_r) of 20% is considered to generate the R–O model (Rice et al. 2003).

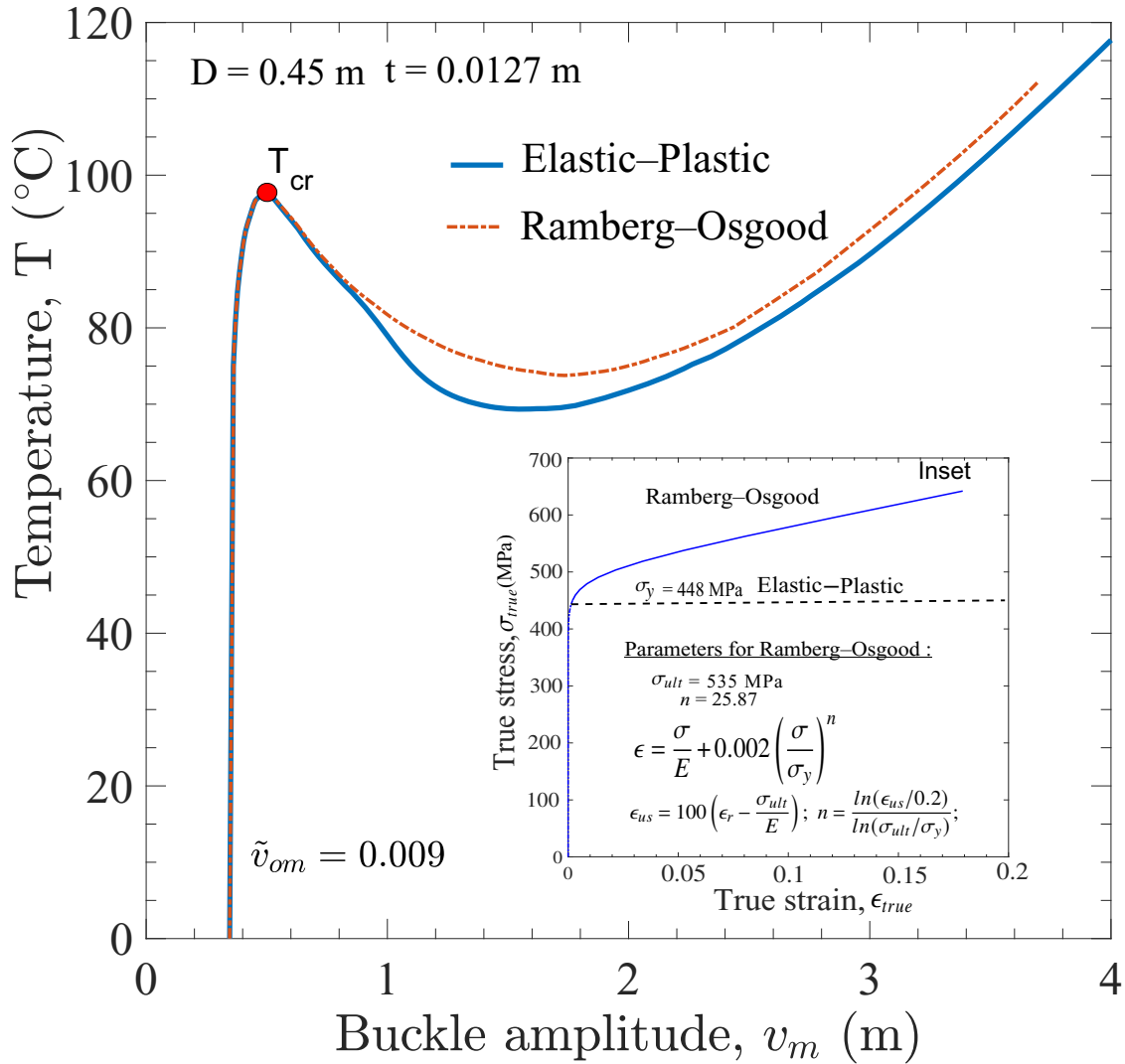


Figure 4.18: Effects of pipeline material models: (a) Buckling response with temperature increase

Figure 4.18(a) shows that both pipeline models give the same critical temperature. However, the safe temperature is $\approx 7^{\circ}\text{C}$ smaller in the elastic-plastic model (75°C vs 68°C). The sectional moment capacity of the pipeline with R–O model is significantly higher than that with E–P model (Fig. 4.18(b)). The distribution of equivalent plastic strain (ϵ_q^p) and associated local buckling in

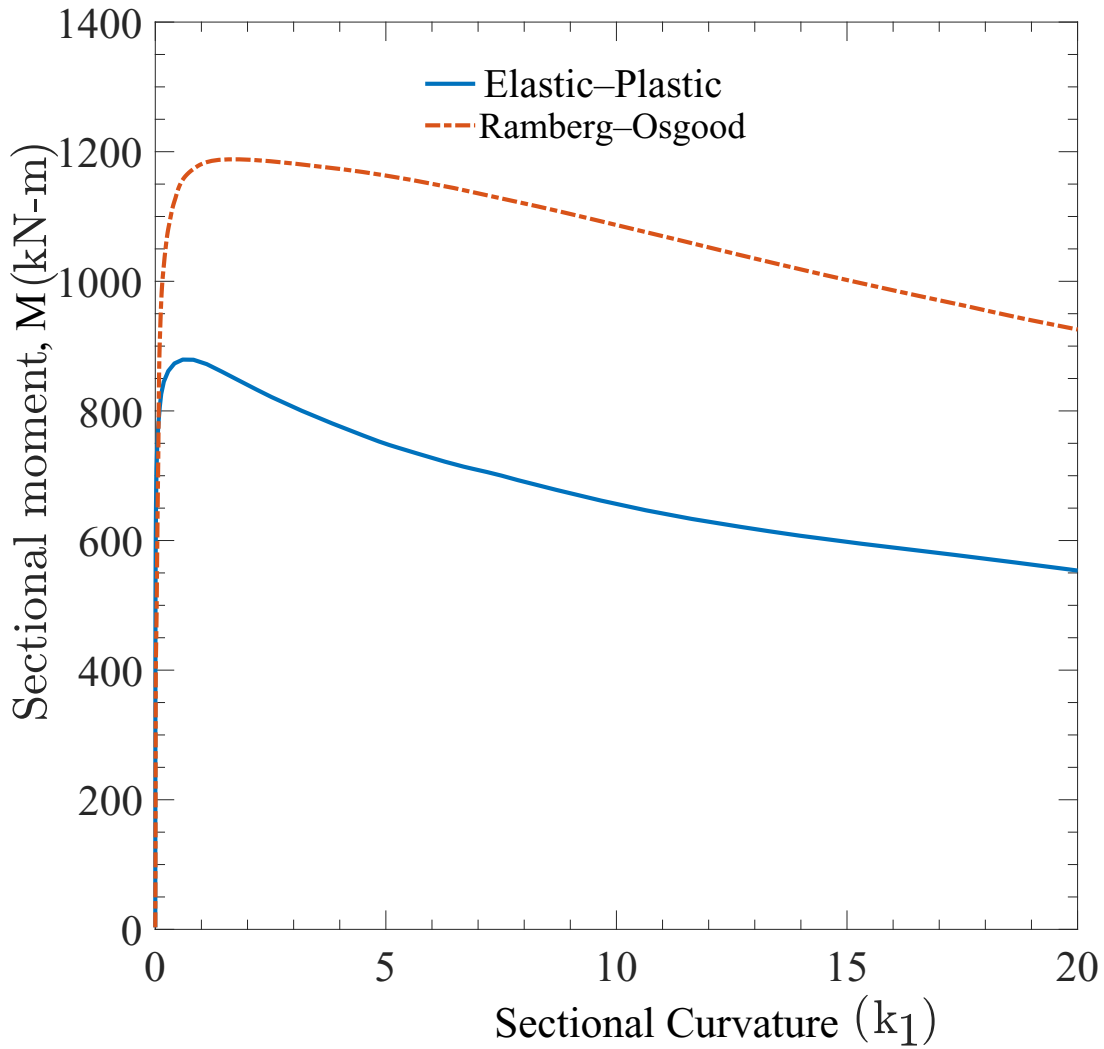


Figure 4.18: Effects of pipeline material models: (b) Moment–curvature behaviour

compression and tension side in the central 50 m segment is shown in Fig. 4.18(c) and Fig. 4.18(d), respectively, at $v_m = 3$ m and $T = 95^\circ\text{C}$. Inward local buckling occurred in both cases; however, a wider segment deformed inward when the elastic-plastic model is used (insets of Fig. 4.18(c)). The maximum plastic strain on the tension side (crown) is smaller ($\epsilon_q^p = 0.03$) (Fig. 4.18(d)) than that of the compression side (invert) (Fig. 4.18(c)). In the tension side, R–O model gives a larger plastic strain over a wider area than that with E–P model (inset of

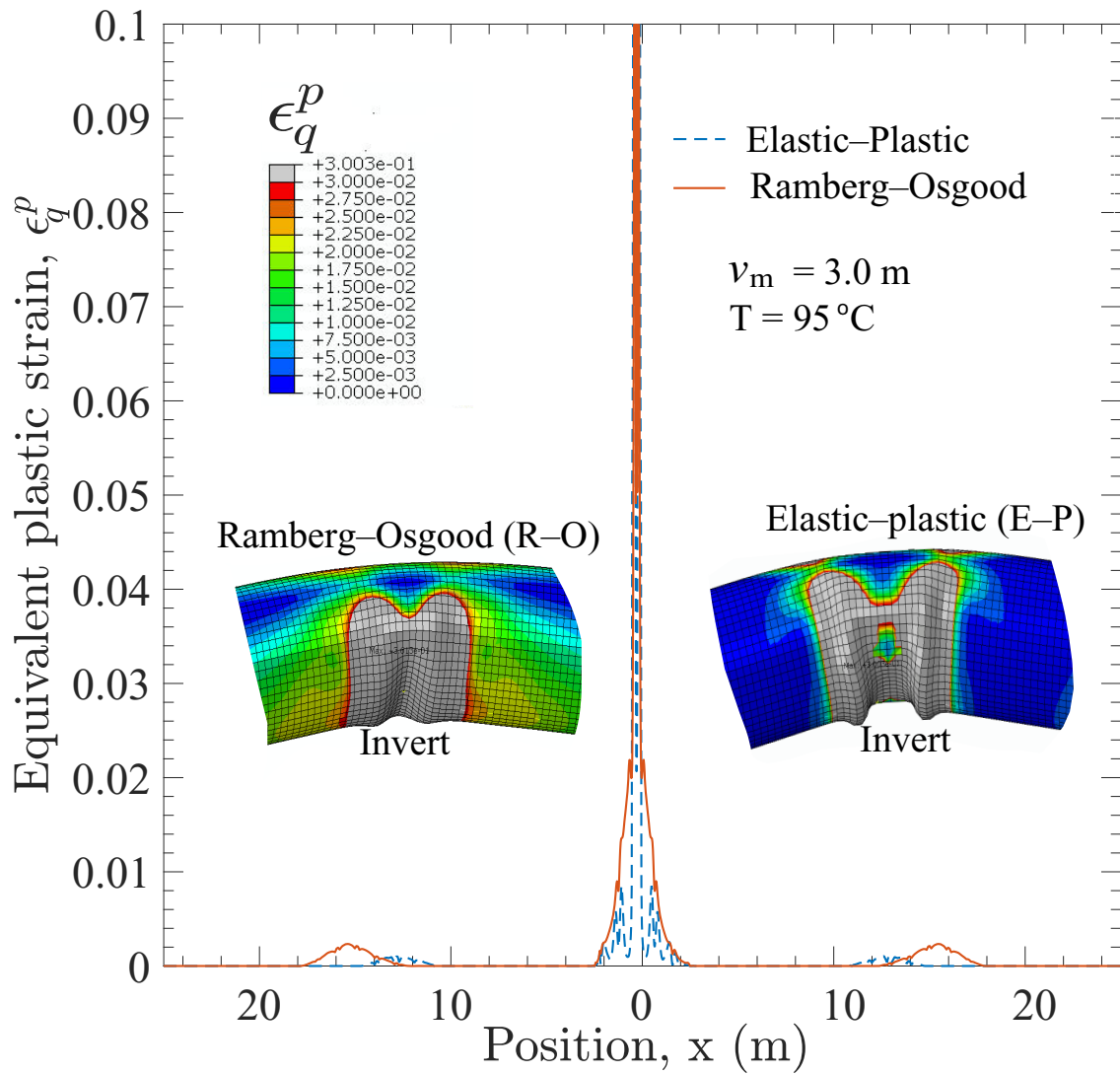


Figure 4.18: Effects of pipeline material models: (c) Plastic strain development at invert

Fig. 4.18(d)). At the tension side of the pipe, where the material is being stretched and elongated, the R-O model exhibits slightly higher plastic deformation compared to the E-P model. The strain-hardening behaviour enables the R-O model to accommodate more deformation in the plastic range, resulting in a higher strain at the tension side (Fig. 4.18(d)).

Figure 4.18(e) shows the moment-strain plots for both R-O and E-P models. The plastic strain at the onset of local buckling is ≈ 0.025 and ≈ 0.007 for the R-O and E-P models, respectively.

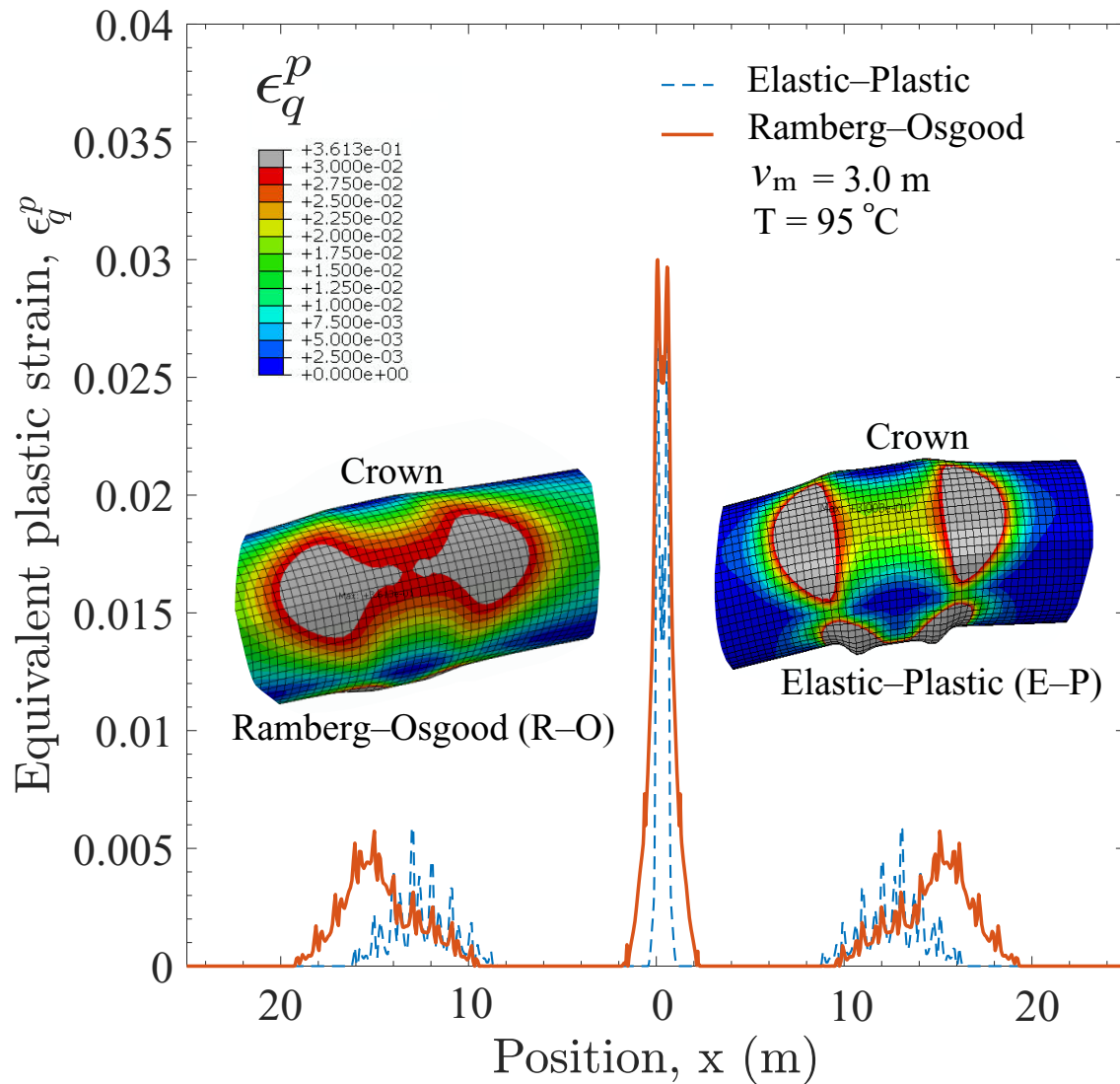


Figure 4.18: Effects of pipeline material models: (d) Plastic strain development at crown

Also, for ϵ_q^p of 0.03, the moment capacity is 1,160 kN-m and 700 kN-m for R-O and E-P models, respectively. Figure 4.18(f) shows the plastic strain development with pipeline displacement. Local buckling initiates at $v_m = 1.2$ m and $v_m = 2.6$ m with E-P and R-O model, respectively. However, the plastic strain increases rapidly after local buckling in R-O model while it gradually increases in E-P model. Figure 4.18(g) depicts the distribution of plastic strain along the longitudinal profile of both the E-P and R-O models when subjected to an uplift movement of 3

m at the operating temperature of 95°C and pressure of 5 MPa. At this level of uplift displacement, the E–P model displays the development of secondary local buckles at the sides. In contrast, the R–O model does not exhibit any secondary local buckles at the sides. The above results indicate that the elastic-plastic pipeline has a lower moment capacity and higher local buckling potential. In the following section, all the analyses are performed using E–P model.

4.8.2 Effect of initial imperfection

Figure 4.19(a) shows the temperature–buckle amplitude plot for three initial imperfections. The critical temperature is higher for the case with a small initial imperfection (\tilde{v}_{om}) of 0.005, displaying a high snap-through buckling behaviour. Conversely, the critical temperature is reduced for cases with larger initial imperfections (\tilde{v}_{om}) of 0.009 and 0.013, resulting in a closer to stable buckling response.

In Figure 4.19(b) the moment–curvature plot for the three different initial imperfections is shown. It is evident that the critical moment is higher for the case with a larger initial imperfection. Note that the analyses started from an initially stress-free imperfect pipeline. After the peak, the moment drops rapidly for the largest initial imperfection, compared to the other imperfections.

The moment-strain behaviour of the pipeline with three different initial imperfections is presented in Fig. 4.19(c). After the ultimate moment, it is observed that the moment capacity decreases with an increase in plastic strain. At the plastic strain of 3%, the sectional moment is higher for the case with a larger initial imperfection of 0.013, and lower for the case with a smaller initial imperfection of 0.005, as shown in Fig. 4.19(c). These findings highlight how the initial imperfection affects the post-buckling behaviour of the pipeline. With larger initial imperfections, the pipeline can sustain higher sectional moments at the same plastic strain level compared to pipes with smaller initial imperfections. This behaviour is because of imperfections on the structural response and the ability of the pipeline to accommodate larger plastic deformations before reaching failure.

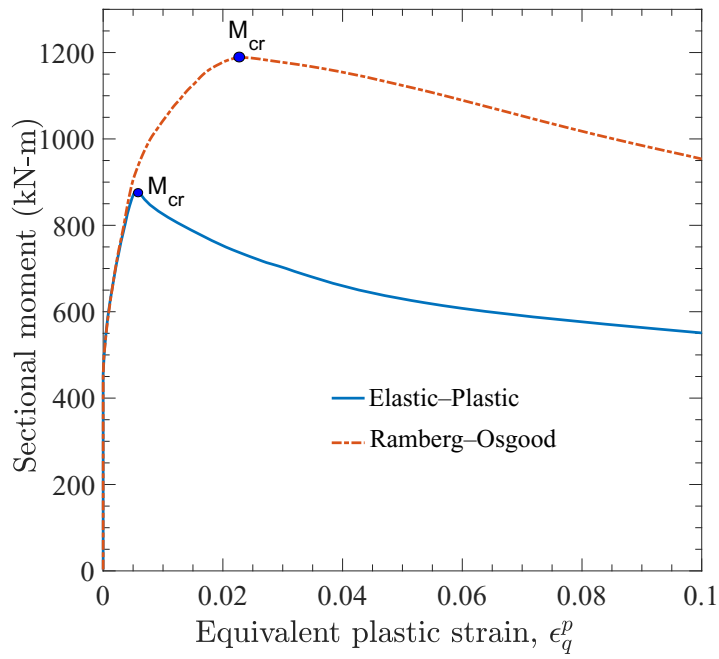


Figure 4.18: Effects of pipeline material models: (e) Plastic strain increment with sectional moment

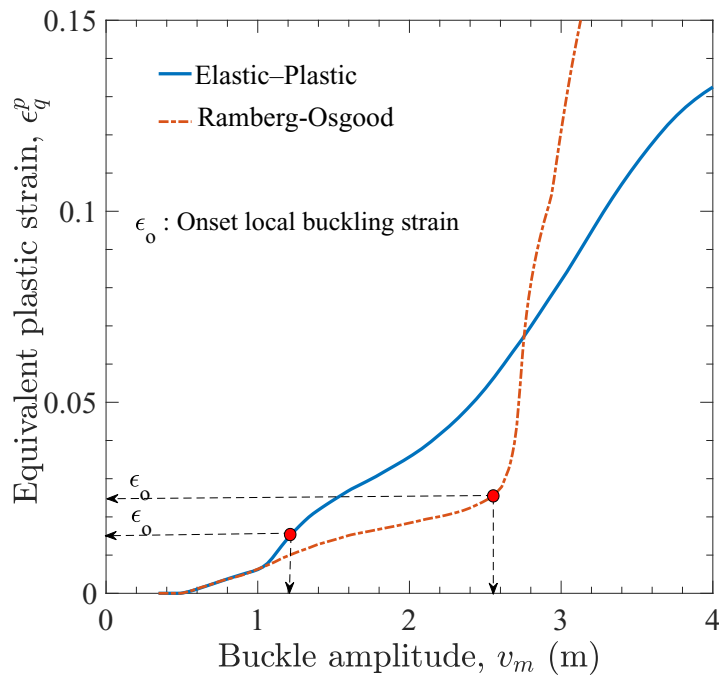


Figure 4.18: Effects of pipeline material models: (f) Plastic strain increment with buckle amplitude

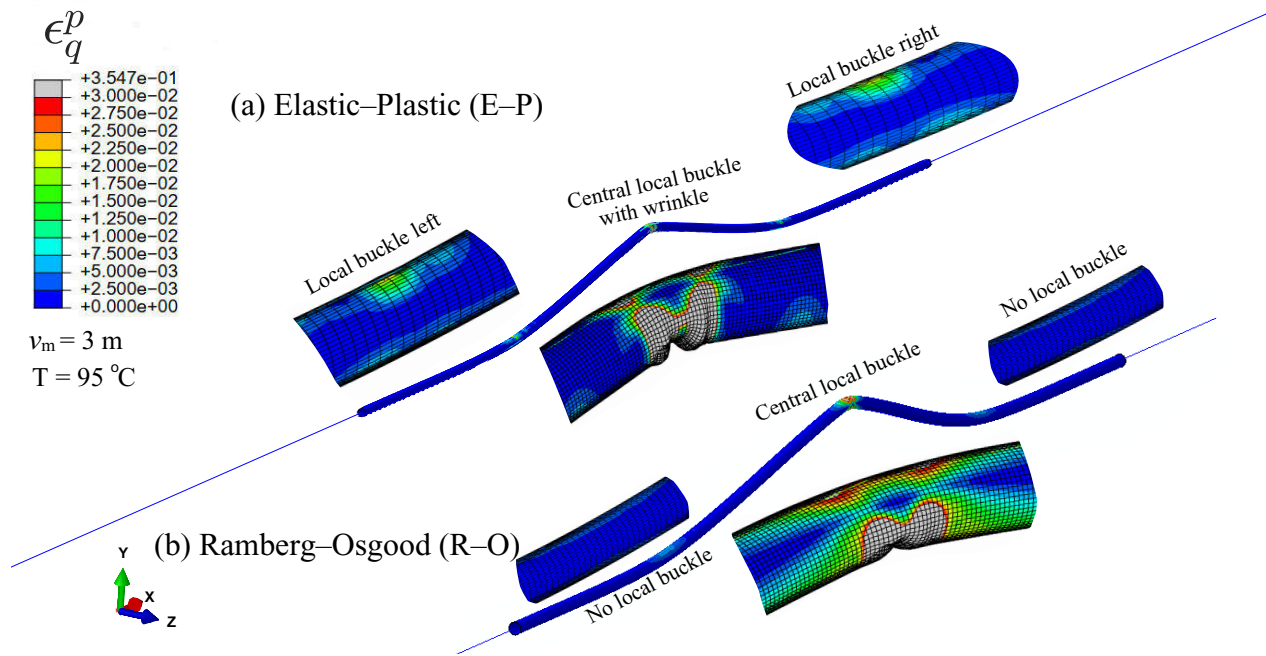


Figure 4.18: Effects of pipeline material models: (g) Plastic strain profile along the pipe length

Figure 4.19(d) shows the development of plastic strain during the upward movement of the pipeline. At lower ϵ_q^p (e.g., 2.5%), the buckle amplitude is more for the larger initial imperfection. However, no such trend is found at larger amplitude when significant plastic strains develop. Figure 4.19(e) presents the axial force–buckle amplitude for the three initial imperfections. The peak point (marked as a red circle) corresponds to the limit point for initiating global buckling, where local buckling will not yet form. Beyond this peak point, plastic deformation commences, and local buckling starts to initiate, forming wrinkles (as shown by the circle).

As the uplift displacement increases, the axial force decreases significantly, and severe wrinkling forms on the pipeline. Despite the reduced axial force, the pipeline still experiences the action of self-load and pressure components. However, as energy dissipates through the formation of wrinkles, the pipeline gradually regains its strength, and therefore the axial force increases slightly at large buckle amplitude (Fig. 4.19(e)).

In Fig. 4.19(f), the plastic strain development profile along the central imperfection zone of the pipeline is displayed for three initial imperfections (0.005, 0.009, and 0.013) at a selected

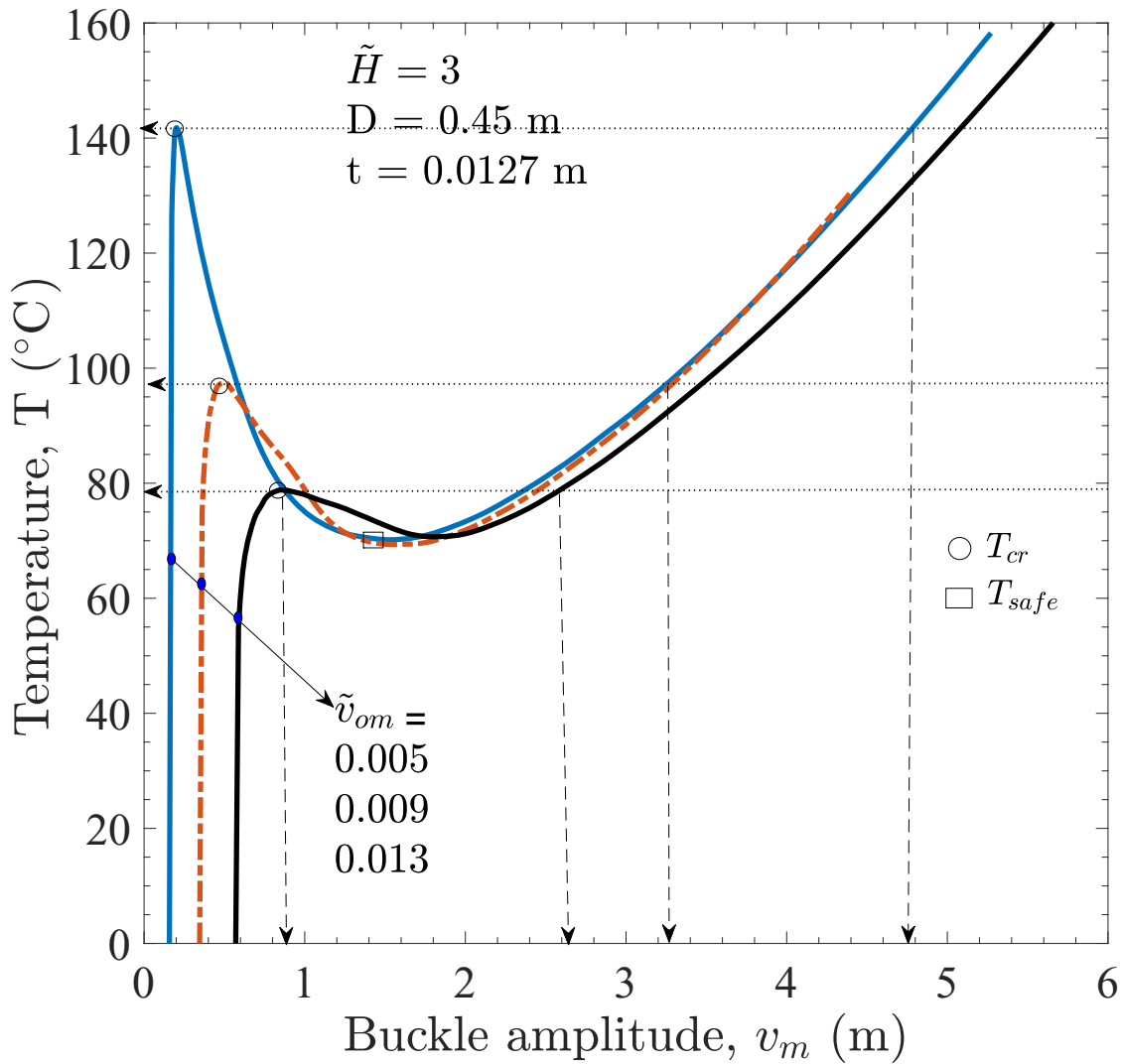


Figure 4.19: Effects of initial imperfection on local buckling: (a) Buckling response with temperature increase

temperature of 100°C. It is observed that the model with \tilde{v}_{om} 0.013 attains higher level of plastic strain than the other model with \tilde{v}_{om} of 0.009 and 0.005 at 100°C. The larger initial imperfection leads to more extensive plastic deformation along the central imperfection zone of the pipeline, as evident from the plastic strain profile. This behaviour aligns with the earlier observations, where larger initial imperfections result in higher deformations and influence the pipeline’s post-buckling

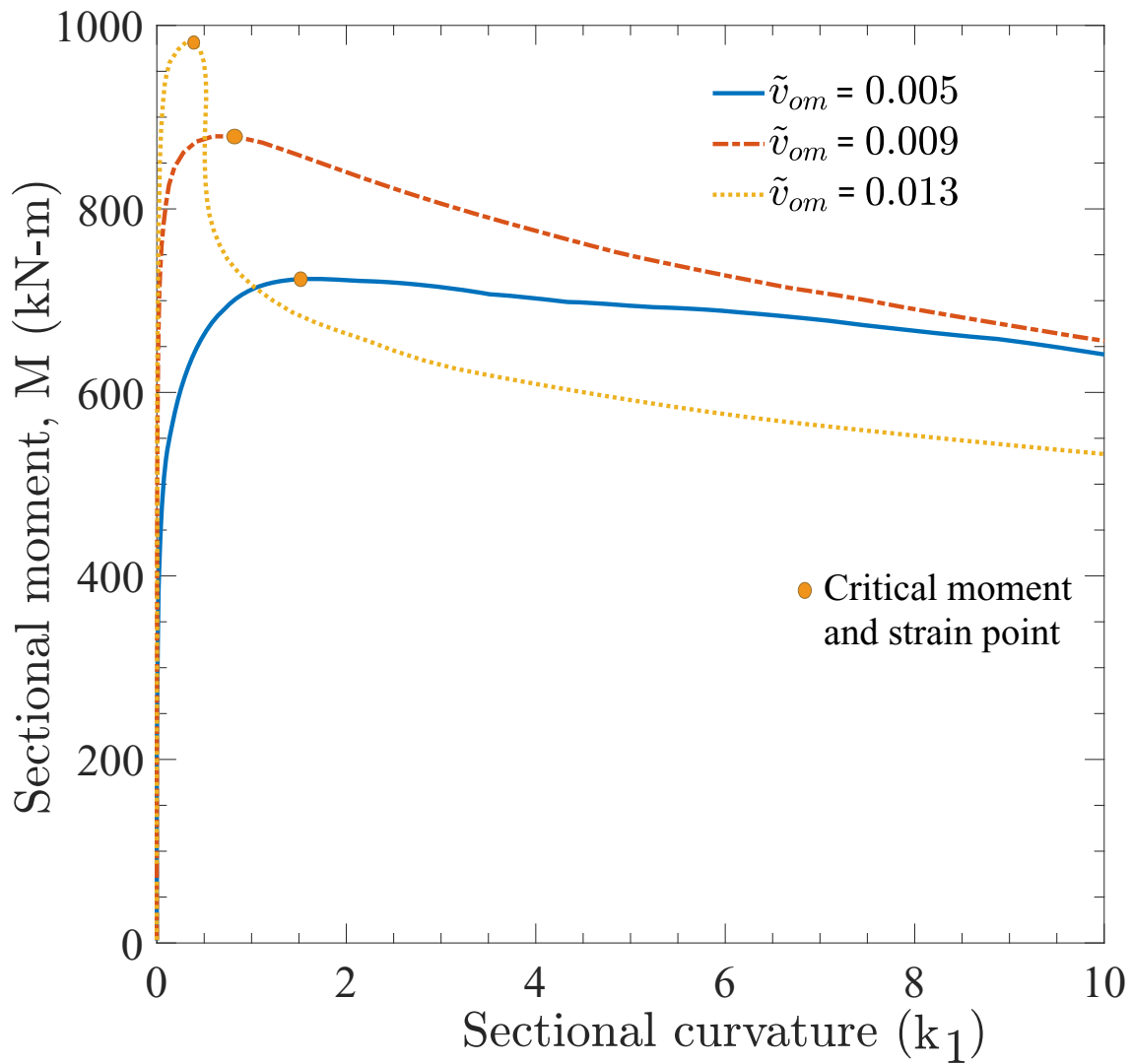


Figure 4.19: Effects of initial imperfection on local buckling: (b) Moment–Curvature response

behaviour significantly.

4.8.3 Effects of soil resistance models on local buckling

To examine the effects of post-peak uplift resistance degradation with the guidelines, the following three types of uplift resistance model (Ref. Section 4.4.1) are examined: (a) bi-linear

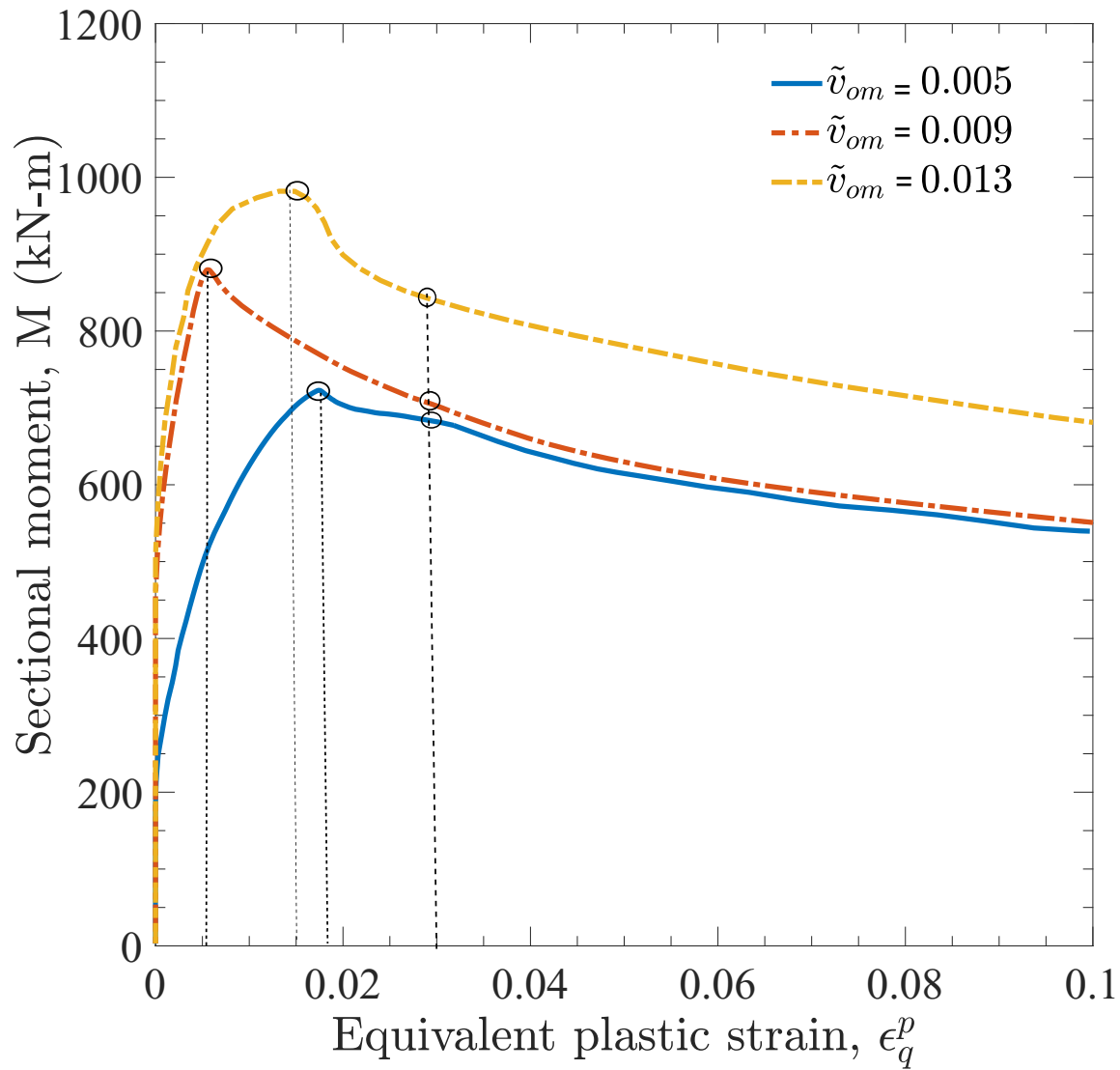


Figure 4.19: Effects of initial imperfection on local buckling: (c) Plastic strain increase with moment

ALA (2005), (b) tri-linear DNV (2007), and (c) linear degradation (LD) model . Figure 4.20(a) shows the temperature rise versus uplift displacement plot for the three soil models. The critical buckling temperature is determined to be 90°C, 95°C, and 102°C for ALA, LD, and DNV models, respectively. Beyond the critical temperature, the LD model exhibits a significant drop in

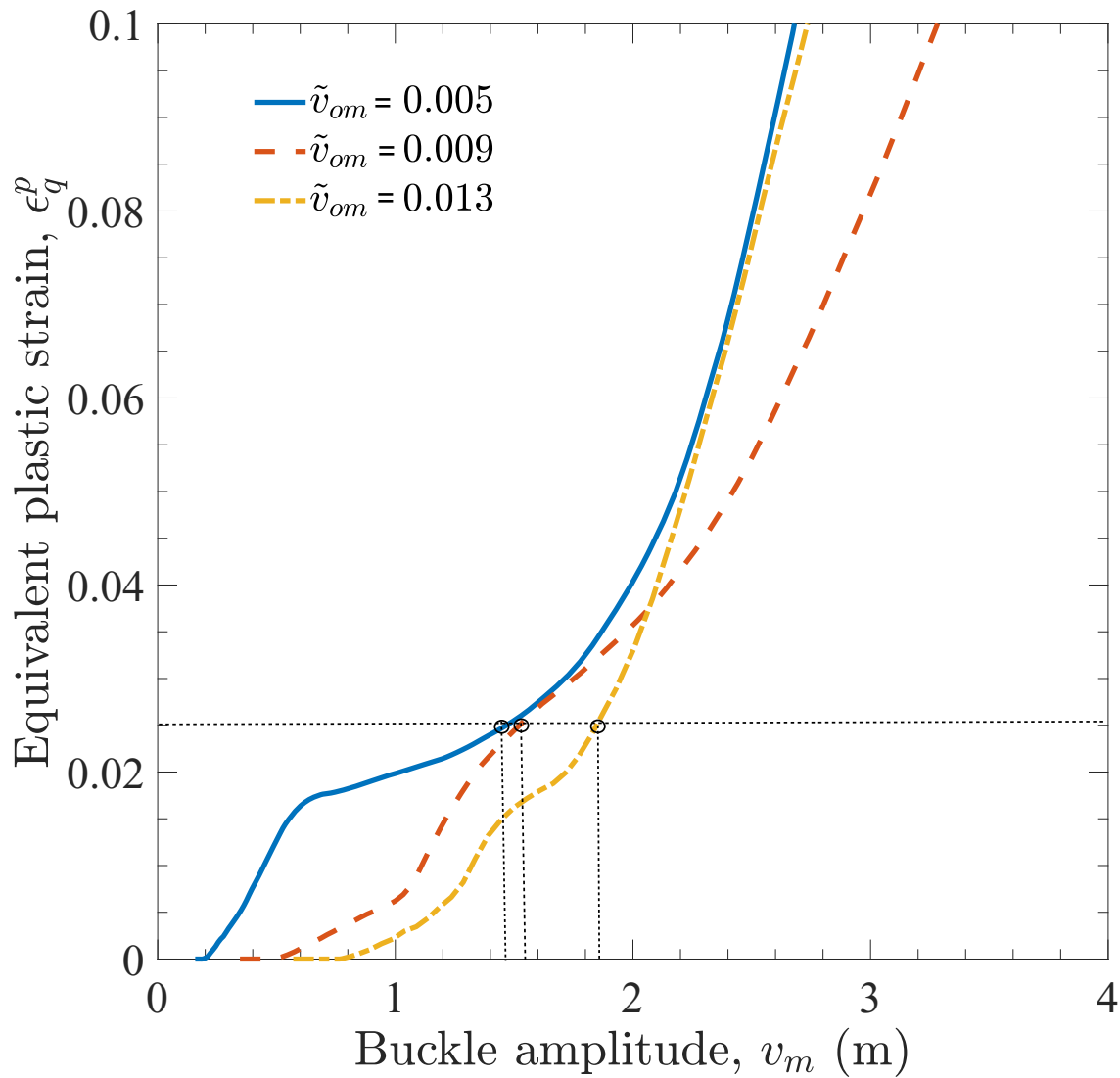


Figure 4.19: Effects of initial imperfection on local buckling: (d) Plastic strain development with buckle amplitude

temperature compared to the other two models (ALA and DNV).

Figure 4.20(b) shows the von Mises stress and local axial strain generation during the upward movement of the pipeline for the three different soil models. Three salient feature points are selected in the post-buckle profile: A (central region), B (left), and C (right). The stress and strain

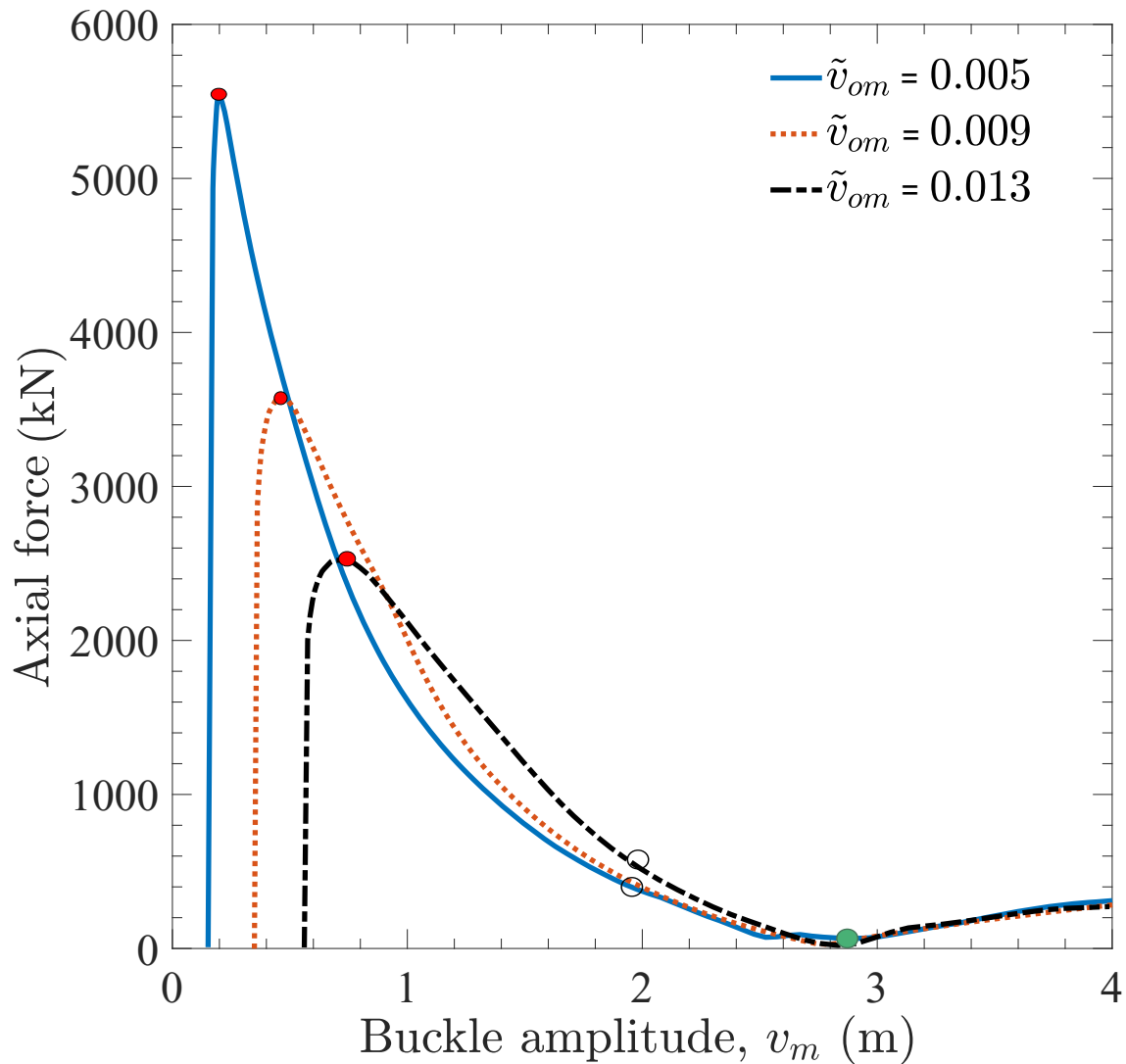


Figure 4.19: Effects of initial imperfection on local buckling: (e) Plastic strain development with buckle amplitude

contours observations reveal that the secondary local buckling distance B–C (Fig. 4.20(b)) for the linear degradation model in the present study is greater (28.3 m) compared to the ALA (20.3 m) and DNV (20 m) soil models. This secondary local buckling distance difference is attributed to reduced soil resistance as the pipeline moves up from its burial position in the linear degradation

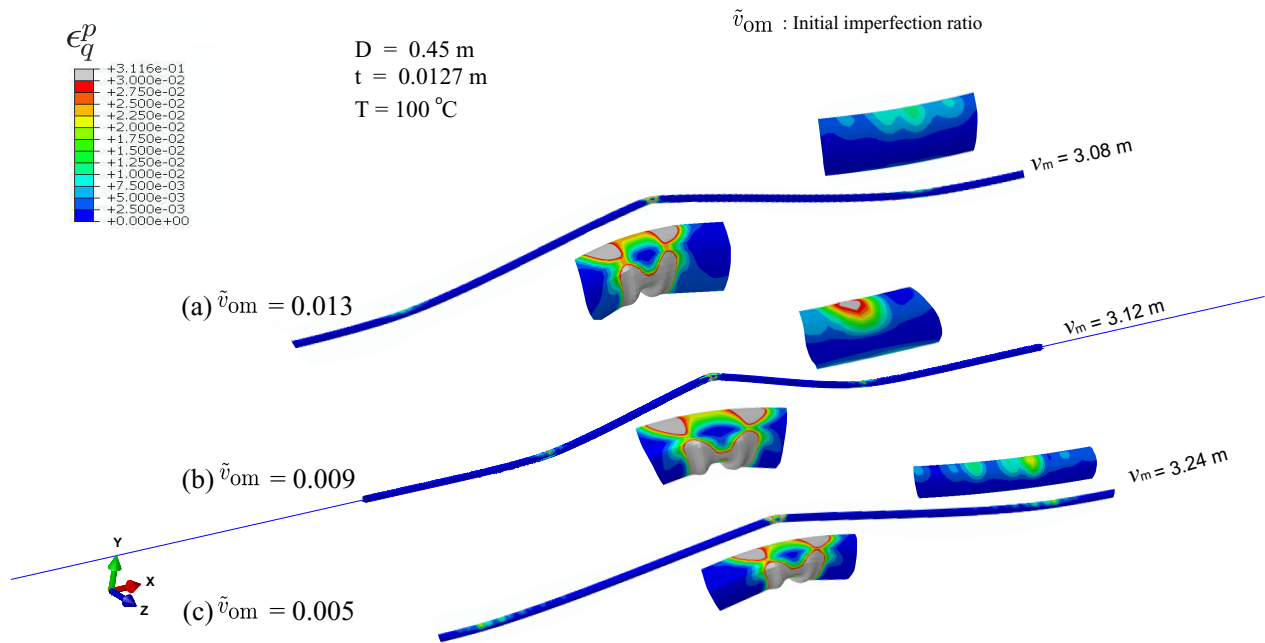


Figure 4.19: Effects of initial imperfection on local buckling: (f) Plastic strain development along the pipe length at operating temperature T of 100 °C

model used in the present study.

The moment–strain relationship in Fig. 4.20(c) reveals that the LD model exhibits a higher critical moment than the others. At the selected plastic strain level of 3%, the sectional moment measures 740 kN-m from the linear degradation model, 640 kN-m from the DNV model, and 550 kN-m from the ALA model. For this selected plastic strain of 3%, the buckle amplitude is approximately 2 m from the ALA model, 1.94 m from the linear degradation model, and 1.05 m from the DNV model. The pipeline initiates early local buckling with the ALA model, indicating that buckling occurs at a lower uplift displacement than the LD soil model. On the other hand, the local buckle starts later under the LD model, implying that the pipeline exhibits higher resistance to buckling and initiates buckling at a higher uplift displacement.

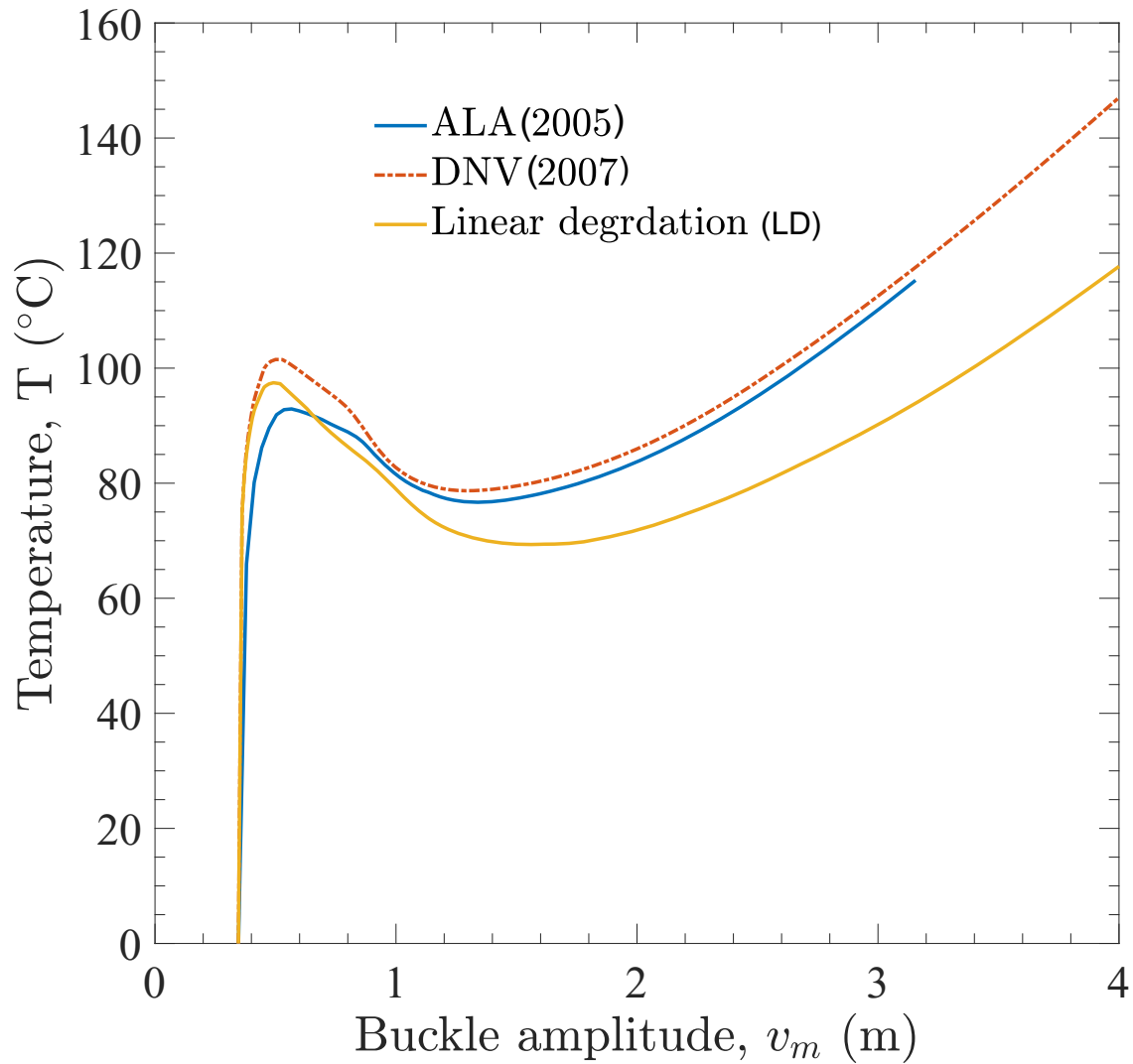


Figure 4.20: Effects of soil resistance models on local buckling: (a) Temperature–uplift movement

4.8.4 Effects of pipeline sectional parameter (D/t) on local buckling

This section shows a numerical result for varying D/t ratios for two different initial imperfection ratios, \bar{v}_{om} of 0.009 and 0.013 at 3D embedment depth. Here D/t is varied by changing the diameter ($D = 0.15$ m, 0.3 m, 0.45 m, 0.65 m, and 0.9 m), keeping pipe wall thickness constant ($t = 12.7$ mm). Figure 4.21(a) presents the temperature–displacement variation for varying pipe

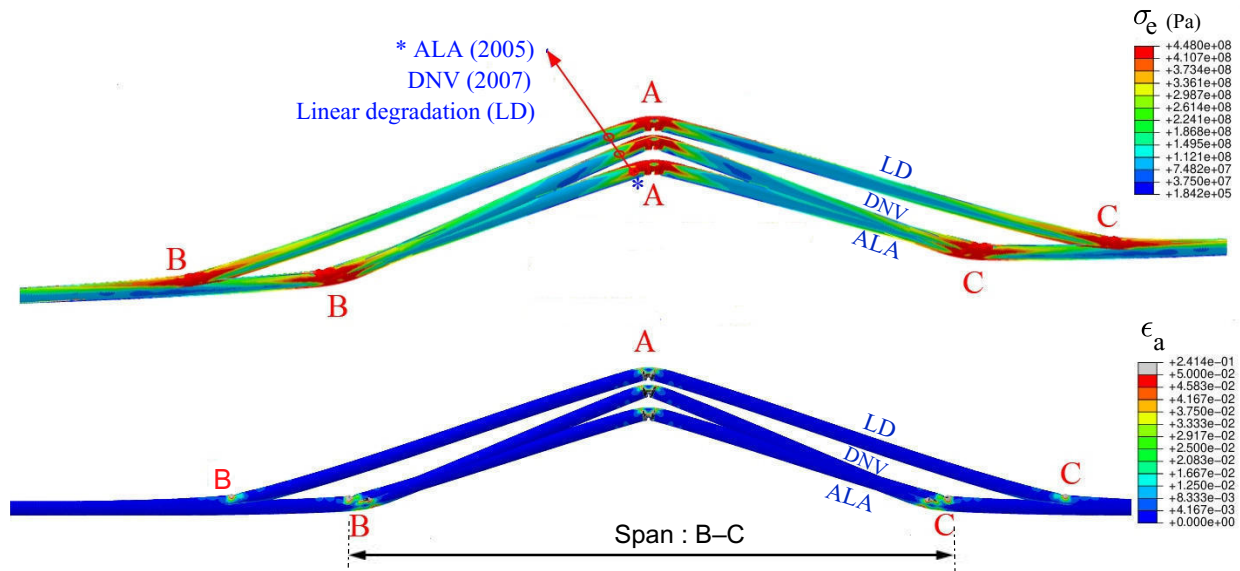


Figure 4.20: Effects of soil resistance models on local buckling: (b) von Mises and axial strain distribution along the pipe

diameters for two initial imperfections \tilde{v}_{om} of 0.009 and 0.013). The response differs significantly depending on pipe diameter (D) and initial imperfection ratio (\tilde{v}_{om}).

Figure 4.21(b) shows the calculated critical temperature (T_{cr}) for varying D/t ratios. Buckling occurs at lower temperatures for small D/t cases, indicating that these sections are more susceptible to buckling at lower operating conditions. On the other hand, as the D/t increases, the critical buckling temperature also increases, suggesting that larger pipe sections can withstand higher temperatures before experiencing local buckling. Additionally, the critical buckling temperature reduces with an increase in initial imperfection.

Figure 4.21(c) shows the variation of equivalent plastic strain with buckle amplitude for different pipe sections. The pipe section with a diameter of 0.15 m and a D/t ratio of 11.82 (thick pipe) buckles at a large vertical displacement of 3.5 m, but the equivalent plastic strain remains below 2%. This suggests that there is no local buckling occurring in this case. As the pipe diameter increases to 0.3 m with a D/t ratio of 23 (thin pipe), buckling occurs at more than 2.5 m, and the plastic strain reaches 3%. Here, the pipeline experiences local buckling and wrinkling due to the

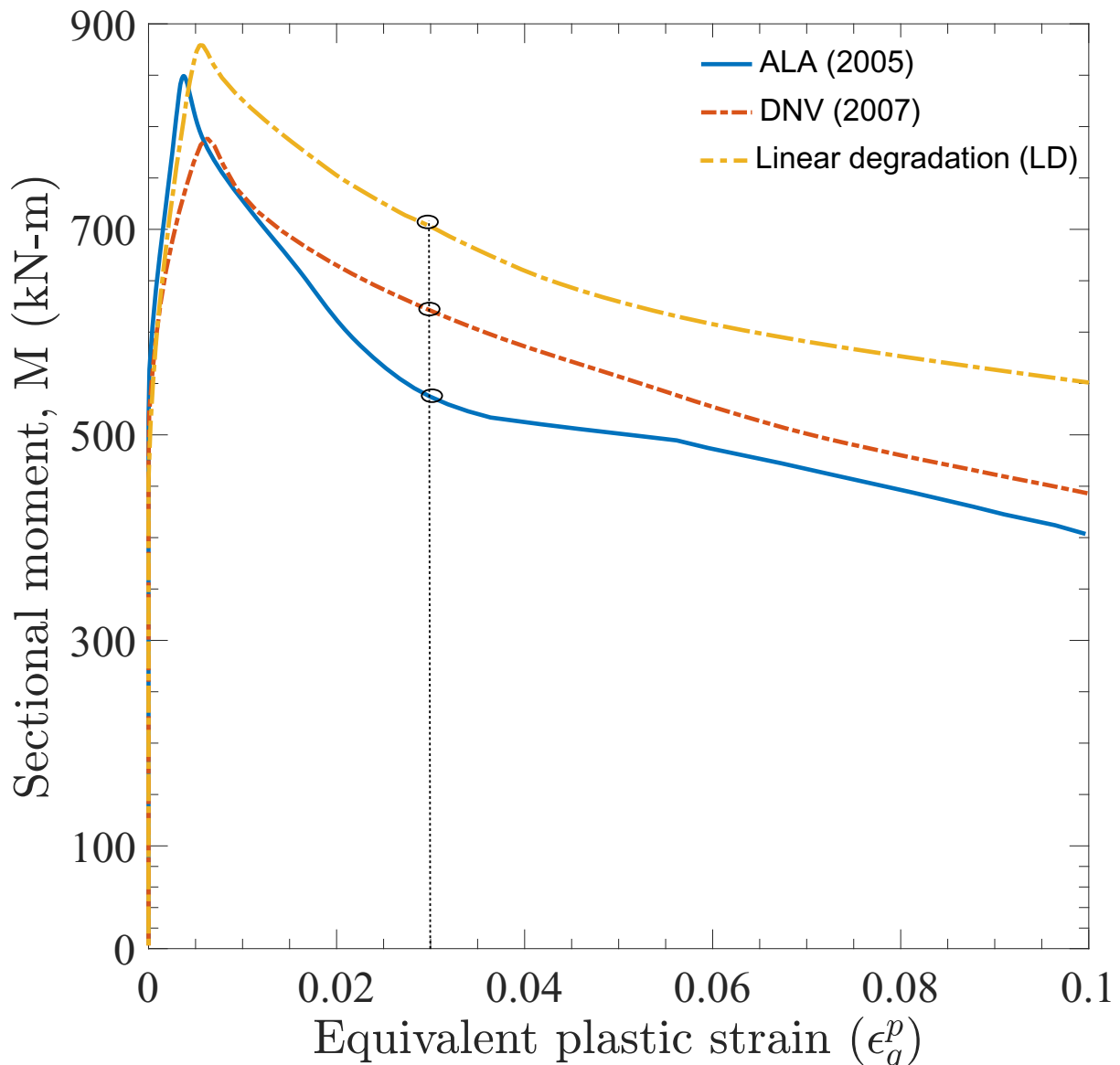


Figure 4.20: Effects of soil resistance models on local buckling: (c) Plastic strain increment with moments

thinner wall thickness relative to the diameter. Finally, as the pipe diameter increases from 0.45–0.65 m with D/t ratios of 35.43 and 51.18, the plastic strain develops at very small uplift displacements compared to the smaller pipe sections. At the same time, the critical temperature for buckling is higher for larger-diameter pipes.

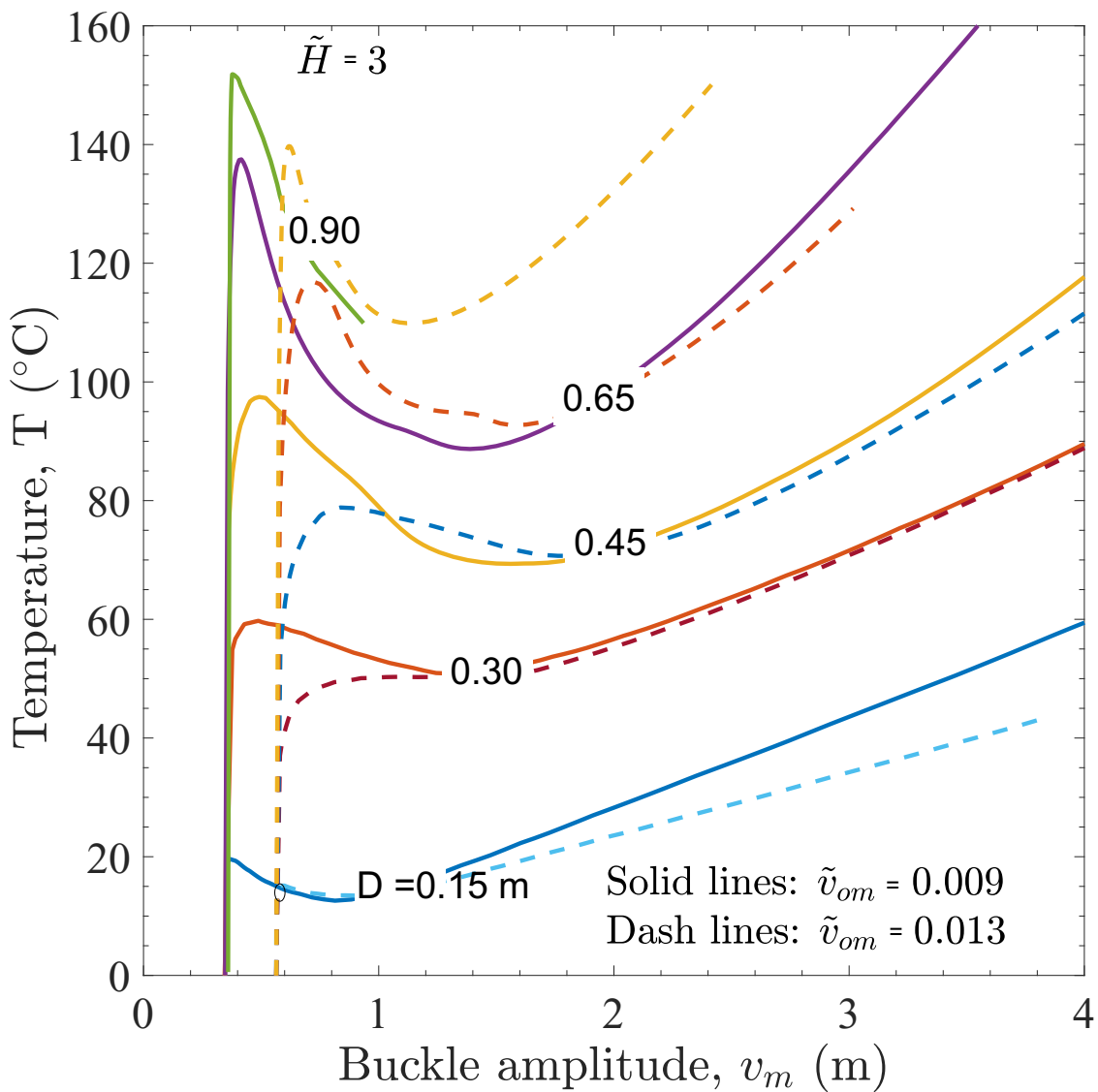


Figure 4.21: Effects of D/t on local buckling: (a) Uplift displacement response with temperature increase

Figure 4.22(a) shows the local buckling profile for an initial imperfection ratio of 0.009, showing the development of equivalent plastic strain (PEEQ) in the pipeline at an uplift displacement of 2.0 m. The observations reveal distinct behaviours based on the pipe section size and the D/t ratio. For the large pipeline section with a higher D/t ratio, significant local buckling and wrinkling occur at

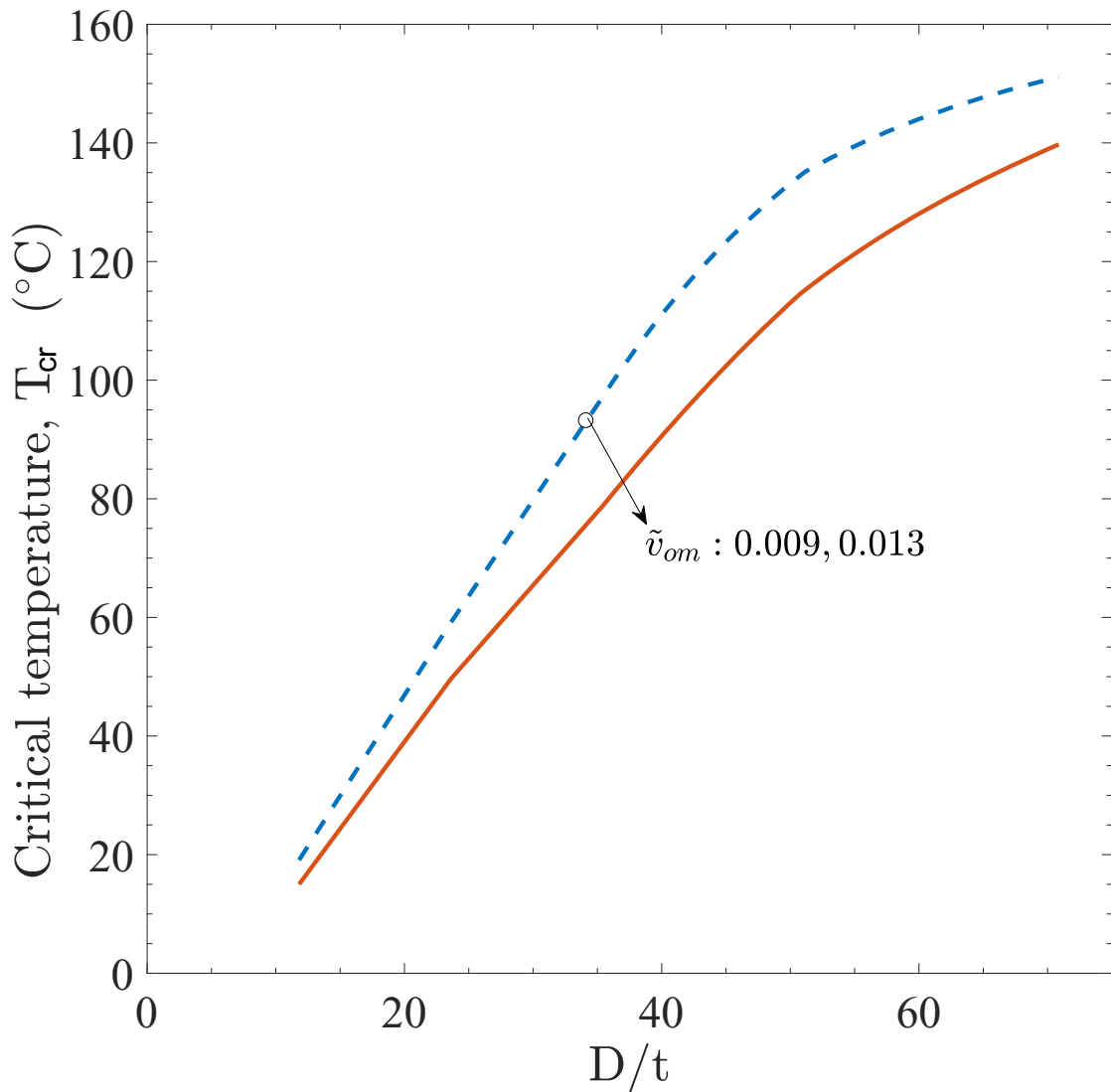


Figure 4.21: Effects of D/t on local buckling: (b) Critical temperature trend with variable D/T

a relatively lower uplift displacement. The thinner-walled pipe sections with larger diameters experience higher deformations due to the higher stress concentrations resulting from their geometry. As the initial imperfection size increases, strain localization also increases, leading to more significant deformations and localized buckling. This effect is especially evident in the size of the wrinkles formed on the pipeline's surface. Additionally, it is intriguing that the number of wrinkles with an outer lobe increases as the initial imperfection size increases from 0.009 to 0.013

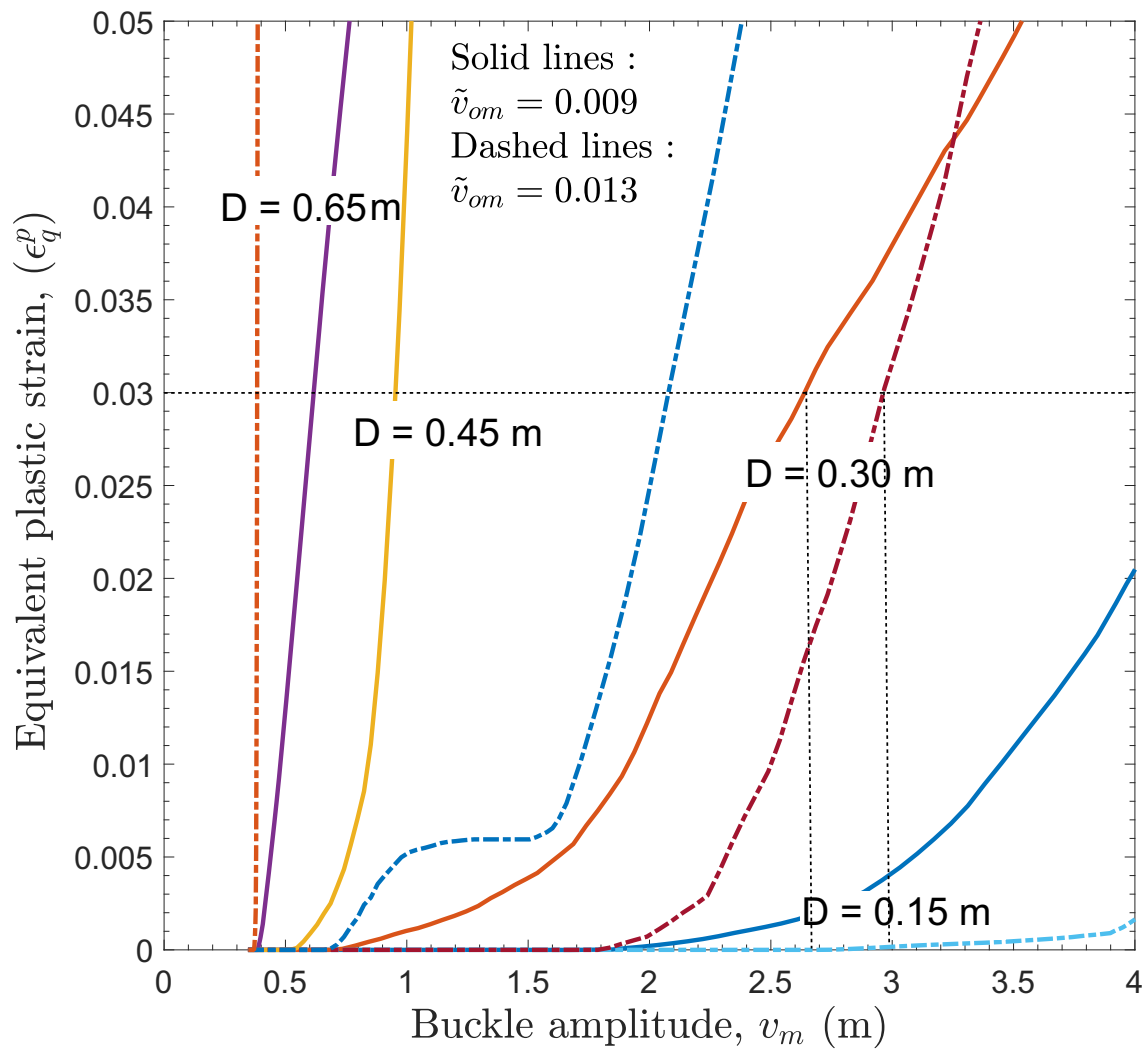


Figure 4.21: Effects of D/t on local buckling: (c) Plastic strain development with buckle amplitude

Fig. 4.22(b). This indicates that larger initial imperfections result in more complex wrinkle patterns, likely due to the increased sensitivity of the pipeline's response to initial geometrical imperfections. Figures 4.23(a) and 4.23(b) illustrate the von Mises stress distribution during upheaval buckling for different pipe sections with imperfections (\tilde{v}_{om}) of 0.009 and 0.013, respectively. The stress distribution reveals important patterns related to the pipe section size and the impact of imperfections on stress localization. Stress localization is observed at the center and

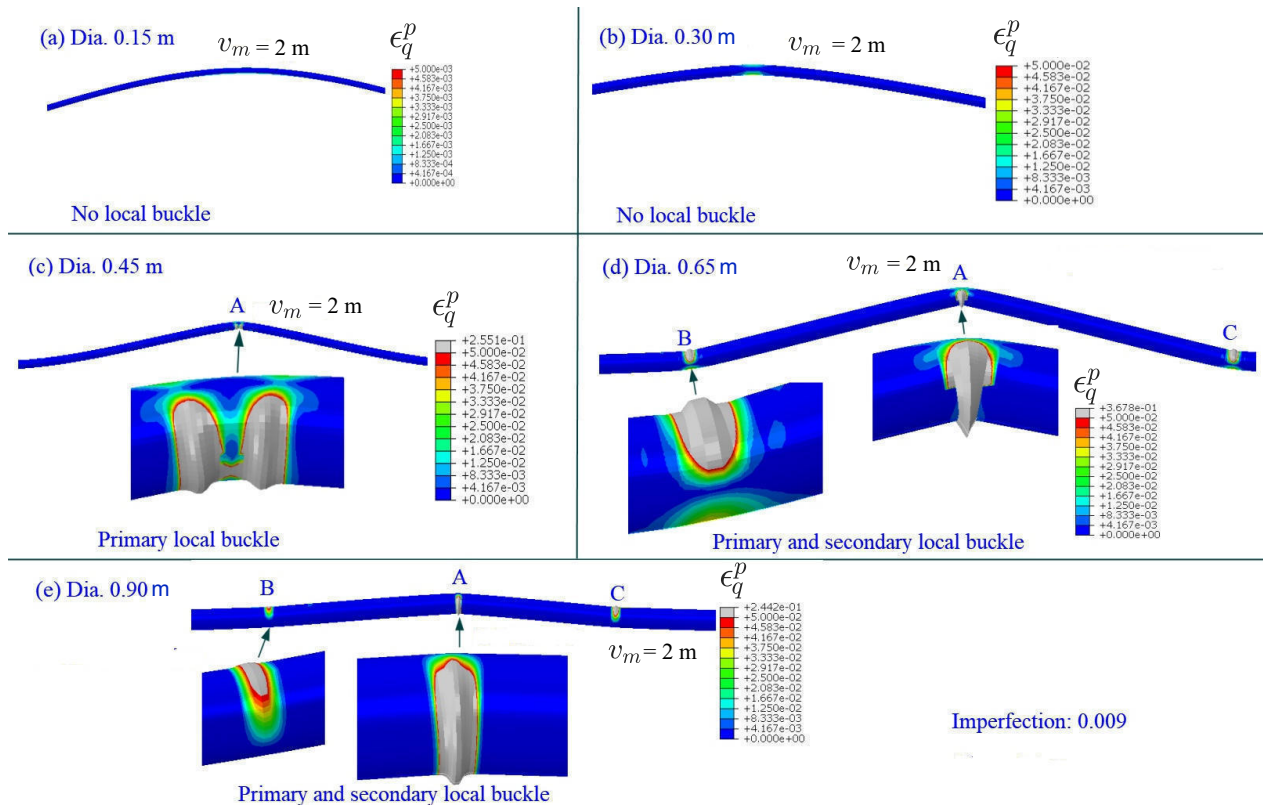


Figure 4.22: Effects of D/t on local buckling: (a) Plastic strain development for $\tilde{\nu}_{om}$ of 0.009

sides of the different pipe sections. The stress concentrations are more pronounced at the center, where the pipe is likely to experience the highest levels of deformation and strain. The stress localization patterns vary based on the pipe section size and the initial imperfections. Larger pipe sections exhibit more significant stress localization due to the higher stress concentrations associated with their larger diameters and thinner walls. Additionally, as the magnitude of the imperfections increases from 0.009–0.013, the stress localization becomes more prominent, indicating the influence of imperfection size on stress distribution during upheaval buckling.

Figure 4.24(a) presents the first (central location A in Fig. 4.22(a) and second-onset (side locations B and C in Fig. 4.22(a)) critical local buckling strains for different pipe sections with imperfections ($\tilde{\nu}_{om}$) of 0.009 and 0.013. The observations show the critical strains at which local buckling initiates for each D/t ratio. For all the D/t ratios studied, the first onset local buckling

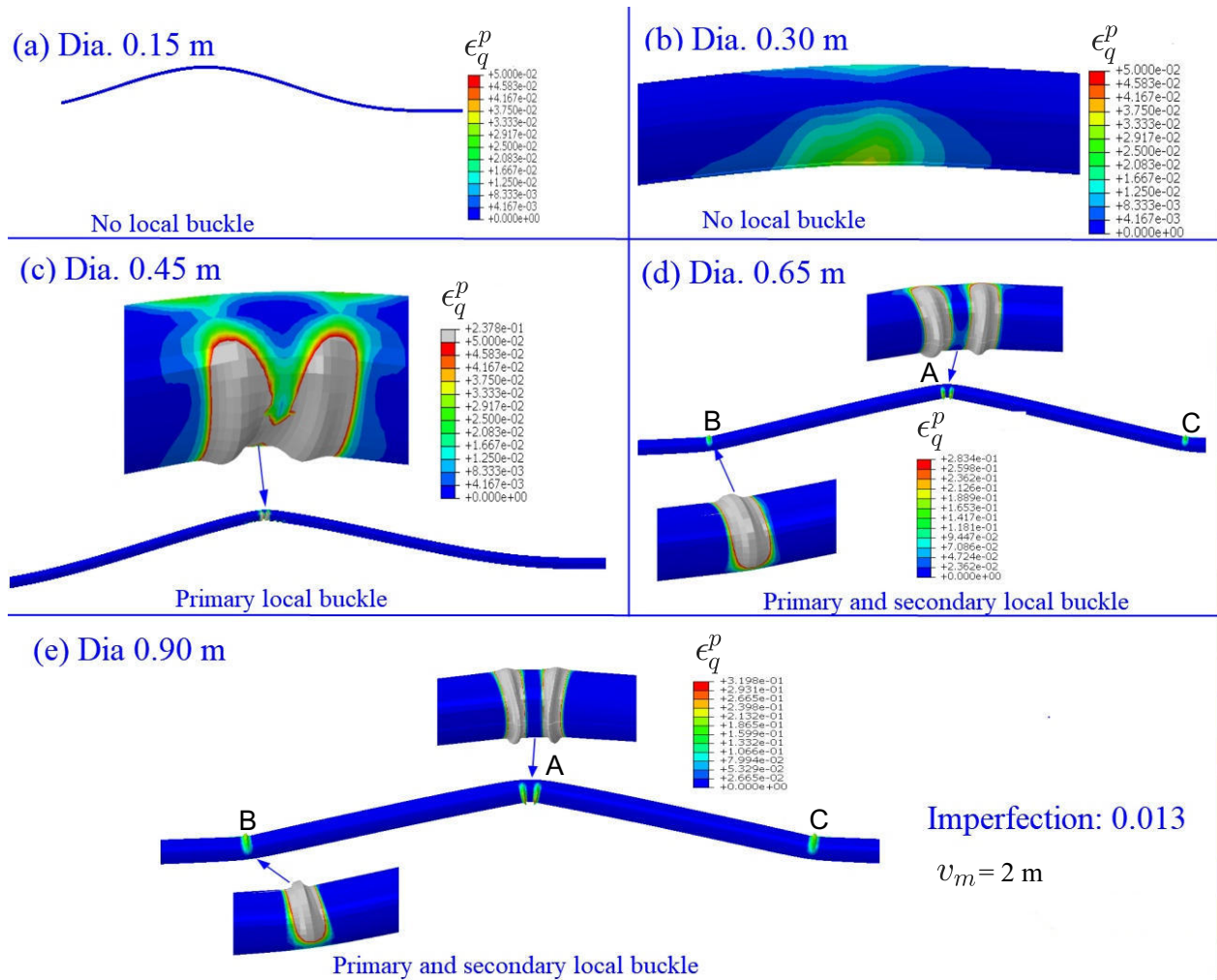


Figure 4.22: Effects of D/t on local buckling: (b) Plastic strain development for $\tilde{\nu}_{om}$ of 0.013

strain remains within the design limit of 3% (CSA (2007) guideline). This indicates that the pipeline can withstand the initial onset of local buckling without exceeding the strain limit. However, the onset strain at the secondary buckling (wrinkle formation) level is significantly higher. At this stage, the pipe at the central section undergoes significant wrinkling and sectional ovalization before forming wrinkles at the sides. This suggests the pipeline can endure higher strains during the secondary buckling phase, which involves more complex deformation patterns and wrinkling. In Fig. 4.24(b), the trend of secondary local buckling span (B–C in Fig. 4.23(a) and Fig. 4.23(b)) for various D/t ratios of the pipeline is presented. The observations reveal two key

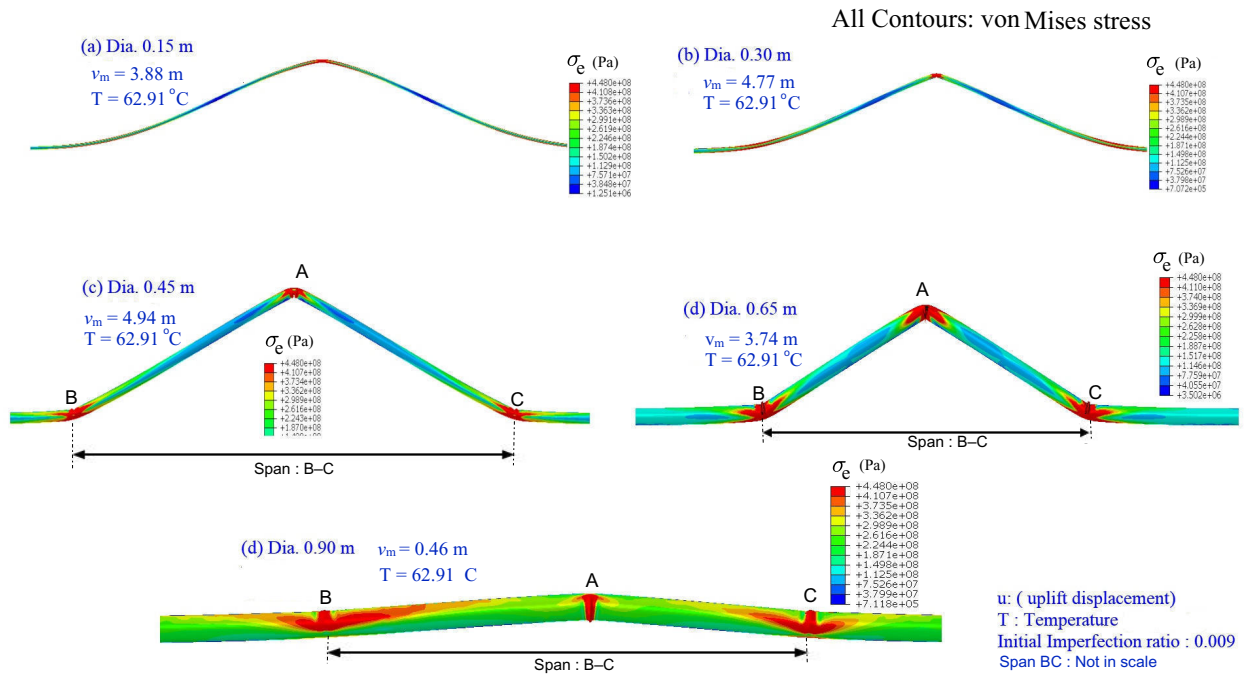


Figure 4.23: Effects of D/t on local buckling: (a) von Mises stress development for \tilde{v}_{om} of 0.009

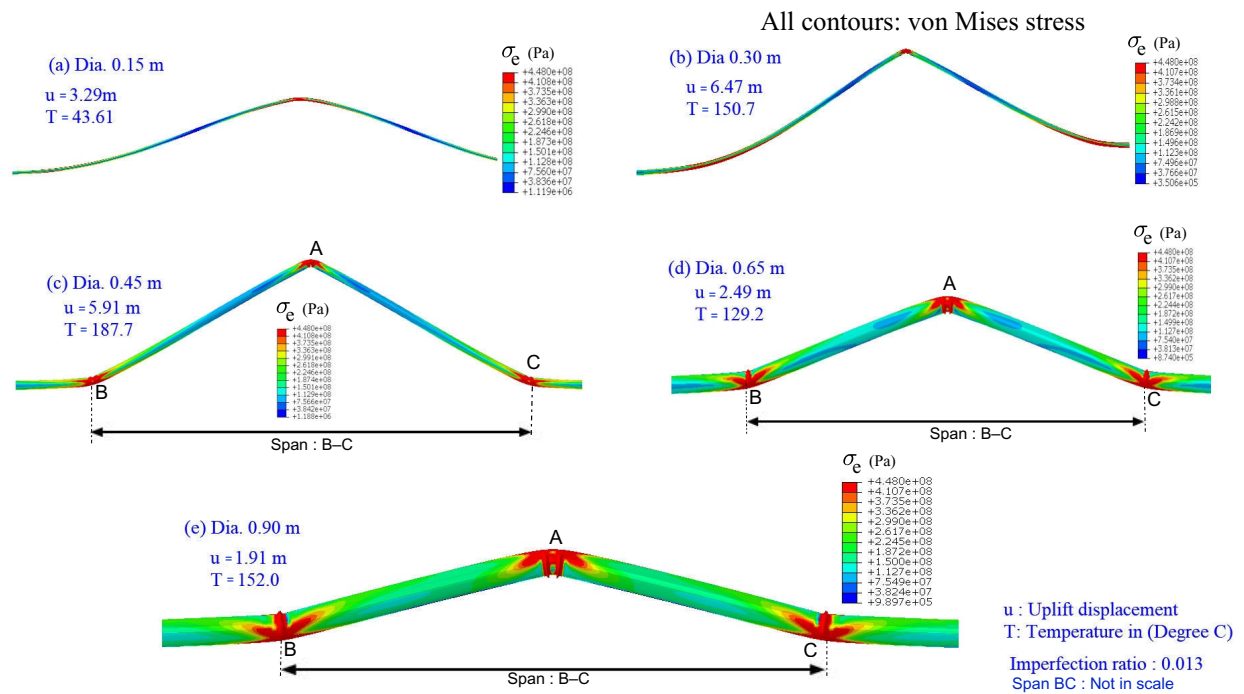


Figure 4.23: Effects of D/t on local buckling: (b) von Mises stress profile for \tilde{v}_{om} of 0.013

trends:

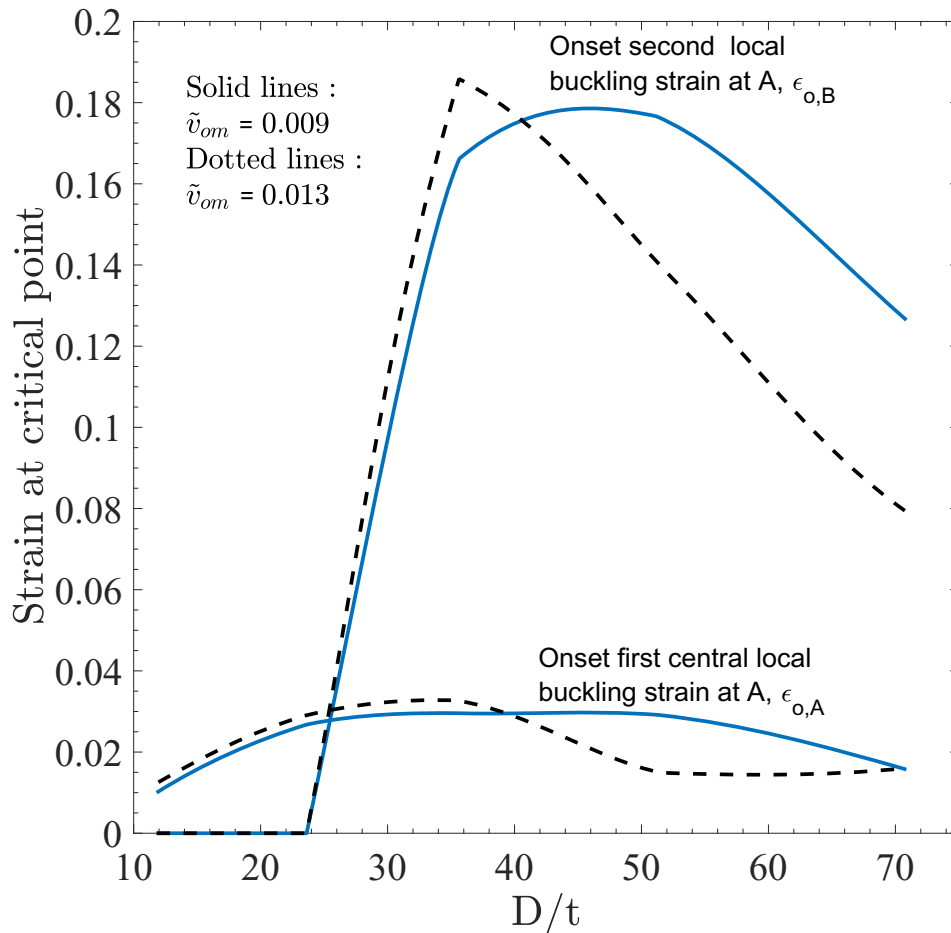


Figure 4.24: Effects of D/t on local buckling: (a) Trend of critical buckling strain in primary and secondary local buckling zones with varying D/t .

- * The buckling span (B–C) increases as the initial imperfection ratio increases. This indicates that larger initial imperfections lead to a more extended buckling span, with the pipeline experiencing more significant deformation and buckling over a larger portion of its length.
- * The buckling span (B–C) reaches its peak (≈ 30 m) at D/t of ≈ 35 and then decreases with the increase in the D/t ratio. This suggests that there is an optimal D/t ratio where the local buckling span (B–C) is the maximum, and beyond that point, as the D/t ratio continues to

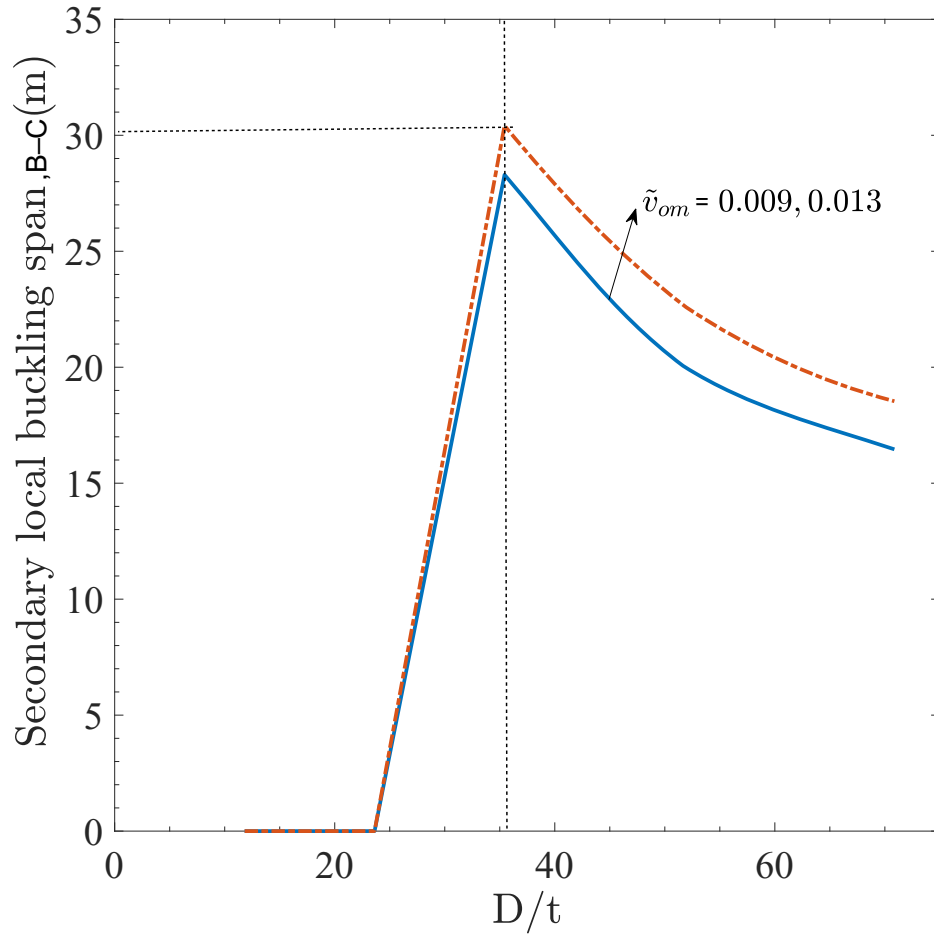


Figure 4.24: Effects of D/t on local buckling: (b) Secondary local buckling span with variable D/t

increase, the buckling span (B–C) decreases. This behaviour is likely due to the interaction between the pipe’s diameter and thickness, affecting its buckling behaviour and response to the applied loads.

4.9 Conclusions

A computationally efficient 3D numerical technique with a hybrid model is developed to investigate the local buckling behaviour of offshore pipelines undergoing large deformation. The numerical result shows a significant reduction in computational time with the proposed hybrid model with

centerline soil spring compared to the full-shell model. Some of the limitations of 1D finite element (FE) buckling model, e.g., local buckling cannot be modelled, has been addressed with the hybrid coupled model. The following conclusions are drawn from this study.

- a) A unique hybrid computationally effective modelling technique has been developed to solve global upheaval buckling, which can effectively model the local buckling and failure of offshore pipelines undergoing large movement beyond the seabed. Compared to beam-based modelling techniques, this approach has several advantages, including the ability to model local buckling due to the aftereffect of upheaval buckling.
- b) The modelling approach adopted in this study reasonably captures the failure mechanisms (i.e., local buckling) resulting from the global upheaval buckling, including the changes in ovalization. These ovalization results vary significantly from the traditional beam-based modelling techniques; therefore, careful consideration of finite element results obtained from the beam-based modelling technique is essential. In other words, the beam-based modelling technique can provide a reasonable (conservative) result for choosing the safe/critical operating temperature but fails to provide insights for the aftermath of global upheaval buckling (e.g., local buckling).
- c) The underlying mechanics of plasticity for the pipe movement have been discussed in the pre-buckling and post-buckling stages. During the post-buckling stage, a large plastic strain develops at the pipe invert (compression side) and gradually transfers the strain to the crown (tension side).
- d) The implementation of the elastic-plastic material model reveals lower moment capacity and a higher potential for local buckling (large plastic deformation) compared to the Ramberg-Osgood model.
- e) The size of the initial imperfection plays a crucial role in both buckling and local buckling phenomena. A larger initial imperfection leads to stable buckling with more pronounced

plastic deformation, while a smaller initial imperfection results in snap-through buckling with lesser plastic deformation.

- f) The effect of various soil spring modelling definitions on local buckling is also investigated. The results indicate that use of a post-peak degradation soil model leads to a higher onset local buckling strain in the pipeline compared to the design guidelines (e.g., ALA 2005; DNV 2007).
- g) The critical buckling temperature decrease with the increase in internal pipeline pressure. The compressive onset strain also decreases with the decrease in differential pressure. The sectional ovalization increases with the increase in differential pressure in the pipeline. The high differential pressure means the pipeline undergoes early local buckling with lower vertical displacement. The traditional equivalent temperature approach may lead to an underestimation of the local buckling behaviour in the pipeline.
- h) With the pipe (D/t) ratio increase, the critical buckling temperature can be increased; however, the strain localization increases with a small amount of vertical displacement.

When designing pipelines to resist upheaval buckling (UHB), it is essential to consider critical factors such as the sectional properties of the pipe, material behaviour, presence of initial imperfections, embedment in the surrounding soil or seabed, and the operational conditions, including temperature and pressure. Considering these factors ensures a robust and reliable design to mitigate the risk of UHB and maintain pipeline integrity. The modelling techniques presented here can be effectively employed to predict local failures in offshore pipelines operating under high temperature and pressure conditions. The hybrid model utilized in this study, which incorporates soil springs, has certain limitations. The response of local buckling in a pipeline with initially stressed imperfection might differ, and this aspect has not considered. Furthermore, the impact of hydrodynamics once the pipeline moves above the seabed has not been considered, which might create different local buckling behaviour. Notably, the soil spring model cannot fully

encompass the more realistic soil mechanical responses, such as pore pressure effects, strain softening and hardening, and shear-induced dilation and compaction. While the three-dimensional continuum FE model can address some of the limitations, it remains computationally expensive and poses numerical challenges. The offshore pipeline, subject to cyclic operational loading conditions like start-up, shutdown, restart, or variable operational pressure, may experience combined vertical movement of the pipe due to a geotechnical ratcheting mechanism. Further investigation is needed to explore this ratcheting mechanism leading to local buckling and failure in offshore pipeline subjected to large vertical displacement.

Chapter 5

Fracture Assessment of Post-buckled Offshore Pipeline using eXtended Finite Element Method

ABSTRACT

Buried offshore pipelines that operate under high pressure and high-temperature conditions often experience upheaval buckling. These pipelines may possess pre-existing defects, such as cracks that originated during fabrication or operation. If an offshore pipeline with an initial defect experiences vertical movement due to upheaval buckling, the crack can propagate in the tensile stress region, leading to fracture. This study presents a numerical modelling technique using the extended finite element method to analyze the initiation and propagation of tensile fractures in a post-buckled pipeline. Conventional fracture mechanics commonly employ damage initiation criteria based on maximum principal stress (MAXPS) or maximum principal strain (MAXPE) with fixed values. However, these criteria has limitations in considering crack-tip constraints (stress triaxiality and lode angle) during the numerical analysis. A modified Mohr–Coulomb (MMC) fracture criterion is implemented in the finite element program Abaqus using a user-defined subroutine to address this limitation. The MMC criterion considers shear slip and ductility, providing a more realistic representation of ductile materials than MAXPS and MAXPE models. The study also discusses the calibration of fracture parameters with different damage degradation models. The findings of this study have practical implications for evaluating crack initiation and propagation in post-buckled offshore pipelines.

Keywords: Offshore pipeline, Fracture, XFEM, CMOD, Tensile strain, Plastic strain, Stress Triaxiality

5.1 Introduction

Exceeding the critical limit of axial compressive forces due to high pressure and high temperature (HPHT) in the buried offshore pipeline can lead to upheaval buckling. The high axial compression and initial structural defects, such as cracks or dents on the pipe surface, may cause tensile fracture or rupture on the tension side of the post-buckled pipeline. The field observation by Nielsen et al. (1990) shows that despite having a certain amount of vertical displacement due to high operating conditions, the offshore pipeline remains in a serviceable condition at some level of strain typically less than 0.5% (stress-based design) Yoosef-Ghodsi (2015). During operation, the vertically buckled offshore pipeline sometimes experiences considerable longitudinal plastic strain typically greater than 0.5% (strain-based design). The performance of the pipes experiencing such considerable strain should be assessed to determine the tensile strain capacity (TSC) rationally.

Post-buckling fracture of an offshore pipeline involves multiple physical processes, including plastic deformation, material failure, and crack propagation. While there has been some research on the subject, the literature on crack opening and propagation behaviour in post-buckled offshore pipelines is relatively limited compared to other areas of offshore pipelines. One reason for this limited study is the difficulty in simulating post-buckling fracture behaviour in laboratory experiments and with numerical simulations. The behaviour of offshore pipelines under loading is highly nonlinear, and the onset of post-buckling fracture is often unpredictable, making it challenging to model and simulate accurately. Some studies often focused on specific aspects of the problem, such as the effects of pipeline curvature, material properties, or loading conditions on post-buckling fracture behaviour (Jayadevan et al., 2004; Østby et al., 2005). Several fracture assessment methodologies have been suggested in the literature for onshore unbuckled pipelines, such as employing parameters like J-integral and crack-tip opening displacements (CTOD) Hutchinson (1983), strain-based engineering criticality assessment (ECA) Linkens et al. (2000), simplified strain-based assessment Østby et al. (2005), strain-based failure assessment diagram

(FAD) Budden (2006), and CTOD estimation equations based on strain under large plastic deformation Zhang et al. (2014b).

The eXtended finite element method (XFEM) has recently been widely used for the fracture assessment of pipelines based on the cohesive zone modelling technique. Fracture analysis using the fixed value of critical stress or strain damage initiation criterion with the XFEM may lead to inaccurate fracture profiles, crack propagating paths, and rate of crack propagation if the crack-tip constraint is not considered. The strain-based modified Mohr–Coulomb (MMC) fracture criterion proposed by Bai and Wierzbicki (2008) considers the crack-tip constraint based on a variable strain profile as a function of stress triaxiality and Lode angle parameter that might provide the realistic fracture behaviour. The implementation of the XFEM-based cohesive zone model (CZM) for studying crack initiation and propagation in the post-buckled offshore pipeline with the MMC fracture criterion has not been widely explored. The XFEM-based cohesive zone model (based on traction-separation cohesive behaviour) was used to study fracture problems by specifying the damage properties of a material, such as initiation and evolution. Liu et al. (2012) used this model to numerically simulate the plastic collapse and crack behaviour of a buried steel pipeline (X65 grade steel with yield stress $\sigma_y = 460$ MPa, ultimate stress $\sigma_u = 667$ MPa) under landslide loading. Several other studies utilized the XFEM-based cohesive zone model to investigate the fracture problems in various pipelines. Hojjati-Talemi et al. (2018) modeled the dynamic brittle fracture of an X70-grade steel pipe with $\sigma_y = 520$ MPa, maximum principal stress $\sigma_{\max ps} = 1064$ MPa. Mondal and Dhar (2019) used the maximum principal stress (MAXPS) damage initiation criterion in XFEM to identify the crack location in a corroded pipeline and calculate the burst pressure using the J-integral. Agbo et al. (2019) evaluated the effect of differential pressure and flaw size on the tensile strain capacity of an X42-grade steel vintage pipe using the damage plasticity model in XFEM. They found that the results were comparable with experimental results. Ameli et al. (2019) and Lin et al. (2020) calibrated the maximum principal stress and fracture energy release rate (G_c) parameters using the maximum principal stress damage initiation criterion in XFEM.

The studies by Ameli et al. (2019) and Lin et al. (2020) found that fracture energy release rate G_c calibrated using the maximum principal stress damage initiation criterion in XFEM can simulate crack propagation in a steel pipeline with MAXPS values ranging from $1.4\sigma_y$ to $4.5\sigma_y$. However, the required MAXPS value is much higher than the measured strength of the steel pipe, suggesting that the MAXPS criterion may not accurately capture the fracture behavior of the material. According to the study by Li and Chandra (2003), the required higher values of MAXPS for ductile fracture are due to the formation of localized necking, while for brittle materials, MAXPS is comparable to the yield strength of the material. Liu (2017) used the XFEM with MAXPE damage initiation criterion to study fracture in the X80 grade steel pipeline and found that the required MAXPE for crack propagation depends on the pipe's thickness and decreases with the increase in pipe thickness. They also suggest that MAXPE is more appropriate for simulating ductile crack propagation in pipelines but is unable to capture the large plastic deformation during the crack propagation. Liu (2017) and Agbo et al. (2019) suggest that for large deformation fracture problems, a strain-based damage initiation criterion may be more appropriate to capture geometric and material non-linearity associated with the plastic deformation. Kofiani (2013) and Lin (2021) successfully employed the MMC fracture criterion for the fracture assessment of onshore pipeline. The challenge of applying that method for offshore HPHT pipelines was not examined.

Developing a computationally efficient approach for analyzing the fracture behavior of post-buckled offshore pipelines is the focus of the current study. The numerical challenges associated with the XFEM for modelling of tensile fracture assessment in a long post-buckled offshore pipeline is significant. For the 3D problem, XFEM modelling is commonly performed with the solid elements in Abaqus FE software, requiring fine mesh with a large number of elements and nodes. Furthermore, the simultaneous analysis of post-buckling and XFEM-based fracture of the pipeline with soil-spring for the buried pipe faces numerical convergence issues. To tackle these challenges, the problem was simplified by converting it into a small pipeline segment

with longitudinal symmetry, featuring post-buckle shape, initial crack and stresses occurring during upheaval buckling.

The axial compressive loading during the post-buckling stage is applied through axial displacement on the pipeline boundary with rigid links. The method involves using XFEM-based cohesive segments, which incorporates the generation of post-buckled shapes and subsequent fracture assessment. The study investigates the tensile fracture initiation and propagation in post-buckled offshore pipelines using three different damage initiation criteria: fixed stress (MAXPS), fixed strain (MAXPE), and variable strain-based damage (MMC). A user subroutine UDMGINI is implemented in Abaqus FE software to utilize the MMC fracture criterion. This study also examined suitable material damage parameters for modelling the initiation and propagation of cracks in X65-grade offshore steel pipelines.

5.2 Problem statement

Centred on phase-III, as expounded in the research motivation within Chapter 1 shown in Fig. 1.2, this study aims to numerically solve the fracture problem in an HPHT offshore post-buckled pipeline. This fracture issue arises from the large vertical movement of offshore pipelines beyond the seabed, leading to a notable development of tensile strain in the crown and eventual pipeline fracture and collapse.

This study uses numerical modelling techniques to analyze and investigate the fracture behaviour of a post-buckled offshore pipeline under a significant tensile strain level. Specifically, it is assumed that the HPHT offshore buried pipeline experiences considerable upheaval buckling (moved beyond the seabed) and already has an initial crack before the onset of local buckling.

The problem of fracture assessment in a post-buckled offshore pipeline involves two steps. The first step involves performing an upheaval buckling analysis of the buried pipeline to determine the post-buckled deformed shape (Section 5.2.1). In the second step, the symmetric post-buckled shape of the pipeline with initial prestress and a predefined initial crack is analyzed with damage

initiation and evolution criterion (Section 5.2.2) in fracture mechanics. Finally, the study aims to characterize the post-buckled pipeline's critical fracture strain and crack mouth opening displacement (CMOD) while considering the crack-tip constraint based on the variable strain profiles.

5.2.1 Problem description for the deformation shape

This problem analyzes upheaval buckling in a buried pipeline made of API X65 grade steel with a 0.3 m outer diameter (D) and 12.7 mm wall thickness (t). The selected pipeline section is widely used in offshore applications and readily available in the industry Palmer et al. (1990); Nielsen et al. (1990); DNV (2007). The numerical modelling to assess the combined buckling and fracture behaviour of a full-length offshore buried pipeline is computationally expensive and challenging. The simplified analysis is often performed through the idealization of the pipe as a beam and the pipe-soil interaction as springs. However, the idealization of the pipe as a beam is unsuitable for capturing the cross-sectional deformation, which is nonlinear at large deflection, particularly at the central segment of the pipe, where the deflection is the maximum. Modelling the pipe as a shell or 3D solid element would be required to capture the cross-sectional deformation. However, the Abaqus FE software used in this study has limitations in using shell elements for fracture analysis with XFEM. To resolve the computational challenges, the upheaval buckling analysis of the 3D coupled HPHT pipeline was first performed with the beam element (PIPE31H) on the outer part (away from the center) and the shell (S4R) elements at the center part using the coupling constraints. Pipe-soil interaction is idealized using the nonlinear soil-spring model. It is assumed that the pipeline is buried in a medium-dense sand at a shallow depth (H), with $\tilde{H} = H/D = 3$ where H is the depth to the center of pipe. Then, a specific section of the post-buckled pipeline and its longitudinal profile were examined, specifically after a peak vertical displacement (v_m) from its original configuration. The first step of analysis aims to understand the behavior of the pipeline under compressive stresses due to HPHT and to determine the post-buckled shape of the pipeline

before the onset of a local buckle on the compression side. The initial imperfection as an empathetic shape based on Taylor and Gan (1986), given in Eq. (5.1) was considered.

$$v_o = v_{om} \left\{ 0.707 - 0.262 \frac{\pi^2 x^2}{L_o^2} + 0.293 \cos \left(2.86 \frac{\pi x}{L_o} \right) \right\} ; \frac{-L_o}{2} \leq x \leq \frac{L_o}{2} \quad (5.1)$$

where v_{om} is the maximum initial imperfection height at the center at $x = 0$; L_o is the initial imperfection length can be calculated from Eq. (5.2) Taylor and Gan (1986)

$$L_o = \left(\frac{\tilde{v} EI}{2.407 \times 10^{-3} q} \right)^{1/3} \quad (5.2)$$

where \tilde{v} is v_{om}/L_o of 0.009 was used for this analysis, and q is the submerged self-weight of the pipeline (per unit length). Figure 5.1 shows the details of the numerical model used in this study. As the central part is expected to undergo the maximum vertical displacement, it is modelled as a shell structure, which is connected to the left and right part of the pipeline modelled by beam elements (Inset-I Fig. 5.1(a)).

Figure 5.2 shows the spring parameters used to represent soil resistances. The bilinear soil-spring in the axial, lateral and bearing directions are modelled using ALA (2005) design guidelines. Physical and numerical studies (Bransby et al. 2002; Wang et al. 2012; Roy et al. 2018b) have demonstrated that uplift resistance decreases as the pipe moves upward and reaches zero when it reaches the ground surface. Therefore, this study employs trilinear pre-peak behaviour (DNV 2007) and a linear post-peak soil strength degradation model (Fig. 5.2(c)) for medium dense sand. The uplift resistance curve for a medium dense sand is developed using $f = 0.6$, $\alpha = 0.75$ and $\beta = 0.2$ based on DNV (2007) guidelines. The parameters used to develop axial, lateral, and bearing resistances are given in Table 5.1. Based on ALA (2005) recommendations, $u_{ap} = 3$ mm and $u_{lp} = 4.2$ mm are used for medium sand. The mobilized peak uplift displacement $v_{up} = 7.2$ mm is used based on DNV (2007) guidelines.

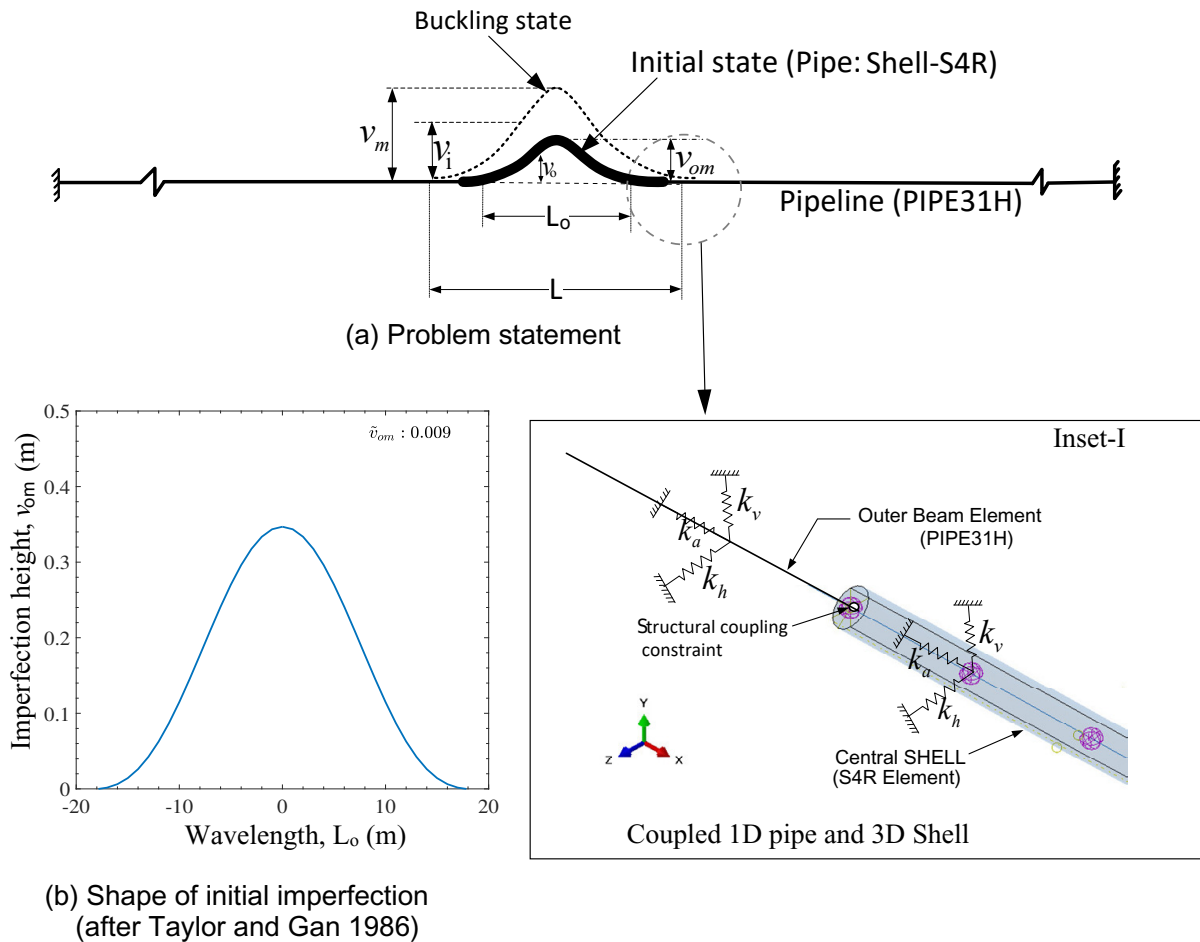


Figure 5.1: Problem statement with an initial imperfection: (a) Problem statement and Inset-I: Coupled 1D pipe and 3D shell (Hybrid FE model); (b) Shape of initial imperfection (\tilde{v}_o)

The FE analysis for UHB consists of three steps: (i) the general static step where the submerged self-weight (q) was applied as a line load; (ii) the static pressure step where the internal pipe pressure, p of 5 MPa was applied; and (iii) temperature loading step where the incremental temperature is applied using the predefined fields for large temperature increase (T). The modified RIKS algorithm available in Abaqus was used that is suitable for capturing the snap-through

Table 5.1: Soil and geometric parameter used to develop nonlinear force-displacement curves

Parameters	Value
Submerged unit weight of soil, γ (kN/m ³)	9.19
Angle of internal friction of soil, ϕ' (°)	35
Axial interface friction angle between pipe and soil, ϕ_μ (°)	28
Coefficient of earth pressure at rest, K_0	0.5
External diameter of pipe, D (m)	0.3
Depth to the center of pipe, H (m)	0.9

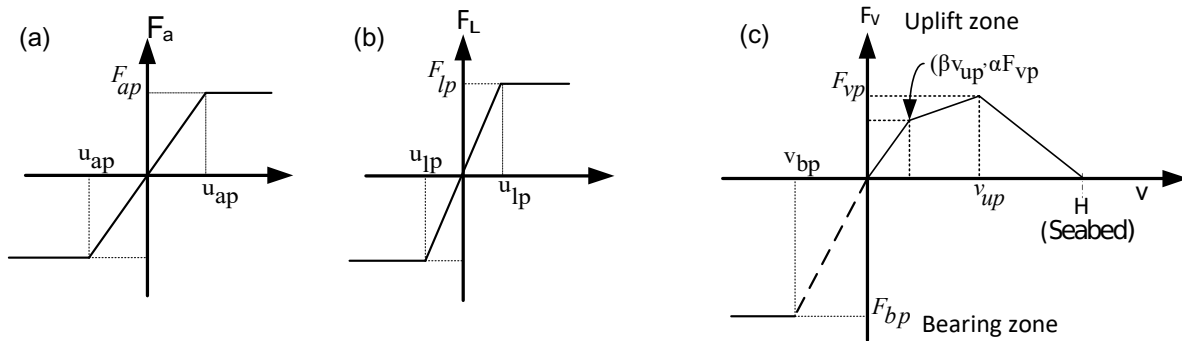


Figure 5.2: Nonlinear soil-spring model used for the 3D FE analysis: (a) Axial; (b) Lateral; and (c) Vertical springs (after ALA 2005; DNV 2007)

behaviour. Both ends of the pipe are applied with the fixed boundary conditions. As a result, the pipeline displaces in the upward direction due to the temperature load. A significant upward distance beyond the seabed occurs before the local buckle develops on the compression side. The post-buckled deformed shape at the onset of local buckle is shown in Fig. 5.3 that was used for the fracture analysis.

For the fracture study (see Section 5.2.2), the symmetric central segment of the post-buckled pipeline corresponding to the onset of local buckle on the compression side was considered (see

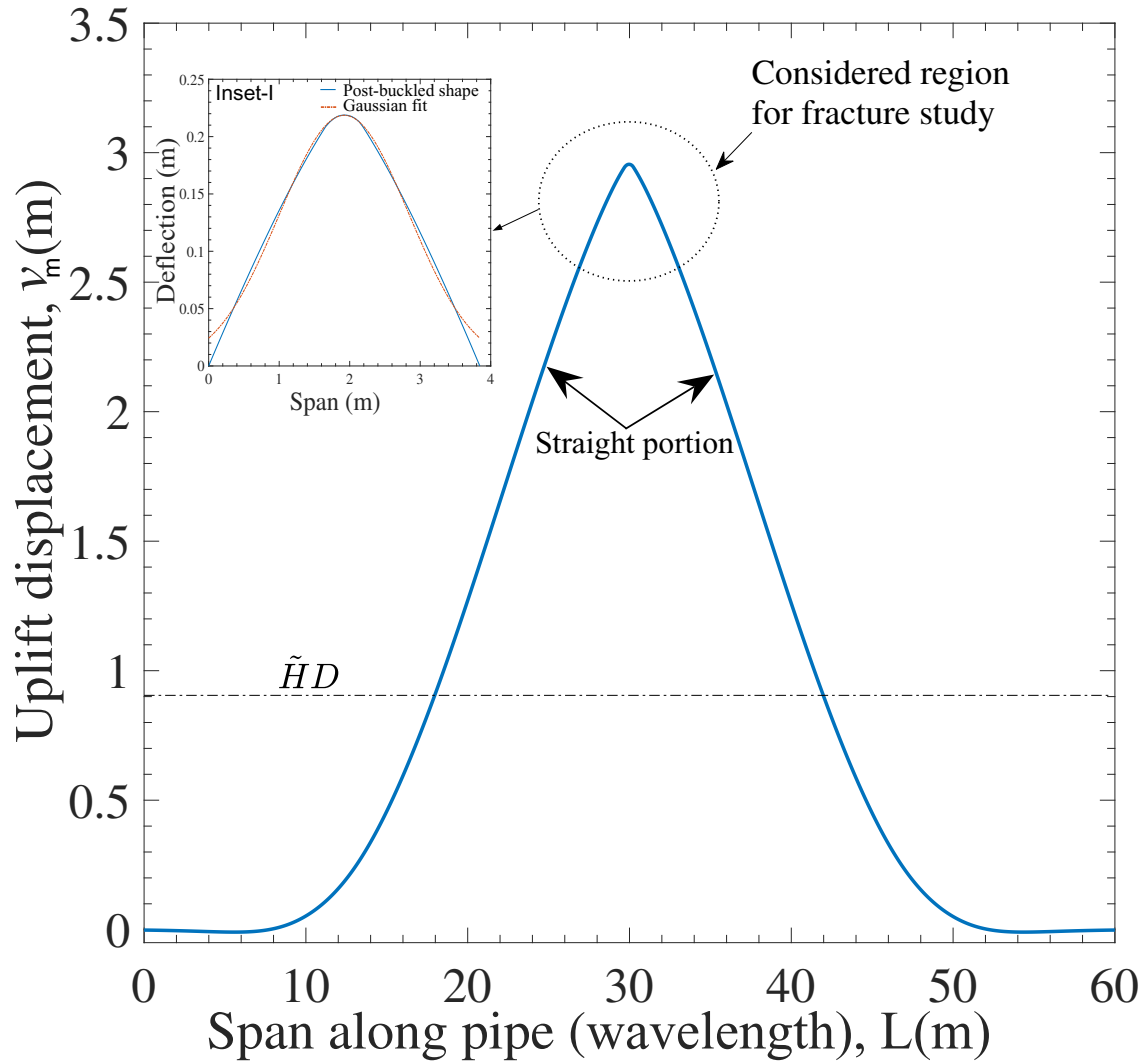


Figure 5.3: Post-buckled shape of the HPHT pipeline at the onset of local buckle on the compression side

Inset-I of Fig. 5.3). The post-buckled shape was obtained through fitting the results of a analysis fitted with a Gaussian function given in Eq. (5.3).

$$y = Ae^{\left(\frac{-(x-\mu)^2}{2\sigma^2}\right)} \quad (5.3)$$

where the parameters $A = 0.2185$; $\mu = 1.923$; and $\sigma = 0.9169$ approximately fits with the post-buckled profile. The span of the central segment with post-buckled shape is 3.85 m and the peak deflection is 0.24 m. This shape only applies to the specific analysis solved here using a specific initial imperfection and specific soil (i.e. medium-dense sand).

5.2.2 Problem description for the fracture analysis

Figure 5.4 shows the segment of the pipe used in the post-buckle fracture analysis. The ends of the segment are connected to a rigid link to apply axial compression (resulting from temperature increase in the offshore pipeline), representing the straight portion in Fig. 5.3. Taking the advantage of symmetry, half of the longitudinal section of the segment was analyzed.

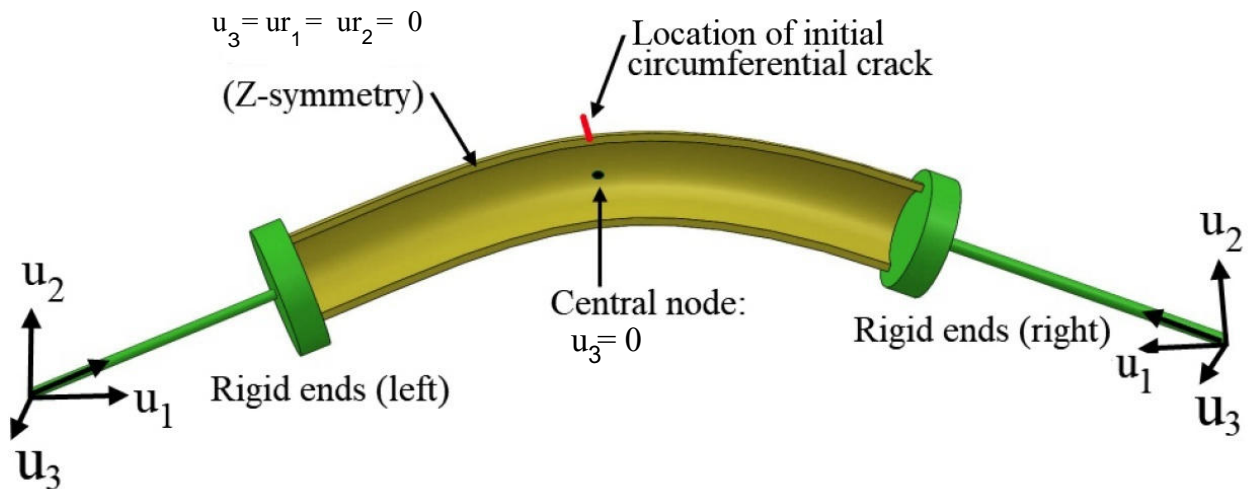


Figure 5.4: FE problem description for the post-buckled fracture assessment (not in scale)

To ensure uniform stress distribution at the pipe segment's ends, a rigid beam of 2 m length with end caps was connected to both ends of the solid pipe (after Mohareb 1995), as shown in Fig. 5.4. The soil response was neglected because the post-buckled segment of the pipe is above the seabed. Also, the effect of external hydrodynamic forces (e.g., waves, currents) on the pipeline was neglected because the hydrodynamic loading on external pressure change is assumed to be less

than that of the internal operating temperature and pressure in the buried offshore pipeline. The numerical model used in this study incorporates an initial curvilinear 3D planar crack with a depth of 0.5 times the thickness of the pipe wall, t (i.e., 6.35 mm) and a circumferential length of 0.062 times the outer perimeter of the pipe, i.e., 59 mm (to avoid the convergence issue in XFEM analysis such that the initial crack cuts at least ten elements in the circumferential direction). The choice of a planar crack shape is motivated by computational efficiency in XFEM. Moreover, we focus on crack opening and propagation analysis, where a planar crack proves to be numerically less time-consuming. Employing the linear elastic fracture mechanics concept with the first mode stress intensity factor (K_I) of X65 pipe material, the approximate initial crack depth (a_c) can be estimated from equation $a_c = \frac{K_I^2}{\beta^2 \sigma \pi}$. where, β is the parameter depends on geometry and crack length, σ is the axial stress in a pipe.

It is difficult to transfer initial stresses from the post-buckled hybrid pipe-shell model to the symmetric solid model with an initial crack (Fig. 5.4) due to incompatible elements. Therefore, to replicate the initial prestress in the post-buckled FE model for fracture assessment, the symmetric segment (shown in Fig. 5.4) was first generated without an initial crack. An upward displacement was then applied to the central cross-section of the curved pipe, ensuring that the stresses at that section of the pipe are similar to the stress obtained from post-buckled analysis (Fig. 5.1).

Fixed boundary conditions were maintained at the ends during this simulation. The output database file generated from this simulation was subsequently imported as a predefined initial stress into another FE model with an initial crack for fracture analysis. The self-weight and differential pressure were applied to the pipe model before applying axial compression at the ends for further simulation.

5.3 Computational techniques used for the analysis

This section provides a theoretical background of numerical simulation employed in this study. The discussion covers the cohesive segment approach within the context of the eXtended finite element

method (XFEM), as well as the criteria for damage initiation and propagation to develop the user subroutine (UDMGINI) in Abaqus FE software.

5.3.1 eXtended finite element method (XFEM)

For numerical modelling of stationary cracks using the conventional finite element method, the mesh needs to conform to the geometric discontinuities which requires additional mesh refinement efforts. Besides, modelling crack growth using the standard finite element method often necessitates the use of special meshing techniques that involve continuously updating the mesh to accurately capture the geometry of the discontinuity as the crack propagates. To address these challenges, the eXtended Finite Element Method (XFEM) was introduced by Belytschko and Black (1999). The XFEM resolves the need for mesh conformation to the crack by extending the conventional finite element method with the concept of partition of unity (as described in Melenk and Babuška 1996), and utilizing enriched shape functions. The XFEM approach approximates the displacement field for stationary cracks as the sum of the standard finite element approximation with the enriched discontinuous displacement term expressed by Eq. (5.4):

$$u^h(x) = \sum_{i \in I} N_i(x) u_i + \sum_{i \in I^{enr}} \psi_i(x) \tilde{N}_i(x) a_i \quad (5.4)$$

where $N_i(x)$ and u^i are the standard finite element shape function and standard degree of freedom at the node respectively applied to all nodes in the model. The term $\psi_i(x)$ is the enrichment function used for the element nodes cut by the crack and a_i is used for the adjustment of the actual displacement field. The shape function used for the enrichment forms a partition of unity Eq. (5.5) given by:

$$\sum_{\forall i} \tilde{N}_i(x) = 1 \quad \forall x \in \Omega \quad (5.5)$$

In Eq. (5.4), the second term for enrichment can be split into two parts. The first part pertains to the element nodes located along the crack faces, whereas the second part refers to the element nodes

located at the crack tip. This is illustrated in Fig. 5.5. The final expression for this term can be obtained by using Eq. (5.6). The rectangular nodes in Fig. 5.5 are the element nodes completely cut by the crack interior which are enriched by Heaviside function $\psi_1^{\text{faces}}(x)$ in Eq. (5.7) and the circular nodes are enriched by the crack tip enrichment function given by ψ_1^{tip} in Eq. (5.8). The dotted line represents the initial crack. The final form of the displacement function used for crack

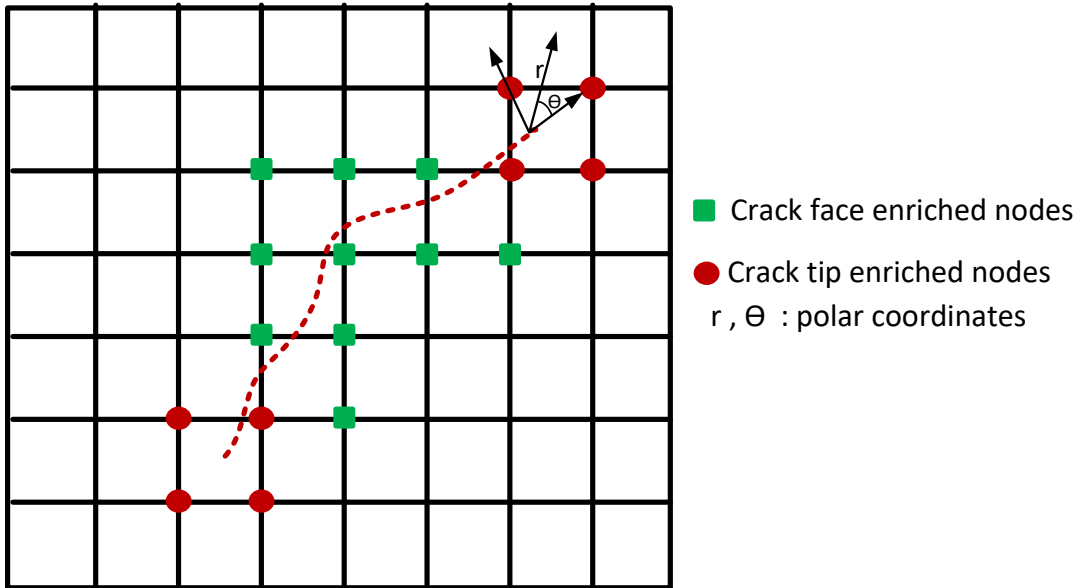


Figure 5.5: The illustration of displacement jump function across the crack surfaces in XFEM

modelling with XFEM is given by Eq. (5.6):

$$u^h(x) = \sum_{i \in I} N_i(x) u_i + \sum_{i \in I_{\text{faces}}^{\text{enr}}} \psi_i^{\text{faces}}(x) N_i(x) a_i + \sum_{i \in I_{\text{tip}}^{\text{enr}}} \psi_i^{\text{tip}}(x) N_i(x) b_i \quad (5.6)$$

The displacement jump across the crack faces given by the level set function $\psi(x)$ from Dolbow et al. (2000) is given by Eq. (5.7).

$$\psi_i^{\text{faces}}(x) = H(\psi(x)) = \begin{cases} 1 & \text{if } \psi(x) > 0 \\ -1 & \text{otherwise} \end{cases} \quad (5.7)$$

The elastic asymptotic crack-tip enrichment function ψ_i^{tip} is given by Eq. (5.8):

$$[\psi_i^{\text{tip}}, i = 1-4] = \left[\sqrt{r} \sin \frac{\theta}{2}, \sqrt{r} \sin \frac{\theta}{2} \sin \theta, \sqrt{r} \cos \frac{\theta}{2}, \sqrt{r} \cos \frac{\theta}{2} \sin \theta \right] \quad (5.8)$$

where (r, θ) is a polar coordinate system with its origin at the crack tip and $\theta = 0$ is tangent to the crack tip line. a_i and b_i are the enriched degrees of freedom at the element nodes. Also, for the geometrical description of the discontinuous surface (crack description and tracking the growth of discontinuities), level set method is used in XFEM without burden of remeshing Simulia (2016). The level set normal function $\phi(x)$ is used to describe the crack surface and the level set tangential function $\psi(x)$ is used to describe the crack front or tip in XFEM. The propagating crack near-tip asymptotic singularity is not considered in XFEM because the crack has to propagate across an entire element at a time to avoid the need to model the stress singularity. The displacement function turns to only the sum of first and second term of the right hand side of the Eq. (5.6).

5.3.2 Cohesive segment approach

The cohesive zone model (CZM) is a commonly employed numerical method for studying crack propagation (Schwalbe et al. 2009; Agbo et al. 2019; Lin et al. 2020). In the continuum mechanics, cohesive elements are used to model a cohesive zone containing material of finite thickness using conventional finite element analysis. However, in cases where the cohesive zone is very thin, such as in fracture analysis, it can be effectively reduced to a zero thickness using

traction-separation laws (Simulia 2016). CZM approach, first introduced by Barenblatt (1959), Dugdale (1960), and Barenblatt (1962), is based on the cohesive elements or on surface based cohesive behaviour that was used to simulate the crack initiation and propagation. The CZM approach in XFEM, as introduced by Wells and Sluys (2001), incorporates the partition of unity technique of finite elements for the cohesive crack. For the modelling of crack initiation and propagation, the traction–separation cohesive behaviour in XFEM framework was implemented in Abaqus with the use of phantom nodes approach (Hansbo and Hansbo 2004). In CZM, the near-tip asymptotic stress singularity is not needed, and only the displacement jump across a cracked element is considered. Therefore, the crack has to propagate across an entire element at a time to avoid the need to model the stress singularity (Simulia 2016). The phantom nodes are used to superimpose the crack with the original nodes to represent the crack element discontinuity. When the element is cut through by a crack as shown by central solid curved line in Fig. 5.6, the cracked element splits into two parts represented by real nodes (Ω_0^+/Ω_0^-) and phantom nodes (Ω_p^+/Ω_p^-).

The amount of separation depends on the cohesive law till the cohesive strength of the cracked element turns to zero. Then, the phantom nodes and its corresponding real node are no longer tied together and can be separated (Simulia 2016). The traction–separation laws based on Scheider

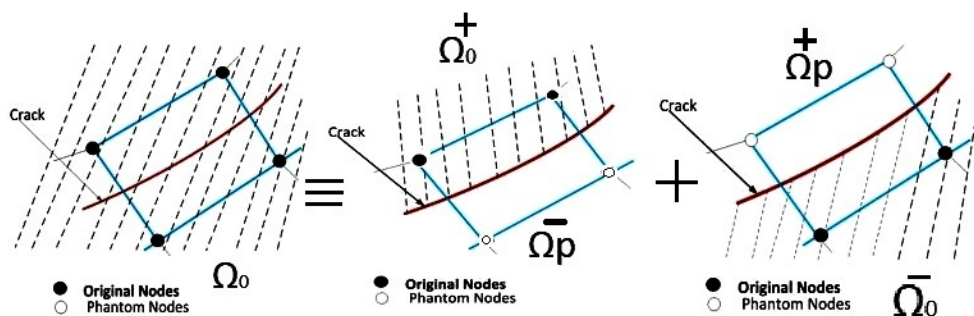


Figure 5.6: The principle of the phantom node approach in XFEM (after Simulia 2016)

(2009) is typically used for the cohesive segment approach and is valid for both the ductile and brittle material. The traction–separation response for brittle material (linear degradation) proposed

by Hillerborg et al. (1976) and for the ductile material (inverted cup shaped-nonlinear) is shown in Fig. 5.7 (Scheider 2001). The area under the traction (T_0)–separation (δ_0) in Fig. 5.7 represents the cohesive energy (Γ_0) required for the initiation of crack. In the numerical model, the energy release rate $G_{IC} = K_{IC}^2/E'$ can be used as a cohesive energy Γ_0 for the brittle material, while J–integral, $J_{IC} = K_{IC}^2/E'$ is used for the ductile materials. The material fracture toughness is denoted by K_{IC} , while E' refers to the modulus of elasticity under plane stress or plane strain conditions. In the case of plane stress, E' is equal to the material’s modulus of elasticity (E). On the other hand, for plane strain conditions, E' is given by $E/(1-\nu^2)$, where ν is Poisson’s ratio. The linear, exponential, or tabular traction separation damage evolution law is available in the Abaqus/Standard software. The XFEM-based cohesive zone modelling was successfully used for

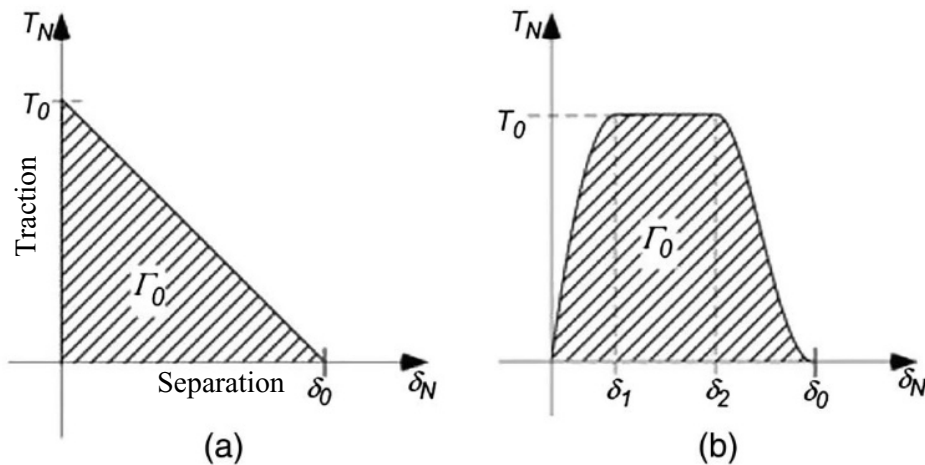


Figure 5.7: The typical traction-separation laws: (a) For brittle material with linear degradation and (b) For ductile material with inverted cup shape nonlinear degradation (after Schwalbe et al. 2013)

the fracture studies of the pipeline by various researchers (Liu et al. 2012; Zhang et al. 2016; Lin et al. 2017; Hojjati-Talemi et al. 2018; Agbo et al. 2019). Their studies were for the surface laid pipeline in tensile loading condition. The current study deals with the fracture assessment of post-buckled offshore pipeline in tensile zone under the axial compressive loadings.

5.4 Damage initiation criterion

5.4.1 MAXPS and MAXPE based criterion

For modelling of crack propagation using the XFEM, both damage initiation criterion and the damage evolution law needs be defined. The initial damage response can be linear or exponential. Once the damage initiation criterion is fully satisfied for the enriched elements, the damage evolution starts. The damage evolution law for the fracture is given by Eq. (5.9).

$$1.0 \leq f \leq 1.0 + f_{\text{tol}} \quad (5.9)$$

where f_{tol} is the tolerance with default value of 0.05. The crack starts to propagate once the value of fracture criterion (f) exceeds the value of 1.0. In the maximum principal stress or strain (MAXPS or MAXPE) criterion, the crack is always orthogonal to the direction of maximum principal stress or strain once the fracture criterion is satisfied Simulia (2016). The maximum principal stress criterion is defined by Eq. (5.10), which states the damage initiates once the maximum principal stress ratio (f) reaches to unity Eq. (5.10).

$$f = \left\{ \frac{\langle \sigma_{\text{max}} \rangle}{\sigma_{\text{max}}^0} \right\} \quad (5.10)$$

where σ_{max}^0 is the maximum allowable principal stress for the material. The Macaulay bracket $\langle \rangle$ signifies that for a purely compressive state of stress, damage will not initiate. In the maximum principal strain criterion, the damage initiates once the maximum principal strain ratio (f) in Eq. (5.11) reaches one.

$$f = \left\{ \frac{\langle \varepsilon_{\text{max}} \rangle}{\varepsilon_{\text{max}}^0} \right\} \quad (5.11)$$

where $\varepsilon_{\text{max}}^0$ is the maximum allowable principal strain. The Macaulay bracket indicates that for a purely compressive state of strain, the damage will not start. In Abaqus the user subroutine UDMGINI can be used to define the damage initiation as well as the normal direction to the crack

plane/line for equivalent fracture strain.

5.4.2 Modified Mohr–Coulomb (MMC) fracture criterion

According to the Mohr–Coulomb fracture criterion, the fracture occurs at the plane where the combined effects of the shear stress (τ) modified by the normal stress (σ_n) becomes maximum critical value given by Eq. (5.12).

$$\max(\tau + c_1 \sigma_n) = c_2 \quad (5.12)$$

where τ and σ_n are the shear and normal stress; c_1 and c_2 are the friction coefficient and shear resistance, respectively. The coefficient c_1 controls the orientation of fracture plane and c_1 and c_2 together controls the onset of fracture (Bai and Wierzbicki 2010). In the limiting condition, the coefficient c_1 becomes zero, then the Mohr–Coulomb (MC) criterion turns to the shear stress based Tresca yield criterion. Although, the Mohr–Coulomb criterion represents simple expression, the determination of parameters c_1 and c_2 is not straightforward. Thus, the reformulated MC criterion called Modified Mohr–Coulomb (MMC) is used to calibrate the fracture parameters for metal (Bai and Wierzbicki 2010).

The modified Mohr–Coulomb criterion (MMC) is used to calculate the equivalent fracture strain ($\bar{\epsilon}_f$) defined as the function of stress triaxiality (η) and normalized lode angle parameter ($\bar{\theta}$). Thus, MMC in a three-dimensional (3D) space is represented by ($\bar{\epsilon}_f, \eta, \bar{\theta}$). The stress triaxiality (η) and normalized Lode angle ($\bar{\theta}$) are defined as (Eqs. (5.13) and (5.14) respectively)

$$\eta = -\frac{p}{q} = -\frac{p}{\sqrt{3}J_2} \quad (5.13)$$

$$\bar{\theta} = 1 - \frac{6\theta}{\pi} = 1 - \frac{2}{\pi} \arccos \xi = 1 - \frac{6}{\pi} \left(\frac{1}{3} \arccos \left(\frac{3\sqrt{3}J_3}{2(J_2)^{3/2}} \right) \right) \quad (5.14)$$

where p is the hydrostatic pressure (mean stress) and q is the equivalent von Mises stress. J_2 and J_3 are the deviatoric stress invariants as defined in Eq. (5.15).

$$\begin{aligned}
p &= -\sigma_m = -(1/3)\text{tr}(\boldsymbol{\sigma}) = -\frac{1}{3}(\sigma_1 + \sigma_2 + \sigma_3) \\
q &= \sqrt{3J_2} = \sqrt{\frac{3}{2}[\mathbf{s}] : [\mathbf{s}]} \\
[\mathbf{s}] &= [\boldsymbol{\sigma}] - \frac{1}{3}\text{tr}([\boldsymbol{\sigma}])[\mathbf{I}]; J_2 = \frac{1}{2}[\mathbf{s}] : [\mathbf{s}], J_3 = \det([\mathbf{s}]) \\
r &= \left[\frac{27}{2}\det([\mathbf{s}]) \right]^{\frac{1}{3}} = \left[\frac{27}{2}(\sigma_1 - \sigma_m)(\sigma_2 - \sigma_m)(\sigma_3 - \sigma_m) \right]^{\frac{1}{3}}
\end{aligned} \tag{5.15}$$

where $[\mathbf{s}]$ is the second order deviatoric stress tensor and r is the polar radius in Eq. (5.8). The stress representation of the Mohr–Coulomb criterion with respect to the stress triaxiality (η) and Lode angle (θ) is given by Eq. (5.16) (Bai and Wierzbicki 2008).

$$\bar{\sigma} = c_2 \left[\sqrt{\frac{1+c_1^2}{3}} \cos\left(\frac{\pi}{6} - \theta\right) + c_1 \left(\eta + \frac{1}{3} \sin\left(\frac{\pi}{6} - \theta\right) \right) \right]^{-1} \tag{5.16}$$

It has been observed that the amount of strain from the stress representation of Mohr–Coulomb fracture criterion is significantly higher for ductile material, which requires the conversion of equivalent stress in terms of equivalent strain (Bai and Wierzbicki 2008). Bai and Wierzbicki (2010) extended the stress-based Mohr–Coulomb fracture formulation to the strain-based one for the ductile fractures. They also proposed the generalized hardening rule as a function of Lode angle (Eq. (5.17)).

$$\bar{\sigma} = A\bar{\epsilon}^n \left[c_3 + \frac{\sqrt{3}}{2-\sqrt{3}}(1-c_3) \left(\sec\left(\frac{\bar{\theta}\pi}{6} - 1\right) \right) \right] \tag{5.17}$$

where c_3 is the third parameter to be obtained from the test. On inverting the Eq. (5.17) with the elimination of equivalent stress from Eq. (5.16), the equivalent plastic strain at fracture with

normalized stress triaxiality and Lode angle can be expressed as Eq. (5.18).

$$\bar{\epsilon}_f = \left\{ \frac{A}{c_2} [1 - c_\eta](\eta - \eta_0) \times \left[c_\theta^s + \frac{\sqrt{3}}{2 - \sqrt{3}}(c_\theta^{\text{ax}} - c_\theta^s) \left(\sec \left(\frac{\bar{\theta}\pi}{6} \right) - 1 \right) \right] \right. \\ \left. \left[\sqrt{\frac{1 + c_1^2}{3}} \cos \left(\frac{\bar{\theta}\pi}{6} \right) + c_1 \left(\eta + \frac{1}{3} \sin \left(\frac{\bar{\theta}\pi}{6} \right) \right) \right] \right\}^{-\frac{1}{n}} \quad (5.18)$$

$$\text{and } c_\theta^{\text{ax}} = \begin{cases} 1, & \text{for } \bar{\theta} \geq 0 \\ c_\theta^c & \text{for } \bar{\theta} < 0 \end{cases}$$

where A and n are the strain hardening parameter for the material; c_1 and c_2 are the primary fracture parameters that need to be calibrated from fracture tests; c_η and η_0 are pressure dependence parameters; the additional Lode angle dependence parameters are c_θ^s and c_θ^c , and n is the material strain hardening parameter. For the von Mises yield condition $c_\eta = 0, c_\theta^s = c_\theta^c = 1$ can be used, whereas for the Tresca yield condition $c_\eta = 0, c_\theta^s = \frac{\sqrt{3}}{2}$ and $c_\theta^c = 1$ is used. Furthermore, the equivalent fracture equation (MMC) is modified with the five constant parameters (n, c_1, c_2, c_3 and c_4) as unknown variables (Lin 2021). The graphical representation of the Lode angle (θ) and the locus of the modified Mohr–Coulomb criterion is shown in Fig. 5.8. The modified equivalent equation for fracture strain is given in Eq. (5.19) (Lin 2021).

$$\bar{\epsilon}_f = \left\{ c_2 \times \left[c_3 + \frac{\sqrt{3}}{2 - \sqrt{3}}(c_4 - c_3) \left(\sec \left(\frac{\bar{\theta}\pi}{6} \right) - 1 \right) \right] \right. \\ \left. \times \left[\sqrt{\frac{1 + c_1^2}{3}} \cos \left(\frac{\bar{\theta}\pi}{6} \right) + c_1 \left(\eta + \frac{1}{3} \sin \left(\frac{\bar{\theta}\pi}{6} \right) \right) \right] \right\}^{-\frac{1}{n}} \quad (5.19)$$

where $c_4 = 1$ for $0 \leq \bar{\theta} \leq 1$

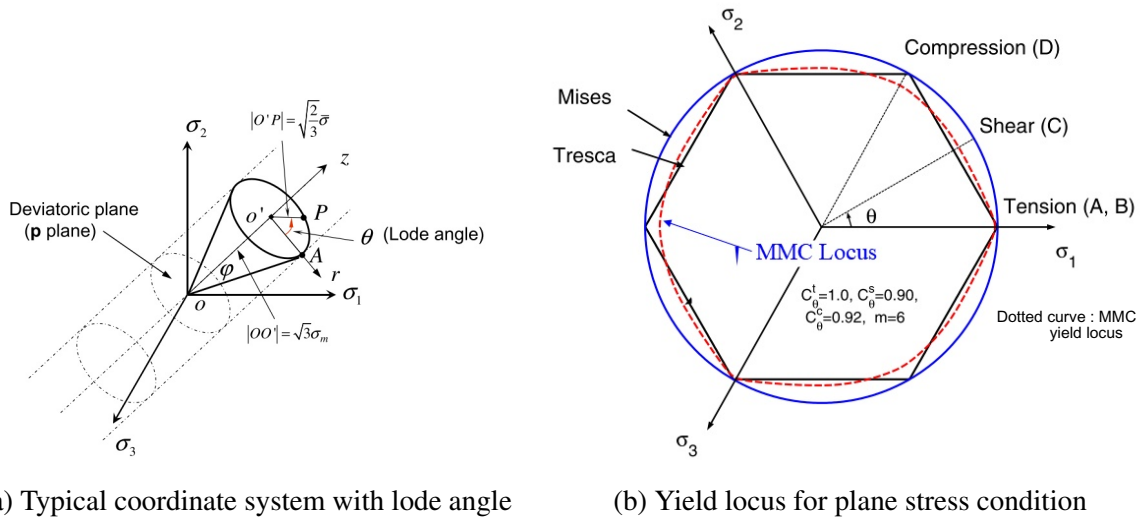


Figure 5.8: Representation of lode angle (θ) and MMC yield locus (after Bai and Wierzbicki 2010):
 (a) Typical coordinate system with lode angle; (b) Yield locus for plane stress condition

The fracture initiates when the damage parameter D defined in Eq. (5.20) reaches unity.

$$D(\bar{\epsilon}_p) = \int_0^{\bar{\epsilon}_f} \frac{d\bar{\epsilon}_p}{\bar{\epsilon}_f(\eta, \bar{\theta})} \quad (5.20)$$

where $d\bar{\epsilon}_p$ is the effective plastic strain increment and $\bar{\epsilon}_f$ is the strain to fracture as calculated from MMC in Eq. (5.19).

In the damage models defined above, the maximum energy release criterion is used to define the crack propagation once the maximum energy release rate (G_θ) in Eq. (5.21) reaches the critical value (G_c).

$$G_\theta = \frac{1-\nu^2}{E} (K_{I\theta}^2) \quad (5.21)$$

The crack propagates along the direction of the maximum energy release rate, defined by Eq. (5.22).

$$\left. \frac{\partial G_\theta}{\partial \theta} \right|_{\theta=\theta_0} = 0, \quad \left. \frac{\partial^2 G_\theta}{\partial \theta^2} \right|_{\theta=\theta_0} < 0 \quad (5.22)$$

5.5 Numerical Modelling using XFEM

5.5.1 Modelling of the geometry

In the current study, an XFEM-based cohesive segment approach is used to model crack initiation and propagation in the post-buckled pipeline. The numerical models incorporate linear elastic fracture mechanics approach with linear traction-separation law and damage initiation and evolution models. The FE mesh is refined in the crack zone to reduce mesh dependency and computational time, with a minimum mesh size of $1/12^{\text{th}}$ (1.06 mm) of the pipe wall thickness as recommended by Nonn and Kalwa (2013). The numerical solution involves three analysis steps: first, the initial prestress conditions were assigned to the pipe model from coupled pipe-shell analysis as discussed in Section 5.2.2 and the self-weight of the oil-filled pipeline with the outer concrete cover was assigned as a line load along the longitudinal central axis of the symmetric pipe; second, an internal pipe pressure (p) of 5 MPa was applied; and third, axial compressive loading was applied as a displacement (u_1 and u_2) through a long rigid beam connected at the far ends of the post-buckled pipeline, as shown in Fig. 5.4.

The numerical model uses solid eight-node linear brick elements with reduced integration (C3D8R in Abaqus). An initial crack with a mode-I opening fracture model was applied at the center of the post-buckled segment of the pipe, which is predominant over sliding and shearing modes of the fracture for this case of post-buckled pipeline.

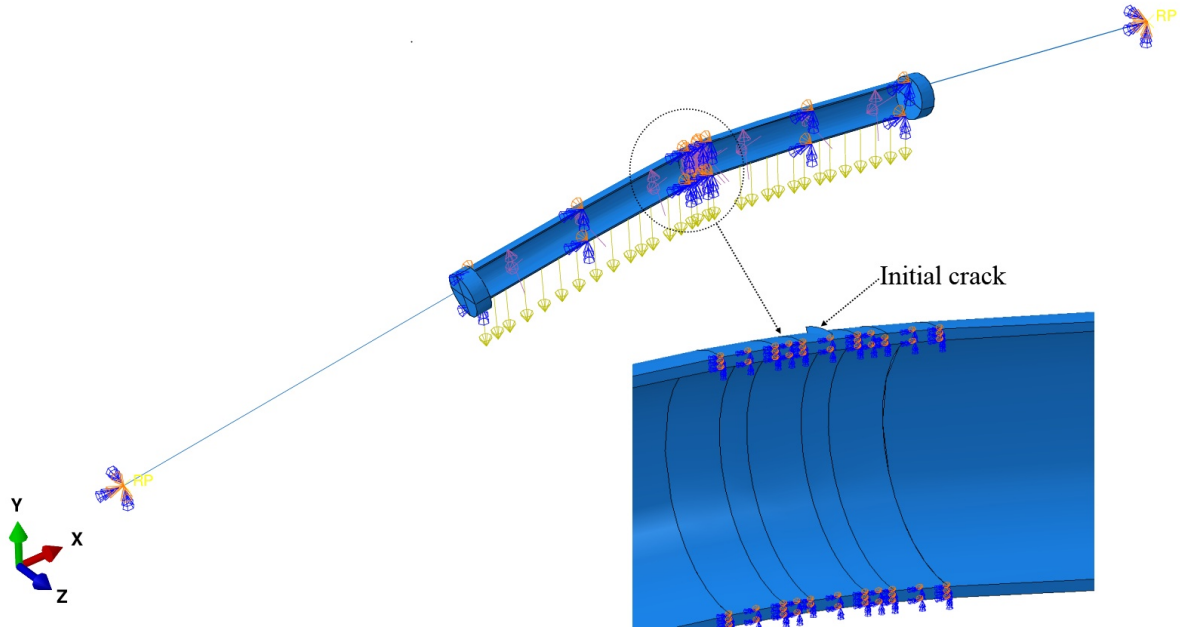
The model was divided into three different solid parts, with the pipe end parts having a coarse mesh and the central part with a fine mesh. The FE Mesh was generated with gradually increasing element size of 2.1x2.1x2.1 mm from the central crack location to the ends. A mesh convergence analysis was carried out to confirm the element size, ensuring that the solution is independent of the mesh. The three parts (central fine mesh, and two outer coarse mesh regions in symmetric model) (see Fig. 5.4) are coupled using surface-to-surface contact discretization methods. The central solid part, which contains the initial crack, is 0.2 m in length, whereas the outer solid pipe

is 1.83 m in length on each side. Rigid end plates are added at each end of the solid pipe with tie constraints to distribute stress uniformly at the pipe ends. Symmetric boundary conditions was applied along the line of symmetry, and the displacement was restrained in the u_3 direction at the central node, as shown in Fig. 5.4. FE mesh and the boundary conditions are shown in Fig. 5.9. The numerical model takes into account the effects of nonlinearity in geometry and large strain. The FE analyses of crack propagation were carried out using built-in damage initiation criteria, which rely on the maximum principal stress, maximum principal strain, and a modified Mohr–Coulomb criterion (MMC) using the UDMGINI (user defined damage initiation criterion) subroutine available in Abaqus software for enriched elements. The rigid ends are subjected to a displacement-based boundary condition in two directions, u_1 and u_2 , zero rotation in the axial direction ($ur_1 = 0$) and zero displacement in u_3 direction to account for axial compression and bending moment during the upward movement of the pipeline.

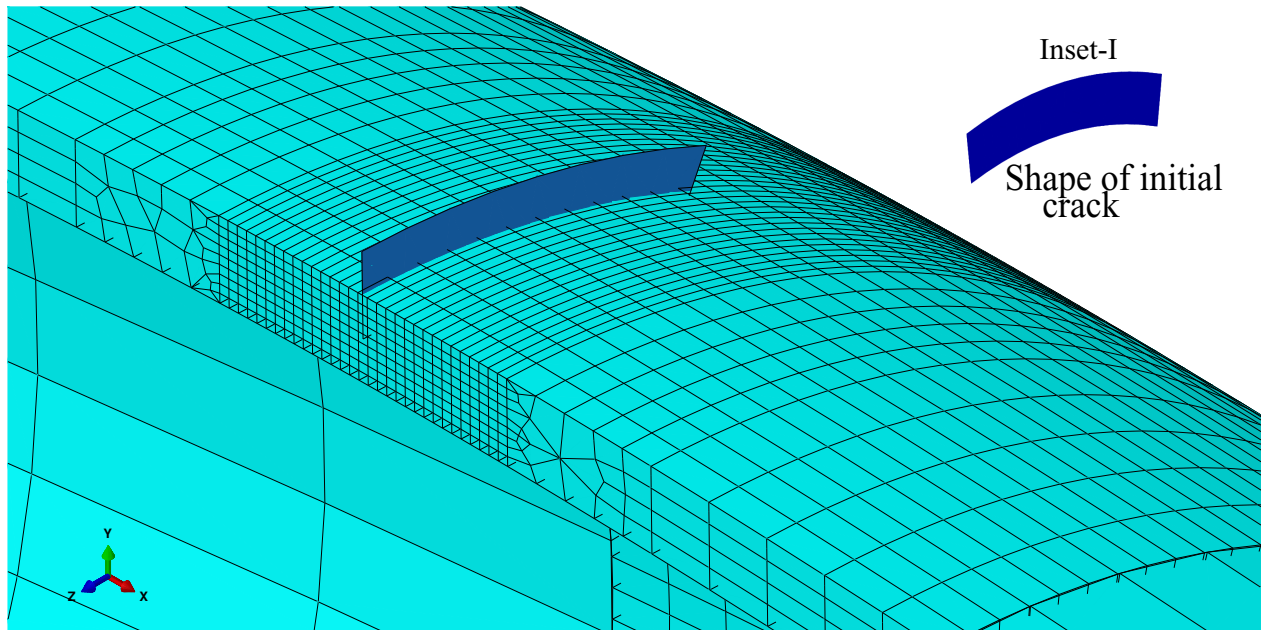
5.5.2 Material properties for the fracture analysis

The material properties used in the model are given in Table 5.2. The true stress–strain curve available in Oh et al. (2011) with isotropic power-law hardening was used in the analysis as shown in Fig. 5.10. Table 5.3 provides the plasticity and fracture modelling parameters for the strain-based modified Mohr–Coulomb (MMC) fracture model of API X65 steel pipe (seamless and seam welded) as reported in the literature Kofiani (2013); Paredes et al. (2018); Mohajer et al. (2018).

The resistance of a steel pipeline against crack opening and propagation is dependent on important parameters such as the maximum principal stress ($\sigma_{\max,ps}$) and the fracture energy (G_c). Unfortunately, limited experimental data are available in the literature for these parameters. To address this, Scheider et al. (2014) conducted experiments on X65 steel pipe using drop-weight tear testing (DWTT) and cohesive zone modelling, which led to the calibration of the maximum principal stress and fracture energy values to be 1375 MPa and 900 J/m² (N/mm), respectively.



(a) Finite element symmetric model with loading and boundary conditions



(b) Location of initial crack and mesh distribution

Figure 5.9: Symmetric finite element model with mesh distribution for post-UHB fracture assessment: (a) Finite element symmetric model with loading and boundary conditions; (b) Location of initial crack and mesh distribution (shape of initial crack at Inset-I)

Table 5.2: Geometry and material properties used for the fracture assessment

Parameters	Value
External diameter of pipe, D (m)	0.3
Wall thickness of pipe, t (m)	0.0127
Poisson's ratio of pipe (μ)	0.3
Young's modulus of pipe, E (GPa)	206
Submerged weight of oil-filled pipe, q (N/m)	1594
Yield stress of pipe material, σ_y (MPa)	448
Ultimate tensile strength of pipe material, σ_{ult} (MPa)	531
Coefficient of thermal expansion, (α)	11×10^{-6}
Effective differential pressure, p (MPa)	5
Thickness of concrete cover (m)*	0.05
Density of steel, ρ_s (kg/m^3)*	7850
Density of concrete, ρ_c (kg/m^3)*	2800
Density of oil, ρ_o (kg/m^3)*	800

* Parameters used to calculate submerged weight of oil-filled pipe per meter length

However, it is worth noting that the maximum principal stress is over three times the yield strength of the steel pipe material. According to Schwalbe et al. (2009), for ductile materials, the cohesive strength can be estimated as approximately three times the yield stress of the material. This is a rough approximation that assumes that the material behavior is isotropic, homogeneous and free from defects. However, in practice, the cohesive strength (force required to cause fracture or separation) of a material can be significantly higher than its yield stress due to a variety of factors such as the presence of defects, notches or sharp corners (acts as a stress concentrations within the material), and anisotropic behavior (varying mechanical properties with the loading direction). Therefore, it is important to carefully consider the specific material properties and loading

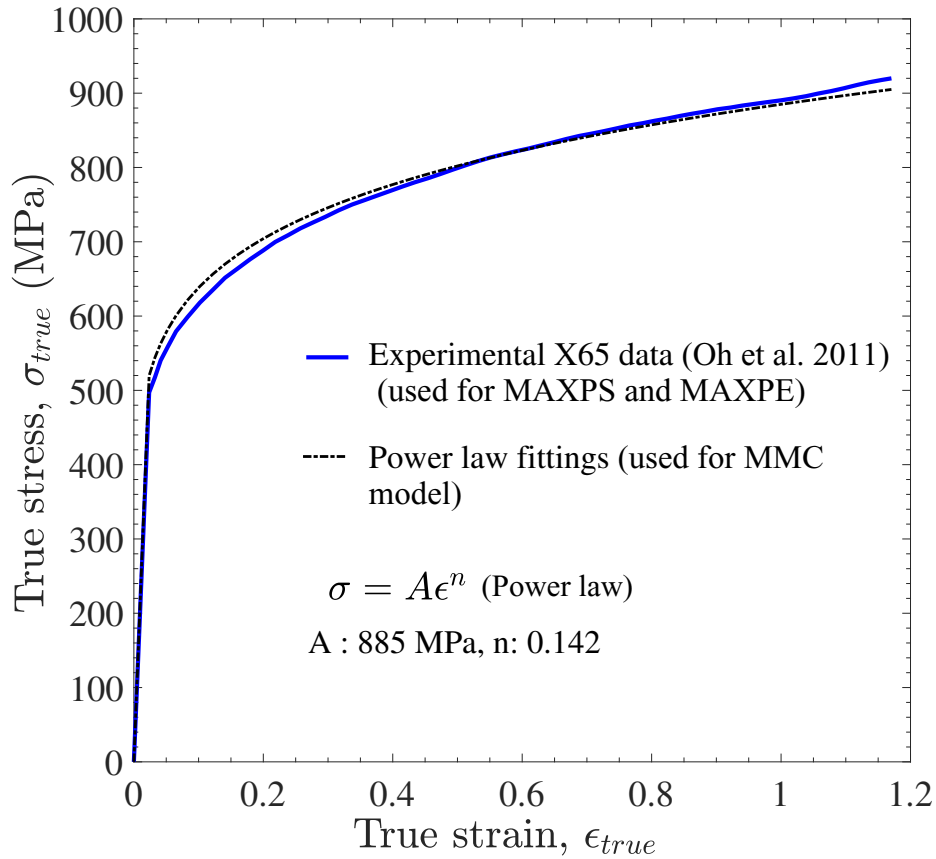


Figure 5.10: True stress–strain curve for X65 steel pipe with power law fitting

conditions when determining the cohesive strength of a material. This study examines the notable variations in fracture behavior of post-buckled pipeline associated with different values of maximum principal stress (MAXPS) and fracture energy (G_c).

5.6 Verification and calibration of the fracture parameters

Proper selection of damage parameters, such as energy release rate (G_c), maximum principal stress (MAXPS as σ_1), and maximum principal strain (MAXPE as ϵ_1), is necessary for crack propagation analysis using XFEM with MAXPS damage criterion. Liu (2017) found that fracture initiation and propagation are strongly influenced by material fracture properties and specimen geometry.

Proper selection of maximum principal strain and fracture energy release rate is critical in the

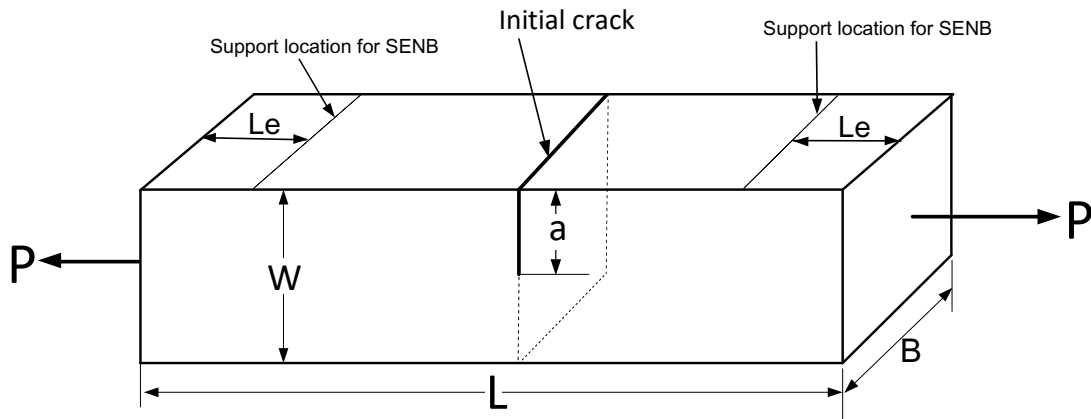
Table 5.3: Plasticity and fracture parameter for strain-based MMC fracture model API X65

Pipe	Plasticity parameters		Fracture Parameters				Reference	
	n	$A(\text{MPa})$	c_1	$c_2^* (\text{MPa})$	$c_2 = \frac{A}{c_2^*}$	c_3		c_4
X65 seamless (SL)	0.2	991.19	0.12	598.44	1.66	0.9	1	Paredes et al. (2018)
X65 seamless (SL)	0.0984	844.6	0.05	454	1.86	0.91	1	Kofiani (2013)
X65 seam welded (SW)	0.054	722.35	0.029	381.77	1.89	0.87	1	Paredes et al. (2018)
X65 seam welded (SW)	0.0834	830.96	0.0499	458.98	1.81	0.912	1.031	Mohajer et al. (2018)
X65 (Used in this study)	0.142	885	0.1	465	1.903	0.9	1	Oh et al. (2011)

maximum principal strain-based damage criterion. According to Agbo et al. (2019), this criterion is better suited for capturing geometric and material nonlinearity in highly ductile materials. In XFEM, the maximum principal stress or strain controls damage initiation, while the energy release rate G_c controls crack propagation speed. To validate XFEM based fracture parameters, test results reported in Oh et al. (2011), commonly used single edge notched tension (SENT) and single edge notched bend (SENB) tests, were simulated using FE analysis.

Figure 5.11 shows the specimens with an initial crack utilized for SENT and SENB tests to validate XFEM and model parameters. The Fig. 5.11 illustrates the dimensions for the SENT and SENB FE model. In the case of the SENT specimen, the tensile load is applied at the ends, while for the SENB specimen, the bending is applied with a load at the center of bottom face of the specimen. The top face of the SENB specimen is fixed with a rigid support at a distance of L_e from each end. The dimensions of these specimens are based on the experimental study conducted by Oh et al. (2011). The nonlinear stress–strain behaviour of X65 grade steel (Fig. 5.10) was used in the analysis.

Figure 5.12 shows the FE model for SENT and SENB specimens respectively, including FE mesh



For SENT:

W = 12.5 mm
 L = 80.0 mm
 B = 25.0 mm
 a = 6.25 mm

For SENB:

W = 10 mm
 L = 60 mm
 B = 10 mm
 a = 5 mm
 Support radius = 5 mm
 Support location (Le) = 10 mm

Figure 5.11: Specimen for SENT and SENB test

and boundary conditions. To improve computational efficiency, the C3D8 (8-node linear brick) and C3D4 (4-node linear tetrahedron) elements were utilized to discretize the SENT and SENB numerical model, as illustrated in Fig. 5.12(a) and 5.12(b), respectively. The central part cut by the crack was meshed with C3D8 brick elements whereas the interface is meshed with tetrahedron C3D4 elements as shown in Fig. 5.12(a). A kinematic coupling constraint was imposed to fix the displacement and rotation of one end of the specimen, with the other end subjected to axial loading. The axial displacement-based loading is applied through the single node at the planar center using the kinematic coupling constraint such that the degree of freedom in translation and rotation is fixed and the boundary effect is minimized.

The initial 3D planar crack of rectangular shape was positioned at the specimen's central location as shown in Fig. 5.12(a) and Fig. 5.12(b). In both numerical models, the equivalent energy release rate based on BK law (Simulia 2016) with a power of 2.274 was employed, and the crack depth to the

specimen height ratio of 0.5 was used. To ensure numerical accuracy, a fine mesh with an element size of 0.15 mm was used along the crack propagation direction, satisfying the minimum mesh size recommended by Nonn and Kalwa (2013) and Scheider et al. (2014) of $1/12^{\text{th}}$ (i.e., 1.06 mm) of the wall thickness. The cohesive crack initiates once the maximum principal stress reaches the critical limit and then propagates based on the linear or exponential traction-separation softening response. The FE simulation results for tensile specimens with crack development, using both linear and exponential softening damage models at the axial displacement (u_z) of ≈ 2.6 mm are presented in Fig. 5.13. Upon examining the results, several key observations can be made. In the case of the linear softening damage model with the MAXPS criterion, the crack mouth opening width (CMOD) (a in Fig. 5.13) reaches 2.69 mm, accompanied by a propagation depth (d in Fig. 5.13) of 5.75 mm. On the other hand, the exponential softening damage model with the MAXPS criterion results in a larger crack opening width of $a = 2.75$ mm, but with a smaller propagation depth $d = 4$ mm compared to the linear model. Note that the exponential softening damage model demonstrates a greater ability to account for excessive plastic deformation when compared to the linear damage model.

In Fig. 5.14, the relationship between axial force and CMOD (a) is presented for different damage parameters with different modelling techniques used in SENT and SENB simulation. Despite the FE simulations being conducted using displacement-based loading, the axial force is employed in this analysis to maintain consistency with the results reported in the literature (DNV 2006, Kofiani 2013, Zhang et al. 2014a). The axial tensile force is equal to the reaction force at the location where axial displacement is applied. The axial tensile force and CMOD for a propagating crack during SENT tests are depicted in Fig. 5.14(a) for varying values of maximum principal stress ($\sigma_{\text{max,ps}}$) and fracture energy (G_c). To obtain the CMOD, the absolute differences in nodal displacements along the longitudinal direction were measured at the nodes located at the mouth of the resulting crack Kofiani (2013) (Fig. 5.13). When the lower values of maximum principal stress and fracture energy are used in the linear softening model, it shows an early onset and propagation of the crack.

On the other hand, the exponential softening model exhibits a greater degree of plastic deformation during crack propagation. Figure 5.14 shows that the linear and exponential softening traction-separation damage evolution model results in significant differences in force-CMOD response.

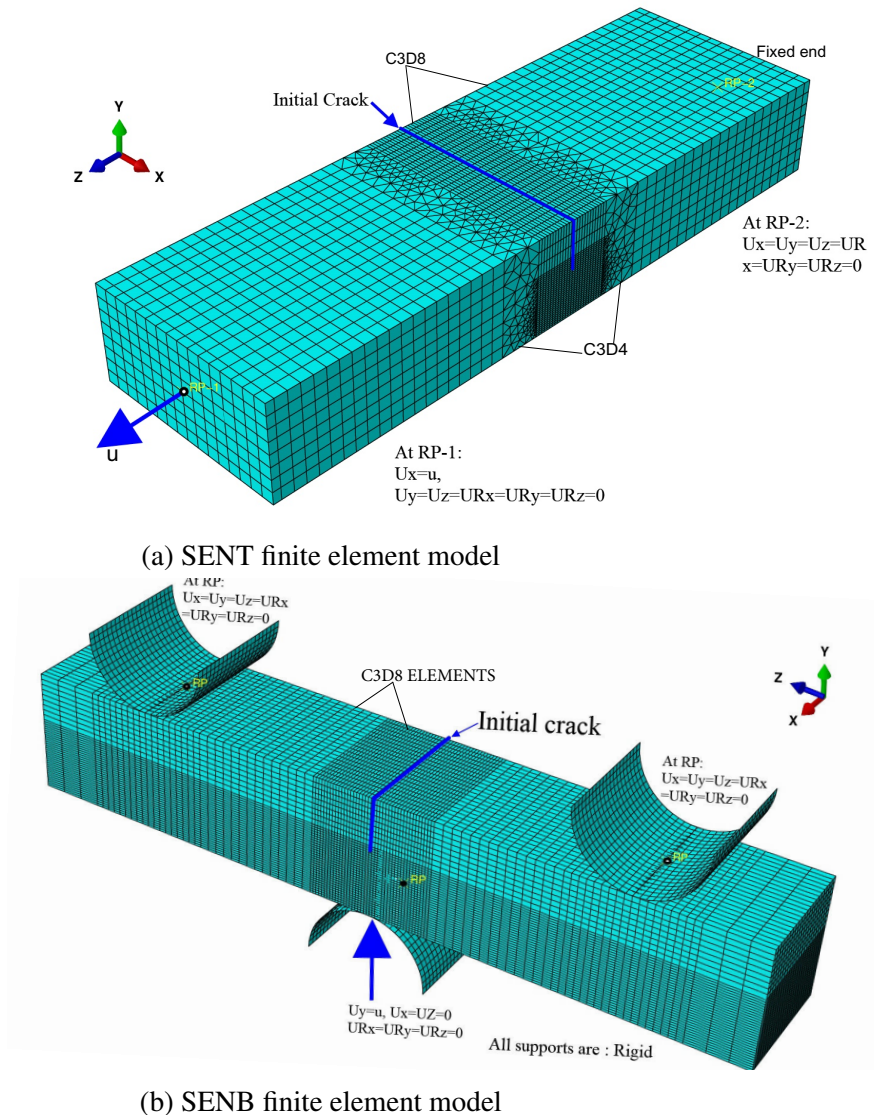


Figure 5.12: SENT and SENB finite element models with boundary conditions: (a) SENT finite element model; (b) SENB finite element model

The results in Fig. 5.14(a) and Fig. 5.14(b) show that the MMC damage model with linear softening (refer Section 5.7.3) accurately predicts the crack behaviour prior to undergoing significant plastic deformation during crack propagation. The numerical simulation calibrated the appropriate values

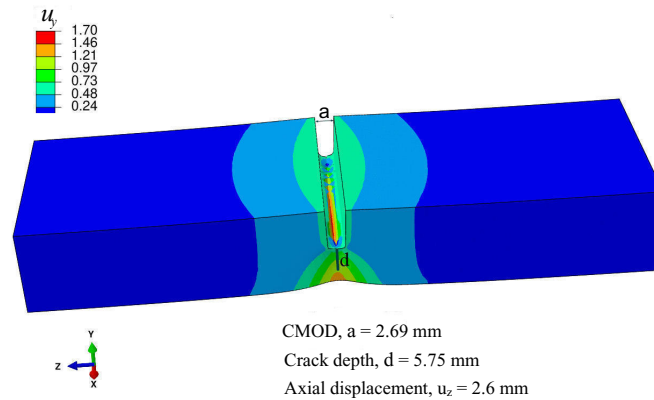
of $\sigma_{\max,ps}$ and G_c for the pipe material through the XFEM-based approach. With a linear softening response of damage evolution, a minimum deviation from the experimental results was observed for $G_c = 450$ N/mm (Fig. 5.14). Also, the computational cost is less for the linear softening model than the exponential model. Therefore, for further fracture analysis of pipe, a linear softening traction-separation damage degradation model is used for MAXPS, MAXPE and MMC models. The parameters used for the MMC model are shown in Table 5.3.

5.7 Results of pipeline analysis

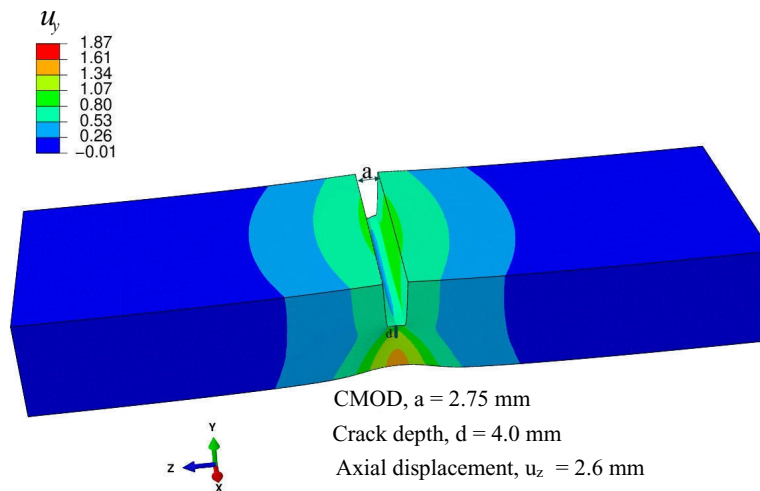
This section presents the results obtained using various fracture criteria used to study post-buckling fracture behaviour of the offshore pipelines. The results include those obtained using the maximum principal stress damage criterion (MAXPS), maximum principal strain damage criterion (MAXPE), and the modified Mohr–Coulomb fracture criterion (MMC). Based on the analysis, it is observed that different damage initiation criteria can lead to variations in fracture characteristics. Although the critical fracture parameters differ for each criterion, the focus of the study is on the fracture surface response, tensile strain at the onset of crack propagation and the CMOD. The model with initial crack is depicted in Fig. 5.9(a). The initial configuration of the post-buckled shape of pipeline is determined by the shape function described in Eq. (5.3).

5.7.1 Results from MAXPS fracture criterion

The maximum principal stress fracture criterion employs two parameters: the maximum principal stress (MAXPS) and a linear damage evolution law with energy release rate (G_c). To avoid convergence issues in the FE model, a damage tolerance of 0.05 is used. The FE simulation investigates the variation of axial force (equivalent resultant reaction force at the point of application of displacement, refer to Fig. 5.4) with CMOD for different values of MAXPS and G_c . As illustrated in Fig. 5.15, the peak axial force steadily increases with CMOD to the crack propagation stage (See the red filled circle in Fig. 5.15). After the crack propagation stage, a sharp



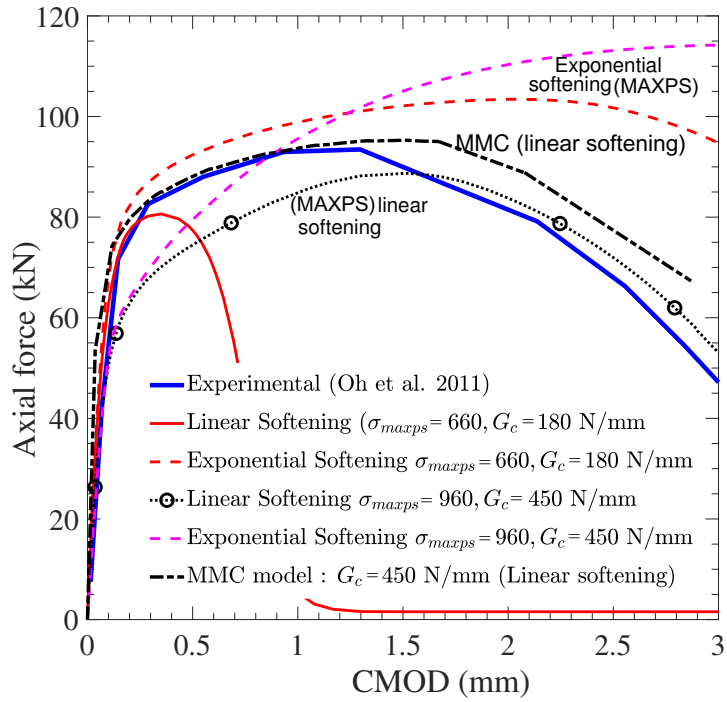
(a) Crack propagation in SENT model with linear softening damage model



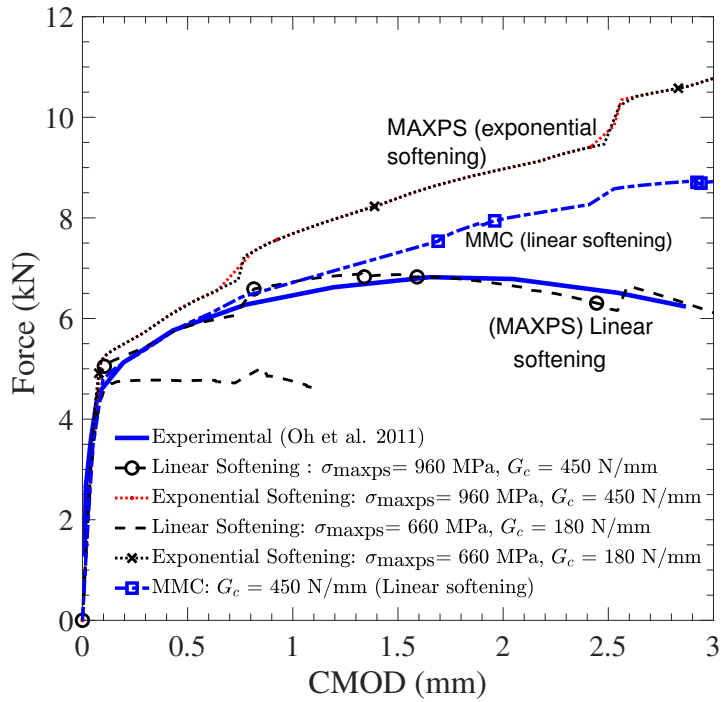
(b) Crack propagation in SENT model with exponential softening damage model

Figure 5.13: Crack opening and propagation at SENT specimen with linear and exponential softening damage model: (a) Crack propagation in SENT model with linear softening damage model; (b) Crack propagation in SENT model with exponential softening damage model

drop in axial force is observed when the fracture parameter from Scheider et al. (2014) is used (black dash-dotted line in Fig. 5.15), whereas the analyses with SENT and SENB calibrated parameters show a smooth drop in axial force with CMOD due to uplift displacement of the pipe.



(a) SENT specimen Force-CMOD relation



(b) SENB specimen Force-CMOD relation

Figure 5.14: SENT and SENB specimen force-deformation responses with XFEM based fracture analysis with MAXPS and MMC: (a) SENT specimen Force-CMOD relation; (b) SENB specimen Force-CMOD relation

This discrepancy is attributed to the higher MAXPS and G_c values from Scheider et al. (2014), which require a greater amount of fracture energy for crack propagation. The lower bound MAXPS fracture parameters provided a smooth drop in axial force with crack opening (blue dashed line in Fig. 5.15).

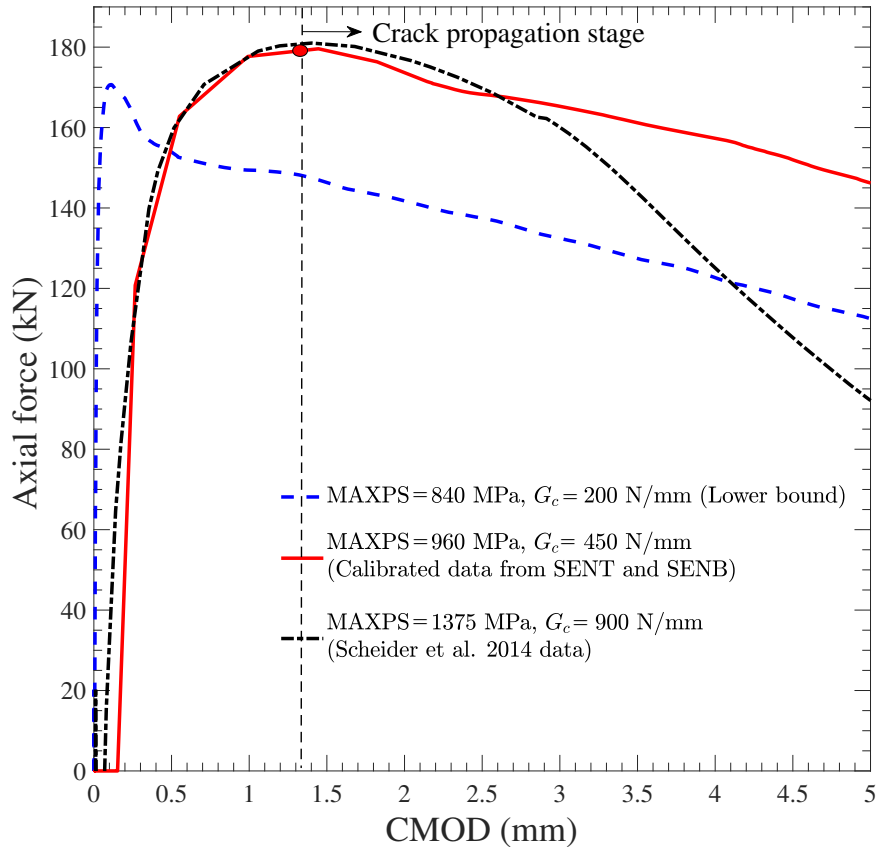


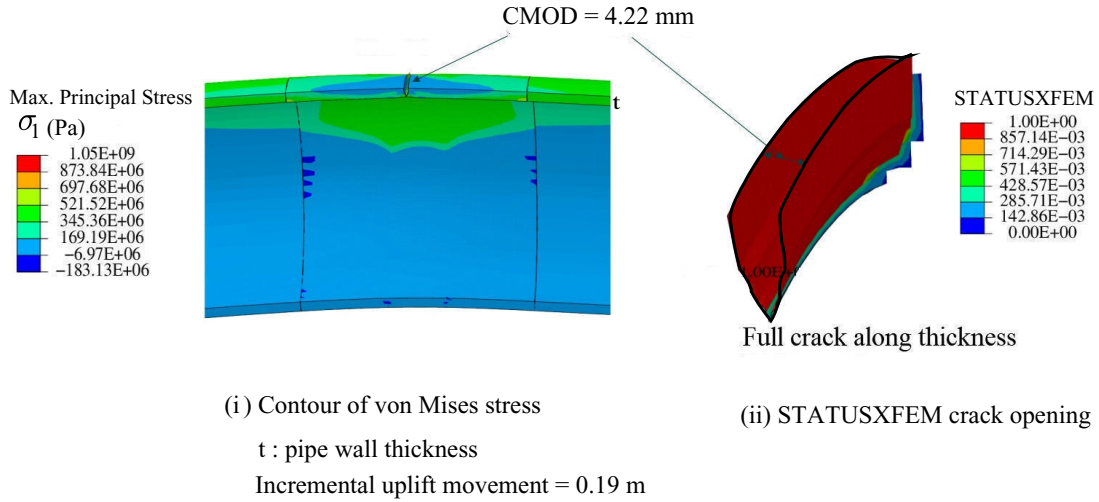
Figure 5.15: Axial force versus CMOD variation based on MAXPS fracture criterion for pipe

Figure 5.16 shows the fracture profiles for various values of the MAXPS damage criterion for pipe uplift displacement of 0.19 m. In this analysis, the uplift displacement refers to the incremental upward displacement of the post-buckled pipe from the initial condition used in the analysis shown in Fig. 5.4. The results show that at the uplift movement of 0.19 m, for damage parameters of 960 MPa and 450 N/mm, the tensile crack opens, propagates and completely penetrates through the thickness of the pipe as shown in Fig. 5.16(a). The crack mouth opening distance is 4.22 mm.

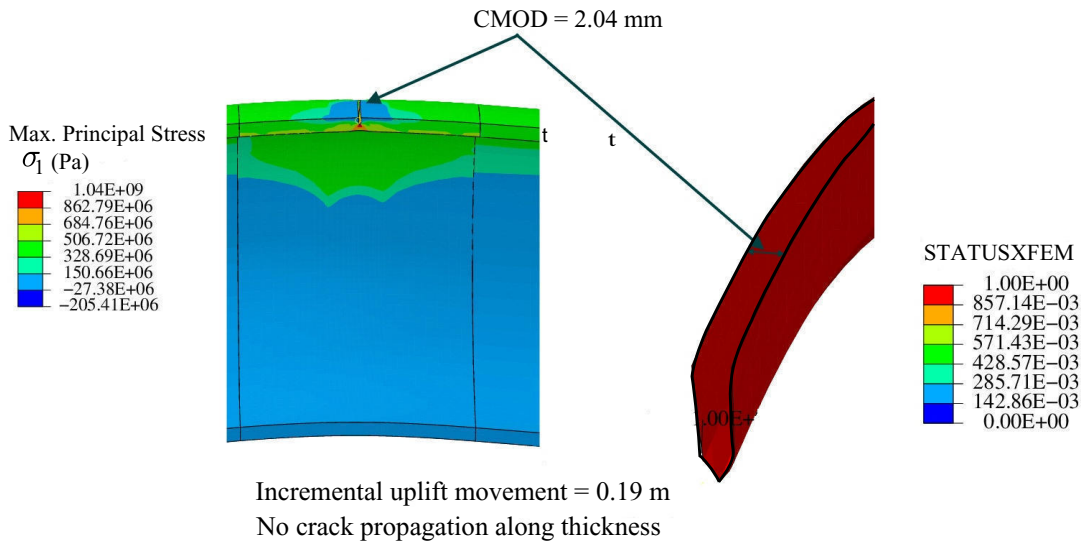
The fractured elements reached a maximum principal stress of 1050 MPa at the instance of full crack penetration, which exceeds the MAXPS damage parameter. The STATUSXFEM on the right-hand side of Fig. 5.16(a) illustrates elements that have been either fully or partially fractured. An element with a STATUSXFEM value of 1.0 indicates complete fracture, whereas a value less than 1.0 indicates partial fracture of the element. At the uplift displacement of 0.19 m, most of the elements are completely fractured, as observed from the STATUSXFEM.

However, at the same uplift displacement of 0.19 m, the fracture profile obtained using the damage parameters from Scheider et al. (2014) (shown in Fig. 5.16(b)) shows that the crack opens but does not propagate. At that instance, a crack opening of 2.04 mm is calculated, which is lower than the one with the damage parameters used in the previous case (i.e., 4.22 mm). Additionally, the fracture element attains a maximum principal stress of 1040 MPa, which is lower than the MAXPS parameter of 1375 MPa. Furthermore, the STATUSXFEM on the right of Fig. 5.16(b) shows that the elements with a complete fracture at the initial crack level, without any partial fracture elements. This comparison shows that the fracture parameters available from Scheider et al. (2014) can underestimate the crack propagation behavior for X65 pipe. For X65-grade steel pipe using a linear softening degradation model with the MAXPS fracture criterion with the parameters of 960 MPa and G_C of 450 N/mm is a viable option for fracture assessment.

Figure 5.17 illustrates the stages of crack propagation in a post-buckled pipeline during upward movement with the damage parameters of 960 MPa and G_C of 450 N/mm. In this figure, PHILSM represented by $\phi(x)$ (details in Section 5.3.1) function in XFEM is used to show the location of crack evolution along the pipe thickness. $\phi(x)$ is the level set signed distance function from the initial position of the crack to the resulting crack surface. Here, the x, y, and z axes in Fig. 5.17 represent the axial, vertical, and radial directions, respectively. Figure 5.17(a) is the initial prestress state with an initial crack. As the uplift displacement reaches 0.19 m (Fig. 5.17(b)), the crack fully cuts through the wall thickness and begin to propagate along the circumference. Once the upward displacement reaches 0.24 m (Fig. 5.17(c)), the initial crack fully opens through the



(a) MAXPS 960 MPa and fracture energy release rate 450 N/mm



(b) MAXPS 1375 MPa and fracture energy release rate 900 N/mm

Figure 5.16: Fracture profile and status of XFEM enriched elements based on different values of MAXPS damage criterion: (a) MAXPS 960 MPa and fracture energy release rate, G_c of 450 N/mm; (b) MAXPS 1375 MPa and fracture energy release, G_c of 900 N/mm

pipe circumference, and it initiates to propagate along the circumference. The location of the propagated crack along the circumference at the uplift displacement of 0.35 m is shown in Fig. 5.17(d).

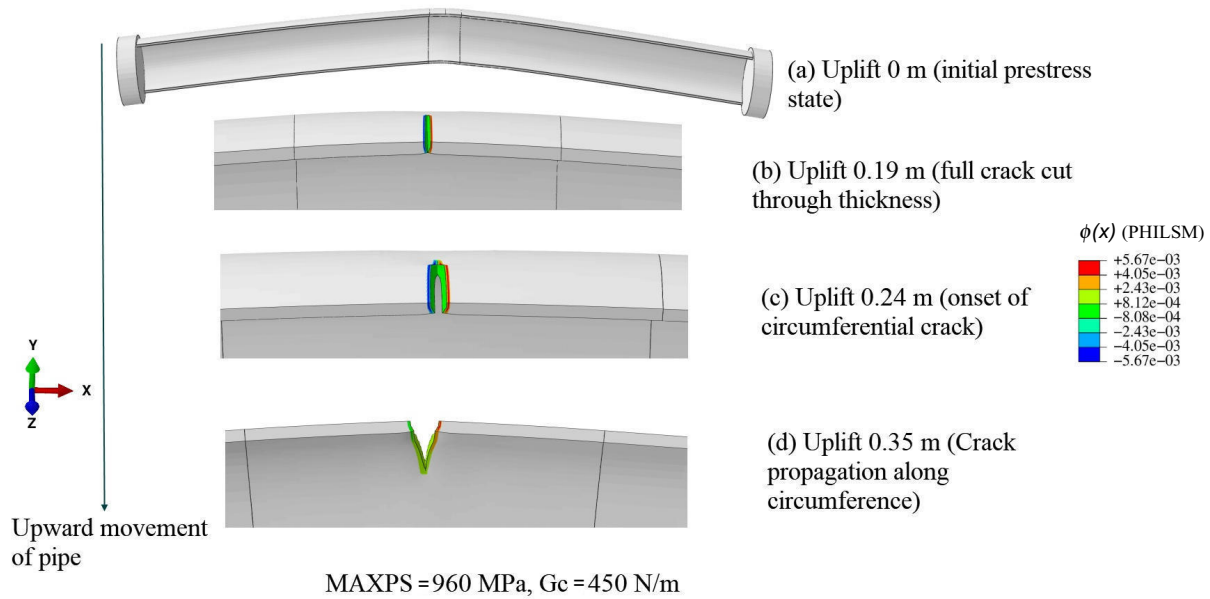


Figure 5.17: Tensile crack propagation stages during uplift movement of the pipeline based on MAXPS damage criterion: (a) Uplift at 0; (b) Uplift at 0.19 m; (c) Uplift at 0.24 m; (d) Uplift at 0.35 m

5.7.2 Results from MAXPE fracture criterion

The maximum principal strain damage criterion consists of the fixed value of maximum principal strain and the linear damage evolution law with energy release rate (G_c). In this analysis, the maximum principal strain value of 0.013 and 0.15 is used, based on the study of Agbo et al. (2019), with the energy release rate of 200 N/mm and 450 N/mm. The CMOD variation with the axial compressive force is shown in Fig. 5.18. The fracture result with maximum principal strain of 0.15 and G_c of 450 N/mm (black dash-dotted line) shows a similar trend with the results based on

maximum principal stress criterion with parameters of 960 MPa and G_c of 450 N/mm (solid green line). The dotted red and solid blue line shows the results for MAXPE of 0.013 (Agbo et al. 2019) with G_c of 450 N/mm and 200 N/mm, respectively. The result shows that a lower value of MAXPE leads to the early initiation of a crack, exhibiting a brittle-like fracture behavior. The fracture profile with the maximum principal strain (ϵ_1) development based on MAXPE damage criterion is shown in Fig. 5.19 for the uplift displacement of 0.18 m. Figure 5.19 depicts that when the energy release

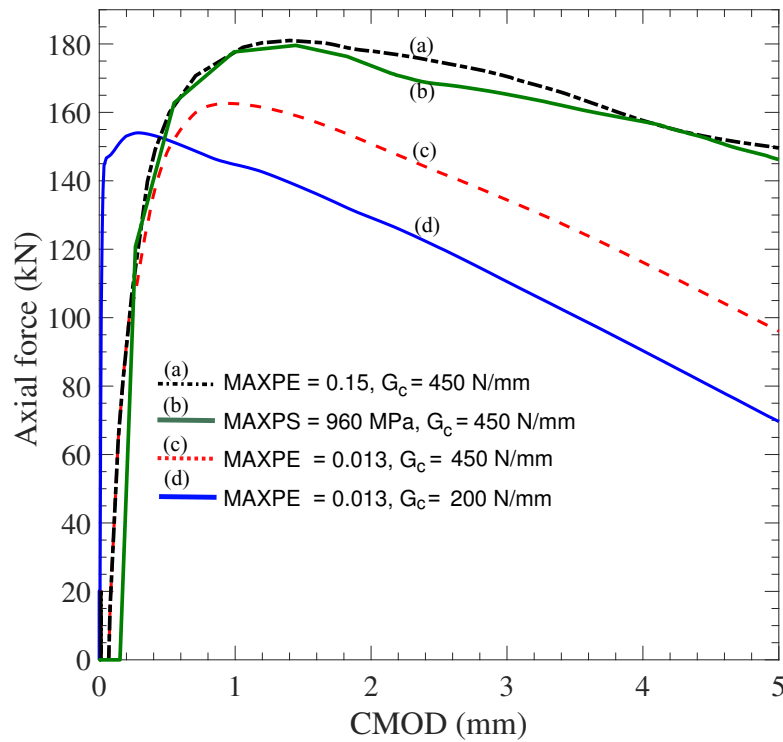


Figure 5.18: Axial compression versus CMOD variation based on fixed MAXPE fracture criterion rate G_c is 450 N/mm, the crack propagates more quickly under the principal strain of 0.013 than for the principal strain of 0.15. The tensile crack growth depicted in Fig. 5.19(i) and Fig. 5.19(ii) reveals that, with a MAXPE of 0.013, the crack has already traversed more than half of the pipe cross-section at an upward displacement of 0.18 m, exhibiting a crack opening of 19.27 mm. In contrast, with a maximum principal strain of 0.15 (Fig. 5.19(ii)), the crack has only reached the full thickness and just begun to propagate circumferentially, with an opening displacement of 2.52 mm.

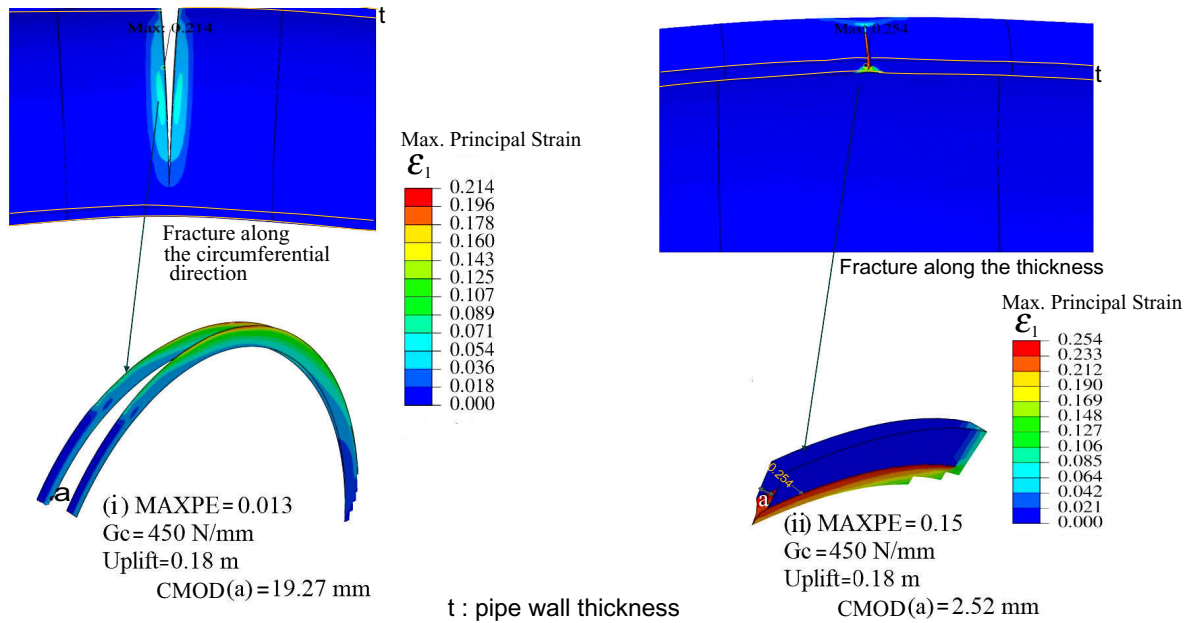


Figure 5.19: Fracture propagation stages during uplift movement based on MAXPE damage criterion: (i) MAXPS = 0.013, $G_c = 450$ N/mm; (ii) MAXPE = 0.15, $G_c = 200$ N/mm

For a similar upward displacement (i.e., 19 mm), MAXPS criterion with MAXPS = 960 MPa and $G_c = 450$ N/mm (Fig. 5.16(a)) provided a similar crack propagation pattern (i.e., crack reached the full thickness but not propagated in the circumferential direction). Thus, MAXPE values of 0.15 and a G_c value of 450 N/mm are comparable to the damage parameters with MAXPS of 960 MPa and G_c of 450 N/mm.

5.7.3 Results from MMC fracture criterion

The modified Mohr–Coulomb fracture criterion was implemented in the user defined damage initiation (UDMGINI) subroutine available in Abaqus FE software. In this analysis, the five calibrated constants fracture parameters for X65 grade steel pipe material Kofiani (2013); Lin (2021), namely c_1 , c_2 , c_3 , c_4 and c_5 (n) are set to 0.1, 1.903, 0.9, 1.0, and 0.142, respectively. The hardening parameter (n) of 0.142 and power law coefficient (A) of 885 were obtained from the power law fitting with the stress–strain behaviour of X65 pipe used in this study (Fig. 5.10).

Despite the slight variation from the data available in the literature presented in Table 5.3, the selected parameters for the MMC fracture criteria have been thoroughly validated with the tensile and bending specimen for X65 steel pipe as discussed earlier (Fig. 5.14). Figure 5.20 shows the axial force-CMOD relations based on the MMC fracture criterion. It reveals that there are no significant differences in the force-CMOD behavior obtained using the MMC fracture criteria with energy release rates G_c of 450 and 900 N/mm. On the other hand, there is considerable variation in the axial force-CMOD response for the energy release rates of 450 N/mm and 200 N/mm (shown in Fig. 5.20). Figure 5.21 shows the equivalent plastic strain (ϵ_q^p) distribution with crack opening and propagation profiles obtained based on the MMC damage model. The crack fully propagates along the thickness at the large plastic strain ϵ_q^p of ≈ 0.58 with MMC model. It can be observed that at an uplift displacement of 0.36 m, the crack fully penetrates the thickness when employing the MMC model (Fig. 5.21 (a)), whereas, the crack fully penetrates at the uplift displacement of 0.19 m when using the MAXPS damage model (as shown in Fig. 5.16(a)). The observed results indicate that the MAXPS damage model exhibits relatively a conservative behavior of fracture propagation.

The crack opening width is also greater with the MMC model compared to the MAXPS model (i.e., 5.72 mm from the MMC model Fig. 5.21(a), and 4.22 mm from the MAXPS model Fig. 5.16(a)). With the MMC damage model the initial crack starts to open wider with significant plastic deformation rather than the propagation along the depth. The STATUSXFEM plot reveals a higher number of elements with both full and partial fractures when utilizing the G_c of 450 N/mm compared to the G_c of 200 N/mm. The MMC criteria is suitable to predict not only the onset and advancement of a crack, but also its progression and detailed evolution until complete separation. These characteristics of crack initiation and propagation during upheaval displacement of pipe is shown in the Fig. 5.22 with distribution of equivalent plastic strain (ϵ_p^q). In this figure, the development of plastic strain as well as the width of crack opening during the uplift movement of the pipeline is shown. The crack initially remains planar within the half of the thickness of the

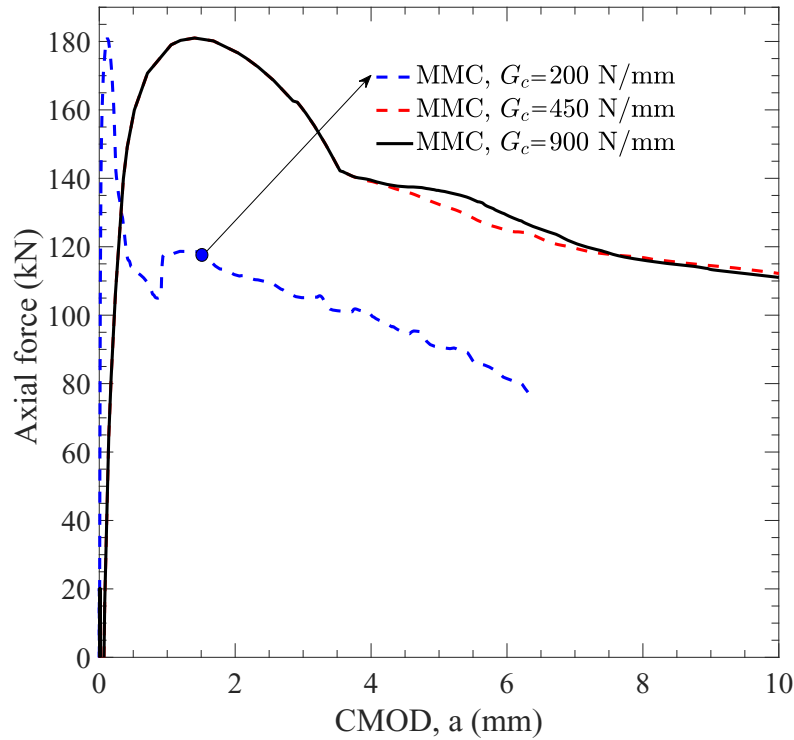


Figure 5.20: Axial compression versus CMOD variation based on variable MMC fracture criterion

pipe, but with increasing upward movement, it progressively propagates through the thickness, then in the circumferential direction, and eventually to complete separation, with corresponding increases in crack opening. Figure 5.22 shows the different stages (from initial to final state) of deformation at which the crack initiation and propagation occur during the uplift movement of a pipeline at different plastic strain level ϵ_q^p , using the MMC damage criterion with fracture energy of 450 N/mm. Initially the crack is planar at no uplift movement (Fig. 5.22(a)). At an uplift movement of 0.32 m, the crack begins to propagate along the thickness, resulting in crack width of 3.54 mm (Fig. 5.22(b)). As the uplift movement reaches 0.36 m, the crack fully penetrates through the thickness, resulting in a crack width of 5.72 mm (Fig. 5.22(c)). Again, at further uplift movement of 0.47 m, the crack fully penetrates through the circumferential direction, resulting in a crack width of 12.17 mm (Fig. 5.22 (d)). Finally, at the large uplift movement of 0.92 m, the crack completely separates the pipe segment, resulting in a crack width of 70.16 mm (Fig. 5.22

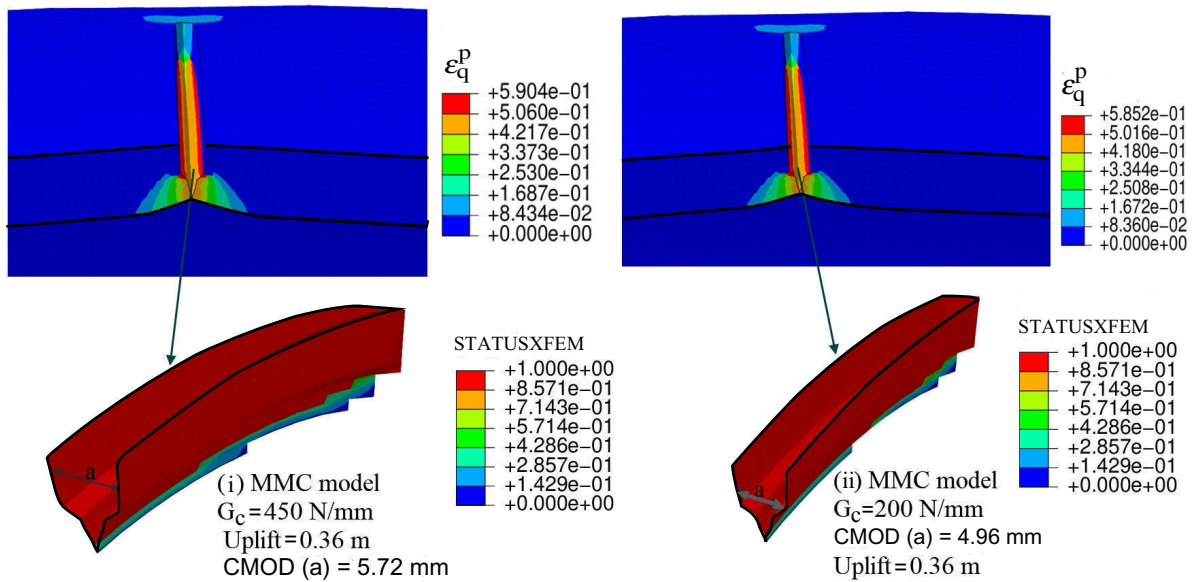


Figure 5.21: Fracture surface profile and XFEM enriched element conditions based on MMC damage criterion: (i) $G_C = 450 \text{ N/mm}$; (ii) MMC model with $G_C = 200 \text{ N/mm}$

(e)).

5.7.4 Fracture profile comparison with different damage models

In this section, a comparison of fracture behavior is presented using the specific fracture parameters discussed in the previous sections for the MAXPS, MAXPE, and MMC criteria. A linear damage softening model with a constant energy release rate (G_C) of 450 N/mm was used in all of the analyses. For the MAXPS criterion, the maximum principal stress, while for the MAXPE criterion, the maximum principal strain is used. The MMC criterion employed the values of the constants given in Table 5.3. The crack opening and propagation profiles generated by three different damage initiation criteria at the instance of full thickness crack penetration are presented in Fig. 5.23, while various fracture behaviors are shown in Fig. 5.24. In Fig. 5.23, for the MAXPE model, the uplift movement is 0.18 m, for the MAXPS model the uplift movement is 0.19 m and for the MMC model the uplift movement is 0.36 m require to fully penetrate the crack through the

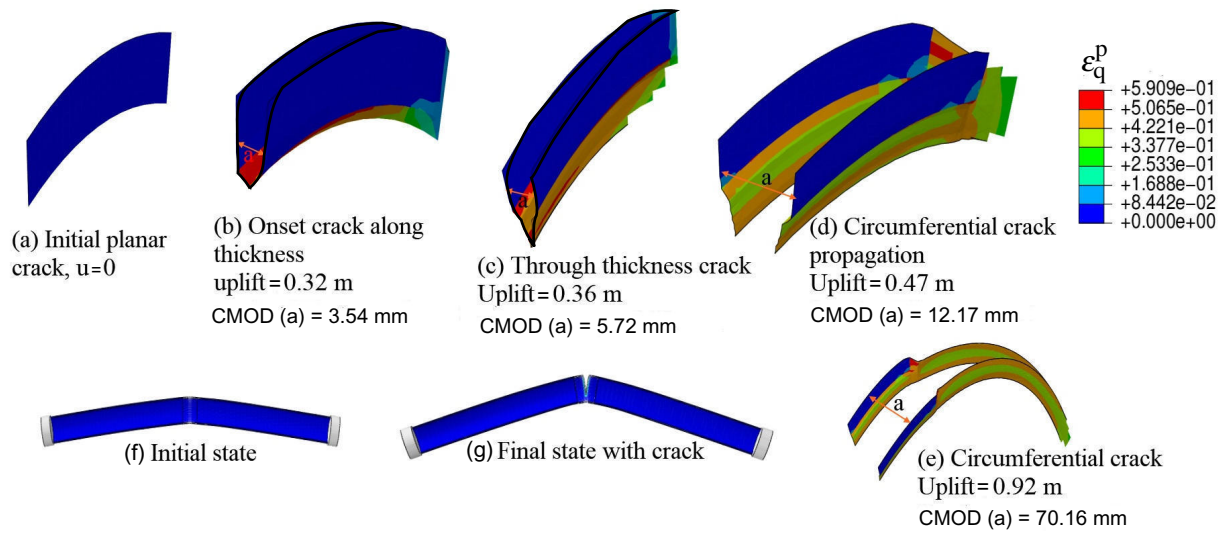


Figure 5.22: Fracture propagation stages during uplift movement of pipe based on MMC damage model: (a)–(e) from initial to final stage

thickness of the pipe. According to the simulation results depicted in Fig. 5.23, it can be observed the MMC model predicts wider crack opening with higher level of plastic deformation than other models. This indicates that the crack opening width is underestimated by the MAXPE and MAXPS criteria, compared to the MMC criterion.

In the MMC-based fracture criterion, the crack initially opens at a certain level of strain, and when the fracture criterion is reached at all the crack tip elements, the crack begins to propagate. In addition, among the fracture criteria considered, the MMC-based fracture model is more realistic in predicting large plastic strain at the onset and propagation of cracks (Kofiani 2013; Lin 2021).

Figure 5.24(a) shows the variation of axial force with the crack mouth opening displacement (CMOD) for the three different damage models. The chosen damage parameters for MAXPS, MAXPE, and MMC provided similar force–CMOD response from the analysis. Figure 5.24(b) illustrates the variation of crack mouth opening displacement (CMOD) during pipe uplift movement of the pipe. It is observed that the MAXPS and MAXPE damage models predict a

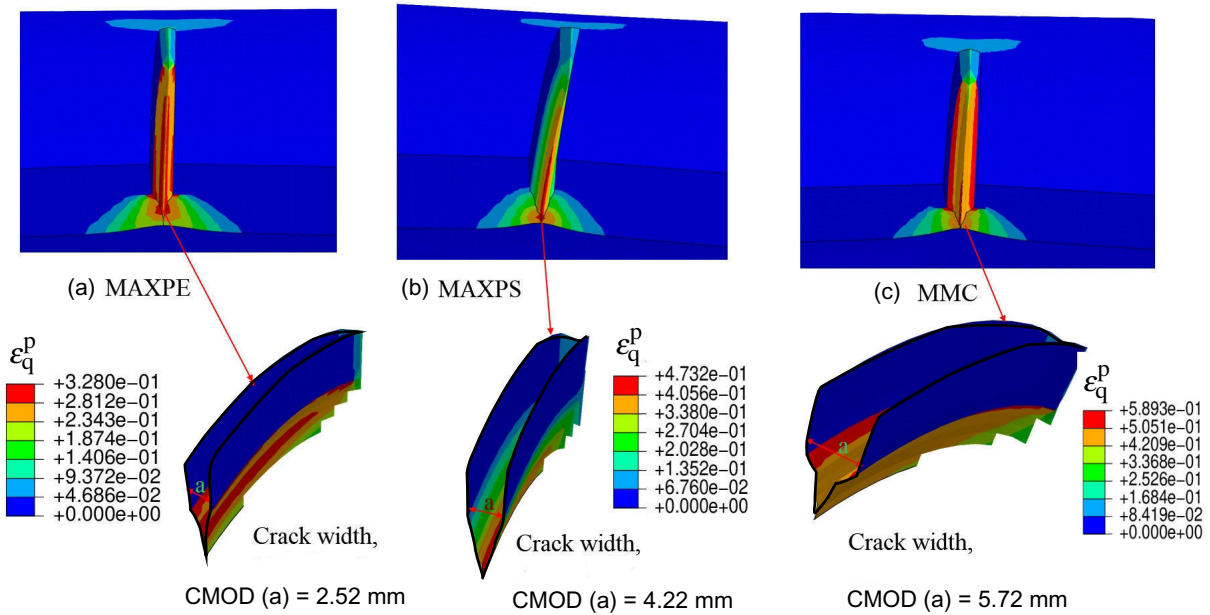
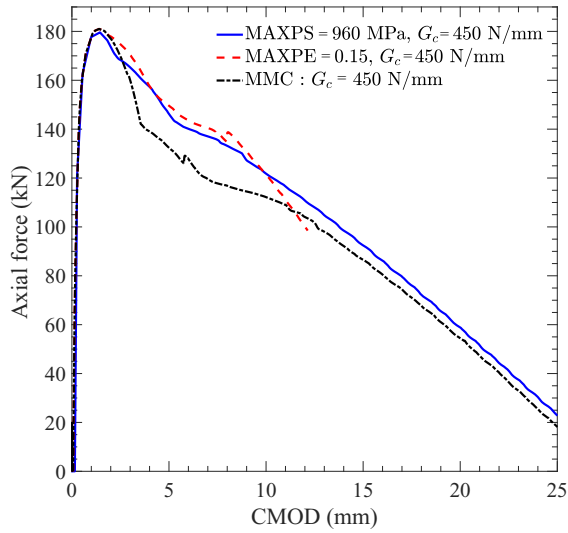
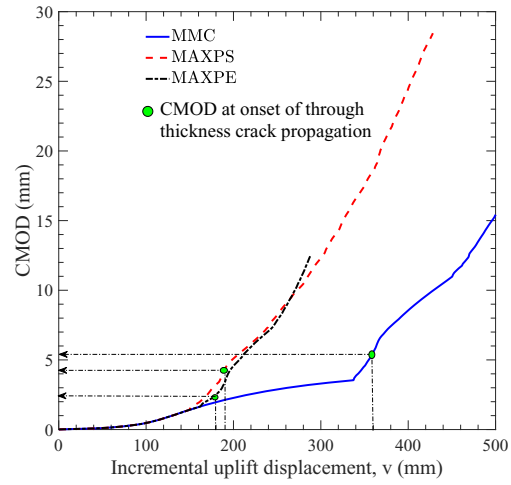


Figure 5.23: Comparison of fracture opening and deformation with different damage initiation criterion: (a) MAXPE; (b) MAXPS; (c) MMC

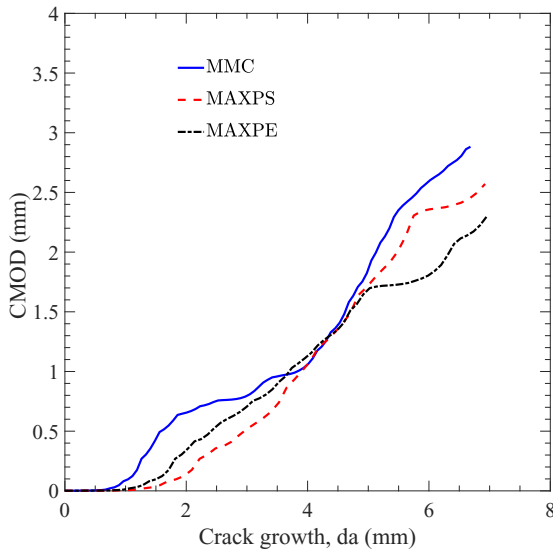
smaller CMOD than the MMC model at the instance when the crack cuts through the thickness during the uplift movement of the pipe. The uplift displacement required for full through thickness crack propagation was also larger from the MMC model. Figure 5.24(c) illustrates the incremental crack mouth opening displacement (CMOD) during the vertical movement of the pipe as the crack advances through the thickness. Observations reveal that the MMC model demonstrates a notable increase in CMOD compared to the MAXPS and MAXPE models. Furthermore, the MMC model exhibits a slower crack growth rate than the other models. This distinction can be attributed to the incorporation of crack tip plasticity in the MMC model. Figure 5.24(d) shows the development of tensile strain at the crack mouth element during pipe uplift movement. It is observed that the MAXPS and MAXPE damage models exhibit a lower level of tensile strain at the onset of crack propagation compared to the MMC model. At the uplift displacements of 0.15 m and 0.17 m the crack propagation starts for MAXPE and MAXPS damage models, respectively, while for the MMC model the crack propagation starts at the uplift movement of 0.32 m with high level of



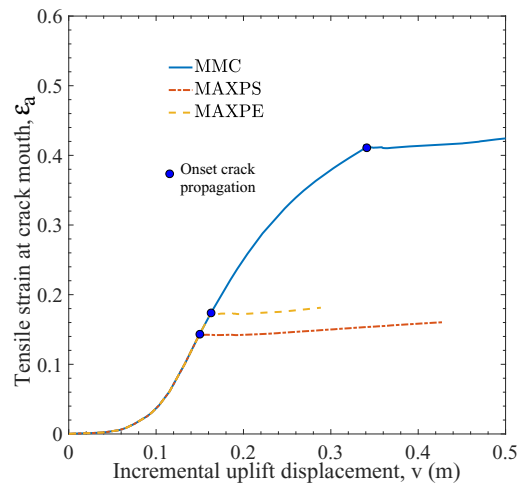
(a) Axial compression versus CMOD



(b) CMOD versus uplift displacement



(c) CMOD versus crack growth



(d) Tensile strain development during uplift displacement at the crack mouth element

Figure 5.24: Comparisons of fracture behaviour for three different damage criterion: (a) Axial compression versus CMOD; (b) CMOD versus uplift displacement; (c) CMOD versus crack growth; (d) Tensile strain development during uplift displacement at the crack mouth element

tensile strain than those from the other models, as shown in Fig. 5.24(d).

In Fig. 5.25, the variation of tensile strain (axial strain) development for various fracture models during the uplift movement of the pipeline at the onset and full separation of crack is shown. In

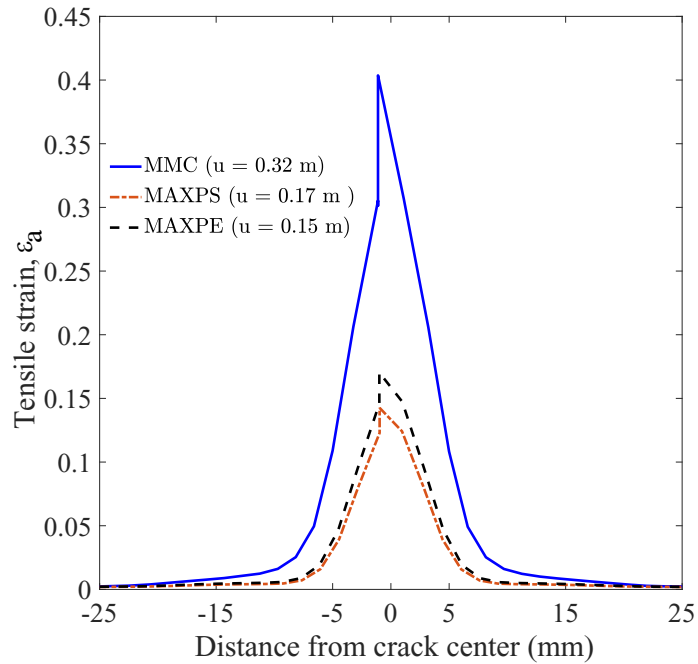


Figure 5.25: Tensile strain development during the onset and full separation of crack: (a) Tensile strain at the onset of crack propagation along thickness

Fig. 5.25(a), the initiation of crack propagation at the critical element is depicted by the onset tensile strain (ϵ_a) development. It has been observed that the MMC model exhibits a higher level of tensile strain (ϵ_a) development compared to the other models. Moreover, once the crack fully passes through the thickness, the MMC model also yields a higher level of tensile strain (ϵ_a) in comparison to other models, as illustrated in Fig. 5.25(b). The tensile strain during the initiation of crack and the propagation stage based on all damage models, exceeds the recommended maximum value of 0.025 specified in the CSA (2007) guideline at the uplift displacements exceeding 0.16 m. The results for the crack opening displacement (COD) along the crack propagation in the thickness direction are presented for different damage models in Fig. 5.26. It has been observed that the MMC model exhibits a significantly higher amount of crack opening compared to the other models. This is because the MMC model is capable of capturing the detailed evolution of the crack surface during onset and propagation for large strain deformation

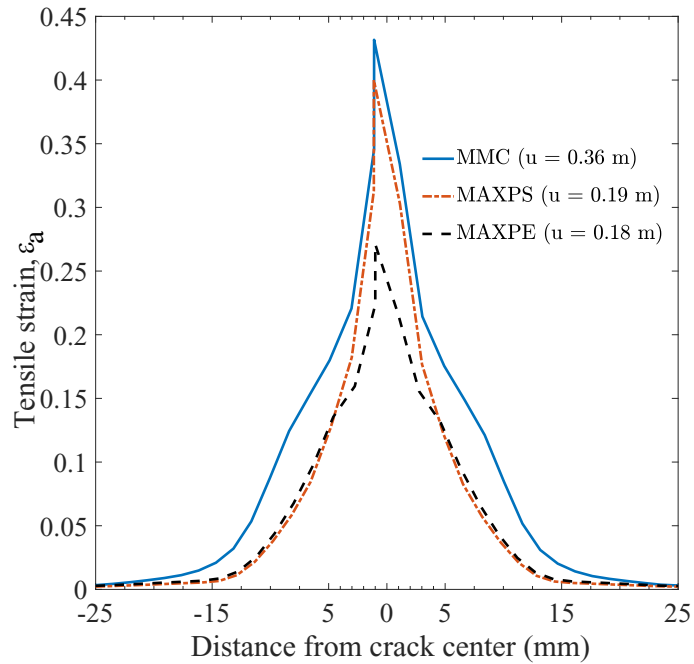


Figure 5.25: Tensile strain development during the onset and full separation of crack: (b) Tensile strain at the instance when the crack fully extends through the thickness

problems that occurs in offshore post-buckled pipelines. On the other hand, Fig. 5.27 illustrates the COD along the circumferential direction of crack propagation for various fracture models at the corresponding uplift displacement. From the results shown in Fig. 5.27, it is observed that the MAXPE damage model exhibits a faster crack propagation rate with smaller crack openings, whereas the MMC model exhibits a slower rate of crack propagation with wider crack openings. Also, the circumferential crack initiation occurs at an uplift displacement of 0.3 m for the MAXPE model, which is earlier than that for the MAXPS model (0.43 m) and the MMC model (0.92 m). The stress triaxiality variation (η) at the crack mouth element during pipe uplift movement is shown in Fig. 5.28. Prior to crack propagation, the MAXPS and MAXPE damage models exhibited higher stress triaxiality values (2–3), indicative of a stress state dominated by hydrostatic and brittle cleavage fracture. In contrast, the MMC damage model showed lower stress triaxiality values (0.45–1), signifying shear slip and greater ductility with plastic deformation. Based on

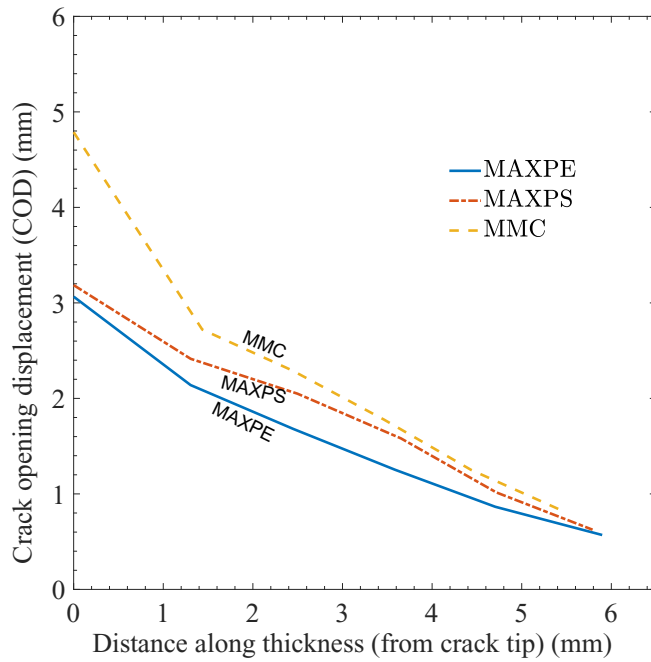


Figure 5.26: Crack opening displacement (COD) along the pipe thickness from the crack tip

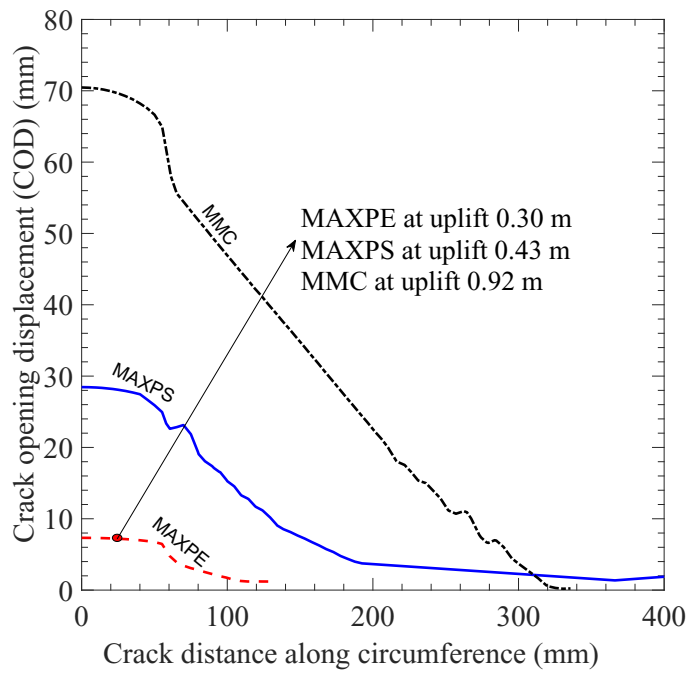


Figure 5.27: Crack opening displacement (COD) along the circumferential crack propagation

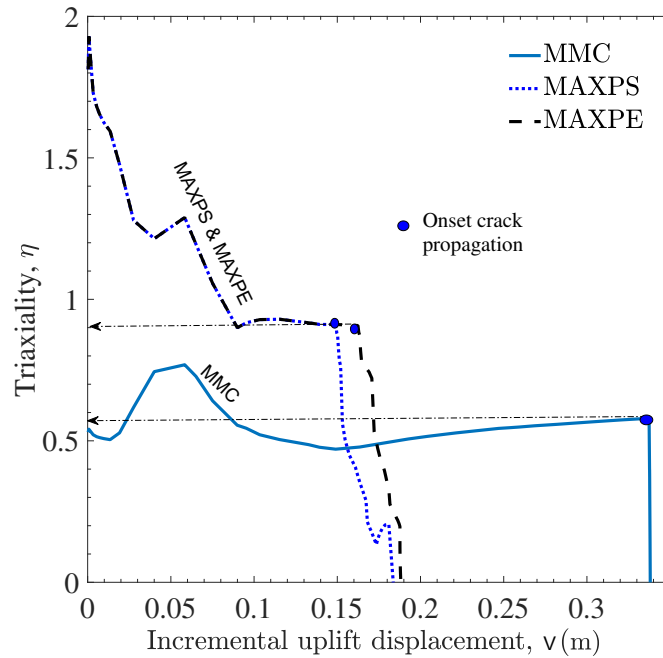


Figure 5.28: Variation of stress triaxiality at the crack mouth element during incremental uplift movement of pipe

these findings, it can be concluded that the MMC damage model can provide a more realistic representation of ductile fracture with large plastic deformation for post-buckled pipeline in comparison to the other damage models.

5.8 Conclusions

This study introduces a numerical modelling approach for evaluating the fracture behaviour of a post-buckled offshore pipeline with an initial crack. A numerical approach is presented to estimate the global post-buckled deformation shape for fracture assessment of the offshore HPHT buried pipeline. The XFEM-based cohesive segment method is used to investigate fracture behaviour. FE results suggest that the linear degradation damage model is suitable and computationally efficient for fracture assessment of pipelines with nonlinear material behaviour. Three different damage models, namely maximum principal stress (MAXPS), maximum principal strain (MAXPE), and

modified Mohr–Coulomb (MMC), are presented for fracture assessment using the XFEM technique. The MMC-based fracture model uses the user-defined damage initiation (UDMGINI) subroutine in Abaqus finite element software. The results indicate that the MMC damage model, which takes into account the crack-tip constraint (stress triaxiality and lode angle), can predict the more realistic fracture behaviour of the post-buckled offshore pipeline at large vertical deformation than the other inbuilt damage models (i.e., MAXPS and MAXPE) available in the software. While the hydrostatic and brittle behaviour dominates the crack propagation behaviour according to MAXPS and MAXPE models, shear slip and ductility with plastic deformation dominate the crack propagation according to the MMC model. Simulations using the MAXPS and MAXPE models provided higher crack propagation rates than those from the MMC model. Parameters for the analysis in this study were obtained through calibrations of SENT and SENB test results available in the literature, identifying the fracture parameters for steel pipe materials. One limitation of this study is that the fracture analysis focuses on a post-buckled initial shape specific to medium sand with particular burial conditions and a specific shape of initial imperfection. It is recommended to conduct further studies to explore the fracture behaviour of post-buckled pipelines under different initial imperfections, varying pipe sizes, loadings, burial depths, and soil parameters.

Chapter 6

Conclusions and Recommendations for Future Research

6.1 Conclusions

For the safe and economical design of buried offshore pipelines operating under high pressure and temperature (HPHT) conditions, soil resistance is an important factor to be considered. Although the buried offshore pipelines are designed to remain in the wished-in-place condition, field evidence indicates that these pipelines can experience significant uplift movement even beyond the seabed with an acceptable level of operating conditions. The uplift soil resistance decreases gradually with the upward movement of pipe. However, most of the current design guidelines do not consider the post-peak softening behaviour of uplift soil resistance. This research investigated the importance of post-peak degradation of soil resistance to assess the pre- and post-buckling structural performance of the offshore pipeline. An efficient numerical modelling technique is proposed to investigate the upheaval buckling, local buckling, and fracture in post-buckled offshore pipelines through finite element (FE) analysis using the Abaqus/Standard FE software.

The following general conclusions are drawn through the course of this thesis. The problem-specific conclusions are presented at the end of each chapter in Chapter 3 (Sc.3.7), Chapter 4 (Sc.4.9), and Chapter 5 (Sc.5.8), as well as in the Appendix A.1.

1. Chapter 3 presents the numerical modelling of upheaval buckling of offshore pipeline with unstressed and stressed initial imperfections. The upheaval buckling responses of offshore pipeline buried in loose, medium, and dense sand conditions with post-peak degradation in uplift soil resistance investigated. The analysis results show that the capacity of the pipeline reduces significantly with the consideration of the post-peak degradation soil model than the

constant post-peak soil resistance model recommended by the design guidelines. A few other general conclusions from this chapter are listed below:

- The conventional equivalent effective temperature approach gives a higher critical buckling temperature than the direct application of pressure in the finite element (FE) model with pipe elements.
- Not only the shape and size but also the stressed or unstressed conditions of initial imperfection plays a key role in the buckling behaviour of offshore pipelines.
- While the one-dimensional (1-D) FE method is numerically easy to implement and computationally efficient, it has some limitations regarding plastic strain development and local buckle formation at large displacements.

2. Chapter 4 describes a numerically efficient hybrid FE model (coupled with pipe and shell elements) to investigate the response of pipelines for global upheaval buckling, leading to local buckling. The hybrid FE model also considers the post-peak degradation of uplift soil resistance. The FE results show that the post-buckled pipeline exhibits local buckling and wrinkling at considerably lower vertical displacements compared to a similar problem solved with the 1-D FE model described in Chapter 3. A few other general conclusions from this chapter is listed below:

- During a large vertical movement of the pipe, significant plastic strain develops in the compression side (invert), resulting in outward wrinkles for a pressurized pipe, in contrast to inward wrinkles observed in an unpressurized pipe condition. This large plastic strain indicates that the post-buckled offshore pipe may fail due to the local buckling and wrinkling at some stage of vertical movement beyond the seabed.
- A slight increase in internal pressure in offshore pipelines considerably reduces the pipe capacity against buckling, forming large plastic strains at a significantly lower buckle amplitude as compared to pipes with lower operating pressures.

- The FE results show that the ovalization limit proposed by API overestimates the buckling response as the pipe already may experience wrinkling at the proposed ovalization limit. The ovalization limit proposed by DNV is more practical.
 - Larger-sized pipes are susceptible to early local buckling at a considerably lower buckle amplitude as compared to smaller pipes under similar operating conditions. Larger pipe sections undergo primary and secondary local buckling, while smaller sections experience only primary buckling at larger movements.
3. Chapter 5 investigates the fracture of post-buckled offshore pipeline with the eXtended finite element method (XFEM) available in Abaqus FE software. As the post-buckled pipeline moves up beyond the seabed, it might get impacted by offshore activities, which may result in a crack on the pipe surface. As a result, the tension side of the post-buckled pipe is susceptible to undergoing fracture and failure eventually. The numerical model developed in this chapter can capture the fracture response of a post-buckled pipeline undergoing large plastic strains on the tension side. The fracture response on the post-buckled offshore pipeline with traditional fracture criterion such as Maximum principal stress (MAXPS) and Maximum principal strain (MAXPE) is compared with the Modified Mohr–Coulomb (MMC) fracture model proposed in the present study. The MMC model is implemented in Abaqus using a user-defined subroutine UDMGINI. A few other general conclusions from this chapter is listed below:
- The XFEM method employed in this study efficiently captures the crack propagation behaviour compared to the traditional J-integral based FE method.
 - The linear degradation (traction-separation) model in XFEM based cohesive segment approach is suitable and computationally efficient to capture the fracture in a post-buckled pipeline undergoing large deformation.
 - The MMC model, which considers the crack-tip constraints (stress triaxiality (η) and

lode angle ($\bar{\theta}$) at each increment of loading with the extension of crack, is better in predicting the fracture behaviour of post-buckled pipeline compared to the traditional fracture models such as MAXPS and MAXPE.

Overall, this thesis examined the deformation stages of an offshore pipeline undergoing upheaval buckling, local buckling, and fracture. The plastic strain generation at the onset of upheaval buckling is found to be significantly low (approximately 1–2%) (Chapter 3) in both the 1D and Hybrid FE models. As the buckle amplitude progresses, local buckling initiates with the onset plastic strain of approximately 3% (Chapter 4). With a further increase in operating temperature, the plastic strain rapidly increases to a significantly higher value of approximately 10% (Chapter 4). Under further temperature increase, the pipeline either collapses due to local buckling with significant wrinkle formation at a plastic strain of approximately 15–25% (Chapter 4) or experiences total fracture (leakage) due to the complete extension of a crack through the thickness at a tensile fracture strain of 20–40% (Chapter 5).

The **main contributions of this thesis** are outlined as follows:

- The most accurate post-peak degradation soil resistance model for loose, medium, and dense sand conditions is presented for assessing offshore buried pipelines undergoing large deformation beyond the seabed.
- Introduction of axial, lateral, bearing, and uplift soil resistance curves necessary for investigating the post-buckling behaviour of offshore pipelines.
- Demonstration of a finite element (FE) numerical model featuring unstressed and stressed initial imperfections for solving the global buckling problem in buried offshore pipelines.
- Provision of a critical and safe temperature relationship for varying sizes of initial imperfections, embedment, initial stress, variable pipe diameter, and wall thickness. This information is valuable for the offshore pipeline industry in determining safe operating temperatures and pressures.

- A novel FE numerical model named hybrid pipe-shell soil-spring model is introduced to address the local buckling issues in post-buckled offshore pipelines. This model aids in predicting potential local buckling failure and ovalization in buried offshore pipeline experiencing significant deformation due to high-temperature and high-pressure conditions.
- Presentation of a computationally efficient methodology for analyzing possible fractures in postbuckled offshore pipelines. The proposed eXtended finite element, coupled with the modified Mohr-Coulomb fracture criterion, is capable of capturing crack tip constraints and exhibits superior performance in predicting the ductile fracture behaviour of X65 offshore steel pipelines.

The research has **some limitations**, including:

- In the numerical model, the axial soil resistance remains constant during the uplift displacement of the pipeline, even beyond the seabed. The study demonstrates that the variable axial resistance has an insignificant impact on the pipeline's buckling behavior. To address this limitation, a long pipeline model was incorporated in the FE model. However, computational challenges persist in including variable axial soil resistance with the non-linear soil spring model in ABAQUS using the USDFLD subroutine.
- The hybrid finite element model utilized for local buckling analysis is limited to scenarios involving a continuous rise in temperature and pressure loadings. A comprehensive study of the pipeline's local buckling response should incorporate a fatigue model to address scenarios such as shutdown and restart cycles in offshore pipelines.
- The presented hybrid model is limited to unstressed initial imperfections. Extending the hybrid model to include stressed initial conditions introduces additional advancement in FE model.
- The hybrid model is limited in using soil as a nonlinear spring. While a continuum model of the soil might better represent the local buckling, it is computationally expensive for long

pipelines.

- The post-buckled fracture model introduced here is limited to planar cracks and a specific post-buckled initial shape tailored to medium sand under specific burial conditions. The fracture behaviour of the pipeline may vary when subjected to surface dent/impact and multiple cracks/holes (circular/elliptic). Nonetheless, it is essential to note that the methodology proposed in this study applies to a broad range of crack types and shapes of initial imperfections.

6.2 Recommendations for future research

The following recommendations and areas for further exploration have been identified from this research:

- (a) Further investigation is recommended to study the post-buckling response of pipes buried in clay conditions, as it is expected to be a different buckling response with the fluidization effects of clay.
- (b) It is recommended to conduct further exploration to investigate the effect of installation factors, such as stressed initial imperfections, on local buckling behaviour. This aspect was not considered in the current study and could provide valuable insights into the structural response of offshore pipelines.
- (c) While investigating the vertical movement of the pipeline during upheaval buckling, only a monotonic increase in temperature was considered. However, real-world offshore operations involve cyclic loading situations (e.g., start-up, shutdown, and restart) or variations in operating pressure, which can induce a different local buckling response due to a geotechnical ratcheting mechanism. Further research is recommended to understand and address these dynamic effects.

(d) Further research is needed to account for the possibility of multiple initial cracks on the pipe surface in fracture assessments of post-buckled pipelines. The presence of these cracks may lead to crack branching during temperature variations. Utilizing the eXtended Finite Element Method (XFEM) with the development of user elements (UEL) and the damage model, UDMGINI can provide a suitable approach to study crack branching during fracture or collapse.

Bibliography

- (2011). *Upheaval Buckling Assessment Based on Pipeline Features*, volume All Days of OTC Offshore Technology Conference.
- Agbo, S., Lin, M., Ameli, I., Imanpour, A., Duan, D.-M., Cheng, J. R., and Adeeb, S. (2019). Evaluation of the effect of internal pressure and flaw size on the tensile strain capacity of X42 vintage pipeline using damage plasticity model in extended finite element method (XFEM). In *Pressure Vessels and Piping Conference*, volume 58967. American Society of Mechanical Engineers.
- ALA (2005). Guidelines for the design of buried steel pipe. In *American Society of Civil Engineers*.
- Ameli, I., Asgarian, B., Lin, M., Agbo, S., Cheng, R., Duan, D. m., and Adeeb, S. (2019). Estimation of the CTOD-crack growth curves in SENT specimens using the eXtended finite element method. *International Journal of Pressure Vessels and Piping*, 169:16–25.
- API (1999). Operation and maintenance of offshore hydrocarbon pipelines (limit state design). *API recommended Practice*, 1111.
- ASCE (2009). Buried flexible steel pipe: Design and structural analysis. In *Whidden, William Robert*. American Society of Civil Engineers.
- Bai, Y. and Bai, Q. (2005). *Subsea pipelines and risers*, volume 3. Elsevier.
- Bai, Y. and Wierzbicki, T. (2008). A new model of metal plasticity and fracture with pressure and lode dependence. *International journal of plasticity*, 24(6):1071–1096.
- Bai, Y. and Wierzbicki, T. (2010). Application of extended Mohr–Coulomb criterion to ductile fracture. *International Journal of Fracture*, 161(1):1–20.
- Barenblatt, G. (1959). The formation of equilibrium cracks during brittle fracture. General ideas and hypotheses. Axially-symmetric cracks. *Journal of Applied Mathematics and Mechanics*, 23(3):622–636.
- Barenblatt, G. I. (1962). The mathematical theory of equilibrium cracks in brittle fracture.

Advances in applied mechanics, 7:55–129.

- Belytschko, T. and Black, T. (1999). Elastic crack growth in finite elements with minimal remeshing. *International Journal for Numerical Methods in Engineering*, 45(5):601–620.
- Bransby, M., Brunning, P., Newson, T., and Davies, M. (2001). Numerical and centrifuge modelling of the upheaval resistance of buried pipelines. *Proceedings of the International Conference on Offshore Mechanics and Arctic Engineering - OMAE*, 4:265–273.
- Bransby, M., Newson, T., and Brunning, P. (2002). The upheaval capacity of pipelines in jetted clay backfill. *International Journal of Offshore and Polar Engineering*, 12.
- Bransby, M. F. and Ireland, J. (2009). Rate effects during pipeline upheaval buckling in sand. *Proceedings of the Institution of Civil Engineers - Geotechnical Engineering*, 162(5):247–256.
- Bruton, D., White, D., Cheuk, C., Bolton, M., and Carr, M. (2006). Pipe/soil interaction behavior during lateral buckling, including large-amplitude cyclic displacement tests by the safebuck jip. In *Offshore Technology Conference*, pages OTC–17944. OTC.
- Budden, P. (2006). Failure assessment diagram methods for strain-based fracture. *Engineering Fracture Mechanics*, 73(5):537–552.
- Carr, M., Bruton, D., and Leslie, D. (2003). Lateral buckling and pipeline walking, a challenge for hot pipelines. In *Offshore Pipeline Technology Conference*, pages 1–36.
- Cheuk, C. Y. (2005). *Soil-pipeline interaction at the seabed*. PhD thesis, University of Cambridge, UK.
- Cheuk, C. Y., White, D. J., and Bolton, M. D. (2008). Uplift mechanisms of pipes buried in sand. *Journal of Geotechnical and Geoenvironmental Engineering*, 134(2):154–163.
- Chin, E., Craig, W., and Cruickshank, M. (2006). Uplift resistance of pipelines buried in cohesionless soil. In *Proc., 6th Int. Conf. on Physical Modelling in Geotechnics*, volume 1, pages 723–728. Taylor & Francis, London.
- Clukey, E., Jackson, C., Vermersch, J., Koch, S., and Lamb, W. (1989). Natural densification by wave action of sand surrounding a buried offshore pipeline. In *Offshore Technology Conference*.

OnePetro.

- Crisfield, M. (1981). A fast incremental/iterative solution procedure that handles "snap-through". In *Computational Methods in Nonlinear Structural and Solid Mechanics*, pages 55–62. Elsevier.
- Croll, J. G. et al. (1998). A simplified analysis of imperfect thermally buckled subsea pipelines. *International Journal of Offshore and Polar Engineering*, 8(04).
- CSA (2007). Oil and gas pipeline systems, CSA Z662. *Canadian Standards Association*.
- De Normalisation, C. E. (1998). Eurocode 8, part 4: Silos, tanks and pipelines. *CEN EN*, 4.
- DNV (2007). Global buckling of submarine pipelines, structural design due to high temperature/high pressure. *RP-F110, Oslo, Norway*.
- DNV, G. (2006). Dnv-rp-f108: fracture control for pipeline installation methods introducing cyclic plastic strain. *London: BSI*, pages 1–24.
- DNV, O. (2010). F201. *Offshore Standard for Dynamic Risers, Norway*.
- Dolbow, J., Moës, N., and Belytschko, T. (2000). Discontinuous enrichment in finite elements with a partition of unity method. *Finite elements in analysis and design*, 36(3-4):235–260.
- Dorey, A. B., Murray, D. W., and Cheng, J. J. R. (2005). Critical buckling strain equations for energy pipelines—a parametric study. *Journal of Offshore Mechanics and Arctic Engineering*, 128(3):248–255.
- Dugdale, D. S. (1960). Yielding of steel sheets containing slits. *Journal of the Mechanics and Physics of Solids*, 8(2):100–104.
- Erdogan, F. and Sih, G. C. (1963). On the crack extension in plates under plane loading and transverse shear. *Journal of Basic Engineering*, 85(4):519–525.
- Gao, X.-f., Liu, R., and Yan, S.-w. (2011). Model test based soil spring model and application in pipeline thermal buckling analysis. *China Ocean Engineering*, 25(3):507.
- Goplen, S., Strom, P., Levold, E., and Mork, K. J. (2005). Hotpipe JIP: HP/HT buried pipelines. In *ASME 2005 24th International Conference on Offshore Mechanics and Arctic Engineering*, pages 691–699. American Society of Mechanical Engineers.

- Gresnigt, A. (1986). Plastic design of buried steel pipelines in settlement areas. *Heron (Delft)*, 31(4):1–113.
- Hansbo, A. and Hansbo, P. (2004). A finite element method for the simulation of strong and weak discontinuities in solid mechanics. *Computer methods in applied mechanics and engineering*, 193(33-35):3523–3540.
- Hauch, S. R. and Bai, Y. (2000). Bending moment capacity of pipes. *J. Offshore Mech. Arct. Eng.*, 122(4):243–252.
- Hillerborg, A., Modéer, M., and Petersson, P.-E. (1976). Analysis of crack formation and crack growth in concrete by means of fracture mechanics and finite elements. *Cement and concrete research*, 6(6):773–781.
- Hobbs, R. (1981). Pipeline buckling caused by axial loads. *Journal of Constructional Steel Research*, 1(2):2–10.
- Hobbs, R. E. (1984). In-service buckling of heated pipelines. *Journal of Transportation Engineering*, 110(2):175–189.
- Hojjati-Talemi, R., Cooreman, S., and Van Hoecke, D. (2018). Finite element simulation of dynamic brittle fracture in pipeline steel: A XFEM-based cohesive zone approach. *Proceedings of the Institution of Mechanical Engineers, Part L: Journal of Materials: Design and Applications*, 232(5):357–370.
- Hooper, J., Maschner, E., and Farrant, T. (2004). Penguins pipeline system—design challenges for the world’s longest snaked lay HP/HT pipe tie-back. In *Offshore Pipeline Technology Conference*.
- Hutchinson, J. (1983). Fundamentals of the phenomenological theory of nonlinear fracture mechanics. *Journal of Applied Mechanics*.
- Jayadevan, K., Østby, E., and Thaulow, C. (2004). Fracture response of pipelines subjected to large plastic deformation under tension. *International Journal of Pressure Vessels and Piping*, 81(9):771–783.

- Ju, G. T. and Kyriakides, S. (1988). Thermal buckling of offshore pipelines. *Journal of Offshore Mechanics and Arctic Engineering*, 110(4):355–364.
- Jung, J. K., O'Rourke, T. D., and Olson, N. A. (2013). Uplift soil–pipe interaction in granular soil. *Canadian Geotechnical Journal*, 50(7):744–753.
- Karampour, H., Albermani, F., and Gross, J. (2013). On lateral and upheaval buckling of subsea pipelines. *Engineering Structures*, 52:317–330.
- Kenny, S. and Jukes, P. (2015). Pipeline/soil interaction modeling in support of pipeline engineering design and integrity. *Oil and Gas Pipelines*, pages 99–142.
- Kerr, A. D. (1972). On the stability of the railroad track in the vertical plane. Technical Report 131-142, Rail International.
- Klever, F., van Helvoirt, L., and Sluyterman, A. (1990). A dedicated finite-element model for analyzing upheaval buckling response of submarine pipelines. In *Offshore Technology Conference*. OnePetro.
- Kofiani, K. N. (2013). *Ductile fracture and structural integrity of pipelines & risers*. PhD thesis, Massachusetts Institute of Technology, MIT.
- Kouretzis, G. P., Karamitros, D. K., and Sloan, S. W. (2014). Analysis of buried pipelines subjected to ground surface settlement and heave. *Canadian geotechnical journal*, 52(8):1058–1071.
- Li, H. and Chandra, N. (2003). Analysis of crack growth and crack-tip plasticity in ductile materials using cohesive zone models. *International Journal of Plasticity*, 19(6):849–882.
- Limam, A., Lee, L.-H., Corona, E., and Kyriakides, S. (2010). Inelastic wrinkling and collapse of tubes under combined bending and internal pressure. *international journal of mechanical sciences*, 52(5):637–647.
- Lin, M. (2021). *Novel XFEM Variable Strain Damage Model for Predicting Fracture in Small-scale SENT and Full-scale Pipeline Fracture Tests*. PhD thesis, University of Alberta, University of Alberta.
- Lin, M., Agbo, S., Cheng, J. R., Yoosef-Ghodsi, N., and Adeeb, S. (2017). Application of the

- extended finite element method (XFEM) to simulate crack propagation in pressurized steel pipes. In *Pressure Vessels and Piping Conference*, volume 57953, page V03BT03A024. American Society of Mechanical Engineers.
- Lin, M., Agbo, S., Duan, D.-M., Cheng, J. R., and Adeeb, S. (2020). Simulation of crack propagation in API 5L X52 pressurized pipes using XFEM-based cohesive segment approach. *Journal of Pipeline Systems Engineering and Practice*, 11(2):04020009.
- Linkens, D., Formby, C., and Ainsworth, R. (2000). A strain-based approach to fracture assessment—example applications. In *Proc. 5th International Conference on Engineering Structural Integrity Assessment*.
- Liu, P., Zhang, B., and Zheng, J. (2012). Finite element analysis of plastic collapse and crack behavior of steel pressure vessels and piping using XFEM. *Journal of failure analysis and prevention*, 12(6):707–718.
- Liu, R., Wang, W.-g., and Yan, S.-w. (2013). Finite element analysis on thermal upheaval buckling of submarine burial pipelines with initial imperfection. *Journal of Central South University*, 20(1):236–245.
- Liu, R., Xiong, H., Wu, X., and Yan, S. (2014). Numerical studies on global buckling of subsea pipelines. *Ocean Engineering*, 78:62–72.
- Liu, X. (2017). Numerical and experimental study on critical crack tip opening displacement of X80 pipeline steel. *Mechanics*, 23(2):204–208.
- Mahdavi, H., Kenny, S., Phillips, R., and Popescu, R. (2013). Significance of geotechnical loads on local buckling response of buried pipelines with respect to conventional practice. *Canadian geotechnical journal*, 50(1):68–80.
- Maltby, T. and Calladine, C. (1995a). An investigation into upheaval buckling of buried pipelines—i. experimental apparatus and some observations. *International Journal of Mechanical Sciences*, 37(9):943–963.
- Maltby, T. and Calladine, C. (1995b). An investigation into upheaval buckling of buried

- pipelines—ii. theory and analysis of experimental observations. *International Journal of Mechanical Sciences*, 37(9):965–983.
- Martinet, A. (1934). *Flambement des voies sans points sur ballast et rails de grande longueur (buckling of tracks without points on ballast and long rails)*, volume 55 of 212-230. *Revue Generale des Chemins de Fer*.
- Melenk, J. and Babuška, I. (1996). The partition of unity finite element method: basic theory and applications. TICAM report. *Texas Institute for Computational and Applied Mathematics, University of Texas at Austin*.
- Moës, N., Dolbow, J., and Belytschko, T. (1999). A finite element method for crack growth without remeshing. *International journal for numerical methods in engineering*, 46(1):131–150.
- Mohajer, N., Xia, M., Liu, X., Cheng, J. R., Sen, M., and Adeeb, S. (2018). Post-buckling failure modes of X65 steel pipe: An experimental and numerical study. *Journal of Pressure Vessel Technology*, 140(5):051207.
- Mohareb, M. E. (1995). *Deformational behaviour of line pipe*. PhD thesis, University of Alberta.
- Mondal, B. C. and Dhar, A. S. (2017). Upheaval buckling of surface-laid offshore pipeline. *Applied Ocean Research*, 66:146–155.
- Mondal, B. C. and Dhar, A. S. (2019). Burst pressure assessment of corroded pipelines using fracture mechanics criterion. *Engineering Failure Analysis*, 104:139–153.
- Murray, D. W. (1997). Local buckling, strain localization, wrinkling and postbuckling response of line pipe. *Engineering Structures*, 19(5):360–371.
- Nielsen, N. J. R., Pedersen, P. T., Grundy, A. K., and Lyngberg, B. S. (1990). Design criteria for upheaval creep of buried sub-sea pipelines. *Journal of Offshore Mechanics and Arctic Engineering*, 112(4):290–296.
- Ning, J., Liu, S., Lin, T., and Huang, W. (2022). Pipeline element for upheaval buckling analysis of submarine pipelines with geometric-imperfections under high temperature high pressure. *Ocean Engineering*, 264:112456.

- Nonn, A. and Kalwa, C. (2013). Analysis of dynamic ductile fracture propagation in pipeline steels: A damage mechanics approach. In *6th Pipeline Technology Conference (2013), Ostend, Belgium*.
- Oh, C.-S., Kim, N.-H., Kim, Y.-J., Baek, J.-H., Kim, Y.-P., and Kim, W.-S. (2011). A finite element ductile failure simulation method using stress-modified fracture strain model. *Engineering fracture mechanics*, 78(1):124–137.
- Østby, E., Jayadevan, K., and Thaulow, C. (2005). Fracture response of pipelines subject to large plastic deformation under bending. *International Journal of Pressure Vessels and Piping*, 82(3):201–215.
- Ozkan, I. F. and Mohareb, M. (2009a). Moment resistance of steel pipes subjected to combined loads. *International Journal of Pressure Vessels and Piping*, 86(4):252–264.
- Ozkan, I. F. and Mohareb, M. (2009b). Testing and analysis of steel pipes under bending, tension, and internal pressure. *Journal of structural engineering*, 135(2):187–197.
- Palaniswamy, K. (1978). On the problem of crack extension in brittle solids under general loading. *Mechanics today*, 4:30.
- Palmer, A., Baldry, J., et al. (1974). Lateral buckling of axially constrained pipelines. *Journal of Petroleum Technology*, 26(11):1–283.
- Palmer, A., Ellinas, C., Richards, D., and Guijt, J. (1990). Design of submarine pipelines against upheaval buckling. In *Offshore Technology Conference*. OnePetro.
- Palmer, A. C. and King, R. A. (2004). *Subsea pipeline engineering*. PennWell Books.
- Palmer, A. C. and Williams, P. J. (2003). Frost heave and pipeline upheaval buckling. *Canadian Geotechnical Journal*, 40(5):1033–1038.
- Paredes, M., Lian, J., Wierzbicki, T., Cristea, M. E., Münstermann, S., and Darcis, P. (2018). Modeling of plasticity and fracture behavior of X65 steels: seam weld and seamless pipes. *International Journal of Fracture*, 213(1):17–36.
- Pedersen, P. T. and Jensen, J. J. (1988). Upheaval creep of buried heated pipelines with initial

- imperfections. *Marine Structures*, 1(1):11–22.
- PRCI, P. . (2009). Guidelines for constructing natural gas and liquid hydrocarbon pipelines through areas prone to landslide and subsidence hazards. *PRCI*.
- Ramberg, W. and Osgood, W. R. (1943). Description of stress-strain curves by three parameters. *National Advisory Committee for Aeronautics (NACA)*.
- Randolph, M. F. and Houlsby, G. (1984). The limiting pressure on a circular pile loaded laterally in cohesive soil. *Geotechnique*, 34(4):613–623.
- Rice, R. C., Goode, R., Bakuckas, J., and Thompson, S. (2003). Development of MMPDS handbook aircraft design allowables. In *7th Joint DOD/FAA/NASA Conference on Aging Aircraft*. Citeseer.
- Riks, E. (1979). An incremental approach to the solution of snapping and buckling problems. *International Journal of Solids and Structures*, 15(7):529–551.
- Roy, K., Hawlader, B., Kenny, S., and Moore, I. (2018a). Uplift failure mechanisms of pipes buried in dense sand. *International Journal of Geomechanics*, 18(8):04018087.
- Roy, K., Hawlader, B., Kenny, S., and Moore, I. (2018b). Upward pipe–soil interaction for shallowly buried pipelines in dense sand. *Journal of Geotechnical and Geoenvironmental Engineering*, 144(11):04018078.
- Schaminee, P., Zorn, N., Schotman, G., et al. (1990). Soil response for pipeline upheaval buckling analyses: full-scale laboratory tests and modelling. In *Offshore Technology Conference*. Offshore Technology Conference.
- Scheider, I. (2001). Simulation of cup-cone fracture in round bars using the cohesive zone model. In *Computational fluid and solid mechanics (First MIT Conference)*, volume 1, pages 460–2. Elsevier.
- Scheider, I. (2009). Derivation of separation laws for cohesive models in the course of ductile fracture. *Engineering Fracture Mechanics*, 76(10):1450–1459.
- Scheider, I., Nonn, A., Völling, A., Mondry, A., and Kalwa, C. (2014). A damage mechanics

- based evaluation of dynamic fracture resistance in gas pipelines. *Procedia Materials Science*, 3:1956–1964.
- Schwalbe, K., Scheider, I., and Cornec, A. (2009). The siam method for applying cohesive models to the damage behavior of engineering materials and structures, GKSS.
- Schwalbe, K., Scheider, I., and Cornec, A. (2013). *Guidelines for Applying Cohesive Models to the Damage Behaviour of Engineering Materials and Structures*. Springer Berlin, Heidelberg.
- Shaw, P. K. and Bomba, J. G. (1994). Finite-element analysis of pipeline upheaval buckling. *American Society of Mechanical Engineers*.
- Shi, R., Wang, L., Guo, Z., and Yuan, F. (2013). Upheaval buckling of a pipeline with prop imperfection on a plastic soft seabed. *Thin-Walled Structures*, 65:1–6.
- Shinkai, H., Hatsuda, Y., and Suzuki, N. (2012). Seismic design guidelines to mitigate upheaval buckling of small diameter pipes. In *International Pipeline Conference*, volume 45158, pages 233–240. American Society of Mechanical Engineers.
- Simulia, D. (2016). Abaqus version 2016 documentation usa. *Johnston, RI: Dassault Systems Simulia Corp*.
- Souza de Neto, E. A., Peric, D., and Owen, D. R. (2011). *Computational methods for plasticity: theory and applications*. John Wiley & Sons.
- Takada, S., Hassani, N., and Fukuda, K. (2001). A new proposal for simplified design of buried steel pipes crossing active faults. *Earthquake engineering & structural dynamics*, 30(8):1243–1257.
- Taylor, N. and Gan, A. B. (1986). Submarine pipeline buckling—imperfection studies. *Thin-Walled Structures*, 4(4):295–323.
- Taylor, N. and Tran, V. (1996). Experimental and theoretical studies in subsea pipeline buckling. *Marine Structures*, 9(2):211–257.
- Thusyanthan, N., Mesmar, S., Wang, J., and Haigh, S. (2010). Uplift resistance of buried pipelines and DNV-RP-F110 guidelines. In *Proc. Offshore Pipeline and Technology Conference*, pages

24–25.

- Trautmann, C. H., O'Rourke, T. D., and Kulhawy, F. H. (1985). Uplift force-displacement response of buried pipe. *Journal of Geotechnical Engineering*, 111(9):1061–1076.
- Tvergaard, V. and Needleman, A. (1981). On localized thermal track buckling. *International Journal of Mechanical Sciences*, 23(10):577–587.
- Vazouras, P., Tsatsis, A., and Dakoulas, P. (2021). Thermal upheaval buckling of buried pipelines: Experimental behavior and numerical modeling. *Journal of Pipeline Systems Engineering and Practice*, 12(1):04020057.
- Vesic, A. S. (1969). Breakout resistance of objects embedded in ocean bottom. Technical report, DUKE UNIV DURHAM NC.
- Wang, J., Eltaher, A., Jukes, P., Sun, J., Wang, F. S., et al. (2009). Latest developments in upheaval buckling analysis for buried pipelines. In *The Nineteenth International Offshore and Polar Engineering Conference*. International Society of Offshore and Polar Engineers.
- Wang, J., Haigh, S., Thusyanthan, N., and Mesmar, S. (2010). Mobilisation distance in uplift resistance modeling of pipelines. *Proc. International Symposium on Frontiers in Offshore Geotechnics*, pages 8–10.
- Wang, J., Haigh, S. K., Forrest, G., and Thusyanthan, N. I. (2012). Mobilization distance for upheaval buckling of shallowly buried pipelines. *Journal of Pipeline Systems Engineering and Practice*, 3(4):106–114.
- Wang, Z., Huachen, Z., Liu, H., and Bu, Y. (2015). Static and dynamic analysis on upheaval buckling of unburied subsea pipelines. *Ocean Engineering*, 104:249–256.
- Wells, G. N. and Sluys, L. (2001). A new method for modelling cohesive cracks using finite elements. *International Journal for numerical methods in engineering*, 50(12):2667–2682.
- White, D., Barefoot, A., and Bolton, M. (2000). Centrifuge modelling of upheaval buckling in sand. *International Journal of Physical Modelling in Geotechnics*.
- Williams, E. S. (2014). *Upheaval buckling of offshore pipelines buried in loose and liquefiable*

- soils*. PhD thesis, University of Oxford.
- Yimsiri, S., Soga, K., Yoshizaki, K., Dasari, G., and O'Rourke, T. (2004). Lateral and upward soil-pipeline interactions in sand for deep embedment conditions. *Journal of geotechnical and geoenvironmental engineering*, 130(8):830–842.
- Yoosef-Ghodsi, N. (2015). Strain-based design of pipelines. *Oil and Gas Pipelines*, pages 37–48.
- Zeng, X., Duan, M., and Che, X. (2014). Critical upheaval buckling forces of imperfect pipelines. *Applied Ocean Research*, 45:33–39.
- Zhang, B., Ye, C., Liang, B., Zhang, Z., and Zhi, Y. (2014a). Ductile failure analysis and crack behavior of X65 buried pipes using extended finite element method. *Engineering Failure Analysis*, 45:26–40.
- Zhang, W. and Tuohy, J. (2002). A three-dimensional finite element analysis of unburied flexible flowline: A case study. In *International Conference on Offshore Mechanics and Arctic Engineering*, volume 36134, pages 435–442.
- Zhang, Y., Fan, M., Xiao, Z., and Zhang, W. (2016). Fatigue analysis on offshore pipelines with embedded cracks. *Ocean Engineering*, 117:45–56.
- Zhang, Y., Xiao, Z., Zhang, W., and Huang, Z. (2014b). Strain-based CTOD estimation formulations for fracture assessment of offshore pipelines subjected to large plastic deformation. *Ocean Engineering*, 91:64–72.
- Zimmerman, T., Timms, C., Xie, J., and Asante, J. (2004). Buckling resistance of large diameter spiral welded linepipe. In *International Pipeline Conference*, volume 41766, pages 365–373.

Appendix A

Conference Paper

A.1 Some aspects of offshore pipeline design against upheaval buckling

This paper has been published and presented in the Canadian Geotechnical Conference (Geo St. John's 2019), St. John's, Newfoundland, Canada, September 29–October 2, 2019. Most of the research work presented in this paper was conducted by the first author. He also prepared the draft manuscript. The other authors supervised the research and reviewed the manuscript.

Some aspects of offshore pipeline design against upheaval buckling

Rabindra Subedi, Bipul Hawlader & Ashutosh Dhar
*Faculty of Engineering and Applied Science
Memorial University of Newfoundland, St. John's, NL, Canada*



ABSTRACT

Pipelines are often used to transport hydrocarbon in onshore and offshore environments. In offshore, proper trenching and back-filling are difficult. Therefore, an offshore pipeline might experience both lateral and upheaval buckling during operation at high temperature and high pressure (HT/HP), depending upon the soil resistance. The initial imperfection is another factor that governs the initiation and type of buckling. The existing theoretical solutions have some limitations in modelling initial imperfection and soil resistances. Finite element (FE) simulation is performed for varying initial imperfection and nonlinear soil resistances to investigate the structural response of the pipeline. The effects of burial depth, pipe diameter and wall thickness on operating temperature are studied. The post-peak degradation of uplift resistance plays a significant role in post-buckling behaviour.

RÉSUMÉ

Les pipelines sont souvent utilisés pour transporter des hydrocarbures dans des environnements onshore et offshore. En offshore, il est difficile de creuser des tranchées et de remblayer. Par conséquent, un pipeline offshore peut subir un flambage latéral et bouleversant lors de son fonctionnement à haute température et haute pression (HT/HP), en fonction de la résistance du sol. L'imperfection initiale est un autre facteur qui gouverne l'initiation et le type de flambement. Les solutions théoriques existantes présentent certaines limites pour la modélisation des imperfections initiales et des résistances du sol. En effectuant des simulations par éléments finis (FE) pour faire varier les imperfections initiales et les résistances non linéaires du sol, la réponse structurelle du pipeline est étudiée. Les effets de la profondeur d'enfouissement, du diamètre de la conduite et de l'épaisseur de la paroi sur la température de fonctionnement sont étudiés. La dégradation post-pic de la résistance au soulèvement joue un rôle important dans le comportement après le flambement.

1 INTRODUCTION

Global buckling is one of the major issues in the design of pipeline in offshore environments. The initial out-of-straightness or crookedness which is known as imperfection in a pipeline. The imperfect pipelines might buckle during operation at high temperature and pressure flow of hydrocarbon. In shallow water depths, the pipelines are buried through trenching and backfilling. The burial provides flow assurance and prevents movement of the pipeline during operation. As the lateral resistance is higher, the buried pipeline are typically more susceptible to upheaval buckling (UHB), where the pipeline might move vertically in the upward direction. If an upheaval buckling occurs, the pipeline might come out of the seabed, which creates additional design issues, such as the damage by fishing gears, dropped object and submarine debris flow impact on the suspended section of pipeline. Nielson et al. (1990) reported upheaval buckling at 26 locations of a buried pipeline in the Danish sector of the North Sea. In one segment, a 10-m section moved 1.1 m above the seabed, although the structural failure of the pipeline did not occur.

Offshore pipelines operate at the high-temperature of more than 100 °C and the maximum pressure of around 35 MPa (Hooper et al. 2004). The high temperature and pressure generate axial compressive stress, which could result in the upheaval buckling of the pipeline. Hobbs

(1984) used the concept of Tvergaard and Needleman (1981) to develop analytical solutions for upheaval and lateral buckling of submarine pipelines. Nielsen et al. (1988) established a new design procedure for the uplift resistance to control the upward movement of the imperfect pipe below the critical values to avoid progressive upheaval buckling. Palmer et al. (1990) developed a semi-empirical simplified solution for the preliminary design of submarine pipelines against upheaval buckling. Taylor and Gan (1986), and Taylor and Tran (1994) proposed the empathetic, isoprop and blister imperfection models for the submarine pipeline, and theoretically and experimentally analyzed the vertical and lateral buckling. Previous studies like Bransby et al. (2002), Palmer and King (2004), Cheuk (2005) conducted physical modeling for assessment of uplift resistance of buried pipelines. Some studies recognized the effect of post-peak degradation of uplift resistance on UHB (Klever et al. 1990; Goplen et al. 2005; Wang et al. 2009; Thusyanthan et al. 2010). Roy et al. (2018) conducted a numerical analysis to show the importance of post-peak softening in dense sand.

Albeit experimental evidence shows that both the loose and dense sands exhibit a post-peak degradation of uplift resistance, the current design guidelines, such as ALA (2005) uses a bi-linear and DNV (2007) uses a tri-linear force-displacement model for uplift resistance without considering post-peak degradation. The study aims to present finite element (FE) analyses of upheaval buckling of buried offshore pipelines in the sand. The effects of

degradation of post-peak uplift resistance and other parameters are examined. The initiation of buckling and post-buckling behaviour are studied from buckled configuration and plastic strain generation in the pipe.

2 PIPELINE IMPERFECTION

A proper representation of initial imperfection is necessary for modelling UHB. A simple mathematical function may not always represent the actual shape of the imperfect pipe. For example, Mandal and Dhar (2017) compiled the information of a seabed profile and showed that the vertical alignment of the pipe is rather complex. Based on physical imperfection and mathematical reasoning, several methods have been proposed to define the initial imperfection in buckling analysis, which includes isoprop and blister model, empathetic and sinusoidal model, and pipeline weight dependent shape (Taylor and Tran 1996; Palmer and King 2004; Karampour et al. 2013).

In the present study, the initial imperfection, as an empathetic shape (Eq. (1)), is used for numerical analysis (Taylor and Tran 1994)

$$v_o = v_{om} \left\{ 0.707 - 0.262\pi^2 \frac{x^2}{L_o^2} + 0.293 \cos\left(2.86 \frac{\pi x}{L_o}\right) \right\} \quad [1]$$

where v_o and v_{om} represent the imperfection (vertical distance from the datum to the pipe center) at any point and at the midpoint ($x = 0$), respectively. The imperfection ratio, $\tilde{v}_{om} (= v_{om}/L_o)$, plays a significant role in UHB, which are related as (Taylor and Gan 1986):

$$\frac{v_{om}}{L_o} = 2.407 \times 10^{-3} \frac{q}{EI} \quad [2]$$

where q is the submerged self-weight of pipe per unit length; EI is the flexural rigidity of the pipe.

3 NUMERICAL MODELLING AND VERIFICATION

The FE model is verified first by comparing the results with the analytical solution developed by Taylor and Gan (1986). They considered the axial resistance per unit length of the pipeline (F_a) as a function of axial displacement (u).

$$F_a = q\phi_a \left(1 - \exp(-25u/u_\phi) \right) \quad [3]$$

The value of $\phi_a = 0.7$ and $u_\phi = 5$ mm have been suggested to use by ALA (2005). The pipeline has been assumed to be on a rigid seabed.

In the present FE analysis, the pipeline is idealized as one-dimensional beam elements supported by the axial and vertical downward nonlinear soil springs (Fig. 1). For this analysis, the axial spring has been defined using Eq. (3). A large value of spring constant has been used for the vertical downward spring to simulate a rigid seabed similar to the work of Taylor and Gan (1986) where the upward resistance is zero.

FE analyses are performed using Abaqus/Standard FE software (2014). The modified static RIKS method in the

software is used to avoid numerical issues related to unstable buckling behaviour during snap-through buckling, as discussed in the following sections.

For the verification of FE model, a pipeline of 0.65-m outer diameter with a wall thickness of 15 mm having submerged self-weight of 3.8 kN/m is considered. Modelling is performed for a 3,500-m long pipeline section to eliminate the boundary effects on buckling that occurs at the middle of the pipeline. An initial imperfection is provided at the central portion of the pipeline using Eq. (1). The pipeline is discretized using B21H elements, which are a 2-node linear beam in a plane with the hybrid formulation. A mesh sensitivity analysis is performed for varying element length of (0.1 m– 1.0 m); however, no significant change in buckling is found for element size less than 1.0 m. Therefore, all the analyses are performed using 1.0-m long beam elements.

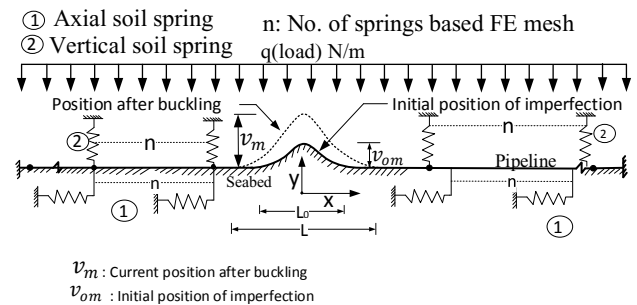


Figure 1. Problem statement and finite element modeling

The soil is modelled using nonlinear springs (SPRING1 in the software) by providing the force–displacement curves as the input for the axial and bearing resistances. The FE analysis consists of two steps: (i) the general static steps for the submerged self-weight of the pipeline was applied as a line load; and (ii) the static RIKS step where the modified RIKS algorithm is used. Also, the temperature is defined in the predefined fields in the ABAQUS for RIKS step. The geometric nonlinearity is considered in both steps. The pipe is modelled as an elastoplastic material.

A fixed boundary condition is applied at the end of the pipe. The numerical simulations are performed for three initial imperfection ratios, $\tilde{v}_{om} = v_{om}/L_o$, of 0.003, 0.007 and 0.010. The FE calculated buckle amplitude (v_m) with pipe temperature (T) is shown in Fig. 2. The dashed lines in Fig. 2 shows the $T-v_m$ curves obtained from theoretical solution (Taylor and Gan 1986). As the same pipe–soil interaction properties (spring constants in FE) are used, the FE calculated curves match well with the theoretical solution. This also implies that the developed FE model can capture snap-through and stable buckling properly. Figure 2 also shows the results obtained from Hobbs (1984), which has been developed for a perfect pipeline (i.e., no initial imperfection).

Figure 2 shows an unstable buckling for a small initial imperfection of 0.003, whereas buckling is stable for higher values of initial imperfection ratio. The critical temperature (T_{cr}) is the maximum temperature before going to the unstable buckle for a small imperfection whereas, for the

higher imperfections, it is the point of intersection of two tangents drawn from the initial and final slopes from stable buckling profile Arman et al. (2017). The safe temperature for buckling is the lowest temperature in a snap through behaviour, whereas it is beyond the point of tangency in stable buckling such that the yield stress does not exceed.

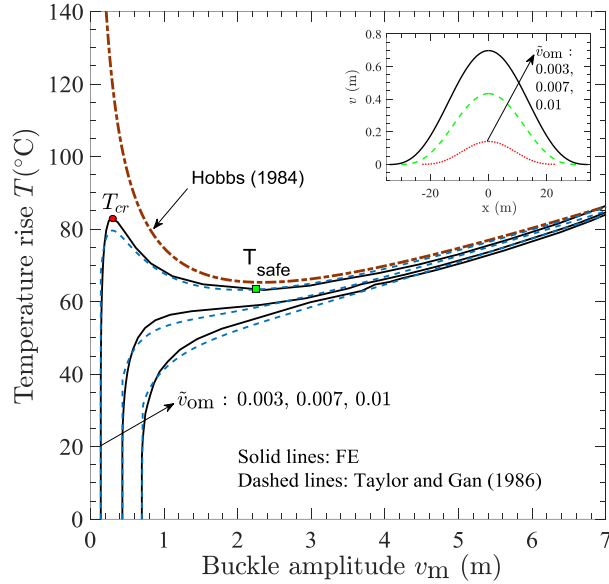


Figure 2. Comparison of FE analysis results with theoretical solutions

4 SOIL RESISTANCE IN DESIGN GUIDELINE

ALA (2005) and DNV (2007) are the two widely used guidelines for pipeline design. In ALA, bi-linear curves are used to define the force–displacement behaviour using soil springs for axial, lateral and vertical directions for a 3D pipeline. Based on ALA (2005), the spring force increases linearly with relative displacement up to the maximum value and then remains constant.

The maximum axial soil resistance per unit length of the pipeline (F_{ap}) buried in sand can be calculated as:

$$F_{ap} = 0.5 \pi D H \gamma (1 + K_0) \tan(\phi_\mu) \quad [4]$$

where γ is the effective unit weight of soil; H is the burial depth from the center of the pipe; D is the diameter of the pipe; K_0 is the coefficient of earth pressure at rest; ϕ_μ is the axial interface friction angle between pipe and soil. The burial depth is expressed in a normalized form for using embedment ratio, \tilde{H} ($= H/D$). ALA (2005) also suggested that the relative axial displacement (u) required to mobilize the peak (u_p) is 3 mm and 5 mm for dense and loose sands, respectively.

The maximum bearing resistance (F_{bp}) for sand can be calculated as (ALA 2005):

$$F_{bp} = N_q \gamma H D + 0.5 D^2 \gamma N_\gamma D^2 \quad [5]$$

where $N_q = e^{(\pi \tan \phi')} \tan^2(45^\circ + \phi'/2)$, $N_\gamma = e^{(0.18\phi' - 2.5)}$ are the bearing capacity factors. Again, the vertical penetration resistance (F_b) increases linearly with downward movement (v_b), at $v = v_{bp}$ it reaches the F_{bp} and then remains constant. Moreover, v_{bp} is related to the diameter of the pipe as $v_{bp} = 0.1D$, for sand.

The maximum vertical uplift resistance (F_{up}) for the pipeline in sand can be calculated as (ALA 2005):

$$F_{up} = N_{qv} \gamma H D \quad [6]$$

where $N_{qv} = \phi'H/44D$ ($\leq N_q$ in bearing capacity equation (Eq. (5)) and ϕ' is in degree. Again, the upward resistance (F_u) increases linearly with upward displacement (v) and, at $v = v_p$, the maximum resistance F_{up} is mobilized. After v_p , the upward resistance remains constant at F_{up} . ALA (2005) suggested that v_p is related to burial depth (H) as $v_p = 0.01H - 0.02H$ for sand.

DNV (2007) suggested a trilinear force–displacement curve for uplift resistance. The peak uplift resistance can be calculated as:

$$F_{up} = (1 + f\tilde{H})\gamma\tilde{H}D^2 \quad [7]$$

where f is the uplift resistance factor. DNV (2007) suggested $f = 0.1 - 0.3$ and $f = 0.4 - 0.6$ for loose and medium/dense sands, respectively. The maximum uplift resistance mobilizes at $v_p = 0.005H - 0.008H$, which is lower than the v_p recommended by ALA (2005), as mentioned above.

The force–displacement curve prior to the peak is defined by two linear segments that intersect at a point below the peak (βv_p , αF_{up} , where α and β are two constants). DNV (2007) recommended $\beta = 0.2$, and $\alpha = 0.75 - 0.85$ and $\alpha = 0.65 - 0.75$ for loose and dense sands, respectively. The lower and upper values of f and α represent the lower bound (LB) and upper bound (UB), respectively. The geometry and material properties used in the current analysis is shown in Table 1.

5 LIMITATIONS IN MODELING OF UPLIFT BEHAVIOUR

DNV (2007), ALA (2005) guidelines suggest that the uplift resistance after the peak remains constant. However, the works by Trautmann et al. (1985), Nielsen et al. (1990), Klever et al. (1990), Cheuk (2005), Goplen et al. (2005), Wang et al. (2012) suggest that the soil resistance gradually decreases after the peak for shallow to intermediate burial depths. At a large displacement, the reduction of uplift resistance is significant. Physical experiments show that it becomes zero (as expected) when the pipeline moves to the ground surface (Wang et al. 2012). Observing large upward displacement in the field, Nielsen et al. (1990) schematically show the typical nonlinear uplift resistance curve (solid line in Fig. 3). Three discrete points are used to characterize the force–displacement behavior. The submerged self-weight of the pipe plus the weight of the soil column directly above the

pipe corresponds to point 1 where the upward displacement is assumed to be zero.

From point 1 to 2, the continuous upward movement of the imperfect pipe section mobilizes at an uplift resistance Table 1. Geometry and material properties used in analysis

Parameters	Value
Length of pipe, L (m)	3500
External diameter of pipe, D (mm)	300
Wall thickness of pipe, t (mm)	12.7
Thickness of concrete cover (m)	0.05
Density of steel, ρ_s (kg/m ³)	7850
Density of concrete, ρ_c (kg/m ³)	2800
Density of oil, ρ_o (kg/m ³)	800
Submerged weight of oil-filled pipe, q (N/m)	1594
Angle of internal friction of soil, ϕ' (°)	35
Coefficient of earth pressure at-rest, K_0	0.5
Effective unit weight of soil, γ (kN/m ³)	9
Axial interface friction angle, ϕ_{μ} (°)	28
Young's modulus of pipe, E (GPa)	206
Poisson's ratio of pipe (ν)	0.3
Yield stress of pipe, σ_y (MPa)	448
Ultimate strength, σ_{ult} (MPa)	531
Coefficient of thermal expansion, α (1/°C)	11×10^{-6}

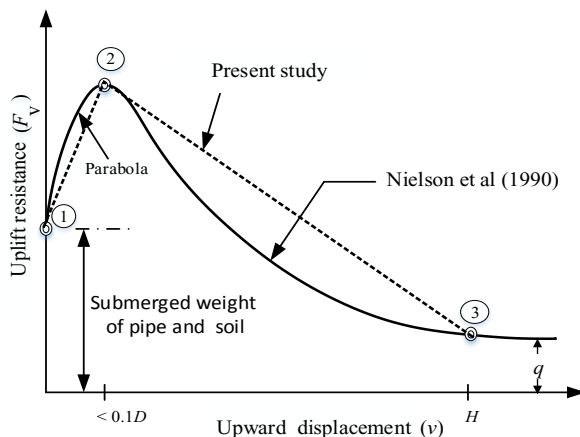


Figure 3. Uplift force–displacement behavior

due to the activation of shear stresses in the soil. Based on physical experimental results (Trautmann et al. 1985), Nielsen et al. (1990) suggested that the displacement required to reach the peak uplift resistance at point 2 is $(0.02 + 0.008H/D)D \leq 0.1D$. Once the upward movement of the pipe exceeds the displacement required to reach the peak uplift resistance, the general shear failure occurs in the soil, resulting in degradation of uplift resistance until the point 3 when the pipe reaches the ground surface or seabed.

Numerical modeling also shows a nonlinear post-peak reduction of uplift resistance, F_v (Roy et al. 2018). For

dense sand, F_v reduces quickly immediately after the peak, which is due to the reduction of shear strength parameters (friction and dilation angles) with the development of plastic shear strains. At large displacements, the reduction of F_v mainly occurs due to the reduction of cover depth.

Although the post-peak behaviour is nonlinear, a linear degradation of uplift resistance, as shown by the dashed line in Fig. 3, is used in this study. Note that a linear post-peak degradation model will not be valid for pipelines at large burial depths. Therefore, the analyses are performed for the embedment ratio (\bar{H}) of 1–3. The peak value (F_{up}) is calculated based on ALA (2005) and DNV (2007) (Eqs. 6 and 7). In the calculation with DNV, $\alpha = 0.65$ (LB), $\alpha = 0.75$ (UB), $\beta = 0.2$, $f = 0.4$ (LB) and $f = 0.6$ (UB) are used. As an example, for the soil parameters listed in Table 1 and $\bar{H} = 3$, the calculated $F_{vp} = 5921$ N/m (ALA) and $F_{vp} = 5459$ N/m (DNV LB) and $F_{vp} = 6948$ N/m (DNV UB). Note that DNV (2007) somehow recognized the importance of post-peak degradation of uplift resistance, but ALA (2005) is silent on post-peak degradation. In the following sections, where the post-peak degradation is considered, the force–displacement relationship up to the peak is calculated based on DNV (2007) upper or lower bounds.

6 EFFECTS OF AXIAL RESISTANCE IN BUCKLED SECTION

The axial soil resistance has a significant impact on UHB. Theoretically, the axial resistance should be reduced once the pipe buckles upward from the initial position because of reduction of cover depth, and the axial resistance will be zero when it moves above the seabed. However, the variation in axial spring resistance with upward displacement adds additional complexities in numerical simulation using the built-in modelling approaches available in the software. Therefore, to check the effect of this, analyses are performed for the following axial resistances in the central portion ($2L_0$) of the pipeline (Fig. 1) where buckling occurs: (i) full axial resistance using Eq. (4), (ii) no axial resistance, which is a conservative assumption, and (iii) half of the axial resistance based on Eq. (4) (average of the above two). Outside the possible buckled zone, i.e. beyond $2L_0$ length of initial imperfection full axial resistance is used for all three cases.

Figure 4 shows that the variation in axial resistance in the buckled segment (full to zero) does not have a significant effect on the critical temperature. However, the safe temperature decreases considerably—as an example, for the initial imperfection ratio of 0.003 the safe temperature decreases by ~ 12 °C when zero axial resistance is used instead of full resistance (see the inset of Fig. 4). In the following sections, all the analyses are performed with the full axial resistance.

7 EFFECTS OF INITIAL IMPERFECTION AND EMBEDMENT RATIO

The temperature rise versus maximum buckle amplitude for different initial imperfections and embedment ratios are presented in Fig. 5(a). In these simulations, the peak

resistance is calculated using ALA (2005) and DNV (2007) (Eqs. 4–7), together with the linear decrease in post-peak resistance (Fig. 3) for DNV only. Both critical and safe temperatures increase with embedment ratio (Fig. 5(b)). The critical and safe temperature is higher if the post-peak degradation in uplift resistance is not considered (i.e., soil resistance remains constant after the peak). Due to post-peak degradation, the safe temperature decreases more than the critical temperature, and it is even more significant for larger burial depths.

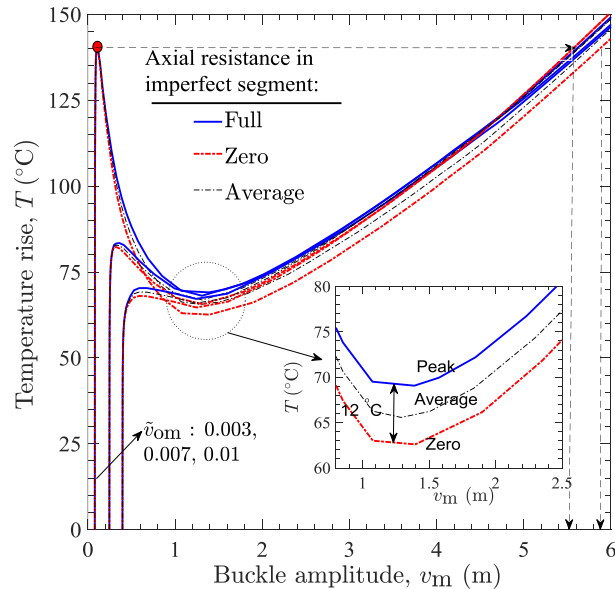


Figure 4. Effects of axial resistance in imperfect section

Similar analyses are performed with DNV (2007) upper bound up to the peak, together with a linear decrease in the post-peak region. The temperature rises with maximum buckle amplitude is shown in Fig. 6. Again, the post-peak degradation in uplift resistance significantly reduces the safe temperature as compared to the critical temperature.

8 VERTICAL DEFORMATION AND PLASTIC SHEAR STRAIN

The selection of maximum buckling temperature and corresponding maximum buckle amplitude for the design of offshore pipeline is challenging. If the design is based on a strain-based design criterion, the pipe might be able to move a sufficiently large vertical distance from the initial position without failure Bai and Bai (2005).

Figure 7(a) shows the vertical displacement of the pipe (including the initial imperfection v_0) along the length from the midpoint for a pipeline of $\tilde{v} = 0.003$ and $\tilde{H} = 3$. The maximum (critical) temperature (T_{cr}) before snap-through is 139 °C, which increases gradually with an increase in vertical displacement. As the maximum buckle amplitude before reaching T_{cr} is small (≤ 0.096 mm), the pipe displacements for this range is shown in the inset of Fig. 7(a). After reaching the critical temperature, the pipe

temperature decreases but the vertical displacement continues because of snap-through buckling (see Fig. 6). Figure 6 also shows that, if the operating temperature somehow exceeds the critical temperature, a sudden uplift of 5.8 m occurs, as shown by drawing a horizontal line from T_{cr} to the $T-v_m$ curve in Fig. 6. This could result in movement of a segment of the pipe above the seabed. Nielson et al. (1990) reported a 10-m pipe segment moved above the seabed due to upheaval buckling. The lowest (safe) temperature is 69 °C.

The strain-based criteria are currently used in the design of the pipeline, where the strain is maintained below an allowable strain, typically 1%–2% (Palmer et al. 1990). Figure 7(b) shows the longitudinal plastic strains (ϵ_p) developed in the pipe. The plastic strains generated at the midsection of the pipe and at the end of the buckled section where the curvature is high (Fig. 7(a)). For this analysis, $\epsilon_p \geq 0.02$ in the snap-through zone when $T \sim 110$ °C and the maximum buckle amplitude of 4.2 m.

9 EFFECTS OF PIPE DIAMETER AND WALL THICKNESS

The cross-sectional properties of pipe play an essential role in buckling, which is investigated using varying pipe diameter and wall thickness. Only one parameter is varied in the analysis, while the other parameters are the same as Table 1. The uplift force–displacement behaviour based on DNV LB with post-peak softening (Fig. 3) is considered. Analyses are performed for $\tilde{H} = 3$, and two imperfection ratios, $\tilde{v}_{om} = 0.003$ and 0.01.

9.1 Diameter

Three pipelines of 0.1413-m, 0.2985-m, and 0.4064-m diameter, with the same wall thickness of 0.0127 m, are considered, which covers the commonly used offshore pipeline sizes. The submerged self-weight of the pipeline for the oil-filled condition is calculated as 0.85 kN/m, 1.59 kN/m, 2.05 kN/m, respectively. Figure 8 shows the buckling response for six analyses. As the pipe diameter is different, initial imperfection, including initial buckle amplitude v_{om} is different for a given \tilde{v}_{om} .

Figure 8 shows that the critical and safe buckling temperatures increase with pipe diameter. For example, $T_{cr} = 60$ °C and 121 °C for 141.3-mm and 298.5 mm diameter pipes, respectively, for the initial imperfection ratio of 0.003.

9.2 Wall Thickness

Four analyses are performed for varying wall thickness, t ($= 8.8$ mm, 10.3 mm, 12.7 mm, and 14.3 mm) for pipe diameter of 0.3 m. The other parameters are listed in Table 1. The submerged weight of the pipe decreases with a reduction in wall thickness, which lowers the effective axial compression. The numerical analyses show that the thinner pipe wall has higher upheaval buckling resistance than the thicker pipe wall for the same outer diameter (Fig. 9). The critical and safe buckling temperature decreases

with the increase in pipe thickness. Palmer et al. (1990) suggested a reduced wall thickness to minimize potential upheaval buckling.

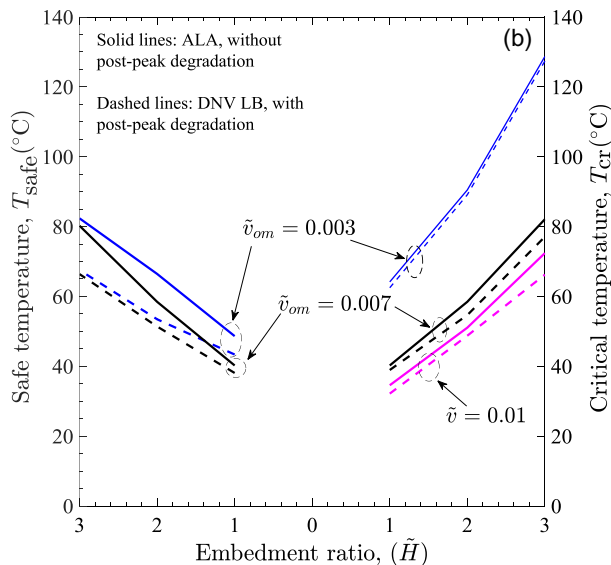
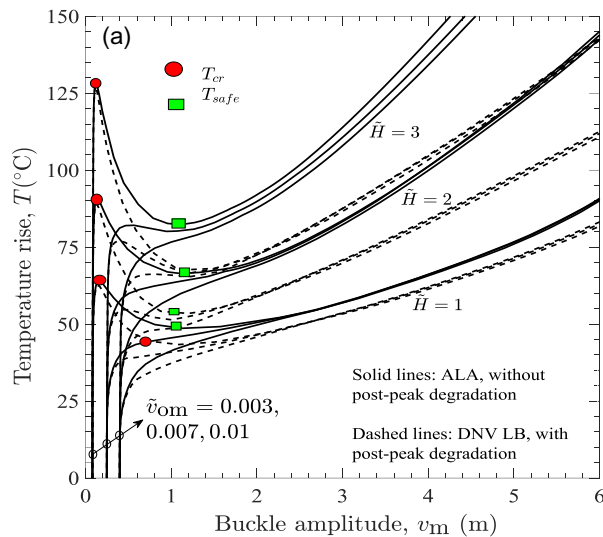


Figure 5. Effects of burial depth: (a) Buckling profile; and (b) Safe and critical temperatures

10 CONCLUSIONS

The aim of the current design guidelines for upheaval buckling is to ensure that the pipeline remains in place during operation (DNV 2007). However, many field observation shows significant upward displacements due to upheaval buckling. The present study examines the response of buried offshore pipelines if upheaval buckling occurs. The upward displacement of the pipe could reduce

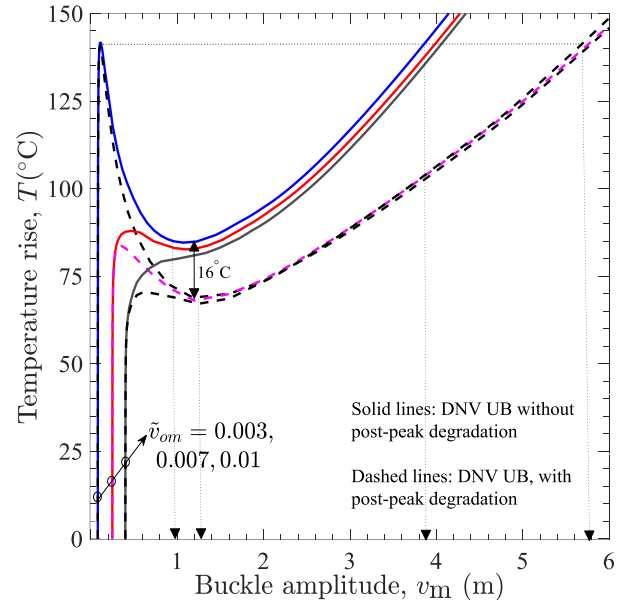


Figure 6. Effects of post-peak softening with DNV UB soil spring properties

the uplift resistance, which is considered in the analysis using a linear post-peak degradation model as a function of upward displacement. It is shown that the pipeline might displace a large vertical distance, even might move above the seabed, especially in snap-through buckling cases. However, the generated plastic strains might be within the allowable limit for this large displacement, and therefore, structural failure may not occur. One of the limitations of this study is that the linear post-peak strength degradation model used in this study is valid for loose to medium sand and the pipelines at shallow burial depths.

11 ACKNOWLEDGEMENTS

The works presented in this paper have been supported by the Research and Development Corporation of Newfoundland and Labrador through the ArcticTECH program and the Natural Sciences and Engineering Research Council of Canada (NSERC).

REFERENCES

- Abaqus, V. 2014. 6.14 documentation. Dassault Systemes Simulia Corporation, 651.
- ALA 2005. Guidelines for the design of buried steel pipe. In American Society of Civil Engineers.
- API Design, C. 1999. Operation and maintenance of offshore hydrocarbon pipelines (limit state design). API recommended Practice, 1111.
- Amin Arman, Riyadul & Roy, Kshama & Hawlader, Bipul & Dhar, Ashutosh. 2017. Finite Element Analysis of Upheaval Buckling of Submarine Pipelines with Initial Imperfection.

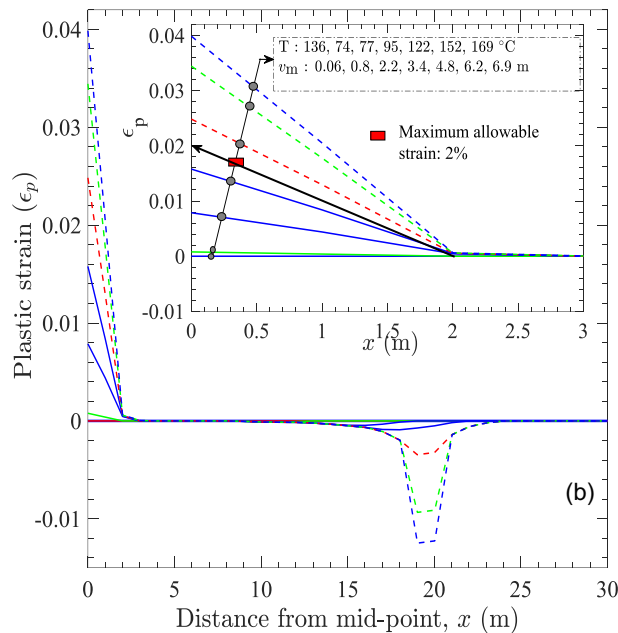
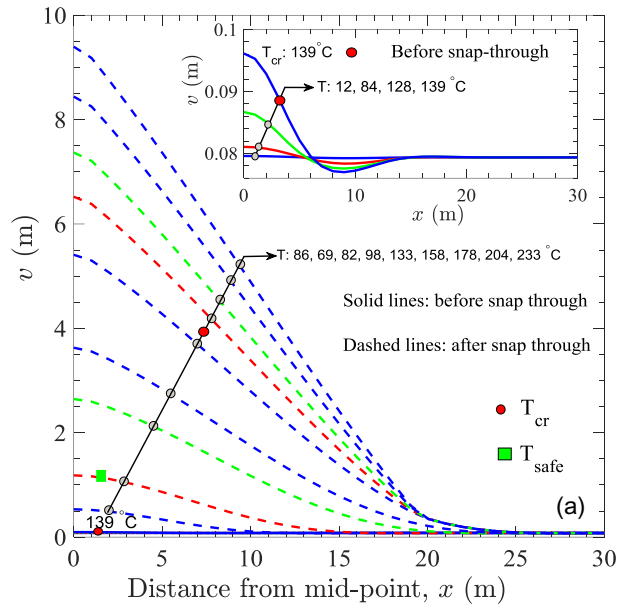


Figure 7. Response to temperature loading: (a) Pipeline profile; and (b) Plastic strain in pipeline

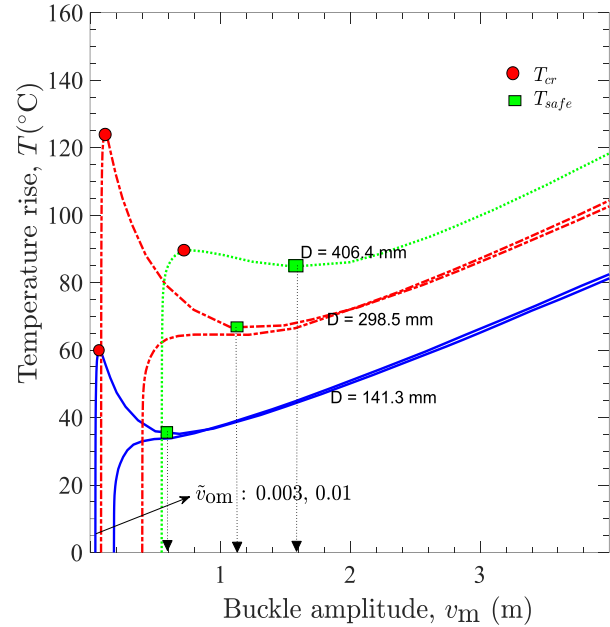


Figure 8. Effects of the pipe diameter

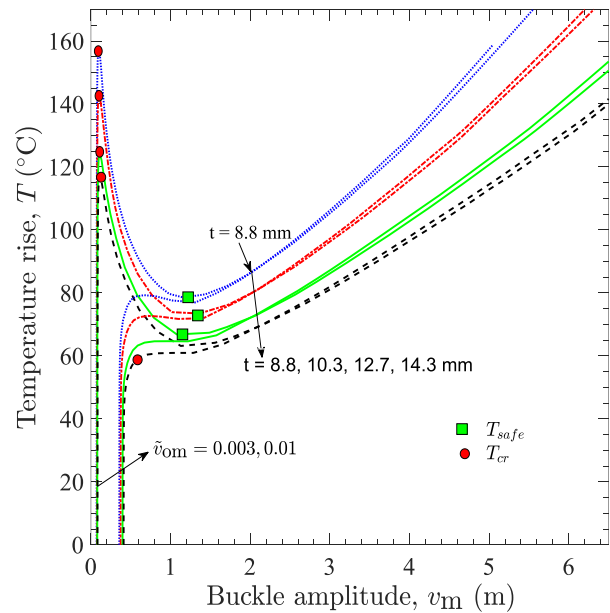


Figure 9. Effects of pipe wall thickness

Bransby, M., Newson, T., and Brunning, P. 2002. The upheaval capacity of pipelines in jetted clay backfill. *International Journal of Offshore and Polar Engineering*

Cheuk, C. Y. 2005. Soil-pipeline interaction at the seabed. PhD thesis, University of Cambridge, UK.

Crisfield, M. 1981. A fast incremental/iterative solution procedure that handles "snap-through". In *Computational Methods in Nonlinear Structural and Solid Mechanics*, pages 55–62. Elsevier.

DNV 2007. Global buckling of submarine pipelines—structural design due to high temperature/high pressure. RP-F110, Oslo, Norway.

Goplen, S., Strom, P., Levold, E., and Mork, K. J. 2005. Hotpipe JIP: HP/HT buried pipelines. In *ASME 2005 24th International Conference on Offshore Mechanics and Arctic Engineering*, pages 691–699. American Society of Mechanical Engineers.

Hobbs, R. E. 1984. In-service buckling of heated pipelines. *Journal of Transportation Engineering*, 110(2): 175–189.

- Hooper, J., Maschner, E., and Farrant, T. 2004. Penguins pipeline system—design challenges for the world's longest snaked lay HP/HT pipe tie-back. In Offshore Pipeline Technology Conference
- Karampour, H., Albermani, F., and Gross, J. 2013. On lateral and upheaval buckling of subsea pipelines. *Engineering structures*, 52:317–330.
- Klever, F., Van Helvoirt, L., Sluyterman, A., et al. 1990. A dedicated finite-element model for analyzing upheaval buckling response of submarine pipelines. In Offshore Technology Conference.
- Liu, R., Wang, W.G., and Yan, S.W. 2013. Finite element analysis on thermal upheaval buckling of submarine burial pipelines with initial imperfection. *Journal of Central South University*, 20(1):236–245.
- Maltby, T. C. and Calladine, C. R. 1995. An investigation into upheaval buckling of buried pipelines—ii. Theory and analysis of experimental observations. *International journal of mechanical sciences*, 37(9):965–983.
- Mondal, B.C. and Dhar, A.S., 2017. Upheaval buckling of surface-laid offshore pipeline. *Applied Ocean Research*, 66, pp.146-155.
- Nielsen, N., Pedersen, P., Gundby, A., and Lyngberg, B. 1988. Design criteria for upheaval creep of buried subsea pipelines. *Offshore Mech Arct Eng ASME*, 112:11–22.
- Palmer, A., Ellinas, C., Richards, D., Guijt, J., et al. 1990. Design of submarine pipelines against upheaval buckling. Offshore Technology Conference.
- Palmer, A. C. and King, R. A. 2004. Subsea pipeline engineering. PennWell Books.
- Roy, K., Hawlader, B., Kenny, S., and Moore, I. (2018). Upward pipe–soil interaction for shallowly buried pipelines in dense sand. *Journal of Geotechnical and Geo-environmental Engineering*, 144(11): 04018078.
- Taylor, N. and Gan, A. B. 1986. Submarine pipeline buckling imperfection studies. *Thin-Walled Structures*, 4(4): 295–323.
- Taylor, N. and Tran, V. 1994. Experimental and theoretical studies in subsea pipeline buckling. *Marine Structures*, 9(2):211–257.
- Thusyanthan, N., Mesmar, S., Wang, J., and Haigh, S. 2010. Uplift resistance of buried pipelines and dnv-rp-f110 guidelines. In Proc. Offshore Pipeline and Technology Conference, pages 24– 25.
- Tvergaard, V. and Needleman, A. 1981. On localized thermal track buckling. *International Journal of Mechanical Sciences*, 23(10):577–587.
- Wang, J., Eltaher, A., Jukes, P., Sun, J., Wang, F. S., et al. 2009. Latest developments in upheaval buckling analysis for buried pipelines. In the Nineteenth International Offshore and Polar Engineering Conference. International Society of Offshore and Polar Engineers.
- Wang, J., Haigh, S., Thusyanthan, N., and Mesmar, S. 2010. Mobilization distance in uplift resistance modeling of pipelines. Proc. International Symposium on Frontiers in Offshore Geotechnics, pages 8–10.
- Yong Bai and Qiang Bai 2005. Subsea Pipelines and Risers, Elsevier
- Zeng, X., Duan, M., and Che, X. 2014. Critical upheaval buckling forces of imperfect pipelines. *Applied Ocean Research*, 45:33–39.